Stony Brook University

Evolution of Immiscibly Blended Functionalized Polymers with Respect to Cure Parameters and Formulation

A Dissertation Presented

by

Nicholas Walter Medicus Heller

to

The Graduate School

in Partial Fulfillment of the

Requirements

for the Degree of

Doctor of Philosophy

in

Materials Science and Engineering

Stony Brook University

December 2016

Stony Brook University

The Graduate School

Nicholas Heller

We, the dissertation committee for the above candidate for the

Doctor of Philosophy degree, hereby recommend

acceptance of this dissertation.

Clive R. Clayton
Leading Professor, Department of Materials Science and Engineering

Gary P. Halada
Associate Professor, Department of Materials Science and Engineering

Taejin Kim
Assistant Professor, Department of Materials Science and Engineering

James H. Wynne
Senior Research Chemist, Naval Research Laboratory, Coating Chemistry

This dissertation is accepted by the Graduate School

Nancy Goroff
Interim Dean of the Graduate School

Abstract of the Dissertation

Evolution of Immiscibly Blended Functionalized Polymers with Respect to Cure Parameters and Formulation

by

Nicholas Walter Medicus Heller

Doctor of Philosophy

in

Materials Science and Engineering

Stony Brook University

2016

Powder coatings are becoming ubiquitous in the coating marketplace due to the absence of solvents in their formulation, but they have yet to see implementation in low-reflectance outdoor applications. This demand could be met by utilizing polymer blends formulated with low loadings of matting agents and pigments. The goal of this research is a thorough characterization of prototype low-reflectance coatings through several analytical techniques. Prototypical thermoset blends consist of functionalized polyurethanes rendered immiscible by differences in polar and hydrogen bonding characteristics, resulting in a surface roughened by droplet domains. Analysis of both pigmented and control clear films was performed. This research project had three primary aims: (1) determine the composition of the resin components of the polymer blend; (2) to monitor the evolution of domains before and during curing of clear polymer blends; (3) to monitor the evolution of these domains when pigments are added to these blends.

The clear films enabled unhindered analysis by Fourier transform infrared (FTIR) and Raman spectroscopy on the binder. However, these domains provided no spectroscopic signatures despite their observation by optical microscopy. This necessitated the development of a new procedure for cross-section preparation that leaves no contamination from polishing media, which enabled Raman mapping of the morphology via an introduced marker peak from styrene monomer. The clears were analyzed as a powder and as films that were quenched at various cure-times using FTIR, Raman, transmission electron microscopy (TEM), and thermomechanical methods to construct a model of coating evolution based on cure parameters and polymer dynamics. Domains were observed in the powder, and underwent varying rates of coarsening as the cure progressed. TEM, scanning electron microscopy and thermomechanical methods were also used on pigmented systems at different states of the cure, including in powder form. TEM analysis additionally revealed the encapsulation of pigment particles by the domains, which helped explain the interaction between phase separation and pigment materials. The knowledge gained from fundamental characterization could be used to enable future generations of durable powder coatings with dead matte finishes.

Dedication Page

This dissertation is dedicated to the memory of my father, Walter Perrin Heller (1942-2001), whose teachings, guidance, and kindness persist to the here and now, and beyond.

Table of Contents

List of Tables....x
List of Equations....xi
List of Figures....xiv

Chapter 1: Introduction and Background on Powder Coatings....1
1.1 Introduction....1
1.2 Powder coatings....2
1.3 Materials processing and coating application....3
1.4 Pigment wetting and dispersion....6
1.5 Gloss and surface roughness....10
1.6 Polymer blends....11
1.7 Phase separation mechanisms....15
1.8 Compatibilization....19
1.9 Choice of substrate....21
1.10 References....22

Chapter 2: Sample Preparation and Spectroscopic Analysis....26
2.1 Coating preparation....26
2.2 Cross-section preparation....27
2.2.1 Cross-sections for spectroscopic analysis....27
2.2.2 Cross-sections for TEM....30
2.3 Vibrational spectroscopy....30
2.3.1 Fourier transform infrared spectroscopy (FTIR)....30
2.3.2 Raman spectroscopy....36
2.4 X-ray photoelectron spectroscopy (XPS)....44
2.4.1 Instrumentation....44
2.4.2 Theory....50
2.4.3 Equipment....55
2.5 References....56

Chapter 3: Analysis by Electron Microscopy....58
3.1 Transmission electron microscopy (TEM)....59
2.2.1 Instrumentation....59
2.2.2 Electron lensing....62
2.2.3 Electron scattering....65
2.2.4 Sample preparation for TEM....68
2.2.5 TEM equipment....71
3.2 Scanning electron microscopy (SEM)....72
3.2.1 Instrumentation....72
3.2.2 Electron scattering for SEM....73
3.2.3 Focus depth....76
3.2.4 SEM equipment....77
3.3 Energy dispersive x-ray spectroscopy (EDX)....79

3.4 References....78

Chapter 4: Initial Preparation of Cross-Sections and Their Analysis by Raman Spectroscopy....81
4.1 Introduction....81
4.2 Experimental methods....81
8.3.1 Optical microscopy....81
8.3.2 Fourier transform infrared spectroscopy....81
8.3.3 Raman spectroscopy....82
8.3.4 Initial cross-section preparation....82
8.3.5 Final cross-section preparation....83
4.3 Results....83
4.4 Conclusion....90
4.5 References....90

Chapter 5: Selective Staining for Enhanced Micro-Raman Spectroscopy....91
5.1 Introduction....91
5.2 Experiment....95
5.2.1 Coating preparation....95
5.2.2 Optical microscopy....96
5.2.3 Differential scanning calorimetry....96
5.2.4 Raman spectroscopy....97
5.2.5 Cross-section sample preparation....97
5.2.6 Styrene vapor staining....98
5.3 Results/Discussion....98
5.3.1 DSC analysis and optical microscopy of the blend surface....98
5.3.2 Raman spectroscopy of coating surfaces and embedded cross-sections...101
5.3.3 Domain identification by Raman mapping....103
5.3.4 Controlled staining with styrene vapor....110
5.4 Conclusion....113
5.5 References....115

Chapter 6: Monitoring of Crosslink Density by Vibrational Spectroscopy and TEM....117
6.1 Introduction....117
6.2 Experiment....119
6.2.1 Coating preparation....119
6.2.2 Vibrational spectroscopy....120
6.2.3 Transmission electron microscopy (TEM) 122
6.2.4 Analysis of micrographs by ImageJ....122
6.3 Results/Discussion....123
6.3.1 Spectral evolution....123
6.3.2 Carbonyl deconvolution....127
6.3.3 Correlating spectroscopy with morphology....130

6.3.4 ε-caprolactam variations with respect to cure time and cure temperature....135
6.3.5 Resistance to styrene solvent as an experimental model for resistance to ε-caprolactam....137
6.4 Conclusion....142
6.5 References....144

Chapter 7: How Droplet Domains Evolve....147
7.1 Introduction....147
7.2 Experiment....150
7.2.1 Laser scanning confocal microscopy (LSCM) 150
7.2.2 Fourier transform infrared spectroscopy (FTIR)....150
7.2.3 Raman spectroscopy....150
7.2.4 Gloss measurements....151
7.2.5 Differential scanning calorimetry (DSC) 151
7.2.6 Optical microscopy....152
7.2.7 Rheology....152
7.2.8 Transmission electron microscopy (TEM) 152
7.2.9 Coating preparation....153
7.3 Results....154
7.3.1 OM and LSCM of polymer blend surface....154
7.3.2 DSC of quenched samples....157
7.3.3 Rheology of blended resins....158
7.3.4 Reaction monitoring by vibrational spectroscopy....160
7.3.5 Transmission electron micrographs....161
7.4 Discussion....171
7.4.1 Powder to 1.5 minutes: sintering of powder particles and nucleation of domains....171
7.4.2 2- to 3-minute interval: rapid coarsening....173
7.4.3 Secondary glass transition and transient double phase separation....175
7.4.4 Cure dynamics from 4 to 12 minutes....177
7.5 Conclusion....181
7.6 References....184

Chapter 8: Forced Flocculation via Pigment Segregation....187
8.1 Introduction....187
8.2 Experiment....190
8.2.1 Coating preparation....190
8.2.2 Laser scanning confocal microscopy (LSCM)....192
8.2.3 Gloss measurements....192
8.2.4 Optical microscopy....193
8.2.5 Transmission electron microscopy (TEM) 193
8.2.6 Scanning electron microscopy (SEM) 194
8.2.7 X-ray photoelectron spectroscopy (XPS) 194
8.3 Results/Discussion....195
8.3.1 Surface analysis....195

8.3.2 Correlating the surface with optical micrographs of cross-section.....199
8.3.3 Electron microscopy of cross-sectioned black films at various cure times.....200
8.3.4 Complementing TEM with SEM cross-sections of fully cured black, tan, and green films.....210
8.3.5 Insight from XPS studies.....214
8.4 Conclusion.....217
8.5 References.....219

Chapter 9: Investigation of Clear Coatings by XPS.....221
9.1 Introduction.....221
9.2 Instrumentation.....221
9.3 Results/Discussion.....222
9.3.1 Airside.....222
9.3.2 Investigation of polymer adhesion.....229
9.4 Conclusion.....233
9.5 References.....234

Chapter 10: Conclusions and Future Work.....236
10.1 Conclusions.....236
10.2 Future work.....240
10.3 Closing remarks.....242
10.4 References.....242

List of Tables

Table 1-1 – Geometries for specular gloss measurements and applications.....10

Table 5-1 – Coating formulations by percentage based upon raw material.....95

Table 6-1 – Assigned carbonyl peaks from LRS.....130

Table 6-2 – Raman peak area ratio of C=O (x/1600 cm^{-1} peak height × 100).....132

Table 6-3 – Relationship between ε-cap C=O peak area and hole density normalized to low OH film for appropriate column.....135

Table 7-1 – Surface areas of cross-sections of domains over a 2 mm distance plus the ratio of adhered domains to globules (A/G.....181

Table 9-1 – Atomic percentages at 90˚ and 60˚ incident angles of polymer interfaces.....223

Table 9-2 – Contribution of different functionalities to envelope of deconvoluted C 1s XPS spectra at 60˚ and 90˚ incident angles and their ratios for air-side.....225

Table 9-3 – Contribution of different functionalities to envelope of fitted C 1s XPS spectra at 60˚ and 90˚ incident angles and their ratios for substrate-side and tin substrate.....229

List of Equations

Equation 1-1 – Orchard Equation describing surface leveling.....6

Equation 1-2 – Washburn's Equation describing infiltration rate into capillary tube.....7

Equation 1-3 – Blake-Krozeny Equation for wetting of pigment cluster.....7

Equation 1-4 – Hydrodynamic force on a pigment cluster.....8

Equation 1-5 – Cohesive strength of a pigment cluster.....9

Equation 1-6 –Van der Waals force in a dry agglomerate.....9

Equation 1-7 – Hamaker constant within a resin.....9

Equation 1-8 – Calculation of gloss.....10

Equation 1-9 – Relation between specular reflectance and surface roughness.....10

Equation 1-10 – Rayleigh criterion for smooth surfaces.....11

Equation 1-11 – Gibbs free energy of mixing.....15

Equation 1-12 – Entropy of mixing for polymer blends.....15

Equation 1-13 – Enthalpy of mixing for polymer blends.....16

Equation 1-14 – Interaction parameter in terms of solubility parameters.....17

Equation 1-15 – Hansen Solubility Parameters.....17

Equation 1-16 – Interaction parameter in terms of Hansen solubility parameters.....17

Equation 1-17 – Gibbs free energy from concentration fluctuation.....19

Equation 2-1 – Constructive interference in optical path difference.....32

Equation 2-2 – Destructive interference in optical path difference.....32

Equation 2-3 – Fourier transform.....33

Equation 2-4 – Hooke's Law for molecular vibration.....34

Equation 2-5 – Relation between vibrational frequency and wavelength.....36

Equation 2-6 – Kinetic energy of electron entering hemispherical analyzer.....47

Equation 2-7 – Photoelectric effect.....50

Equation 2-8 – TPP-2M predictive equation and various parameters for inelastic mean free path.....52

Equation 2-9 – Equation for Shirley background.....55

Equation 2-10 – Gaussian line shape.....56

Equation 2-11 – Lorentzian line shape.....56

Equation 2-12 – Product of Gaussian and Lorentzian line shapes.....56

Equation 3-1 – Wavelength of imaging electron within microscope.....59

Equation 3-2 – Magnification of image.....63

Equation 3-3 – Newton's lens equation.....63

Equation 3-4 – Lorentz force.....64

Equation 3-5 – Quantum mechanical plane wave of incoming electron.....66

Equation 3-6 – Spherical wave of scattered electron.....66

Equation 3-7 – Superposition of plane wave and scattered wave.....66

Equation 3-8 – Scattering amplitude.....67

Equation 3-9 – Differential elastic cross-section.....67

Equation 3-10 – Total cross-section.....67

Equation 3-11 – Intensity of the final image.....67

Equation 3-12 – Depth of focus.....76

Equation 5-1 – Rayleigh criterion for chemical mapping.....92

Equation 5-2 – Numerical aperture.....93

Equation 5-3 – Peak height ratio for chemical mapping.....104

Equation 7-1 – Capillary number describing domain deformation from hydrodynamic stress...174

Equation 8-1 – Krieger-Dougherty model describing relation between viscosity and PVC.....187

Equation 8-2 – Effective volume fraction from pigments with adsorption layer.....188

List of Figures

Figure 1-1 – Schematic of general powder coating production.....3

Figure 1-2 – Schematic of twin screws within an extruder.....4

Figure 1-3 – Powder coating application via corona-charge spray gun.....5

Figure 1-4 – Schematic representation of surface leveling for a powder coating.....6

Figure 1-5 – Schematic representation of pigment dispersions; a) wetting of agglomerate; b) dispersed; c) flocculated.... 7

Figure 1-6 – How surface roughness affects gloss according to Equations 1-8 and 1-9.....11

Figure 1-7 – Beam of light refracted by incompatible droplets (domains) of a resin with a different index of refraction in a continuous phase of clear binder (n_1).....13

Figure 1-8 – Basic types of phase structures.....14

Figure 1-9 – Schematic representation of spatial arrangements of molecules in a binary mixture of a) low molecular weight components and b) a polymer blend.....16

Figure 1-10 – Phase diagram of a binary symmetric polymer blend with lower critical solution temperature.....18

Figure 1-11 – Formation of the urethane linkage from a diol and a diisocyanate.....20

Figure 1-12 – Deblocking reaction of ε-caprolactam blocked isocyanate to form free isocyanates.....21

Figure 1-13 – Contact angle variation between two immiscible resins (with surface energies γ_A and γ_B) with respect to the type of substrate (γ_S).....22

Figure 2-1 – MOPAS XS Polisher with resin block sample inside jig.....28

Figure 2-2 – Cross-section after final polishing stage.....29

Figure 2-3 – Schematic of typical FTIR instrument.....31

Figure 2-4 – Fourier transform between an interferogram and an actual spectrum.....33

Figure 2-5 – Charge distributions of CO_2 and H_2O. Blue and red colored regions are negatively and positively signed regions, respectively.....36

Figure 2-6 – Typical setup for a Raman dispersive spectrometer with a near-infrared laser attached to a microscope.....37

Figure 2-7 – Diagram of Rayleigh and Raman scattering processes; IR absorbance included for comparison.....40

Figure 2-8 – Dipole and polarization in CS_2, with resultant Raman and IR spectra.....41

Figure 2-9 – Generic monomer unit of an acrylic polyol reactant.....42

Figure 2-10 – Schematic of internal reflections in ATR crystal.....43

Figure 2-11 – Comparison of XPS spectra recorded from copper using AlKα (upper) and MgKα (lower) radiation.....45

Figure 2-12 – Diagram of a typical HSA and transfer lenses.....47

Figure 2-13 – Effects of pass energy variation for Ag 3d peaks.....48

Figure 2-14 – Schematic presenting (a) the operation of a channeltron, and (b) output characteristics.....49

Figure 2-15 – Schematic of photoemission process; (a) photon absorption at K level; (b) photoemission with core hole in K level.....51

Figure 2-16 – Photoelectron spectrum of lead superimposed over a schematic of its electronic structure to illustrate how photoelectron peaks arise out of the orbitals.....52

Figure 2-17 – Electron intensity as a function of depth; the horizontal dashed line indicates a distance from the surface of the attenuation length λ.....53

Figure 2-18 – Sample stage geometry for altering electron emission angle; b) changes in intensity with respect to sampling depth induced by changing the emission angle for a metal oxide sample.....54

Figure 3-1 – Scheme of possible structures in polymers open to analysis by various microscopies.....59

Figure 3-2 – Schematic of TEM.....61

Figure 3-3 – a) Image formation of a point source; b) image formation of a finite object.....63

Figure 3-4 – Comparison between magnetic coil acting upon electron beam and optical lens acting upon photon.....64

Figure 3-5 – a) Particle model depiction of elastic scattering of an electron by an atom; b) wave model depiction of the superposition of incident plane wave and scattered wave.....66

Figure 3-6 – Transmission electron micrograph of cross-section of clear blend coating. Dark streaks are due to folds in the sample.....68

Figure 3-7 – Comparison between a) unstained and b) stained transmission electron micrographs.....71

Figure 3-8 – Schematic of SEM.....73

Figure 3-9 – Diagram of regions within the interaction volume that generates various signals...74

Figure 3-10 – Comparison of cross-sectioned pigmented coating at similar magnifications under accelerating voltages of a) 1 kV, and b) 20 kV. The circle marks the same area in both micrographs to orient the reader.....75

Figure 3-11 – Schematic of depth of focus for SEM.....76

Figure 3-12 – Illustration of characteristic x-ray generation by incident electron. All photons shown are α transitions.....78

Figure 4-1 – Optical micrographs of surfaces of a) low hydroxyl content film; b) high hydroxyl content film; c) Blend A.....84

Figure 4-2 – Cross-section of Blend A that were prepared by wet-polishing; a) digital optical micrograph; b) scanning electron micrograph.....85

Figure 4-3 – Micrograph of polished cross-section of Blend A.....86

Figure 4-4 – Raman spectra of the encapsulated domain (top) and the continuous polymeric matrix (bottom) of cross-sectioned Blend A film.....87

Figure 4-5 – False-color map of the Raman marker peak at 1630 cm^{-1}. Red corresponds to high intensity, and blue corresponds to low intensity.....88

Figure 4-6 – Raman spectra of single component films; (top) high hydroxyl resin; (bottom) low hydroxyl resin.....89

Figure 4-7 – Stacked Raman spectra from both single component films and the phases of the blend.....89

Figure 5-1 – (a) Illustration of sample specimen embedded between two layers of the polyester embedding resin; (b) MOPAS hand polisher with polyester resin block containing embedded film specimen inserted; (c) MOPAS hand-held polisher and Micro-Mesh abrasive cloth.....98

Figure 5-2 – DSC thermogram of Blend A (bottom curve) and the single component high OH (middle curve) and low OH (top curve) resin films.....99

Figure 5-3 – Differential Scanning Calorimetry thermogram of Blend B (bottom curve) and its components as individual films. The high OH film is the middle curve; the low OH film is the top curve.....100

Figure 5-4 – Optical micrograph of Blend B surface with measurements of some domain diameters and lengths.....101

Figure 5-5 – Stacked Raman spectra of single component films and phases of Blend A.....102

Figure 5-6 – Stacked Raman spectra from polyester-embedded cross-sections of Blend A with marker peak heights indicated on a baseline; top: low OH Raman spectrum; middle top: high OH Raman spectrum; middle bottom: Raman spectrum of polymer matrix; bottom: Raman spectrum of domain.....103

Figure 5-7 – Optical micrograph of high OH cross-section; b) close-up on high OH aromatic and carbonyl peaks; c) alkene peak height map of high OH cross-section; d) optical micrograph of low OH cross-section; f) close-up on low OH aromatic, alkene and carbonyl peaks; e) alkene/aromatic peak height ratio map of low OH cross-section.....105

Figure 5-8 – a) Optical micrograph of mapped region; b) selective infiltration in polymer Matrix; c) C=C peak height map; d) ratio of the C=C/aromatic peaks.....107

Figure 5-9 – a) Optical micrograph of Blend B cross-section; b) Alkene peak height map; c) alkene/aromatic peak height ratio map.....108

Figure 5-10 – Raman analysis of Blend B cross-section embedded in fast-cure epoxy.....109

Figure 5-11 – a) Apparatus for vapor staining; b) Low OH film after 72 hours in headspace; c) High OH film after 72 hours; d) Blend B after 72 hours.....110

Figure 5-12 – a) Dark field optical micrograph of Blend B surface; b) small styrene peaks in matrix and low OH spectra; c) alkene peak height map; d) alkene/aromatic peak height ratio map.....111

Figure 6-1 – Raman spectra of the various carbonyl peaks found in reactants (upper two spectra) and PU product at two stages of cure.....124

Figure 6-2 – Stacked FTIR spectra of the reactants and reaction at two stages of the cure; a)-f): OH/NH region; e)-f): double bond region.....126

Figure 6-3 – Fitted spectra of single component polyurethanes; a) Raman spectrum of low OH film; b) ATR-FTIR spectrum of low OH film; c) Raman spectrum of high OH film; d) ATR-FTIR spectrum of high OH film.....129

Figure 6-4 – Transmission electron micrograph of the blend cross-section with FTIR measurements of ester and urethane C=O peaks. The left spectrum is measured from the surface; the right spectrum is measured from the underside.....131

Figure 6-5 – TEM images of cross-sectioned clear films at full cure; a) low OH film; b) high OH film; c) blend.....134

Figure 6-6 – Raman peak intensity evolution for the ε-caprolactam vibration at 1655 cm^{-1} as a function of increasing cure time at 204 ˚C. Intensities are normalized with respect to the aromatic moiety at 1600 cm^{-1}.....136

Figure 6-7 – Raman peak height ratios in both phases of the blend for conjugated alkene vs aromatic styrene as a function of cure time.....138

Figure 6-8 – Comparison of cross-sections between different embedding resins as a function of cure time; a)-b) 4 minutes; c)-d) 6 minutes; e)-f) 9 minutes.....140

Figure 7-1 – Optical micrographs (left) and laser confocal microscopy (right) of film surface showing development of domains and surface roughness.....156

Figure 7-2 – Inverse relationship observed for 60° and 85° gloss properties and mean surface roughness as a function of cure time.....157

Figure 7-3 – Glass transition temperature data from blend samples at different cure-time intervals at 204 ˚C. 158

Figure 7-4 – Resin blend measured at 200 ˚C cure with low shear oscillation.....160

Figure 7-5 – FTIR peak intensity evolution for the isocyanate vibration at 2255 cm^{-1} as a function of increasing cure time at 204 ˚C. Intensities are normalized with respect to the aromatic moiety at 700 cm^{-1}.....161

Figure 7-6 – TEM analysis of domain nucleation in the cross-section; a) domain with wormlike morphology present in powder particle; b) wormlike structure coalescing into spherical domains; c) spherical domains connected to fibrils.....162

Figure 7-7 – Low-magnification cross-sections up to 3 minutes. Blue arrows indicate orientation of large domains. Red boxes indicate a paucity of small domains connected to large domains.....164

Figure 7-8 – Low-mag electron micrographs of cross-sectioned films quenched 4-9 minutes and at full cure.....166

Figure 7-9 – High magnification cross-sections of films quenched 1-3 minutes.....168

Figure 7-10 – High magnification cross-sections of films quenched at 4-9 min and full cure....169

Figure 7-11 – Histograms of domain areas for samples at different stages of the cure.....171

Figure 7-12 – Nanoindentation hardness results for the 2.5 and 3-minute cross-sections.....176

Figure 8-1 – LCM images of black film surfaces; a) low OH; b) high OH; c) blend.....196

Figure 8-2 – Gloss measurements of blended black coatings as a function of time.....197

Figure 8-3 – Evolution of surface roughness for clear coating formulated with only calcium silicate matting agent.....198

Figure 8-4 – Optical micrographs of the cross-section for the black coating at different cure times. The white scale bar is 50 μm.....200

Figure 8-5 – Low mag TEM of cross-sections of black films at various cure-times; a) 2 minutes; b) 2.5 minutes; c) 3 minutes; d) 9 minutes. Red lines connect the spectrum to matting agent particles.....201

Figure 8-6 – TEM of black powder before and during early cure.....204

Figure 8-7 – TEM images of the cross-sectioned black coating at 2.5- and 3-min cures.....207

Figure 8-8 – TEM images of cross-sectioned black coating at a) 4 minutes; b) 6 minutes; c) 9 minutes; d) 12 minutes.....209

Figure 8-9 – TEM and SEM images of cross-sectioned fully cured black coating.....211

Figure 8-10 – TEM and SEM images of fully cured tan coatings; red arrows connect the EDX spectrum to TiO_2 particles.....212

Figure 8-11 – TEM and SEM images of cross-sectioned green coating coating on primer, plus EDAX spectrum of representative regions indicated by red arrows.....213

Figure 8-12 – XPS spectra of TiO_2; a) wide scan; b) high-resolution C 1s.....216

Figure 9-1 – Survey scan of blend underside at 60˚ incident angle.....224

Figure 9-2 – ARXPS spectra of the blend measured from the top surface; a) C 1s at 90˚; b) C 1s at 60˚; c) O 1s at 90˚, d) O 1s at 60˚, e) Ca 2p at 90˚, f) Ca 2p at 60.....228

Figure 9-3 – High-resolution XPS of blend substrate-side; a) C 1s at 90˚; b) C 1s at 60˚; c) O 1s at 90˚; d) O 1s at 60˚; e) Sn $3d_{5/2}$ at 90˚; f) Sn $3d_{5/2}$ at 60.....232

List of Abbreviations

ARXPS.....Angle-resolved XPS
ATR.....Attenuated total reflectance
cm^{-1}.....Wavenumber
$CaSiO_3$.....Calcium silicate
C=O.....Carbonyl
DRIFTS.....Diffuse reflectance infrared transform spectroscopy
DSC.....Differential scanning calorimetry
EDX.....Energy dispersive x-ray spectroscopy
Fe_3O_4.....Black iron oxide/magnetite
FTIR.....Fourier transform infrared spectroscopy
IPDI..... Isophorone diisocyanate
LSCM.....Laser scanning confocal microscopy
LRS.....(Laser) Raman spectroscopy
MOPAS..... Molecular Painting Studies Group
NCO.....Isocyanate
NH.....Amine
nm.....Nanometer
OH.....Hydroxyl
OM.....Optical microscopy
OPD.....Optical path difference
PVC.....Pigment to volume concentration
PU.....Polyurethane
SC.....Single component
SEM.....Scanning electron microscopy
SiO_2.....Silica
S_q.....Surface roughness value
TEM.....Transmission electron microscopy
T_g.....Glass transition temperature
TiO_2.....Titanium dioxide
μm.....Micrometer
VOC.....Volatile organic compound
XPS.....X-ray photoelectron spectroscopy
ZPD.....Zero path difference

Acknowledgments

I cannot really express how grateful I am to have had Dr. Clive R. Clayton as an advisor. He personifies all the ideals of mentorship in a PhD project: guidance, patience, dedication, kindness, and encouragement. I also wish to thank Drs. Gary Halada and Christopher Young for their advice on spectroscopic methods when I started the project. Much gratitude goes to Mr. Michael Cuiffo for his mentorship on bench work, XPS, and assembling of vacuum equipment. I also thank Dr. James H. Wynne for his invaluable discussions at various group meetings, and for serving as my outside committee member.

The successful outcome of this project is the culmination of extensive and fruitful collaboration with expertise provided by the Naval Research Laboratory (NRL) and the Sherwin-Williams Company (SW). Preparation of clear coatings and their subsequent gloss measurements were performed by Mr. Mark Walker (SW). Mr. Mark Wytiaz (SW) prepared the pigmented coatings and subsequently measured their gloss indices. Dr. Spencer Giles (NRL) performed DSC, LSCM, and nanoindentation measurements. They have my sincere appreciation. I am also grateful for editorial support from Dr. Morgan Sibbald on project write-ups. Thanks to Dr. Adelheid Gealt (Indiana University Art Museum) for initiating contact with Dr. Julie Arsanoglu (Metropolitian Museum of Art), who provided invaluable insight into cross-section preparation, and also personally transported the MOPAS Polisher from Amsterdam to New York.

Funding for this project was provided by SERDP Program Manager Dr. Robin Nissan under WP-2207. This material is based upon work supported by the U.S. Army Corps of Engineers, Humphreys Engineer Center Support Activity under Contract No. W912HQ-12-C-0013.

Ms. Susan van Horn at the Central Microscopy Imaging Center (CMIC), Stony Brook University, performed microtome sectioning and heavy metal staining of cross-sections, and provided assistance with the FEI Bio TwinG2 Transmission Electron Microscope. Dr. James Quinn (SBU) assisted with SEM analysis and operation. Mr. Kim Kissinger provided training and assistance for operation of the JEOL JEM-1400 LaB6 instrument at the Center for Functional Nanomaterials, Brookhaven National Laboratory, whose use is supported by the U.S. Department of Energy, Office of Basic Energy Sciences, under Contract No. DE-AC02-98CH10886 and DE-SC-00112704. Rheology measurements performed by Mr. James Heck and Mr. Anthony Hennessey at Elementis. None of this work would have been possible without their contributions.

Greatest of appreciation goes toward my wife, Stephanie Izzi, whom I met at the beginning this project, and whose aid and encouragement proved essential in this intellectual Iliad. I also extend my sincere thanks to my mother, Diemut Heller, *die höchste Korrektor*, and to my sister Marika Heller, the master stickler. Much thanks also goes to my friends back in CA, Sushuma Stone, and Adrian Paladini, for their continued support and friendship.

Chapter One

Introduction and Background on Powder Coatings

1.1 Introduction

An organic coating is a thin continuous layer on a substrate that consists of a polymeric resin or binder containing pigments and additives.[1] Traditional organic coatings also require a solvent such as acetone or methyl ethyl ketone to lower the viscosity for sufficient application on a surface. After application, the solvent evaporates and the film hardens into a final finish. This evaporation is a major source of volatile organic emissions (VOCs), which are a concern for air pollution and have thus undergone increasing regulation by national governments. This led to the growth of waterborne coatings, but they still use some organic solvent, and often have inferior properties for certain applications.[2]

The regulatory environment also induced a growth in powder coatings. This class of coatings does not contain solvents, and therefore, releasing little to no quantities of VOCs in the curing stage. The absence of solvents in a powder coating formulation has led to exponential growth in the powder coatings market that shows no sign of abatement, as the global market was worth $8.3 billion in 2013 and is expected to be worth more than $12 billion by 2019.[3] However, the market has yet to see powder coatings with dull matte or dead matte finishes which simultaneously maintain the durability necessary for chemical resistance and weatherability. This dissertation covers the many types of analytical techniques used to characterize the prototypes of novel powder coatings filling

that void in the powder coating industry. It is to be hoped that the fundamental understanding gained from this investigation could be usefully applied toward future generations of functional powder coatings.

1.2 Powder coatings

Powder coating can be described as finely ground dry paint because of the absence of solvent in their formulation. This typically consists of a polymer resin, pigments, and additives. A curative (crosslinker) is required to cure thermoset powder coatings, while thermoplastic powder coatings do not require a curative.[4] The first powder coatings developed in the 1950s were thermoplastics, but thermosets now are more than 90% of the market share.[2] Crosslinking is a process inherent to thermosets. This allows usage of polymers with low molecular weights and thus low melt viscosities. A crosslinked film is exceptionally resistant to solvents, and has high chemical resistance in general because it is relatively impenetrable to the attacking agent.

Without solvent, powder coatings have to be applied as polymer melts, which behave as non-Newtonian fluids. Such fluids require the surpassing of a minimum shear stress to induce flow and wet the substrate. This minimum shear stress is the yield value, and is sensitive to the myriad molecular interactions between the resin and pigments. Powder coatings thus have low pigment-to-volume concentrations (PVC). Exceeding the PVC would increase the yield value (i.e., melt viscosity) such that poor flow and uneven wetting of the substrate would result.[4] Low gloss powder coatings have been formulated by incorporating micron-sized wax pellets for matte finishes.[5] Several approaches also incorporated surface wrinkling into the finish to reduce gloss.[6] Additionally, Lee et al

have mixed incompatible blends of acrylic and epoxy/polyester resins with two curatives to induce low gloss producing powder coatings with dead matte or matte finishes, although durability did not appear to be a primary concern.[7]

1.3 Materials processing and coating application

The production of processing powders for powder coating applications is complex and subject to stringent requirements in order to reliably produce films with the desired characteristics. Equipment needs are many and production times are longer than for other types of coatings.[8] Processing steps include weighing, premixing, extrusion, milling, filtration, and sieving. The steps are outlined in Figure 1-1.

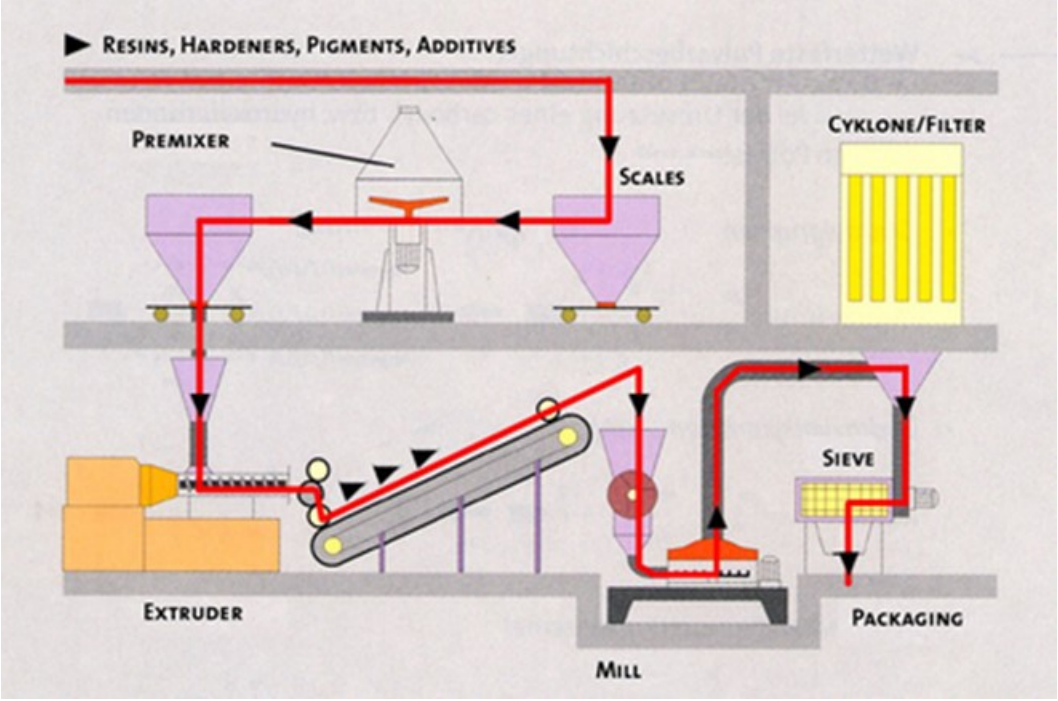

Figure 1-1. Schematic of general powder coating production.[9]

Premixing converts the different sizes of resin flake, pigment powder, and additives into a mix of similar particle size; this is crucial as it ensures good dispersion of the

components prior to subsequent homogenization in the extruder. The extrusion process converts the mixed dry powder into a melt via heating between 90 ˚C and 120 ˚C, which uniformly distributes the pigments and additives within the molten resin to ensure adequate dispersion upon application. Extrusion takes about 20-30 seconds. Powder coatings typically use co-rotating twin screw extruders (Figure 1-2), in which two side-by-side screws turn in the same direction within a barrel. Additionally, while the extruder can be temperature controlled, the grinding alone can raise the temperature high enough to pre-polymerize the starting materials without inducing a premature chemical reaction to completion. The melt exits out the extruder as a viscous mixture of resin with incorporated pigments and additives. This material cools into a solid, then is milled and sieved into a fine powder that is ready for coating application. The packaged powder has particle size distributions of 30-50 μm.

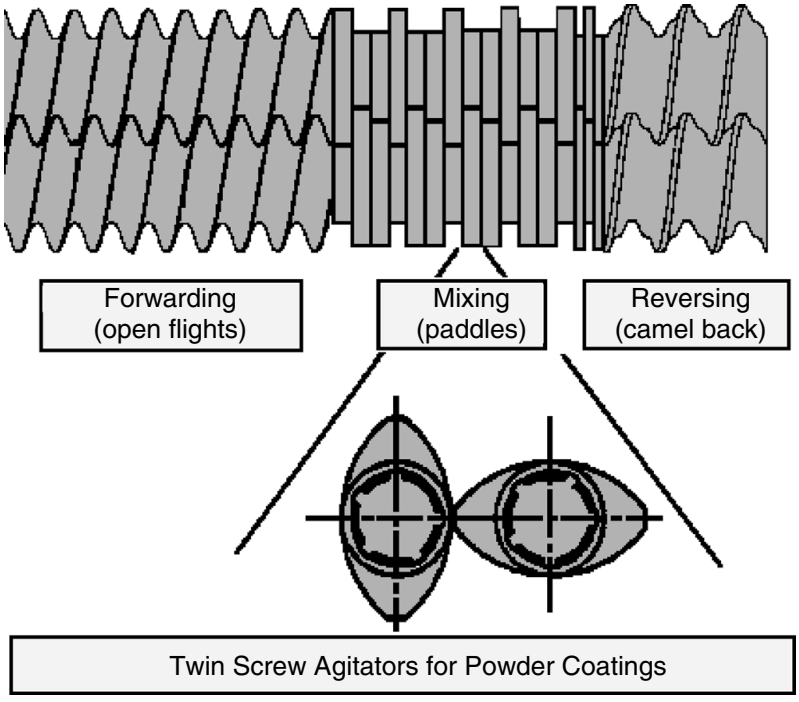

Figure 1-2. Schematic of twin screws within an extruder.[8]

The most widely used method of application is electrostatic spraying, which exploits an attractive electric potential between the grounded substrate and charged powder particles. The powder-air mixture is supplied through a hose from a small fluidized bed in a powder feed hopper. The powder coating spray gun has a high voltage dc electrode which applies a charge to the powder (Figure 1-3). Electrostatic sprays can range from hand held spray guns to automatic sprayers that can be mounted to spray booths on overhead conveyorized paint lines. Electrostatic sprayers have control over the powder flow, shape, size, and density of the powders used to coat objects. Applied film thicknesses of 38–127 μm are typical.

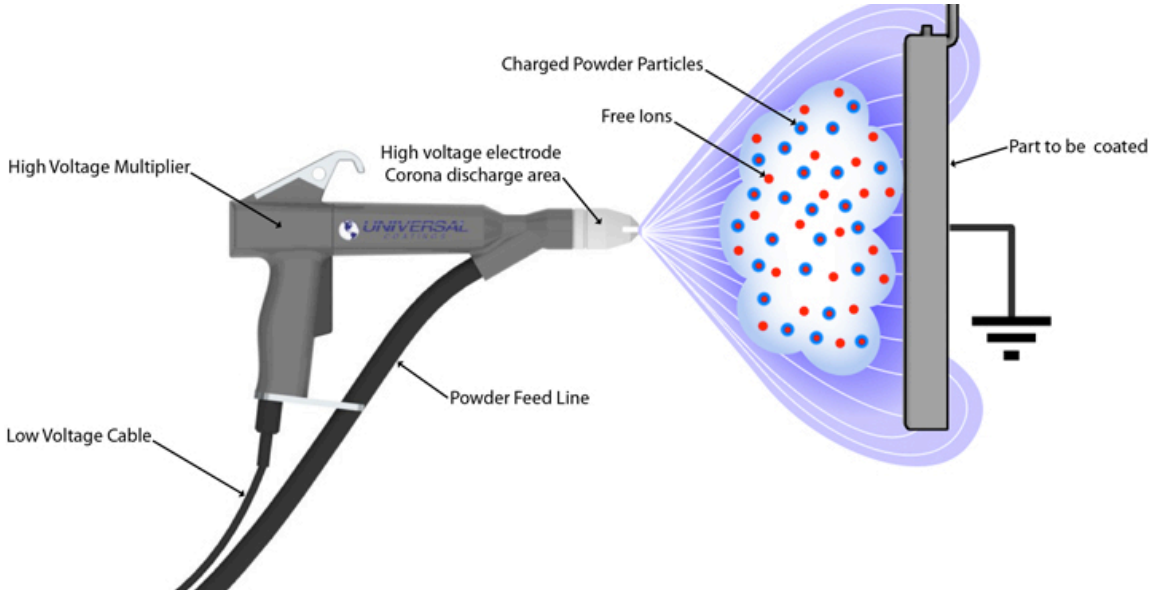

Figure 1-3. Powder coating application via corona-charge spray gun.[10]

After spraying, the temperature is raised to 160-200 ˚C and the powder undergoes three phases of film formation: melting, flow/leveling, and crosslinking. Melting occurs when the powder particles sinter into a continuous film. Surface topology then changes due to the flow induced by surface tension gradients caused by the uneven distribution of powder particles; this is known as Marangoni flow.[4] For most powder coatings, the

surface smoothens due to the flow in a process known as surface leveling. This phenomenon has been approximated as a sinusoidal wave by Orchard,[11] and is schematically illustrated in Figure 1-4.

$$\ln\frac{a_t}{a_0} = \frac{16\pi^4 h^3}{3\zeta^4}\int_0^t \frac{\gamma}{\eta}dt \,, \qquad (1\text{-}1)$$

where a_0 and a_t are the wave amplitudes before and after leveling, respectively, h is the average film thickness, ζ is the wavelength, γ is the surface tension, and η is the viscosity.

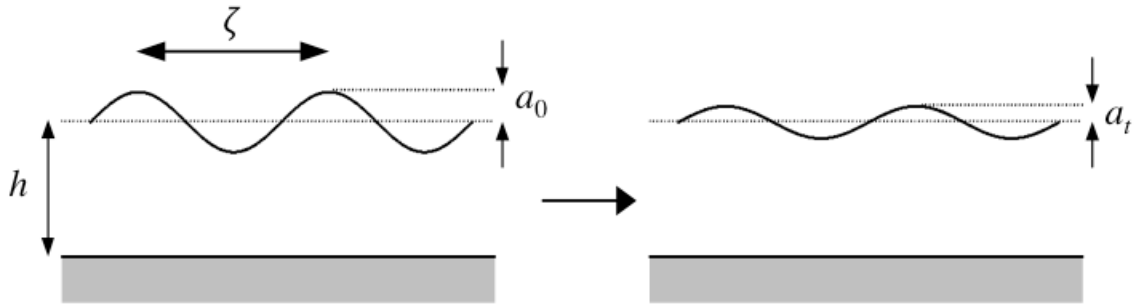

Figure 1-4. Schematic representation of surface leveling for a powder coating.[12]

This process typically smoothens the surface and thus raises the gloss. A powder coating with very low gloss is a primary motivation for this project, but gloss is heavily affected by the distribution of pigments within the coating. A discussion of this phenomenon is warranted before going into the fundamentals of gloss.

1.4 Pigment wetting and dispersion

Before the powder is melted and sprayed onto a work piece, the polymer must first bind to the pigments by wetting. This is necessary to replace air pockets and absorbed moisture from the pigment particle surface and from pigment agglomerates (Figure 1-5a).

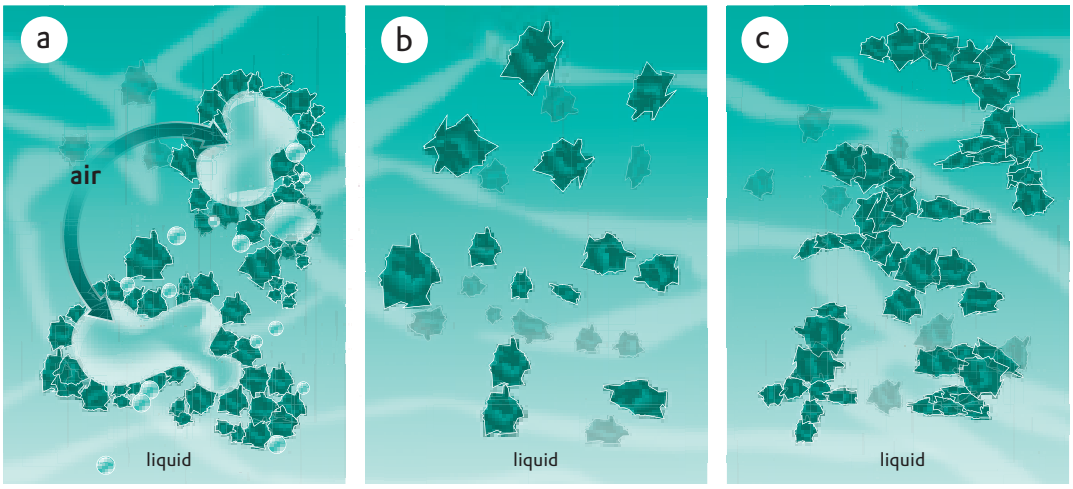

Figure 1-5. Schematic representation of pigment dispersions; a) wetting of agglomerate; b) dispersed; c) flocculated.[13]

Wetting is done within the extruder. For complete wetting of a given pigment particle, pigment agglomerates require break-up in order for the resin to wet the entire surface. Thus, the driving force for the infiltration of the polymer into agglomerate interstices is the surface energy difference between the pigment surface and the polymer fluid. The viscosity of the polymer melt counteracts the polymer flow rate. The rate of infiltration into a capillary tube can be described by Washburn's equation:[14]

$$\frac{l^2}{t} = \frac{R\gamma_{LV}\cos\theta}{2\eta}, \qquad (1\text{-}2)$$

with l the flow length of the fluid in the capillary, R the radius of the capillary, γ_{LV} the liquid-vapor surface energy of the fluid, θ the advancing contact angle, and η the viscosity. Pigment wetting may depend on other factors as well.[15] This equation is valid for a single capillary, but can be expanded to a pigment cluster via the Blake-Kozeny equation:[16-17]

$$\frac{L^2}{t} = \frac{2\gamma_{LV} d\cos\theta}{25\eta}\frac{\varepsilon^2}{\varepsilon - 1}, \qquad (1\text{-}3)$$

where ε is the porosity of the cluster, d is the mean pigment diameter, and L is the flow length of the fluid in the cluster. It is therefore reasonable to assume that the viscosity of the polymer fluid determines pigment wetting. During extrusion, typical viscosities for powder coatings are η = 100-1000 Pa•s.[18] As also indicated by Equation (1-3), porosity figures significantly in the polymer infiltration rate. Porosities larger than a critical value $(\varepsilon_{crit} = 0.65)$ enhance the infiltration rate due to the larger pore diameters within the agglomerates.[19] Pores increase the surface area for the resin to infiltrate, and thereby enhance wetting.[2]

The steps following pigment wetting are agglomerate disintegration and then dispersion (Figure 1-5b). The distribution of the pigment particles is influenced by the residence time of the coating material in the extruder and the consistency of the dry blend.[20] Deagglomeration is a difficult but crucial step that involves dispersive mixing via extrusion in areas with high mechanical stresses. This happens when the cohesive strength of the cluster is exceeded by the magnitude of hydrodynamic forces within the melt. The forces may induce a sudden rupture of the cluster, or a slow erosion, depending on the difference between the cohesive strength of the cluster and the magnitude of the hydrodynamic forces.[19]

Polymer flow in the kneading section of an extruder combines extensional and shear flow.[21] The hydrodynamic force imposed onto a pigment cluster is described by:

$$F_{hyd} = \beta u_* \dot{r} S \,, \qquad (1\text{-}4)$$

where S is the cross-sectional contact area at the fracture plane, u_* is the shear velocity, and $\dot{r}$ is the rate of deformation (either shear rate or elongational rate), and β is a

parameter that depends on the orientation and dimensions of the cluster and its fracture plane with respect to the flow field.[22] The cohesive strength for the pigment cluster is:

$$F_c = \frac{9F_{int}S(1-\varepsilon)}{8\varepsilon d^2} \qquad (1\text{-}5)$$

with F_{int} as the interaction force between two primary particles, ε being the porosity of the cluster, and d the diameter of the primary particles. The number of paired primary particles is related to the porosity of the cluster.[23] Electrostatic, capillary, and Van der Waals forces are encompassed in F_{int}. Capillary forces are very strong compared to van der Waals forces in agglomerates with absorbed moisture, but are nonexistent in dry agglomerates.[24] The absence of a liquid medium indicates that only van der Waals forces should be accounted for, and are given by

$$F_{VW} = \frac{A_{eff}d}{24h^2}, \qquad (1\text{-}6)$$

where A_{eff} is the effective Hamaker constant of the pigment particles and h is the minimum distance between pigment particles within agglomerates (~0.3 nm).[25] The medium between the pigment particles determines the value of the Hamaker constant. For dry agglomerates, $A_{eff} = A_{pig}$. Within a resin, the constant becomes:[26]

$$A_{eff} = \left(\sqrt{A_{pig}} - \sqrt{A_{medium}}\right)^2. \qquad (1\text{-}7)$$

For deagglomeration to occur, $F_{hyd}/F_c > 1$. Pigment wetting is fast when the resin viscosity is low, but the agglomerate can rupture when the viscosity is high.[19]

The degree of pigment dispersion factors significantly in the gloss and haze of the coating by shaping the surface roughness. Flocculation, as depicted in Figure 1-5c, enhances the surface roughness, while a deflocculated state lowers it. It follows that

surface roughness is intimately and inversely linked to gloss, and thus is the next topic of discussion.

1.5 Gloss and surface roughness

Specular gloss is defined as the perception by an observer of the mirror-like appearance of a surface; such perception is subject to change whenever the source alters in its relative position or spectral distribution. The spectral gloss of a material depends on the orientation of the light source, as shown in Table 1.[27]

Table 1-1. Geometries for specular gloss measurements and applications.

Illumination angle (θ)	Applications
20°	High gloss of plastic film, appliance, and automotive finishes
30°	High gloss of image-reflecting surfaces
45°	Porcelain enamels and plastics
60°	All ranges of gloss for paint and plastics
75°	Coated waxes and paper
85°	Low gloss of dead matte paints and camouflage coatings

To reduce the subjectivity, the gloss (G) of a coating is calibrated against a well-defined, optically smooth black tile. It is mathematically expressed as

$$G = R_s/R_{ref} \times 100\%, \quad (1\text{-}8)$$

where R_s is the specular reflectance of the coating, and R_{ref} is the reflectance of the black tile. Dead matte finishes have gloss levels < 10% at $\theta = 60°$.[28]

The key to achieving low gloss is to generate a highly rough coating surface. Specular reflectance and surface roughness are linked with the following equation[29]

$$R_S = Re^{\left(\frac{4\pi\cos\theta_i}{\lambda}\right)^2}, \quad (1\text{-}9)$$

where R is the maximum reflectance of the coating as calculated from Fresnel's equation,[30] σ = surface roughness, λ = wavelength of radiation, and θ_i = angle of the incident radiation.

The surface roughness must cross a certain threshold before it begins to affect the gloss. The threshold is determined by the Rayleigh criterion for smooth surfaces:[31]

$$D < \frac{\lambda}{8\cos\theta_i}, \qquad (1\text{-}10)$$

where D is the height of the surface defect. With equations linking the surface roughness with gloss now established, the resultant plot takes the following form in Figure 1-6.

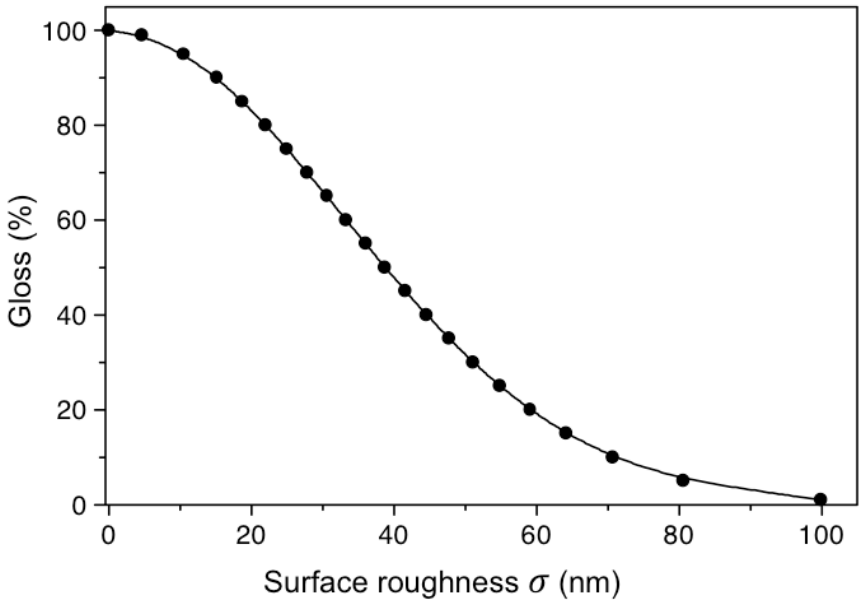

Figure 1-6. How surface roughness affects gloss according to Equations 1-8 and 1-9.[12]

1.6 Polymer blends

The powder coatings analyzed in this thesis are composed of a novel binder. This has tremendous importance, as most of the physical and chemical properties in a coating system derive from the binder.[32] The fully formulated systems analyzed in this thesis are comprised of immiscible polymer blends with low loadings of solids and other apropos

additives that promote durability, ultra-low gloss, and resistance to weather and other sources of corrosion. As previously mentioned, powder coatings require low loadings to keep the melt viscosity low enough for even application over a substrate while maintaining adequate pigment dispersion. However, surfaces with matte gloss are usually produced with high loadings of solids, which are commercially available in solventborne paints. If the resin has multiple indices of refraction inside the bulk and at the surface (see Figure 1-7), then the light is bent multiple times at the surface and within the bulk, which reduces the film transparency and by extension its gloss.[32] The immiscible resin droplets within the film would reduce the necessary loading level of pigments for low gloss. Thus, the combination of immiscible droplets and roughening agents (pigments designed for matte finishes) would open new markets for low VOC coatings. The incorporation of multiple light scattering has already been achieved for powder coatings via urethane polyester blends; a highly reactive resin with a high hydroxyl or "OH number" was mixed with a less reactive resin with a much lower OH number. The high OH resin cured first, but it phase separated and formed a dispersed phase morphology that remained after full cure.[5] Blends of high and low carboxyl functional polyester resins have also produced low gloss powder coatings.[28, 33] Large differences in hydroxyl content are the source of immiscibility for the polymers in this study as well. The starting polymers are acrylic polyols, which undergo an addition reaction with a polyisocyanate curative. This will be detailed in another section.

In addition to gloss reduction, there are other reasons for industrial interests in coatings with immiscible resin blends, as they can provide a method for producing very

finely dispersed microstructures that can significantly enhance material properties, such as scratch resistance, mar resistance, and adhesion durability.[34-35]

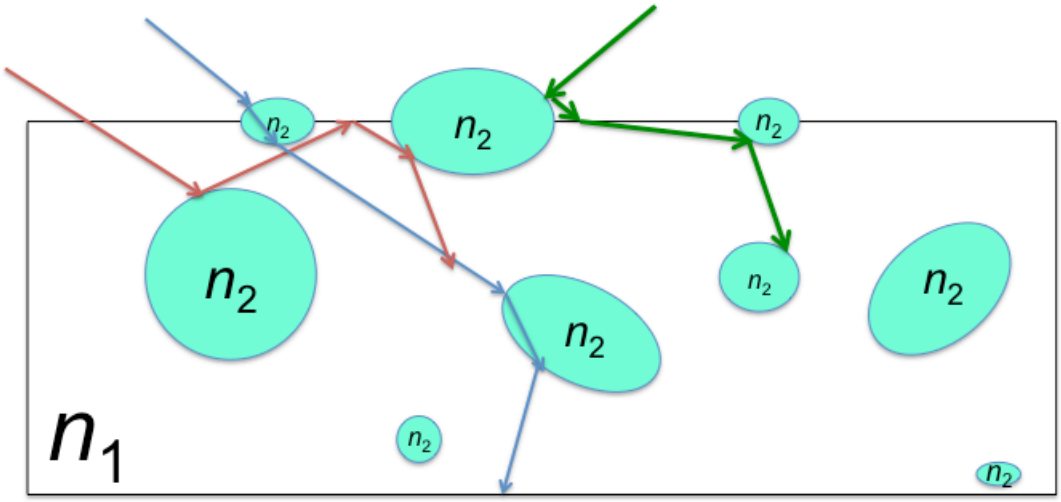

Figure 1-7. Beam of light refracted by incompatible droplets (domains) of a resin with a different index of refraction in a continuous phase of clear binder (n_1).

The cross-sectioned surface depicted in Figure 1-7[32] is a consequence of the blend morphology, which is an easily controlled outcome. Such control is a major advantage of polymer blends, as a diverse range of end-use properties is readily available to the user. These properties are greatly influenced by the phase structure, which is the result of the complex relationships of inner parameters (chemistry and rheology) and outer parameters (temperature and applied flow field) of the components. Changing the composition of the blend or processing conditions enables the creation of materials with morphologies of different types and/or degrees of purity.[36]

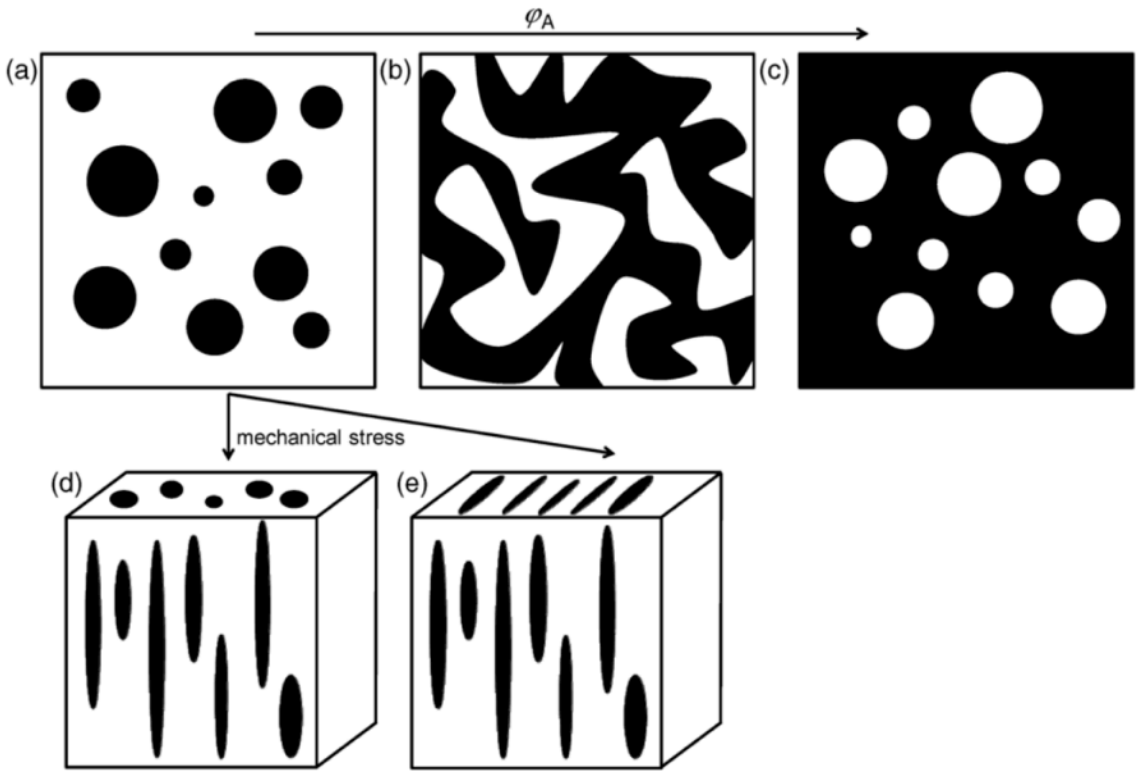

Figure 1-8. Basic types of phase structures.[37]

Blend morphology is typically classified as dispersed or cocontinuous, as shown in Figure 1-8. Dispersed phases are formed when one of the components is the minority component (1-8a and 1-8c). The dispersed particles form spheres to minimize the free surface energy of the system. Anisotropic particle geometries (ellipsoids, fibrils, platelets) are often observed in blends if they are solidified by immediate quenching after melt processing. These shapes stem from deformations induced by shear and/or elongational stresses applied in the mixing devices such as extruders. For the emergence of cocontinuous phases, there exists a critical concentration for geometric percolation that is generally dependent on the viscosity ratio. If the ratio is close to unity, a fully cocontinuous structure appears around 1:1 composition. Otherwise, the component with the lower viscosity forms the continuous phase. Cocontinuous structures are also

determined by the interfacial energy; increasing interfacial energy induces the minor phase to form more spherical domains, which increases the critical concentration for cocontinuity to emerge, while narrowing the permissible range for its manifestation. How these phase morphologies form is the subject of the next section.

1.7 Phase separation mechanisms

Flory and Huggins established the theory of mixing of polymer components, in which species of macromolecules with constant volume are confined in a lattice.[38-39] They describe thermodynamic equilibrium to correspond to the minimum of Gibbs free energy in a system. For a spontaneous process such as mixing, the change in the free energy must be less than zero. For mixing, this is expressed as

$$\Delta G_M = \Delta H_M - \Delta T S_M, \tag{1-11}$$

where ΔG_M is the free energy of mixing, ΔH_M is the enthalpy of mixing, T is the absolute temperature, and ΔS_M is the entropy change in the mixing process. The enthalpy is a quantity of the heat consumed ($\Delta H_M > 0$) or generated ($\Delta H_M < 0$) during mixing at constant pressure. If the mixing is exothermic, then $\Delta G_M < 0$. The entropy of mixing in polymer systems is expressed as

$$\Delta S_M = -kV\left(\frac{\varphi_1}{V_1}\ln\varphi_1 + \frac{\varphi_2}{V_2}\ln\varphi_2\right), \tag{1-12}$$

where k = Boltzmann's constant, V is the total volume of the system, V_n is the volume of species n, and φ_n its volume fraction. The structure of Equation (1-12) is predicated on there being a limited number of spatial arrangements of molecules within a lattice for a binary mixture (Figure 1-9). An increase in the molecular weight of a species

significantly reduces ΔS_M, and by extension ΔG_M. Greater reliance is placed on intermolecular interactions between adjacent lattice sites for mixing to occur. Hence, the small solvent molecules in Figure 1-9a are replaced by a second polymer species in 1-9b.

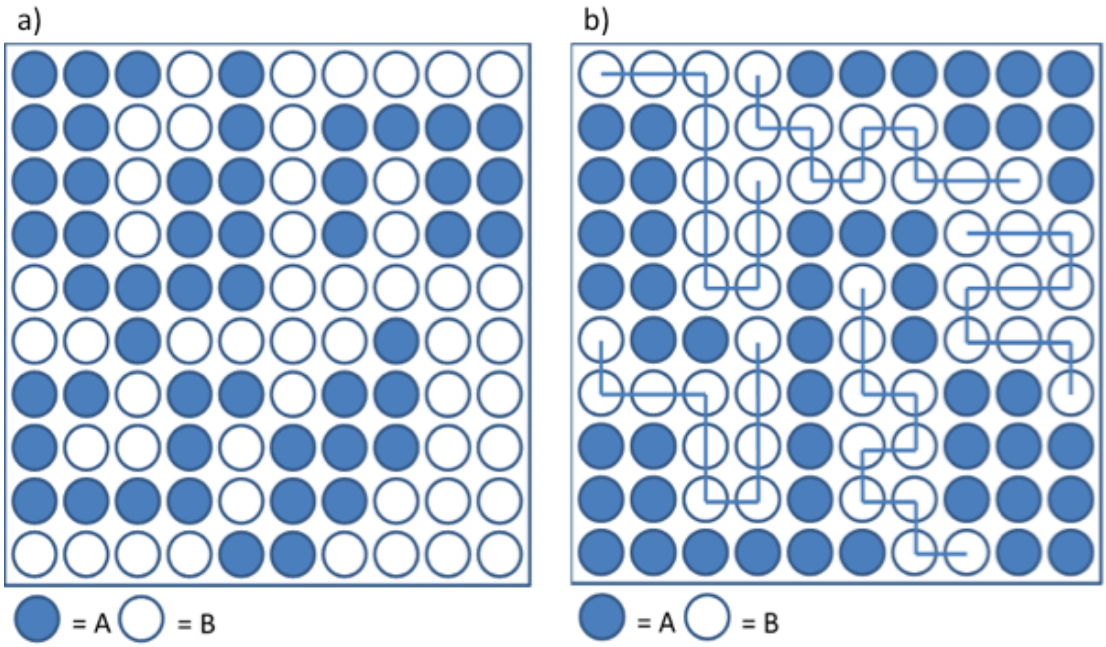

Figure 1-9. Schematic representation of spatial arrangements of molecules in a binary mixture of a) low molecular weight components and b) a polymer blend.

For polymer blends, the enthalpy is expressed as

$$\Delta H_M = kTV\frac{\chi_{12}}{v_r}\varphi_1\varphi_2\,, \qquad (1\text{-}13)$$

where v_r is the volume of the interacting unit (segment or molecule), and the interaction parameter $\chi_{12} = \frac{zw_{12}}{kT}$ is a dimensionless quantity that characterizes the change in enthalpy for each interacting molecule or segment. If there is a net attraction between species, $\chi_{12} < 0$ and homogeneity emerges for all compositions. However, $\chi_{12} > 0$ is a more common situation (polymer species repel each other) because members of a species are

more likely to be attracted among themselves. This parameter can be expressed as the difference in solubility parameters of the blend components via

$$\chi_{12} = \frac{v_r}{kT}\left(\delta_1 - \delta_2\right)^2 , \tag{1-14}$$

where δ_n is the solubility parameter for species n. This parameter is defined as the square root of the cohesive energy density, which is the energy needed to vaporize one mole of a liquid at zero pressure. The solubility parameter can be applied to any substance that is capable of mixing; most discussions on the solubility parameter pertain to mixing of solvents and polymers or solvents by themselves. In the context of polymer blends, the majority component can be treated as a solvent. Equation (1-14) performs poorly for polymer solutions with strong polar or hydrogen bonds.[40] With the advent of Hansen Solubility Parameters (HSP),[41] δ is the square root of the sum of the squares of three components:

$$\delta^2 = \delta_D^2 + \delta_P^2 + \delta_H^2 , \tag{1-15}$$

where δ_D = dispersion solubility parameter, δ_P = polar solubility parameter, and δ_H = solubility parameter for hydrogen bonding. These parameters are typically calculated in modeling software.[42] Incorporating HSP into the interaction parameter yields

$$\chi_{12} = \alpha \frac{v_1}{kT}\left((\delta_{1,D} - \delta_{2,D})^2 + \frac{1}{4}(\delta_{1,P} - \delta_{2,P})^2 + \frac{1}{4}(\delta_{1,H} - \delta_{2,H})^2 \right) , \tag{1-16}$$

where v_1 is the volume occupied by a monomer unit for the polymer species acting as the solvent. Most mixing situations work well with correction constant $\alpha = 1$, although there are instances where $0 < \alpha < 1$, depending on the system being modeled.[43]

With the interaction parameter established, it can be used to infer basic features of phase behavior of polymer blends. For endothermic mixing, χ_{12} is inversely

proportional to the temperature, in which a decrease in the temperature is unfavorable for miscibility and the system shows an upper critical solution temperature (UCST). For exothermic mixing, χ_{12} increases with temperature and lower critical solution behavior manifests, as seen in Figure 1-10. Here, the binodal curve denotes the limits of miscibility. Outside the binodal, the single-phase system has thermodynamic stability. Upon increasing the temperature, phase separation ensues.

The spinodal curve denotes the limits of metastability. Once on the spinodal curve, concentration fluctuations can disrupt the system toward a spontaneous phase separation known as spinodal decomposition, resulting in the cocontinuous phase morphology depicted in Figure 1-8b. The metastable region is where the single-phase structure can withstand small spontaneous local concentration fluctuations. Here, the phase separation mechanism is nucleation and growth. This is the mechanism behind the dispersed phase morphology, as depicted in Figures 1-8a and 1-8c.

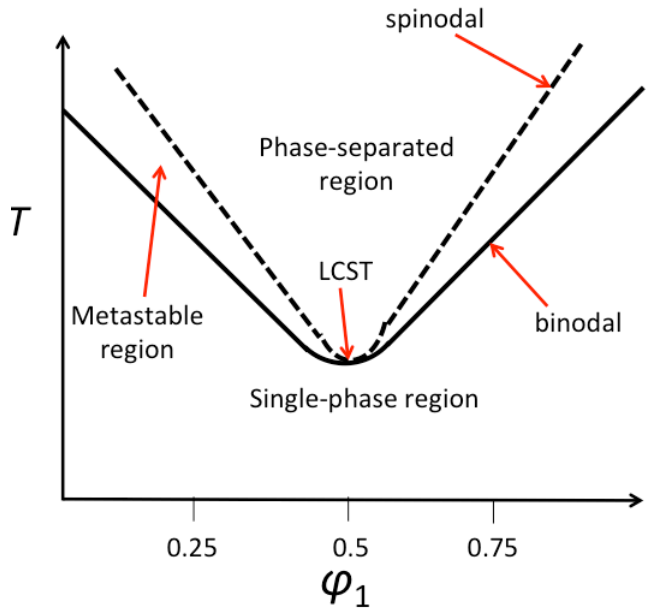

Figure 1-10. Phase diagram of a binary symmetric polymer blend with lower critical solution temperature.

Spinodal decomposition and nucleation and growth can result from a small change in the Gibbs free energy of mixing. Instigation of phase separation is rooted in concentration fluctuations. Thus, the change in Gibbs energy induced by the local concentration fluctuation δG is proportional to the second derivative of ΔG_M:

$$\delta G \sim \frac{\partial^2 \Delta G_M}{\partial \varphi_1^2} . \qquad (1\text{-}17)$$

If the second derivative is > 0, concentration fluctuations lead to a rise in the Gibbs energy. This is unfavorable and such fluctuations are suppressed by the polymer system, preserving its homogeneity. If < 0, the Gibbs energy decreases with any fluctuation. The fluctuations can grow into a separate phase. The polymer blends analyzed in this study possess the dispersed droplet morphology, which makes it likely that nucleation and growth is their mechanism of phase separation. These blends also have a large amount of the dispersed phase, which means the dispersed phase (i.e., domains), undergoes further structural changes by coarsening. Two well-established coarsening mechanisms are coalescence and Ostwald ripening,[44] but these mechanisms assume the polymer blends are quiescent systems. As already discussed in Section 1.3, these systems undergo Marangoni flow, which disrupts the quiescence by subjugating the macromolecules to hydrodynamic forces as well. Additionally, the polymer components are rendered partially miscible with each other by reacting with a compatibilizer, which serves to suppress coarsening up to a point.[45]

1.8 Compatibilization

Compatibilization is a process by which the interfaces within an immiscible polymer blend are modified in a way that reduces the interfacial energy, stabilizes the

morphology against high stresses as it forms, and enhance the adhesion between the phases.[46] The compatibilization reaction in this study is of the form[47-49]

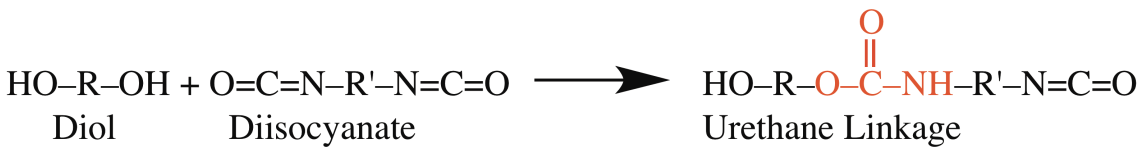

Figure 1-11. Formation of the urethane linkage from a diol and a diisocyanate.

The urethane bond (highlighted in red) is the crosslink and is the chemical method of promoting adhesion between the phases via reactive processing.[36] The isocyanate acts to decrease the average size of domains and stabilize the morphology from the blend processing. However, isocyanates are highly reactive and require blocking agents for stabilization during storage.[48] Among the numerous choices available, ε-caprolactam is the blocking agent of choice for isocyanates in powder coatings because its thermal release occurs at 157 ˚C,[48] although its determination can depend on the method of analysis, heating rate, and other variables.[2] What is important is that the deblocking temperature be between the extrusion temperature (120-130 ˚C) and the cure temperature (204 ˚C), which then enables *in-situ* generation of isocyanates within a curing powder coating.

After deblocking, the ε-caprolactam is highly volatilized and serves to act as an internal solvent within the curing film.[4] The solvation serves to further compatibilize the two resin components and reduce their viscosities for better flow. Of course, Marangoni flow takes place on a substrate, but the substrates encountered in this study are bare metallic substrates, or metallic substrates already coated with a polymer film. Thus, the choice of substrate may have an effect on film morphology.

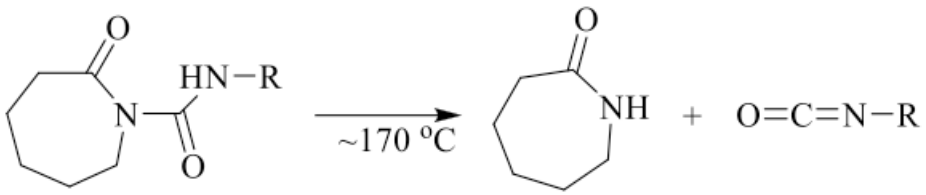

Figure 1-12. Deblocking reaction of ε-caprolactam blocked isocyanate to form free isocyanates.

1.9 Choice of substrate

The choice of substrate could affect the morphology of the domains as well. The polyurethane coatings in this study are usually applied directly on tin-plated steel substrates, but some metal substrates have been pretreated with polytetrafluoroethylene (PTFE) or epoxy primer. Epoxies are commonly used as primers on metals due to their superb adhesion and resistance to heat and chemical attack.[2, 32] The important difference between a bare metal and a polymeric substrate is the surface energy. Surface energies for bare metals range 100-6000 mN/m,[50] while PTFE and epoxy have surface energies of 21-22 mN/m and 42-46 mN/m, respectively.[35]

According to an oft-cited conference paper by Funke and Murase, the morphologies of immiscible powder coating blends of epoxies and acrylics changed with the substrate they were applied on.[51] The epoxy layer consistently adhered to the metal substrate because it had the higher surface energy. While these powder systems produced self-stratified coatings rather than droplet domains, the exhibited dynamics are still analogous. In Figure 1-13, two polymer melts are placed in contact with one another on a metal substrate as well as on PTFE. The figure demonstrates that

- the polymer component with the lower surface energy is always pushed toward the airside, and

- the polymer component with the surface energy closest to that of the substrate exhibits the greater degree of wetting, as exhibited by the smaller contact angle θ in the left schematic of Figure 1-13.

The different behaviors induced by the substrates will have implications for domains near the substrate. This is discussed in extensive detail in Chapters 7 and 8.

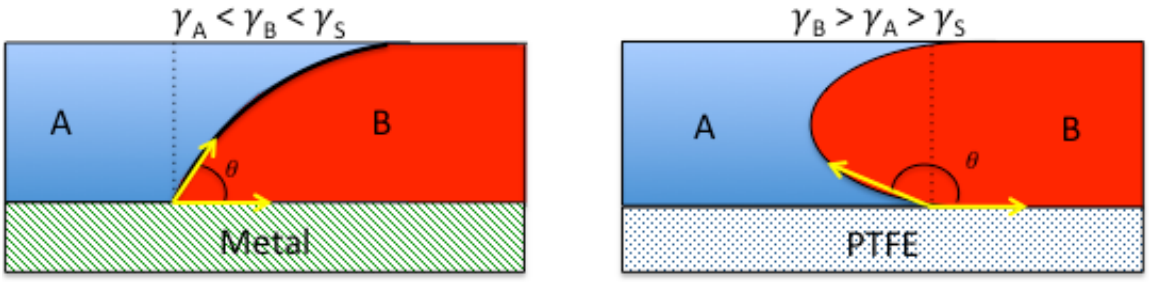

Figure 1-13. Contact angle variation between two immiscible resins (with surface energies γ_A and γ_B) with respect to the type of substrate (γ_S).

1.10 References

1. Paul, S., *Surface Coatings: Science and Technology*. 2nd ed.; John Wiley and Sons: Chichester, England, 1996; p 931.
2. Jr., Z. W. W.; Jones, F. N.; Pappas, S. P.; Wicks, D. A., *Organic Coatings: Science and Technology*. 3rd ed.; Wiley-Interscience: Hoboken, New Jersey, 2007; p 746.
3. Powder Coatings Market by Resin Type (Epoxy, Epoxy-Polyester Hybrid, Polyester, Acrylic, Polyurethane, & Others) and by End-User Industries (Architectural, Appliances, Automotive, General Industrial, Furniture & Others) - Global Forecast to 2019. http://www.marketsandmarkets.com/Market-Reports/powder-coatings-market-151375565.html (accessed July 14, 2016).
4. Misev, T. A., Powder Coatings. In *Surface Coatings*, 2nd ed.; Paul, S., Ed. John Wiley & Sons: Chichester, England, 1996; pp 788-849.
5. Richart, D. S., The Surface Topography of Powder Coatings and its Relation to Gloss. *Powder Coating* **1999,** *2*, 25-35.
6. Basu, S. K.; Scriven, L. E.; Francis, L. F.; McCormick, A. V., Mechanism of wrinkle formation in curing coatings. *Progress in Organic Coatings* **2005,** *53* (1), 1-16.
7. Lee, S. S.; Koo, J. H.; Lee, S. S.; Chai, S. G.; Lim, J. C., Gloss reduction in low temperature curable hybrid powder coatings. *Progress in Organic Coatings* **2003,** *46* (4), 266-272.

8. Tracton, A. A., *Coatings Materials and Surface Coatings*. CRC Press: Boca Raton, Florida, 2007; p 936.
9. Nadeem, B. http://letsfinishit.com/images/process.jpg (accessed June 15, 2016).
10. Electrostatic Spray Powder Coating Process. http://universal-coatings.net/how-powder-coating-works/ (accessed September 17, 2013).
11. Orchard, S. E., On surface levelling in viscous liquids and gels. *Applied Scientific Research, Section A* **1963,** *11* (4), 451-464.
12. Duivenvoorde, F. L. Pigment dispersing in powder coatings: synthesis and use of block copolymer dispersing agents. Doctoral Dissertation, Technische Universiteit Eindhoven, Eindhoven, 2000.
13. Wetting and Dispersing Additives. http://www.tego.de/sites/dc/Downloadcenter/Evonik/Product/Tego/en/Technical-Background/wetting-and-dispersing-additives.pdf (accessed June 19, 2016).
14. Washburn, E. W., The Dynamics of Capillary Flow. *Physical Review* **1921,** *17* (3), 273-283.
15. Popovich, L. L.; Feke, D. L.; Manas-Zloczower, I., Influence of physical and interfacial characteristics on the wetting and spreading of fluids on powders. *Powder Technology* **1999,** *104* (1), 68-74.
16. Cheever, D. G.; Ulicny, J. C., Interrelationships between pigment surface energies and pigment dispersions in polymer solutions. *Journal of Coatings Technology* **1983,** *55* (697), 53-63.
17. Bird, R. B.; Stewart, W. E.; Lightfoot, E. N., *Transport Phenomena*. Wiley: 2007.
18. Duivenvoorde, F. L.; Nostrum, C. F. v.; Laven, J.; Linde, R. v. d., Improving Pigment Dispersing in Powder Coatings with Block Copolymer Dispersants. *Journal of Coatings Technology* **2000,** *72* (909), 145-152.
19. Manas-Zloczower, I.; Agassant, J. F., *Mixing and Compounding of Polymers: Theory and Practice*. Hanser: 2009.
20. Cheng, H.; Manas-Zloczower, I., Distributive Mixing in Conveying Elements of a ZSK-53 Co-rotating Twin Screw Extruder. *Polymer Engineering and Science* **1998,** *38* (6), 926-935.
21. Freakley, P. K.; Clarke, J., Reduction in Viscosity of an SBR Compound Caused by Mastication and Disagglomeration during Mixing. *Rubber Chemistry and Technology* **1995,** *67* (4), 700-715.
22. Nir, A.; Acrivos, A., On the creeping motion of two arbitrary-sized touching spheres in a linear shear field. *Journal of Fluid Mechanics* **1973,** *59* (2), 209- 223.
23. Rumpf, H., Grundlagen und Methoden des Granulierens. *Chemie Ingenieur Technik* **1958,** *30* (3), 144-158.
24. Hornsby, P. R., Rheology, compounding and processing of filled thermoplastics. In *Mineral fillers in thermoplastics I*, Springer: 1999; pp 155-217.
25. Buscall, R., The Hamaker coefficient for titanium dioxide (rutile) in liquid media. *Colloids and Surfaces A: Physicochemical and Engineering Aspects* **1993,** *75*, 269-272.
26. Lyklema, J., *Fundamentals of Interface and Colloid Science: Soft Colloids*. Elsevier Science: Amsterdam, Netherlands, 2005; Vol. 5.

27. Nadal, M. E.; Early, E. A.; Thompson, E. A., Specular Gloss. Commerce, D. o., Ed. U.S. Department of Commerce, Technology Division, National Institute of Standards: 2006.
28. Jacquin, J. D.; McCurdy, M. R.; Dennis, D. J.; Evangelista, M.; Favrin, D.; Minesso, A., New Resin Technology for Semi-Matte and Dull-Matte Powder Coatings—Part 1. *Powder Coating* **2009,** *9*, 37-41.
29. Assender, H.; Bliznyuk, V.; Porfyrakis, K., How Surface Topography Relates to Materials' Properties. *Science* **2002,** *297* (5583), 973-976.
30. Hecht, E., *Optics*. 4th ed.; Addison-Wesley: San Francisco, California, 2002; p 698.
31. Bristow, A., The Surface of Paper. In *Paper Products Physics and Technology*, Walter de Gruyter GmbH & Co. : Berlin, Germany, 2009; Vol. 4, p 342.
32. Hare, C. H., *Protective Coatings: Fundamentals of Chemistry and Composition*. Technology Publishing Company: Pittsburgh, Pennsylvania, 1994; p 514.
33. Jacquin, J. D.; McCurdy, M. R.; Dennis, D. J.; Evangelista, M.; Favrin, D.; Minesso, A., New Resin Technology for Semi-Matte and Dull-Matte Powder Coatings—Part 2. *Powder Coating* **2009,** *10*, 24-37.
34. Verkholantsev, V. V., Heterophase and self-stratifying polymer coatings. *Progress in Organic Coatings* **1995,** *26*, 31-52.
35. Verkholantsev, V. V., Self-stratifying coatings for industrial applications. *Pigment and Resin Technology* **2003,** *32* (5), 300-306.
36. Koning, C.; Duin, M. v.; Pagnoulle, C.; Jerome, R., Strategies for Compatibilization of Polymer Blends. *Progress in Polymer Science* **1998,** *23* (4), 707-757.
37. Starý, Z., Thermodyanamics and Morphology and Compatibilization of Polymer Blends. In *Characterization of Polymer Blends: Miscibility, Morphology, and Interfaces*, 1 ed.; Thomas, S.; Grohens, Y.; Jyotishkumar, P., Eds. Wiley-VCH Verlag GmbH &Co. KGaA: Boschstrasse 12, 69469 Weinheim, Germany, 2015; pp 93-131.
38. Flory, P. J., Thermodynamics of High Polymer Solutions. *The Journal of Chemical Physics* **1942,** *10* (1), 51-61.
39. Huggins, M. L., Theory of Solutions of High Polymers. *Journal of the American Chemical Society* **1942,** *64* (7), 1712-1719.
40. Hiemenz, P. C.; Lodge, T. P., *Polymer Chemistry*. 2nd ed.; CRC PressINC: 2007; p 587.
41. Hansen, C. M., *Hansen Solubility Parameters: A User's Handbook*. 2nd ed.; CRC Press: Baca Raton, Florida, 2007.
42. Hansen, C. M.; Abbott, S.; Yamamoto, H. *Hansen Solubility Parameters in Practice*, 4.1.03; hansen-solubility.com, 2013.
43. Lindvig, T.; Michaelsen, M. L.; Kontogeorgis, G. M., A Flory–Huggins model based on the Hansen solubility parameters. *Fluid Phase Equilibria* **2002,** *203*, 247-260.
44. Fortelný, I.; Zivný, A.; Juno, J., Coarsening of the Phase Structure in Immiscible Polymer Blends. Coalescence or Ostwald Ripening? *Journal of Polymer Science: Part B: Polymer Physics* **1999,** *37*, 181-187.
45. Puyvelde, P. V.; Velankar, S.; Moldenaers, P., Rheology and morphology of compatibilized polymer blends. *Current Opinion in Colloid & Interface Science* **2001,** *6*, 457-463.

46. Utracki, L. A., Compatibilization of polymer blends. *The Canadian Journal of Chemical Engineering* **2002,** *80* (6), 1008-1016.
47. Crawford, D.; Escarsega, J., Dynamic mechanical analysis of novel polyurethane coating for military applications. *Thermochimica Acta* **2000,** *357-358*, 161-168.
48. Wicks, D. A.; Jr., Z. W. W., Blocked Isocyanates III: Part A. Mechanisms and chemistry. *Progress in Organic Coatings* **1999,** *36*, 148-172.
49. Schmitt, F.; Wenning, A.; Weiss, J. V., Diimeric isocyanates in polyurethane powder coatings. *Progress in Organic Coatings* **1998,** *34*, 227-235.
50. Vitos, L.; Ruban, A. V.; Skriver, H. L.; Kollár, J., The surface energy of metals. *Surface Science* **1998,** *411* (1–2), 186-202.
51. Funke, W.; Murase, H., Uber die Bildung Mehrphasiger Filme Aus Pulverförmigen polymer-mischungen. In *15th FATIPEC Congress*, 1980; Vol. 2, pp 387-409.

Chapter Two

Sample Preparation and Spectroscopic Analysis

2.1 Coating preparation

Preparation of polyurethane coatings was based on immiscibility between acrylic polyol resins due to large differences in hydroxyl functionalization. Hydroxyl numbers ranged 20-400 OH. The polyols were purchased from Estron Chemical (Calvert City, KY). Coating samples were prepared at the Arthur W. Steudel Technical Center in Chicago, IL.

This section briefly describes how the powder coatings were prepared. All acrylic polyols in this study were crosslinked by an ε-caprolactam externally blocked aliphatic polyisocyanate (Evonik Industries (Parsippany, NJ). Leveling and degassing agents were added at < 1% wt. Two blended clear films were prepared: Blend A and Blend B. Slightly different resin components were used to prepare them. Three colors were formulated according to published specifications.[1] All colored coatings were formulated with calcium silicate matting agent and with the resins used to prepare Blend B. The black coating was formulated at various weight percentages with carbon black and black iron oxide. The tan coating was formulated with chromium oxide, titanium dioxide, carbon black, carbazole dioxaiine violet, various iron oxides, zinc/magnesium ferrite or other mixed metal oxides. The green coating was formulated with acid insoluble green pigments mostly composed of chromium oxide, and traces of cobalt and zinc; carbazole dioxaiine violet, iron oxides, light stable orange and yellow organic pigments;

zinc/magnesium ferrite or other mixed metal oxides. Coatings without pigments (clear coatings) were also prepared for spectroscopic analysis.

The raw mixtures were dry-blended, then melt mixed via a 30 mm twin screw extruder through increasing zone temperatures of 40, 90, and 120 ˚C. Chilled rollers compressed the extrudates into sheets. After cooling, the sheets were pulverized by a ground rotor mill. The resultant powders were classified into different particle sizes by a 106 μm mechanical sieve. The powders were then electrostatically applied to metallic substrates using a standard gravity-fed powder coating cup gun.

2.2 Cross-section preparation

Three embedding resins were used in this study. Two of them were epoxy resins, one was a commercially available polyester resin called Bio-Plastic™. Bio-plastic was used to prepare cross-sections for chemical mapping. Epoxy resins were used to prepare cross-sections for electron microscopy. Reasons for their usage are explained below.

2.2.1 Cross-Sections for spectroscopic analysis

The composition of Bio-Plastic™ polyester resin (Ward's Science, Rochester, NY) is 50% unsaturated polyester prepolymers, 40% styrene monomer, and 10% methyl methacrylate. 15 mL of resin was mixed with 8 drops of catalyst. Mold release compound was applied in a 2.5" × 2.5" × 0.5" Al square mold. The curing resin was poured into the mold. Film fragments were peeled off the tin substrate and placed onto the resin surface. After 30 minutes, a second layer of 15 mL of curing resin was poured into the mold, sandwiching the sample between the resin layers. The resin block cured

for 72 hours, then was cut into pieces small enough to fit in the sample holder for the Leica SP 1600 microtome saw. The saw feed rate was set between 5 and 10 on the dial for the saw to obtain 0.5” × 0.5” × 0.25” cross-section samples that could fit into the MOPAS XS Polisher (Jaap Enterprise, Amsterdam, Holland) with the coating specimen exposed. A hex key was used to turn the screws in the polisher until the resin block was firmly held (other jigs may require standard screwdrivers for securing the sample, as shown in Figure 2-1).

Figure 2-1. MOPAS XS Polisher with resin block sample inside jig.[2]

Several considerations were taken into account while polishing. The plane of the resin block was kept above the plane of the white ceramic crown by 50-100 μm. Also, when upside down, wobbling of the polisher was kept to a minimum. The polisher was

placed on a 6” × 6” 1800 mesh Micro-Mesh™ polishing cloth (Micro Surface Finishing, Wilton, IA) that is secured to the surface by adhesive tape.

Polishing with the MOPAS (Molecular Painting Studies Group) consisted of two stages. The first was the grinding stage, in which the polisher was maneuvered in a square pattern 10 times (up, right, left, down, etc.). A paintbrush was used to remove particles off the jig and cloth, and the surface of the resin block was checked with a microscope to make sure it had been completely scratched by the cloth. Once the resin block surface had a homogeneous set of polishing tracks, grinding proceeded onto the next grade of abrasive cloth, which was 2400 mesh. The grinding procedure was repeated for 3200 mesh, then 4000.

The polishing stage began with 6000 mesh (it is similar to the grinding stage, except no rubbing noise should be audible). The polisher was maneuvered in the same square pattern, but at a slower pace.

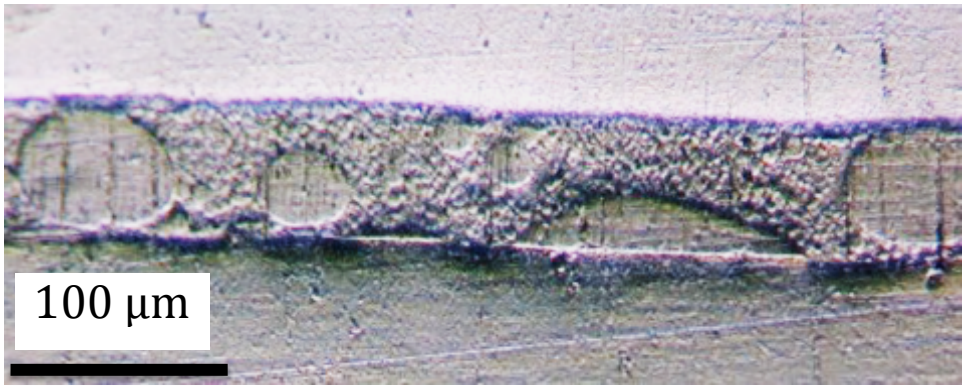

Figure 2-2. Cross-section after final polishing stage.

Loose resin particles were cleaned frequently to avoid “roller tracks” on the surface that could ruin the polish. Once a mirror finish began to develop on the surface, the process was repeated for 8000 mesh, then 12,000 mesh, which resulted in a one micron finish. Such a finish is shown in Figure 2-2.

2.2.2 Cross-sections for TEM

The resin of choice for cross-sections used in TEM was fast cure epoxy (West Systems, Bay City, MI). Unlike Bio-plastic, it does not contaminate the coating samples. This was an excellent resin for samples quenched at different stages of the cure. Bio-plastic was found to damage the morphology of quenched samples for reasons that are explained in chapter 5. The epoxy resin mixture used was 2:1 resin/harder. Coating fragments were placed in a silicone mold tray and cured to completion in about 24 hours. These samples were sent to Central Microscopy Imaging Center (CMIC) at Stony Brook University for microtome sectioning. Microtome cross-section samples were prepared for TEM analysis using a Leica EM UC7 Ultra-Microtome (Wetzlar, Germany) with a diamond sectioning blade; typical thicknesses were 80-150 nm. Quenched coating samples required greater thicknesses due to their brittleness. Pigmented samples were plagued by tearing due to pigment pullout from the microtome blade, especially for the large matting agent particles. Pullout was worse for green and tan coatings due to their higher concentration of pigments.

2.3 Vibrational spectroscopy

2.3.1 Fourier transform infrared spectroscopy (FTIR)

A) Instrumentation

FTIR is one of the most commonly used nondestructive analytical techniques for soft materials. It is used to identify all types of organic and inorganic compounds, to determine what functional groups are present, to quantify species within a mixture, and to

determine the molecular orientation of a macromolecule, among other applications.[3] It can analyze solids, liquids, and gasses, depending on the accessory available. The FTIR spectrometer used in this study is a Thermo Nicolet iS50 Spectrometer.

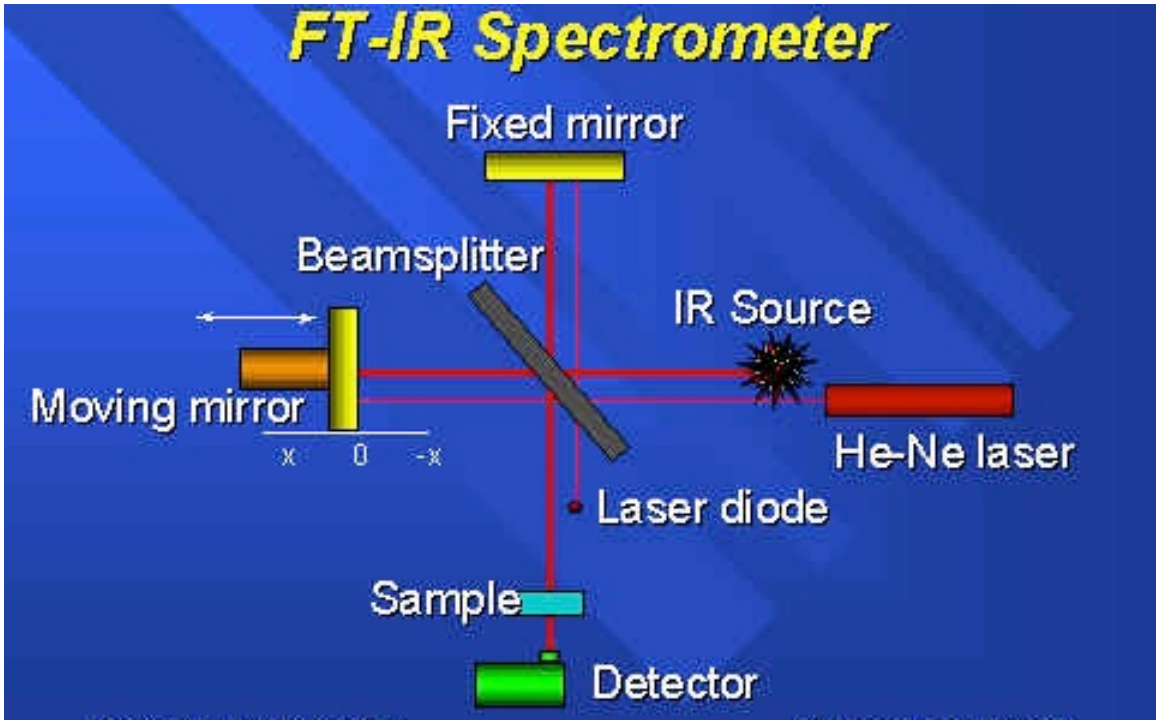

Figure 2-3. Schematic of typical FTIR instrument.

A schematic for a typical Fourier transform spectrometer is found in Figure 2-3. It has three basic components: radiation source, interferometer, and detector. Most designs such as the spectrometer in this study use helium-neon gas (HeNe) as a radiation source. The HeNe laser consists of a mixture of helium and neon gas inside a tube. An electrical discharge excites helium atoms, which transfer their energy to neon atoms via collisions, which induces laser transitions. The transition used for FTIR lasers has a wavelength of 632.8 nm.[4]

The interferometer splits the IR beam into two beams, so that the paths of the two beams are different. The most common type is the Michelson interferometer, which

consists of the following components: fixed mirror, moving mirror, and a beamsplitter. Both mirrors are perpendicular to each other. The beamsplitter is a semi-reflecting device consisting of a thin germanium layer deposited on a flat KBr substrate. At the beamsplitter, the IR beam is split into two halves; one is transmitted to the fixed mirror, and the other reflected to the moving mirror. After the two beams are reflected, they are recombined back at the beamsplitter. Changes in the position of the moving mirror generate an interference pattern in the resultant beam, which then passes through the sample and into the detector.

If both mirrors are equidistant from the beamsplitter, then the situation is defined as zero path difference (ZPD). If the moving mirror is moved away from the ZPD by a displacement x, then total extra distance traveled by the IR beam is $\delta = 2x$. This extra distance is defined as the optical path difference (OPD). If the OPD is in multiples of the wavelength, then constructive interference occurs:

$$\delta = n\lambda, \qquad (2\text{-}1)$$

where $n = 0, 1, 2\ldots$ This situation describes the maximum intensity signal observed by the detector. Conversely, when the OPD is in multiples of $\frac{1}{2}\lambda$, destructive interference occurs, and the detector observes the minimum intensity signal:

$$\delta = (n + \tfrac{1}{2})\lambda. \qquad (2\text{-}2)$$

An OPD in between the two extremes described by Equations 2-1 and 2-2 yields an interference pattern that is also between constructive and destructive. Moving the mirror back and forth increases and decreases the intensity, which gives rise to a cosine wave. The resultant plot is defined as an interferogram. This is shown in the left side Figure 2-4.

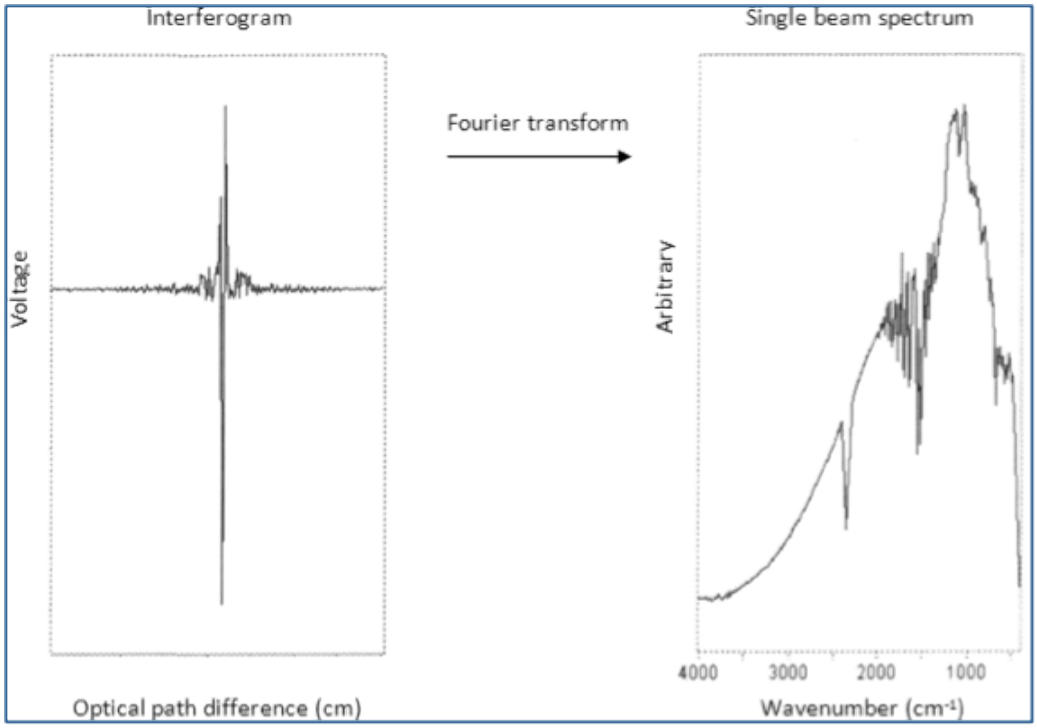

Figure 2-4. Fourier transform between an interferogram and an actual spectrum.[5]

The process for converting an interferogram into a useful spectrum is a mathematical method known as a Fourier transform. The following equation is a common form of the Fourier transform with unitary normalization constants for a function $f(t)$ dependent on time t:

$$F(\omega) = \frac{1}{\sqrt{2\pi}} \int_{-\infty}^{\infty} f(t) e^{-i\omega t}\, dt \qquad (2\text{-}3)$$

in which ω is the angular frequency ($\omega = 2\pi\nu$). While the interferogram is a plot of the intensity of signal versus OPD, its Fourier transform is be considered an inversion of the OPD. The unit of the OPD in the left side of Figure 2-4 is in cm, so the inversion of OPD is in cm^{-1}. Thus, the interferogram is transformed into the IR transmission spectrum on the right side of Figure 2-4 with arbitrary units and recognizable fine structure.

The iS50 Spectrometer uses two photodetectors, which are highly popular among FTIR spectrometers. The majority of the FTIR spectra taken in this study were with the MCT-A detector. The name stands for mercury-cadmium-telluride, which is a ternary alloy that is highly sensitive to IR radiation. It depends on the quantum nature of radiation and exhibits very fast responses, but requires liquid nitrogen for its operation. The "A" indicates that its frequency range is 3600 cm^{-1}-650 cm^{-1}. Other MCT detectors (e.g., MCT-B) have slightly different frequency cutoffs (e.g., 400 cm^{-1}).[6] The other photodetector used in this study is deuterated triglycine sulfate (DTGS). This is a pyroelectric detector that responds to the variations in temperature rather than the value of temperature. It can operate at room temperature, but its acquisition time is longer than for the MCT detector. Noise is a likely nuisance with spectra taken with DTGS, but its frequency cutoff is 400 cm^{-1}. However, typical frequencies of interest for FTIR spectra in this study were 3600 cm^{-1} – 3200 cm^{-1} and 1800 cm^{-1} – 1500 cm^{-1} (well above 650 cm^{-1}). The MCT-A also had the extra benefit of producing spectra with excellent S/N ratios.

B) Theory

The technique is dependent on continuous molecular vibrations being simply induced by the temperature being above absolute zero. When the frequency of the IR radiation matches the frequency of a specific vibration, the molecule absorbs the radiation. The molecules vibrate with a frequency ν according to Hooke's law[7]

$$\nu = \frac{1}{2\pi c}\left(k/\mu\right)^{1/2} \qquad (2\text{-}4)$$

where k is a force constant of the spring, c is the speed of light, and μ is the reduced mass of the atoms involved in the oscillation. This equation links the frequency of vibration, the mass of the interacting atoms, and the strength of the covalent bond between the two

atoms. As simple as Equation 2-4 is, it performs remarkably when compared to frequencies observed by experiment. What it does not account for is the attraction and repulsion of the electron cloud at the edges of the vibrational motion, and does not account for bond dissociation at high amounts of absorbed energy. However, these sources of anharmonicity (deviations from the ideal model in Hooke's Law) do not usually affect quantum transitions from the ground state to the first excited state, which manifest as the most intense bands in IR spectra.

Each atom in a molecule can be described in terms of a minimum set of fundamental vibrations. To start, it has three degrees of freedom corresponding to a threefold set of coordinate axes. A molecule composed of n atoms should have $3n$ degrees of freedom, but is in reality $3n - 6$ degrees when translational and rotational motions of the entire molecule are subtracted out ($3n - 5$ for linear molecules). Moreover, not all vibrations are IR-active. Their detection by FTIR is dependent on the change of the dipole moment for that vibration, as depicted in Figure 2-5b; the CO_2 vibration in 2-5a has no net dipole moment, and thus is IR-inactive.

Absorption bands arise from two different types of vibrations: stretching and bending. Stretching vibrations are typically higher energy than bending vibrations; stretches typically require more energy than bends due to the force of the chemical directly opposing the change in motion. Additional bands could also be generated from overtones, combinations of fundamental frequencies (e.g, the amide II band),[9] coupling interactions of two fundamental absorption frequencies, differences of fundamental frequencies, and coupling interactions between fundamental vibrations and overtones or combination bands. Overtone, combination, and difference bands have smaller

intensities than those of fundamental bands. The panoply of vibrational bands and their potential combinations and interactions thereby create a unique IR spectrum for each compound.

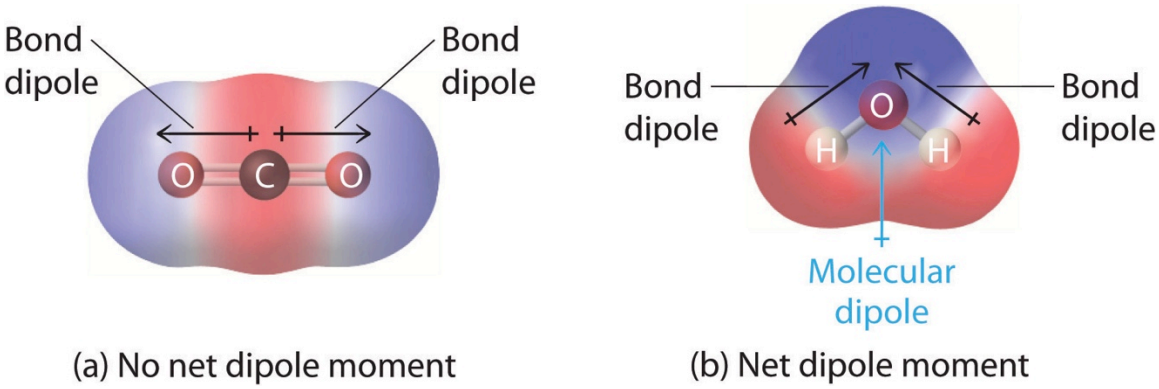

Figure 2-5. Charge distributions of CO_2 and H_2O. Blue and red colored regions are negatively and positively signed regions, respectively.[8]

A convention among spectroscopists is to convert the wavelength from μm to wavenumbers, which is done by[10]

$$\nu(\text{cm}^{-1}) = \frac{1}{\lambda}(\mu\text{m}) \times 10^4 \qquad (2\text{-}5)$$

The infrared (IR) region used by most analysts of organic materials is the mid IR region, defined as the frequency range between 4000 and 400 cm^{-1}. This is the range where the vibrational states of most organic molecules are found. The far IR range is used for analysis of organic, inorganic, and organometallic compounds involving atoms with atomic numbers > 19; its range spans 200cm^{-1}-50cm^{-1}.[3] Near IR is often used in diverse fields such as agricultural and food science, pharmaceutical research, medicine, and atmospheric chemistry; its frequency range is 13,300cm^{-1}-4000 cm^{-1}.[11]

2.3.2 Raman spectroscopy

A) Instrumentation

Complementary to FTIR spectroscopy is laser Raman spectroscopy, or LRS. It has a shorter history of widespread use due to technological limitations that were overcome relatively recently. Labs that acquire Raman instruments choose either a dispersive or an FT spectrometer. Dispersive spectrometers utilize visible lasers for excitation, a CCD (charge-coupled device) detector, and monochromator(s). FT Raman spectrometers utilize near-IR lasers (typically 1064 nm) for excitation, and an interferometer-based system that performs Fourier transforms of the collected interferograms. The Raman spectrometer used in this study is a Thermo Scientific Nicolet Almega™ dispersive spectrometer. The basics of Raman dispersive spectrometers will be thus described here.

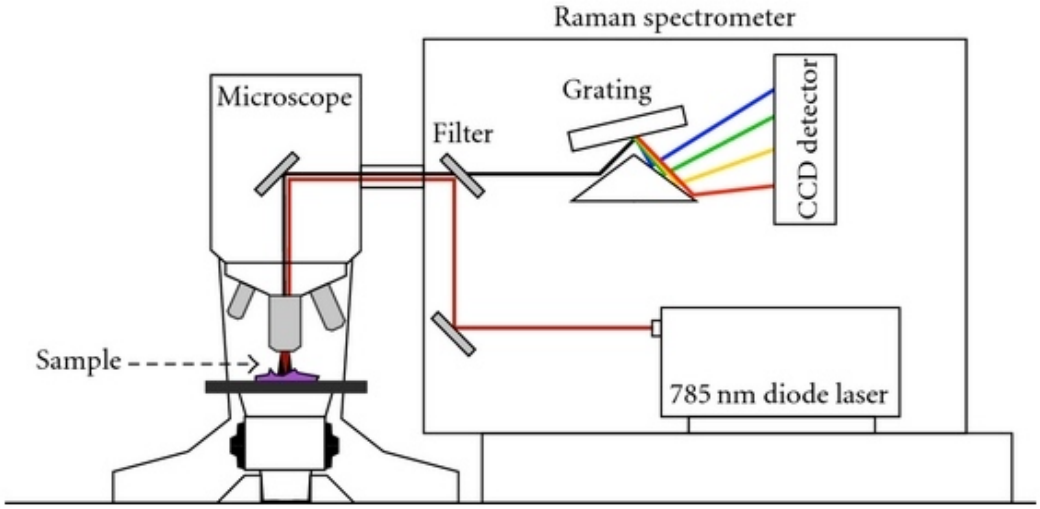

Figure 2-6. Typical setup for a Raman dispersive spectrometer with a near-infrared laser attached to a microscope.[12]

A diagram of a generic dispersive Raman spectrometer is found in Figure 2-6. What follows is a description of the main components encountered by the laser within the spectrometer. Peaks due to Raman scattering are measured as a shift from the excitation source, which indicates a monochromatic light source is needed for obtainment of quality data; hence the employment of lasers. The source was a laser diode that generated a

beam with a wavelength of 785 nm. After exiting the source, the beam may pass through a line filter that blocks out extraneous photons. The laser (drawn as a red line in Figure 2-6) then passes through a pinhole for additional focusing, which occasions collection as an expanded parallel beam. This focused beam then reflects off a notch filter (labeled as 'Filter' in the diagram above) toward the microscope. The beam passes down toward the sample, where it undergoes absorption, scattering, and, if applicable, transmission. The portion that is scattered directly opposite the incident radiation is what is collected by the same optics that transmitted the incident beam. This scattered beam (drawn as a black line in Figure 2-6) comes into contact with the notch filter at an angle that serves to facilitate its total transmission toward a series of monochromators (typically two or three). The first monochromator separates the Raman-shifted scattering from the other radiation; this is typically a Rayleigh filter, which filters out elastic (Rayleigh) scattering. The second monochromator increases the dispersion and separates the individual Raman peaks. Monochromators usually are sold as notch filters, which permit radiation with a narrow frequency range to pass through. They are small and efficient and are a primary reason for the reduced size and cost of Raman spectrometers in recent decades.

An important consideration for Raman spectra is resolution, which determines the amount of detail observed within spectra. Low resolution within a spectrum may render the characterization of closely related compounds an impossible task. Unnecessarily high resolution within a spectrum could add noise without providing a commensurate increase in useful information. Spectral resolution is determined by two factors: the optical design of the spectrograph, and the diffraction grating distribution. Gratings have many grooves etched into the surface, which disperse the incoming radiation. The higher

the number of grating lines per unit length, the broader the dispersion angle, and the greater the acquired resolution. The layout of the gratings is designed for optimal throughput over a relatively narrow wavelength range, which means it is matched specifically to each laser within the spectrometer.

The CCD detector typically is a highly sensitive silicon device. Its surface is composed of a two-dimensional array of light-sensitive elements called pixels that act as individual detectors for specific wavelengths dispersed by the gratings. The CCD detector is designed to have a large wavelength response region, often ranging 400 nm-1000 nm. For additional information on instrumentation for Raman spectroscopy, the textbook by Smith and Dent is a valuable resource.[13]

B) Theory

LRS operates on inelastic scattering of photons, in which some energy is transferred from the incident photon to the molecule and/or vice-versa. In both cases, the energy of the scattered photon differs from the incident photon. This is the essence of Raman scattering, which is a very weak process compared to elastic (Rayleigh) scattering. Only one in 10^6–10^8 photons that scatter off a surface is Raman scattered. However, as addressed in part A of this section, the arrival of highly collimated laser light, efficient Rayleigh filters and the implementation of microscopes overcame this limitation.

At room temperature, most molecules are present in the lowest energy (ground) quantum state. The interaction of the laser with the electron cloud of a molecule polarizes it, which creates virtual quantum states (Figure 2-7).

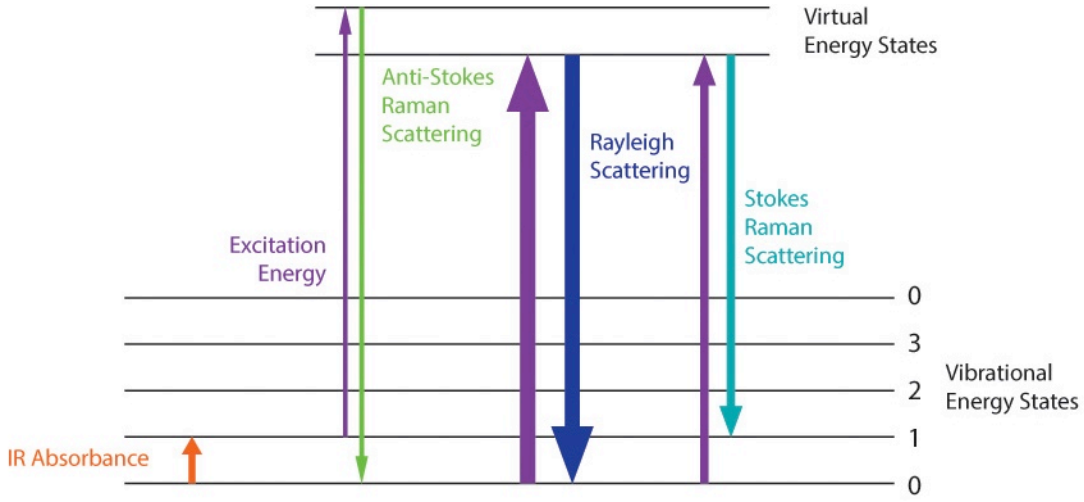

Figure 2-7. Diagram of Rayleigh and Raman scattering processes; IR absorbance included for comparison.[14]

The Rayleigh process involves no energy change, and consequently the photon returns to the same energy state. In the Raman scattering event, an electron in ground state *m* is promoted to a virtual state via absorption of the incoming photon, and then relaxes to a higher energy excited state *n*. This is one of two Raman scattering processes known as Stokes scattering. Anti-Stokes scattering is a weaker event because the transition requires the molecule to be in excited state *n* upon interaction with a photon; at room temperature, the population of molecules in the ground state far exceeds those in excited states. In short, selection rules for Raman spectroscopy require the vibration to display a net change in bond polarizability for a transition, whereas IR spectroscopy requires a change in dipole moment. In Figure 2-5a, the symmetric vibration for CO_2 produced a net change in polarizability, which makes it Raman active; the vibration for water in 2-5b is also symmetric and thus Raman active. An example of a molecule exhibiting vibrational modes active for just one vibrational technique or the other is found in Figure 2-8 for carbon disulfide. As indicated by the arrows in the figure, the sole Raman peak

stems from the vibration labeled V_a, which exhibited nonzero polarizability in the third row.

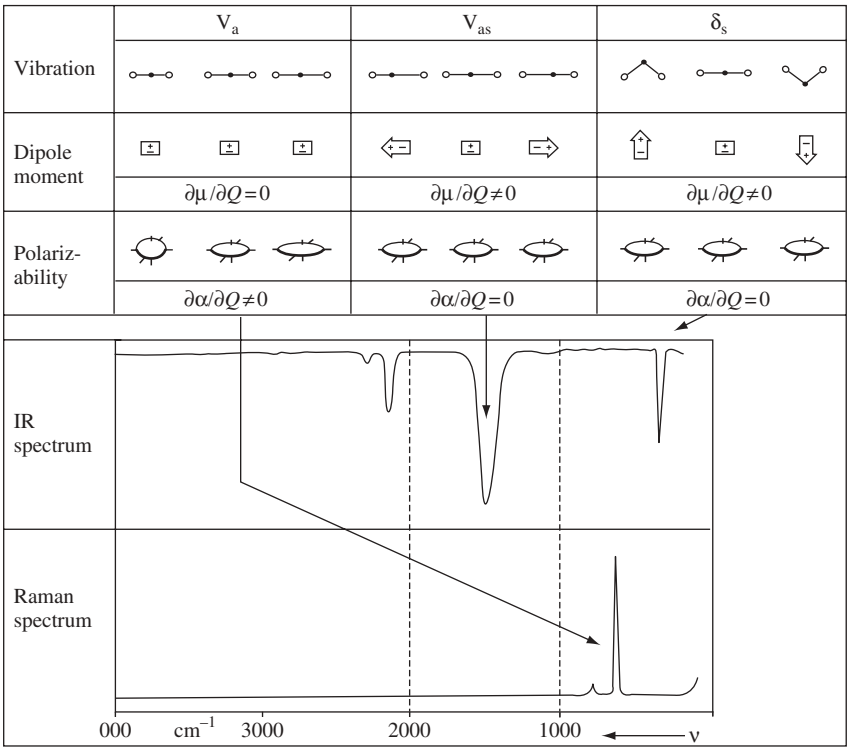

Figure 2-8. Dipole and polarization in CS_2, with resultant Raman and IR spectra.[15]

2.3.3 Complementary Nature of Both Vibrational Spectroscopies

The figure above demonstrates that both vibrational spectroscopies complement each other by detecting vibrational modes that may be detectable in just one of the utilized techniques. The general structure of the monomer unit for the acrylic polyol prior to crosslinking is depicted in Figure 2-9.

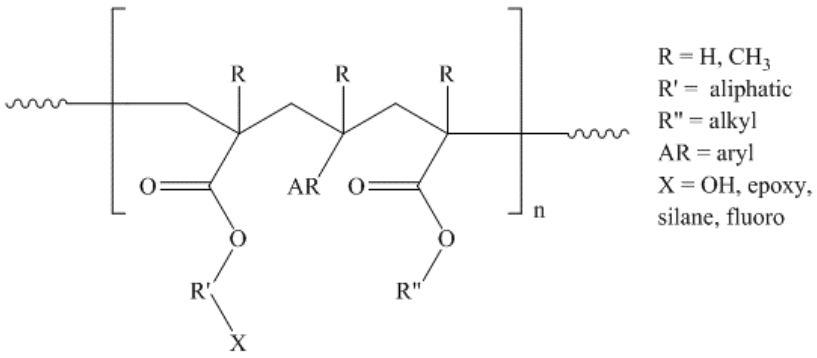

Figure 2-9. Generic monomer unit of an acrylic polyol reactant.

The 'X' is OH in this case, which reacts with isocyantes to generate urethane linkages. The monomer also has ester groups. Urethane, ester, isocyanate, and other unknown polar moieties would be sensitive to FTIR analysis. This would be essential for observing peak changes as the crosslinking reaction progresses. Two types of attachments were used for the Thermo Nicolet iS50 spectrometer. Most commonly used was ATR-FTIR, which allows film samples to be placed in direct contact with a crystal. Three ATR crystals were employed in this study: ZnSe, diamond, and Ge. The incident angle of the radiation was set to $\theta = 45^{\circ}$ for all ATR measurements, which affects the penetration depth. ZnSe and diamond have the same index of refraction ($n = 2.4$), while $n_{Ge} = 4$.[16] ATR works by allowing radiation to enter the film from a medium with a high n into a low n material ($n_{coating} \sim 1.5$). This internal reflectance produces an evanescent wave with a penetration depth of 4.4 μm for ZnSe/diamond, and 0.66 μm for Ge; using multiple crystals on a sample enables sampling of different profiles within the film. The attenuated energy from the wave passes back to the reflecting IR beam. The beam exits the opposite end of the crystal and propagates to the detector. The different refractive indices for each crystal yield different penetration depths. Figure 2-10 illustrates basic

ATR phenomena. The diameter of the diamond crystal is 2 mm, which is far too large to sample individual domains.

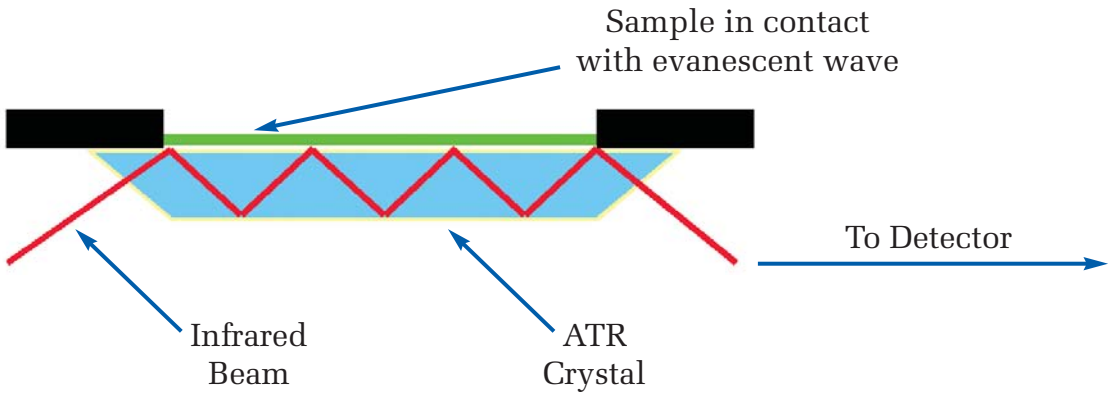

Figure 2-10. Schematic of internal reflections in ATR crystal.[17]

The other FTIR attachment enabled diffuse reflectance infrared Fourier-transform spectroscopy (DRIFTS), which is mainly used for acquiring IR spectra of powders and films with very rough surfaces. The sample scatters photons from the laser in all directions. The diffusely scattered radiation is recollected by large elliptical mirrors that also minimize specular reflectance, which may distort IR spectra. Samples analyzed by DRIFTS required some preparation. This entailed grinding by mortar and pestle, followed by homogeneous dilution to 5-10% by weight in potassium bromide salt. KBr is IR-transparent but hygroscopic; water absorption could contaminate IR spectra if the sample is exposed to air for too long.[18] DRIFTS was used on the reactants (acrylic polyols, polyisocyanate compatibilizer) that generated the polyurethane films, which in raw form consisted of pellets no larger than ~ 1 cm.

Aryl branches are also part of the monomer, and thus may feature prominently with backbone chain vibrations in Raman spectra. Moreover, the spot size of the Raman laser is only 3.1 μm, which permits observation of individual domains. FTIR is a

macroscopic technique, while Raman is a microscopic technique. The features of the monomer unit demonstrate the utility of the complementary nature of both vibrational techniques in this study. No sample preparation was needed for LRS. Analysis of liquids is also possible, but such samples need to be placed in a quartz curvette, since quartz is both transparent and Raman-inactive in the mid-IR range.

2.4 X-ray photoelectron spectroscopy (XPS)

Another spectroscopic technique used in this study is photoelectron spectroscopy, which counts electrons as data instead of IR photons. XPS was used to characterize the airsides and substrate interfaces of the coatings. Its area of analysis is ~1 cm^2, which renders it a macroscopic analytical technique akin to FTIR (thus no coating cross-sections are analyzed by XPS).

2.4.1 Instrumentation

XPS instrumentation is highly complex and is almost never depicted in its entirety in schematic form. Instead, components of XPS will be discussed sequentially in terms of x-ray and photoelectron paths. XPS is an extremely surface sensitive technique and thus requires operational pressures of 10^{-9} torr or lower. Such ultra high vacuum (UHV) pressures are required:

- to prevent potential scattering of photoelectrons by residual gasses within the sample chamber,
- to also prevent a monolayer of gas to be adsorbed onto the surface, which takes about one second to form at pressures of ~10^{-8} torr.

UHV is typically achieved through a combination of a rotary pump, titanium sublimation pump, and an ion pump. Such systems also require occasional baking at temperatures of 100-160 ˚C to remove adsorbed gas layers from the sample chamber walls. Chambers and associated piping are made from stainless steel, while joints are effected via knife-edged flanges that are tightened on copper gaskets.

X-ray generation occurs by bombardment of an anode with high-energy electrons. The electron source is typically an electrically heated tungsten filament, (some instruments use LaB_6). The anode is usually made of Al or Mg. These elements give rise to a very intense $K_{\alpha 1,2}$ doublet that can be resolved into a coherent singlet a by a monochromator. Al and Mg generate x-ray photons at 1486.7 eV and 1253.6 eV, respectively.

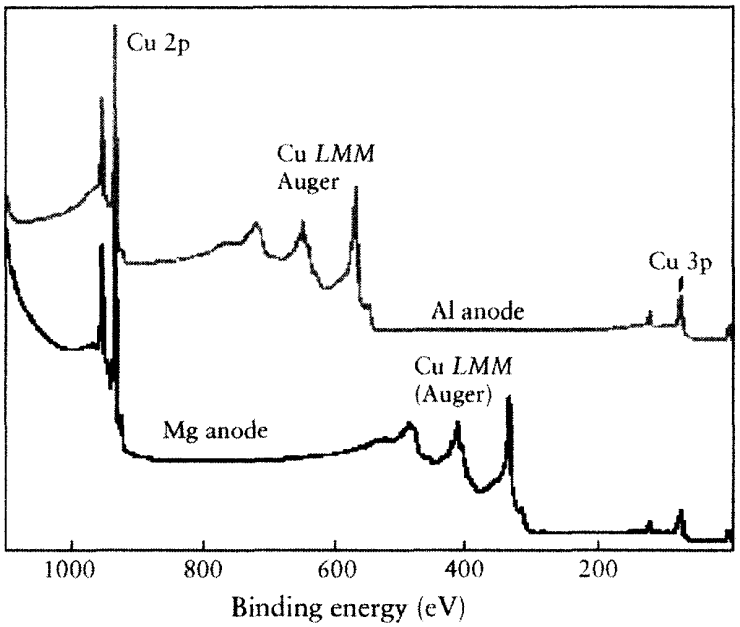

Figure 2-11. Comparison of XPS spectra recorded from copper using AlKα (upper) and MgKα (lower) radiation.[19]

Both anodes are often supplied as a twin anode configuration within a single x-ray gun. The filament is kept at ground, while the anode is kept at potentials of 10-15 kV. Utilizing both anodes on the sample allows one to differentiate between Auger and photoelectron transitions when the two overlap on radiation. XPS peak positions would change by 233 eV on a kinetic energy scale, whereas Auger transitions remain constant, as exemplified in Figure 2-11 for copper.

Since polymeric samples are insulators, photoemission induces an accumulation of positive charges. This shifts photoelectron peak positions toward higher binding energy. The charged surface can be neutralized by attaching an external source to replenish the electrons. This process is called charge compensation, which can be performed in several ways; e.g., use a low-energy electron flood gun. In this study, attaching a gold wire to the sample stage enabled charge compensation.

Measurements were conducted with a hemispherical sector analyzer (HSA). It consists of a pair of concentric hemispherical electrodes that are spaced apart such that there is a gap for electrons to pass. The entrance to the analyzer is accompanied by a transfer lens(es), which performs the following functions:

- maximizes the collection angle to ensure high transmission and sensitivity,
- reduces the kinetic energy of the electron flux prior to its entering the analyzer (retardation)
- varies the area of the sample from which electrons are collected.

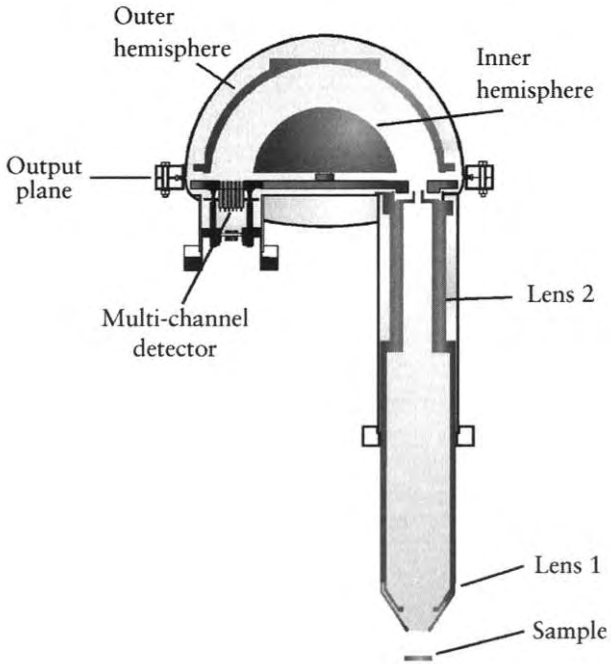

Figure 2-12. Diagram of a typical HSA and transfer lenses.[19]

A schematic of a typical HSA and the transfer lenses is depicted in Figure 2-12. The two hemispheres have an electrostatic potential between them with the outer hemisphere being more negative than the inner one. If electrons enter the input to the analyzer tangentially, they will only reach the detector if their kinetic energy is given by

$$E_k = e\Delta V\left(\frac{R_1 R_2}{R_2^2 - R_1^2}\right) \tag{2-6}$$

where ΔV is the potential difference, e the electron charge, and R_1 and R_2 are the radii of the inner and outer hemispheres, respectively. The bracketed terms in Equation 2-6 can be simplified into a constant, since the radii cannot be varied.

Electrons with kinetic energies exceeding the above term in Equation 2-6 will follow paths with radii larger than the mean radius of the HSA and those with lower kinetic energies will follow paths with smaller radii. If the differences do not differ too greatly from the above term, these electrons will also reach the output plane of the

analyzer. The large energy spread of the electron flux is the impetus for attaching several different detectors at the output plane, where such detectors are arranged radially. These detectors are known as channel electron multipliers, but are commonly called channeltrons; they are discussed in a subsequent paragraph in this section.

The HSA usually has two modes of operation: constant analyzer energy (CAE) and constant retard ratio (CRR). CRR is used for Auger spectroscopy, and will not be discussed here. Under CAE mode, electrons are accelerated or retarded to some user-defined energy known as the pass energy; it is the energy photoelectrons possess as they pass through the analyzer. The pass energy affects both electron flux and resolution.

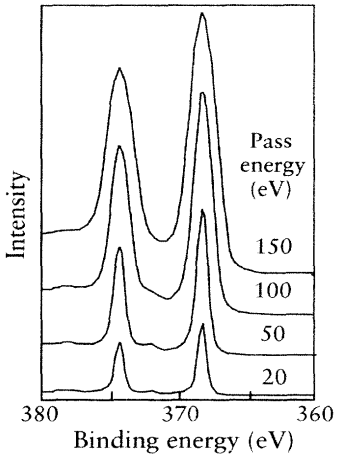

Figure 2-13. Effects of pass energy variation for Ag 3d peaks.[19]

High pass energy allows high flux but low resolution; low pass energy allows low flux but high resolution. The effects of different pass energies are shown in Figure 2-13 for the Au 3d peaks. Pass energies range from 1 eV to several hundred eV. 100 eV is typically used for survey scans, while 20 eV is normally used for high-resolution spectra of core levels. High-resolution spectra are used to identify chemical states of the elements present and for quantification (if applicable).

Channeltron detectors collect photoelectrons of different energies in a way such that adding the signals into the appropriate energy channel can increase the sensitivity of the instrument by a factor equal to the number of detectors. Attaching a high number of channeltrons to the output plane enables acquisition of high-quality spectra without scanning the analyzer. A channeltron consists of a spiral-shaped glass tube with a conical collector at one end and a metal anode at the other end. The inner walls of the detector are coated with a material that enables emission of multiple secondary electrons for a single photoelectron; a cascading effect ensues, which may result in 10^8 electrons reaching the anode for one photoelectron. A large negative voltage permeates the cone (Figure 2-14a).

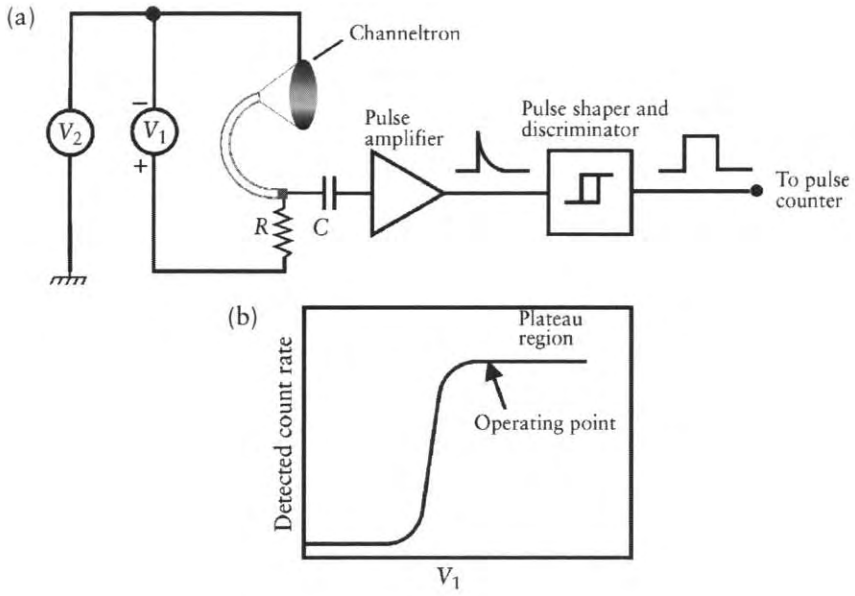

Figure 2-14. Schematic presenting (a) the operation of a channeltron, and (b) output characteristics.[19]

The gain within a channeltron depends upon the voltage between the ends. Below a certain threshold voltage, no output pulses can be detected. Above the threshold, the detection efficiency increases with voltage until a plateau region is reached. At this

plateau, the measured count rate has no dependence on the voltage. The operational voltage should lie within parameters between 2 kV and 4 kV, just after the start of the plateau in count rates (Figure 2-14b). The pulse shaper converts the amplified singles into square waves that can be counted by rate counter, while the discriminator eliminates noise singals emanating from the channeltron or preamplifer.

2.4.2 Theory

XPS is a modern realization of the photoelectric effect, as first explained by Einstein in the seminal 1905 paper that eventually led to his Nobel Prize in 1921.[20] In this effect, a photon of energy $h\nu$ is absorbed by a sample and is followed by the emission of a photoelectron

$$h\nu = E_b(n) + E_k + W, \qquad (2\text{-}7)$$

where $E_b(n)$ is the binding energy of an electron in the nth quantum level of the atom referenced in the vacuum level, E_k is the kinetic energy of the photoelectron, and W is the work function of the analyzer within the spectrometer.

Monochromatic x-rays (or close to monochromatic) photoionize atoms by ejecting electrons out of their atomic shells (Figure 2-15).

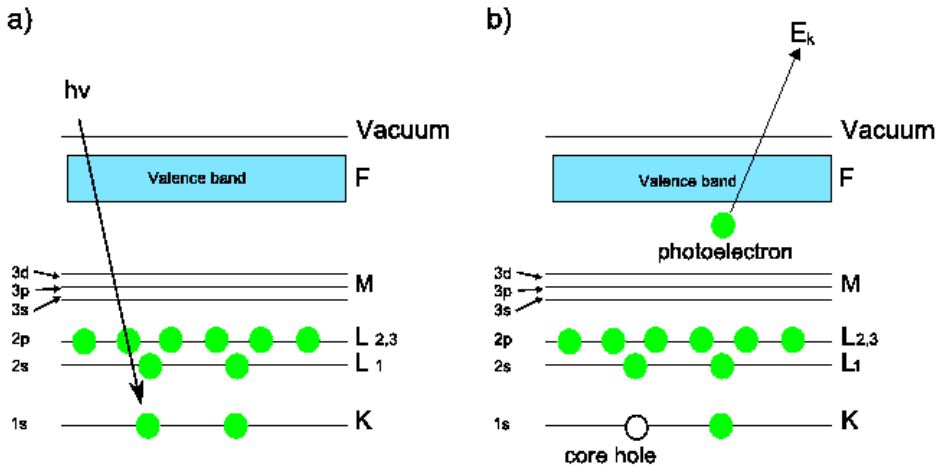

Figure 2-15. Schematic of photoemission process; (a) photon absorption at K level; (b) photoemission with core hole in K level.[21]

The utility of XPS is rooted in element sensitivity, chemical state indication, and surface sensitivity. Every element has a unique set of binding energies that are easily discernible in modern spectrometers. Chemical shifts are indicated by the 'shoulders' or separate peaks relative to the peak spectra that would not be present in simple chemical states. The photoelectron spectrum reproduces the electronic structure of an element with great accuracy since all electrons with binding energies exceeded by the photon energy will appear in the spectrum. This is illustrated in Figure 2-16, where the XPS spectrum of lead is superimposed on a simple diagram of its orbitals. The electrons that escape the specimen without energy loss contribute to the peaks in the spectrum. Electrons that scatter inelastically and thus lose energy contribute to the background of the spectrum.

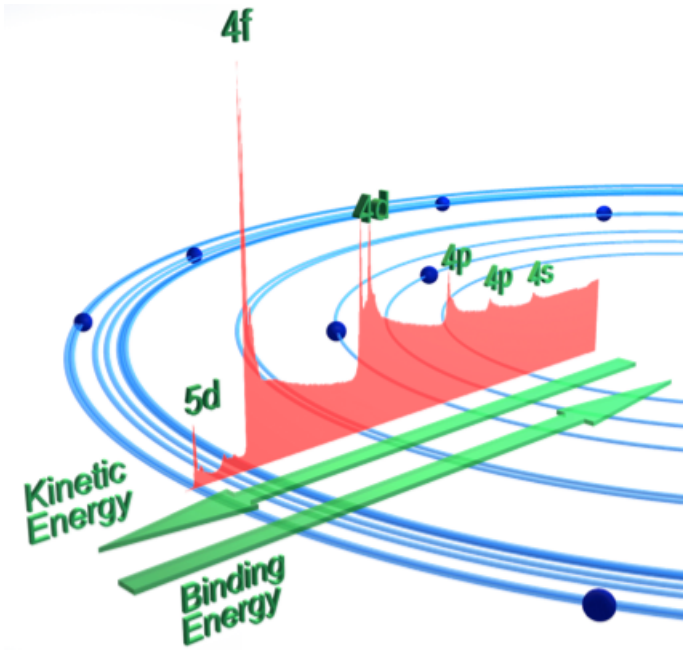

Figure 2-16. Photoelectron spectrum of lead superimposed over a schematic of its electronic structure to illustrate how photoelectron peaks arise out of the orbitals.[19]

XPS is a highly surface-sensitive technique to its low sampling depth. The depth is determined by the attenuation length (λ), which is related to the inelastic mean free path (IMFP). Tanuma, Powell, and Penn have used optical formulas and other physical parameters to develop an empirical formula for the IMFP as a function of the kinetic energy E_k known as the TPP-2M predictive equation:[22]

$$\lambda = \frac{E_k}{E_p^2\left[\beta \ln(\gamma E_k) - C/E_k + D/E_k^2\right]} \qquad (2\text{-}8)$$

$$\beta = -0.10 + 0.944\left(E_p^2 + E_g^2\right)^{-1/2} + 0.069\rho^{0.1}$$

$$\gamma = 0.191\rho^{-1/2}$$

$$C = 1.97 - 0.91U$$

$$D = 53.4 - 20.8U$$

$$U = N_v\rho/M = E_p^2/829.4$$

where $E_p = 28.8\left(N_v\rho/M\right)^{1/2}$ is the free-electron plasmon energy, N_v is the number of valence electrons per molecule (for compounds), ρ is the density, M is the molecular

weight, and E_g is the bandgap. For most organic materials, the IMFP is ≤ 5 nm when the source is a MgKα or AlKα anode (Figure 2-17).

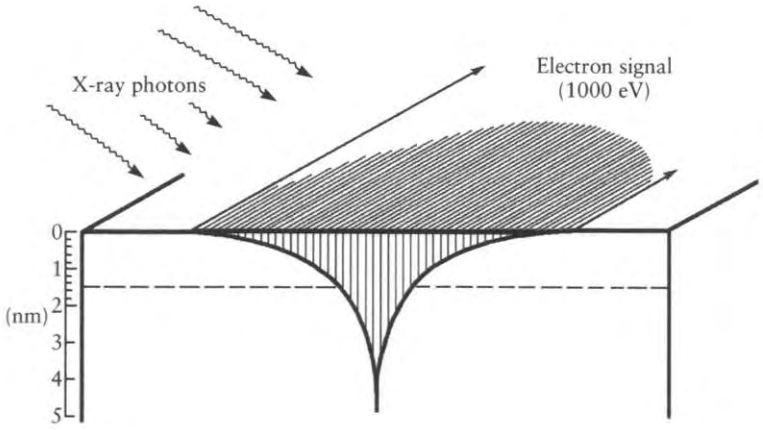

Figure 2-17. Electron intensity as a function of depth; the horizontal dashed line indicates a distance from the surface of the attenuation length λ.[19]

Figure 2-17 also subtly suggests λ has an angular dependence. If photoelectrons are detected at an angle oblique to the sample, λ is reduced by an amount equal to the cosine of the angle between the surface normal and the entrance to the HSA.

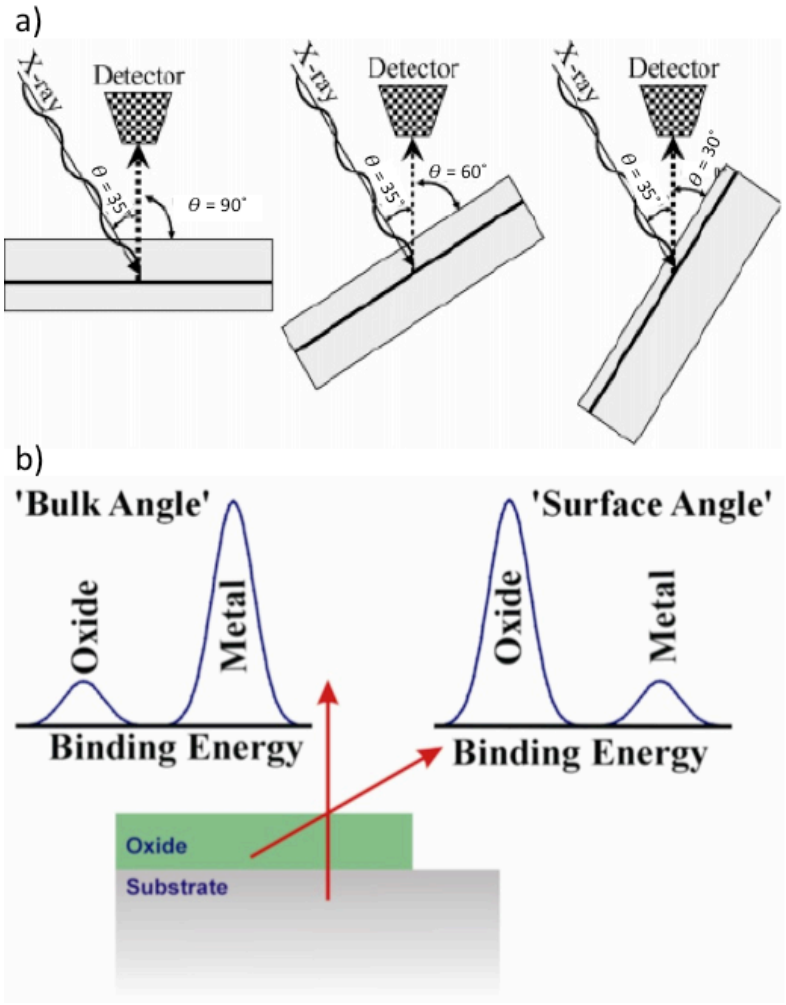

Figure 2-18. a) Sample stage geometry for altering electron emission angle; b) changes in intensity with respect to sampling depth induced by changing the emission angle for a metal oxide sample.[23]

This angle can be changed by tilting the sample holder with respect to the electron emission angle or with respect to the incident x-rays; in this study, sample tilting was oriented with respect to the x-ray source (Figure 2-18a). Changing the angle for XPS measurements leads to analysis by angle-resolved XPS (ARXPS). Application of ARXPS in this study is motivated by the heterogeneity of these coatings, e.g., potential surface segregation of chemical reactants used for their generation. Sample tilting is possible with a twin-axis goniometer, which creates the geometries. Lowering the

incident radiation angle decreases the sampling depth, which increases sampling of the surface itself (Figure 2-18b).[24] This enables measurements of changing chemical states with respect to sample depth.

2.4.3 Equipment

A VG Scientific ESCA-3 x-ray spectrometer with an Al Kα source (1486.6 eV) was used to analyze both pigmented and clear coatings. The two angles of incidence were 90° and 60°. XPS spectra were processed with CASAXPS software.[25] All were peak-fitted with a Shirley background, which has the mathematical form[26]

$$Q_n(i) = J(i) - a_n \sum_{j=i+1}^{i_{\max}} Q_{n-1}(j)\Delta E \qquad (2\text{-}9)$$

Q is the background-corrected spectrum over the energy range over the chosen kinetic energy range $E_{min} < E_k < E_{max}$ with corresponding channels $i_{min} < j < i_{max}$ (full width at half-maximum = ΔE). J is the measured spectrum at channel i, and a_n is a constant found by the requirement that $Q_n(i_{min}) = 0$. Calculating the Shirley background is largely an iterative procedure. The Shirley background incorporates the assumption that each unscattered electron is associated with a flat background of losses, which makes the background intensity proportional to the intensity of the total peak area at any point.[27] This is crucial for accurate quantification of elemental composition at a surface. Curve-fitting of experimental data was performed with products of Gaussian-Lorentzian line shapes. The line shapes are defined as:[28]

Gaussian:

$$G(x:E,F,m)=\exp\left[4\ln 2\left(1-\frac{m}{100}\right)\left(\frac{x-E}{F}\right)^2\right] \quad (2\text{-}10)$$

Lorentzian:

$$L(x:E,F,m)=\frac{1}{1+4\frac{m}{100}\left(\frac{x-E}{F}\right)^2} \quad (2\text{-}11)$$

Product of a Gaussian with a Lorentzian:

$$GL(x:E,F,m)=G(x:E,F,m)L(x:E,F,m) \quad (2\text{-}12)$$

$$x=\left(\frac{E-E_0}{\Delta E}\right)^2$$

where $F(E)$ is defined as the intensity at energy E, E_0 = peak center, and m = mixing ratio (1 for pure Gaussian, 0 for pure Lorentzian).

2.5 References

1. Formulations were prepared according to proprietary procedures, consistent with the requirements of U.S. Government specifications.
2. Boon, J. MOPAS XS Polisher. http://www.jaap-enterprise.com/products/mopas-xs-polisher/ (accessed June 26, 2016).
3. Hsu, C. S., Infrared Spectroscopy. In *Handbook of instrumental techniques for analytical chemistry*, Settle, F. A., Ed. Prentice Hall PTR: Upper Saddle River, New Jersey, 1997.
4. Helium-Neon Lasers. https://spie.org/publications/fg12_p82_helium-neon_lasers (accessed July 22, 2016).
5. Smith, B. C., *Fundamentals of Fourier Transform Infrared Spectroscopy*. 1st ed.; CRC Press: Boca Raton, Florida, 1996; p 224.
6. High-Speed, High-Sensitivity Detectors for Use in the Mid-Infrared Spectral Range. http://mmrc.caltech.edu/FTIR/Nicolet/Nicolet Tech Notes/MCT detector Thermo.pdf (accessed July 23, 2016).
7. Coates, J., Interpretation of Infrared Spectra, A Practical Approach. In *Encyclopedia of Analytical Chemistry*, Meyers, R. A., Ed. John Wiley and Sons Ltd.: Chichester, 2000; pp 10815–10837.
8. Blaber, M. Dipole Moments. http://chemwiki.ucdavis.edu/Core/Physical_Chemistry/Atomic_Theory/Dipole_Moments (accessed June 22, 2016).
9. Socrates, G., *Infrared and Raman Characteristic Group Frequencies: Tables and Charts*. 3rd ed.; John Wiley and Sons: Chichester, England, 2004.

10. Vollhardt, K. P. C.; Schore, N. E., *Organic Chemistry: Structure and Function*. 3rd ed.; W. H. Freeman: New York, New York, 2000; p 1210.
11. Pasquini, C., Near Infrared Spectroscopy: fundamentals, practical aspects and analytical applications. *Journal of the Brazilian Chemical Society* **2003,** *14*, 198-219.
12. Fenn, M. B.; Xanthopoulos, P.; Pyrgiotakis, G.; Grobmyer, S. R.; Pardalos, P. M.; Hench, L. L., Raman Spectroscopy for Clinical Oncology. *Advances in Optical Technologies* **2011,** *2011*, 20.
13. Smith, E.; Dent, G., *Modern Raman Spectroscopy: A Practical Approach*. John Wiley & Sons: Chichester, England, 2005; p 210.
14. Raman. http://oceanoptics.com/measurementtechnique/raman/ (accessed July 25, 2016).
15. Fadini, A.; Schnepel, F.-M., *Vibrational Spectroscopy: Methods and Applications*. Halsted Press: New York, New York, 1989.
16. ATR–Theory and Applications. http://www.piketech.com/files/pdfs/ATRAN611.pdf (accessed July 26, 2016).
17. FTIR Spectroscopy-Attenuated Total Reflecttance (ATR). https://shop.perkinelmer.com/content/technicalinfo/tch_ftiratr.pdf (accessed September 12, 2013).
18. Li-Chan, E.; Chalmers, J.; Griffiths, P., *Applications of Vibrational Spectroscopy in Food Science*. John Wiley & Sons: Chichester, England, 2011; p 872.
19. Watts, J. F.; Wolstenholme, J., *An Introduction to Surface Analysis by XPS and AES*. Wiley: Chichester, England, 2003; p 212.
20. Einstein, A., Über einen die Erzeugung und Verwandlung des Lichtes betreffenden heuristischen Gesichtspunkt. *Annalen der Physik* **1905,** *322* (6), 132-148.
21. Leadley, D. X-ray Photoelectron Spectroscopy (XPS). https://www2.warwick.ac.uk/fac/sci/physics/current/postgraduate/regs/mpags/ex5/techniques/electronic/xps/ (accessed August 15, 2016).
22. Tanuma, S.; Powell, C. J.; Penn, D. R., Calculation of electron inelastic mean free paths (IMFPs) VII. Reliability of the TPP-2M IMFP predictive equation. *Surface and Interface Analysis* **2003,** *35* (3), 268-275.
23. Schneider, T.; Artyushkova, K.; Fulghum, J. E.; Broadwater, L.; Smith, A.; Lavrentovich, O. D., Oriented Monolayers Prepared from Lyotropic Chromonic Liquid Crystal. *Langmuir* **2005,** *21* (6), 2300-2307.
24. Angle Resolved XPS. http://xpssimplified.com/angle_resolve_xps.php (accessed August 16, 2016).
25. Fairley, N. *CASAXPS*, 2.3.16; 2011.
26. Briggs, D., *Surface Analysis of Polymers by XPS and Static SIMS*. Cambridge University Press: New York, New York, 1998; p 198.
27. Végh, J., The Shirley background revised. *Journal of Electron Spectroscopy and Related Phenomena* **2006,** *151* (3), 159-164.
28. Fairley, N. CasaXPS Manual: Introduction to XPS and AES 2016. http://www.casaxps.com/ebooks/ebooks.htm.

Chapter Three

Analysis by Electron Microscopy

Scanning and transmission electron microscopes have seen continued improvements in resolution and have incorporated compositional analysis via energy dispersive x-ray spectroscopy (EDX). They have been a regular fixture for polymer analysis since the 1960s, and can view a variety of structures and morphologies. As seen in Figure 3-1, the polymer blend structure is accessible to three types of microscopies: optical, scanning electron (SEM), and transmission electron (TEM). Electron microscopes require an operational pressure of about 10^{-6} Pa for the following reasons:

- to minimize scattering of the electron beam by gas molecules from air or the sample itself,
- to prevent contamination of fragile components in the microscope by hydrocarbons or water; e.g., cathode, apertures, magnetic lenses.

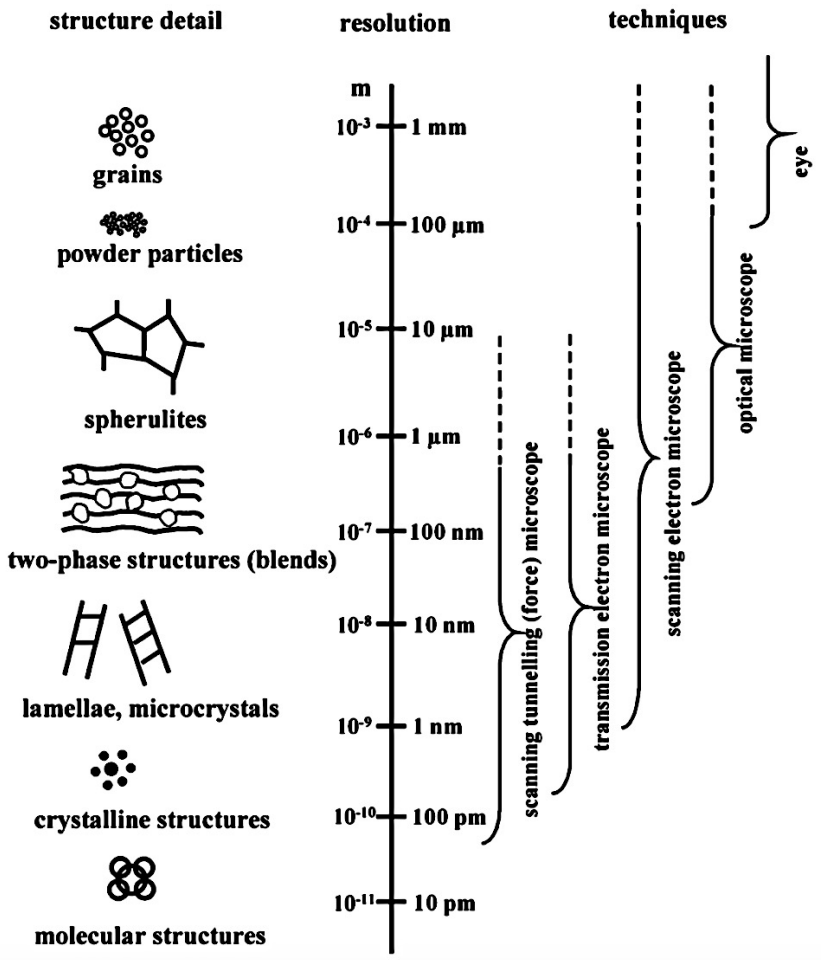

Figure 3-1. Scheme of possible structures in polymers open to analysis by various microscopies.[1]

3.1 Transmission electron microscopy (TEM)

3.1.1 Instrumentation

Fundamentally, electron optics operates on the wavelike nature of matter, as described by de Broglie in the 1920s.[2] The wavelength of an imaging electron within the microscope is

$$\lambda = \frac{h}{p} = h\left[2m_0 eV + \left(\frac{eV}{c}\right)^2\right]^{-1/2}, \qquad (3\text{-}1)$$

where h is Planck's constant, p is momentum, V is the applied voltage, e is electron charge, c is the speed of light, and m_0 is the rest mass of the electron. The resultant wavelength of the beam can be extremely short, but is more likely to interact with a polymeric material than a photon at an equivalent wavelength. The voltage is produced within the electron gun by two electrodes resting at the top of the instrument. Typical voltages are 80-120 kV for analysis of soft materials, with 80 kV being most commonly used, as high voltages can degrade the specimen.

The basic arrangement of the components within the TEM instrument is depicted in Figure 3-2. The electron beam is typically generated by a thermionic or field-emission source. The beam is first focused by a series of condenser lenses and condenser lens aperture. It is then aligned by the condenser lens stigmator, beam tilt, and translate coils. The aligned, focused beam then enters the objective lens and interacts with the sample in various ways. The sample is positioned via the specimen holder and the goniometer stage within the objective lens between the upper and lower pole pieces. After transmission through the sample, the electrons form an image through the combined interaction of the objective lens and an objective aperture in the back focal plane of the lens.

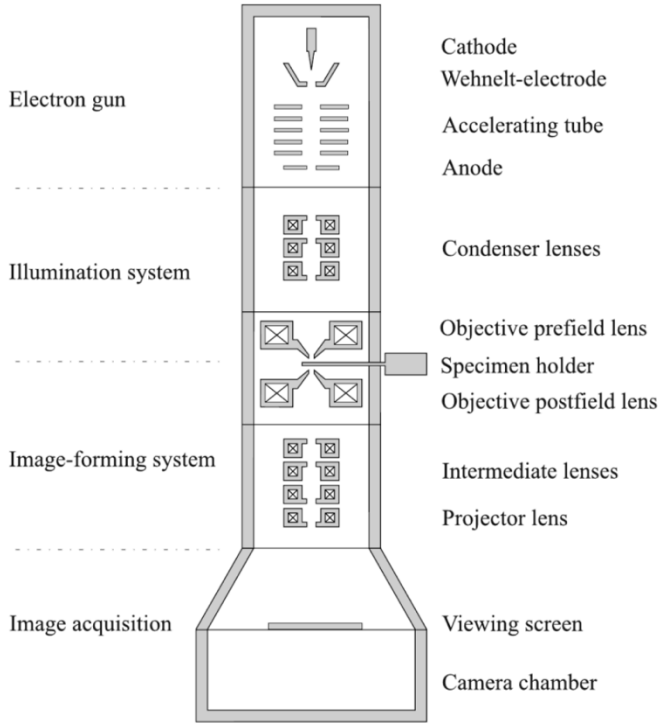

Figure 3-2. Schematic of TEM.[1]

Image correction is performed by an objective stigmator. A series of intermediate and projector lens and alignment units perform magnification of the image, which then reaches the phosphor viewing screen, or the CCD detector for viewing and recording on a computer monitor. As suggested by Figure 3-2, the microscope can be deconstructed into the following basic components: electron gun, illumination system, objective lens and specimen stage, image-forming system, and viewing chamber/image recording.

The electron gun in a TEM instrument generates electrons from a negatively biased cathode, which are accelerated by the anode and the additional electrode(s) in between; the extra electrodes increase the potential for increased acceleration. The cathode traditionally consisted of a tungsten filament, but a small pointed crystal rod of lanthanum hexaboride has become a common source (used by both TEM instruments in

this study). LaB_6 has a lower work function than tungsten, while providing greater brightness and lower energy spread.

3.1.2 Electron lensing

Electron optics share much in common with traditional light optics for describing lensing phenomena, which are depicted by ray diagrams in Figure 3-3. Both figures depict features of image formation by an ideal or thin lens. In Figure 3-3a, the object is assumed to emit radiation ("self-luminous") from an off-axis point in the object plane. The limiting diaphragm in the center confines the angular spread of the electrons.

Electron rays are refracted in the centric plane of the lens such that they form an image point at their crossover (the point of convergence for the rays). This is the first fundamental action of an ideal lens. Only two out of all electron rays are needed to find the location of this point when sketching a ray diagram. The two red rays in the center of Figure 3-3a highlight the location of the image point. One red ray passes through the center of the lens with changing direction. The other red ray has a path parallel to the electron-optical axis prior to entering the lens, which then refracts the ray to which it crosses the electron-optical axis at the back focal plane.

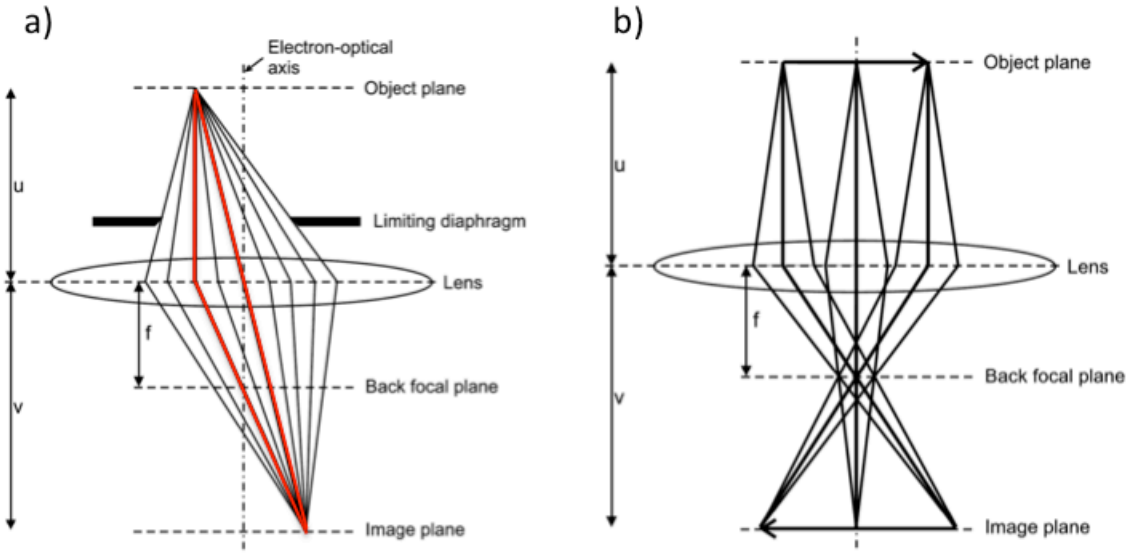

Figure 3-3. a) Image formation of a point source; b) image formation of a finite object.[1]

In 3-3b, a finite object replaces the point source. Three different points are drawn in the object plane. From each point are three electron rays heading toward the lens. The set of rays at each point contains one ray parallel to the electron-optical axis. As seen in 3-3a, each image point is found by finding the crossover point for the set of three rays emerging from the corresponding object point. The object plane is conjugate to the image plane, which bring the planes to electron-optical equivalence. With the distances u and v in both figures above, the magnification M of the image is expressed as

$$M = u/v. \tag{3-2}$$

$$\frac{1}{f} = \frac{1}{u} + \frac{1}{v}. \tag{3-3}$$

With Equations 3-2 and 3-3 and Figure 3-3b, the second fundamental action of the lens is elucidated: parallel rays beginning at different object points are focused to the back focal plane of the lens, while the distance between the focal and the electron-optical axis increases with respect to increasing oblique incidence of the parallel beam.

Electron lenses are typically electromagnetic coils that manipulate the electrons within the beam via the Lorentz force **F**:

$$\mathbf{F} = -e(\mathbf{E} + \mathbf{v} \times \mathbf{B}), \qquad (3\text{-}4)$$

where the vectors **E** and **B** are the electric and magnetic fields, respectively, and e and **v** are the charge and velocity of the electron. The Lorentz force induces electrons initially traveling parallel to the beam axis to travel downward in a helical pattern. While the image in optical microscopy is only inverted, the image in electron microscopy can be rotated according to the strength of the lens (Figure 3-4).

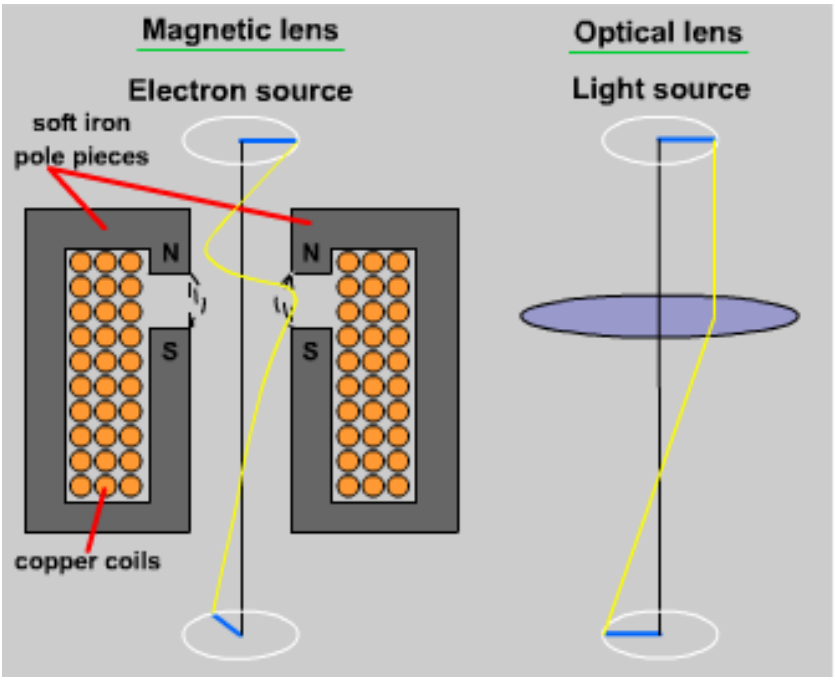

Figure 3-4. Comparison between magnetic coil acting upon electron beam and optical lens acting upon photon.[3]

There are three types of electron lenses in TEM. As indicated in Figure 3-2, the electron beam first encounters condenser lenses, which focus (condense) the beam onto the specimen. At low magnification, the beam is spread onto a large area. At high magnification, the beam is strongly condensed for small areas. Upon an increase in beam

current, apertures between the condenser lenses reduce the beam diameter to reduce potential damage to the specimen.

Near the specimen, objective lenses serve to further focus the image and enhance contrast. It is the most important lens in the microscope because it generates the first intermediate image, which is crucial for determining the resolution of the final image. This intermediate image is then magnified by a series of intermediate lenses before achieving its final magnification with the projector lens. The magnification can be varied between two and three orders of magnitude from the intermediate image, as not all lenses would be needed for lower magnifications.

3.1.3 Electron scattering

As with photons, electrons also scatter inelastically and elastically upon encountering the specimen. Inelastic scattering occurs when an incident electron transfers some of its kinetic energy to an atomic nucleus. This is a likely event if the electron has high kinetic energy and/or a high scattering angle θ; sample degradation may result. Elastic scattering occurs merely by the atomic electron cloud shielding the nucleus. As depicted in Figure 3-5a, the scattering angle is dependent on the closest distance between the electron and the nucleus at the moment of Coulombic interaction. The closer the electron is to the nucleus, the larger the force, and consequently θ. Contrast in polymeric samples is possible with small θ, which is possible by grazing off of the electron cloud, as depicted in the right side of Figure 3-5a. With heavier atoms, the Coulombic interaction increases with atomic weight A. Regions dominated by heavy atoms appear with darker contrast than do regions containing light atoms.

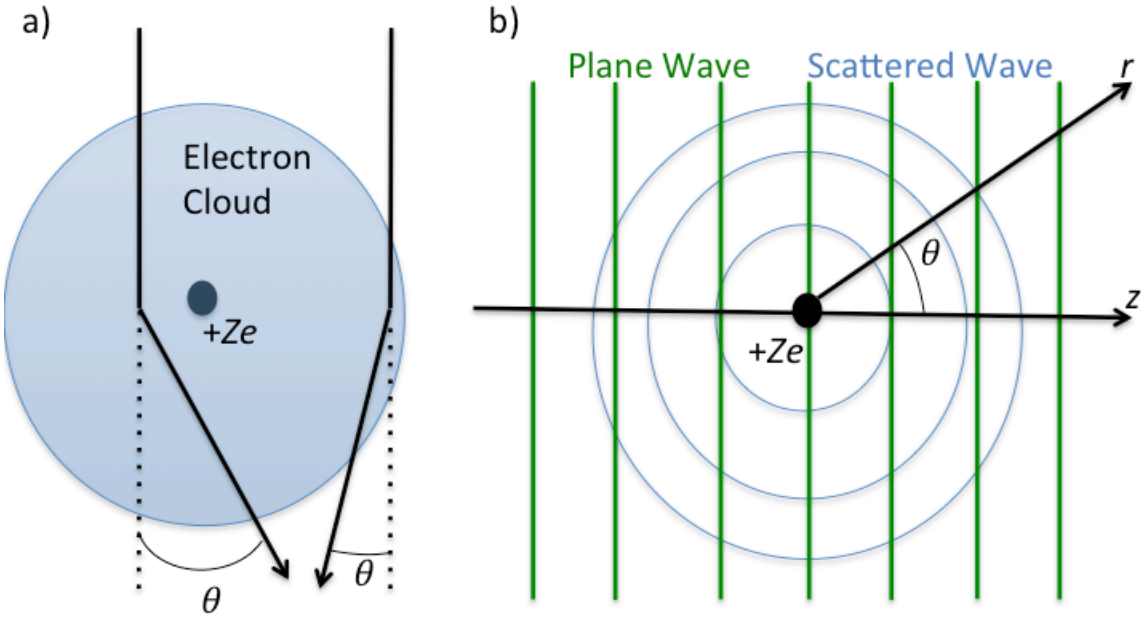

Figure 3-5. a) Particle model depiction of elastic scattering of an electron by an atom; b) wave model depiction of the superposition of incident plane wave and scattered wave.

The scattering event can described in terms of quantum mechanics, with an incoming electron expressed as a time-independent quantum mechanical (QM) plane wave

$$\psi = \psi_0 e^{2\pi i k_0 z}, \tag{3-5}$$

where ψ_0 is the amplitude, k_0 is the magnitude of the wave vector directed toward the z-axis. After the impact, the scattered electron is described by a spherical scattered QM wave with the origin placed at the scattering center:

$$\psi_{sc} = \psi_0 f(\theta) \frac{1}{r} e^{2\pi i k r}, \tag{3-6}$$

where $f(\theta)$ is the scattering amplitude, and k is the wave vector. At a far enough distance away from the nucleus, the complete wave is described as the superposition of the incoming plane wave, and the spherical scattered wave, as depicted in Figure 3-5b:

$$\psi_s = \psi + i\psi_{sc} = \psi_0 \left(e^{2\pi i k_0 z} + i \frac{f(\theta)}{r} e^{2\pi i k r} \right). \tag{3-7}$$

The factor i accounts for the 90° phase shift between the scattered and incident waves. Additionally, $f(\theta)$ is a complex quantity and is expressed as

$$f(\theta) = |f(\theta)| e^{i\eta(\theta)}. \quad (3\text{-}8)$$

in which $\eta(\theta)$ is an extra phase shift that is dependent on the scattering angle. The scattering amplitude is important because the differential elastic scattering cross-section depends on it:

$$\frac{d\sigma_{el}}{d\Omega} = |f(\theta)|^2. \quad (3\text{-}9)$$

The total cross section can be calculated by integrating Equation 3-9 and adding it to the inelastic cross-section σ_{in}:

$$\sigma_t = \sigma_{in} + \int_0^{\pi} \frac{d\sigma_{el}}{d\Omega} 2\pi \sin\theta \, d\theta. \quad (3\text{-}10)$$

The manifestation of the scattering event depends on the total scattering cross-section σ_t of the atom. In reality, the electron is scattered by a large number of atoms as it transmits the specimen. This is why the specimen thickness must be on the order of ~100 nm for polymeric samples. Image intensity also depends on atomic arrangement within the specimen (crystalline vs amorphous). For amorphous polymers such as the samples studied here, the electrons are scattered incoherently, which negates the need to account for phase shifts in scattering events. Thus, only the intensities of individual scattering events are summed. The intensity I of the final image could be calculated as

$$I = I_0 e^{\frac{N_A}{A}\sigma_t \rho T}. \quad (3\text{-}11)$$

where I_0 is the intensity of the incident electron beam, N_A is Avogadro's number, A is the atomic mass, ρ is the local density of the specimen, and T is the total thickness. The product of the density and thickness is called the mass thickness. The contrast that corresponds to the mass thickness is called the mass-thickness contrast, which well

describes the image intensity for magnifications that permit resolution of details ≥ 10 nm. No TEM image in this study exceeds that magnification. For high magnifications that permit resolution of details in the sub-nanometer range, additional attention must be paid to the electron-optical processes, such as microscope aberrations. Contrast variation is thus due to variations in the superscript letters of Equation 3-11. As specimens are cut to uniform thicknesses, the darker regions on an image are regions of higher electron scattering and/or greater thickness. However, polymers have low atomic numbers and scatter electrons weakly, potentially yielding poor contrast. An image of the blend cross-section with poor contrast is shown in Figure 3-6; domains are barely discernible. The solution to improving contrast is discussed in subsection 3.1.4.

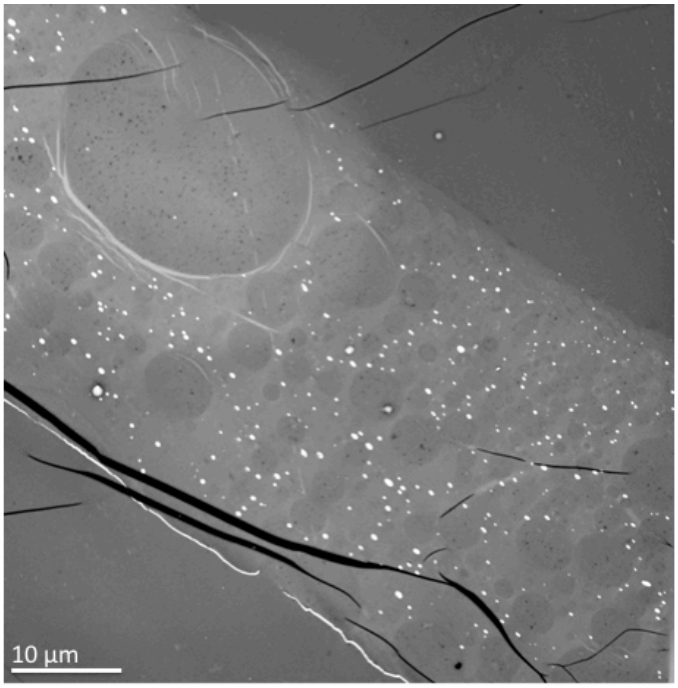

Figure 3-6. Transmission electron micrograph of cross-section of clear blend coating. Dark streaks are due to folds in the sample.

3.1.4 Sample preparation for TEM

Samples for TEM analysis must also be thin enough to fit into a specimen support known as a grid; such a grid is typically made of copper. Its diameter (2-3 mm) is designed to fit into the specimen holder of the microscope. Variations include mesh grids or support film grids, in which ultra-thin polymeric films hold the sample in place. The only way to prepare samples thin enough for TEM is via ultramicrotomy. Sectioning was performed with diamond knives, which have the advantage of remaining sharp after cutting into pigment particles. The microtome used to prepare TEM samples is a Leica EM UC7 Ultra-Microtome (Wetzlar, Germany).

As mentioned previously, imaging of polymers by TEM is limited by poor contrast, but this can be overcome by staining the sample with a solution containing high-density heavy metal compounds. The higher local density imparted by the heavy metals reduces the intensity of the transmitted electron beam, as evident in Equation 3-11. The region of interest can be stained by physical absorption or by chemical interaction, but physical absorptions are prone to evacuation in the vacuum, which makes chemical interaction the preferred method for positive staining. The reaction with the metal compound could be specific to the polymer component, thus rendering the staining as selective to that component. Contrast enhancement is also possible with negative staining, in which the staining agent binds with the smooth continuous phase rather than the dispersed particles within it; this has been a commonly used technique for latex and emulsion materials.[4] It is no coincidence that many staining methods for polymers were directly borrowed from the biological sciences.[5] The known workhorses of staining agents for polymers are osmium tetroxide for unsaturated polymers, ruthenium tetroxide for polymers containing styrene, and phosphotungistic acid for amino polymers.[6] Based

on the monomer unit depicted in Figure 2-9, RuO_4 seems to be the most logical choice due to its styrene units. However, this heavy metal compound is highly toxic, volatile and requires preparation onsite due to its very short shelf life.[7] OsO_4 can be sold commercially, but is still highly toxic and volatile as well.[8]

The staining agents of choice for TEM in this study have been uranyl acetate (UA) followed by lead citrate (LC). These are traditionally applied sequentially to enhance contrast for biological samples.[9] They are both highly toxic but not volatile, traits that in combination render them relatively safe for application. However, after performing independent work on the staining process for SEM analysis (described in the next subsection), it appears that only UA significantly enhances phase contrast with the polymer. The selective staining procedure consisted of immersing sectioned samples in 0.02 g/mL UA in methanol for 10 minutes, followed by 0.0003g/mL aqueous LC for 3 minutes. Personnel at the Central Microscopy Imaging Center (CMIC) at Stony Brook University performed the procedure. Comparison between an unstained and stained specimen are presented in Figure 3-7. Both images were not enhanced by software. The darkened domains are indicative of the heavy metals selectively bonding to them. The polyester embedding resin was also darkened by the heavy metals, which may indicate that the chemistries of the polyurethane domains and the polyester embedding resin contain similar densities of polar groups that are favorable for chemical bonding.

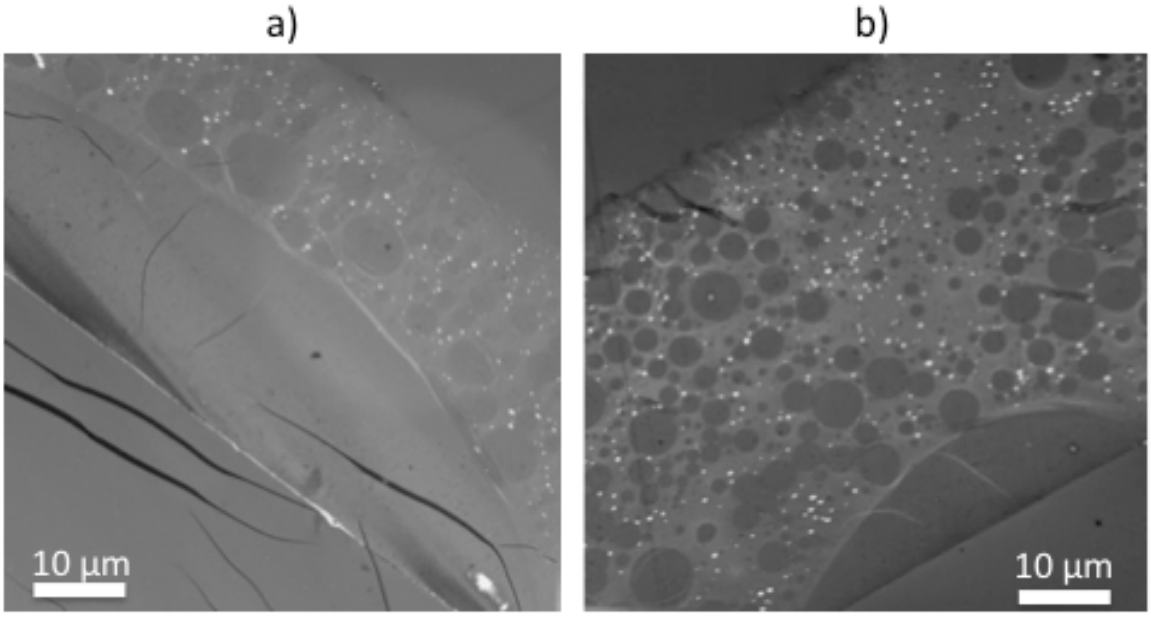

Figure 3-7. Comparison between a) unstained and b) stained transmission electron micrographs.

3.1.5 TEM equipment

Two transmission electron microscopes were used in this study. The first was a Bio TwinG2 Transmission Electron Microscope at the Center for Microscopy (CMIC) in Stony Brook University. The TEM was equipped with an AMT XR-60 CCD digital camera system for image collection. Bright field imaging measurements were performed at an accelerating voltage of 80 keV. No EDX was available, which necessitated access to a second microscope at the Center for Functional Nanomaterials in Brookhaven National Laboratory. It was equipped with a Gatan CCD digital camera for image collection and a TEAM^{TM} EDS Analysis System for TEM with an Octane Silicon Drift Detector for elemental analysis. Bright field imaging was also performed at 80 keV. The resolution of both microscopes reached into the single nanometer range (~50 kX), but most details required magnifications between 500 and 10 kX. Low magnifications were

used to image the entire cross-section of films to observe trends at broad scales. Midrange magnifications were used to observe changes at smaller scales by imaging domains 5-50 μm in diameter, matting agent particles (10-50 μm), and clusters of small pigment particles (TiO_2, Fe_3O_4). There were occasional small pigment particles and domains 0.5-5 μm in diameter that required magnifications up to 30 kX, but such high magnifications usually did not reveal new information about the polymer blends. EDX as an analytical technique is detailed in section 3.3.

3.2 Scanning electron microscopy (SEM)

3.2.1 Instrumentation

SEM is the most popular microscopic techniques for polymers.[1] It utilizes a focused electron beam to scan line by line over the specimen surface in an evacuated sample chamber. Its resolution is only slightly less than that of TEM, but is perfectly suited to observe the morphology of polymer blends. The signals are based on interactions between the beam and sample, which are electronically detected and amplified with appropriate equipment. Achievable resolution is greater than one nanometer. A schematic of a typical SEM is found in Figure 3-8. It shares many components with TEM, such as electron gun, condenser and objective lenses, and apertures for narrowing the electron beam. What sets SEM apart from TEM in terms of instrument design is that the sample is the final destination for the primary electron beam. There are no intermediate and projection lenses in SEM. Instead, the scattered electrons are directly collected by detectors residing within the sample chamber. Polymeric specimens require sputter coating with Au or Cr to prevent charging effects, but is a small price to pay for analysis when compared to microtome sectioning for TEM analysis.

SEM analysis is thereby utilized for bulk specimens of polymeric coatings and does not require microtome sectioning prior to its utilization. The relative ease of sample prep and the smaller number of electron lenses in scanning electron microscopes enables their relatively simpler operation in comparison to TEM.

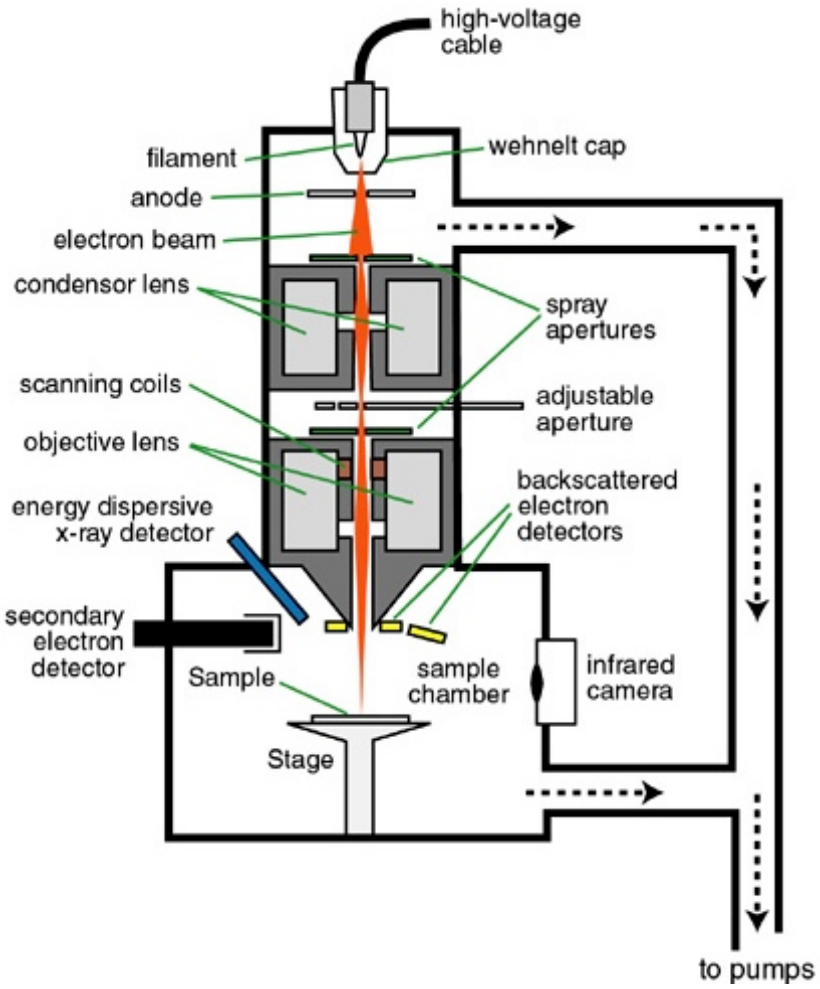

Figure 3-8. Schematic of SEM.[10]

3.2.2 Electron scattering for SEM

In SEM, the signals that reach the detector are generated from the electron beam interacting with the specimen in several ways. As depicted in Figure 3-9, the interaction with the electron beam generates several types of signals, each of which requires specialized detectors built within the instrument. Thus, the instrument has three

detectors, each of which is specialized for a particular secondary beam produced by the primary electron beam. Secondary electrons (SE) originate from the top section of the interaction volume (100 nm below the surface); this allows topographic imaging of the surface, especially if the primary electron beam uses a low accelerating voltage. Backscattered electrons (BSE) are used to produce electron micrographs, while x-rays are used for EDX.

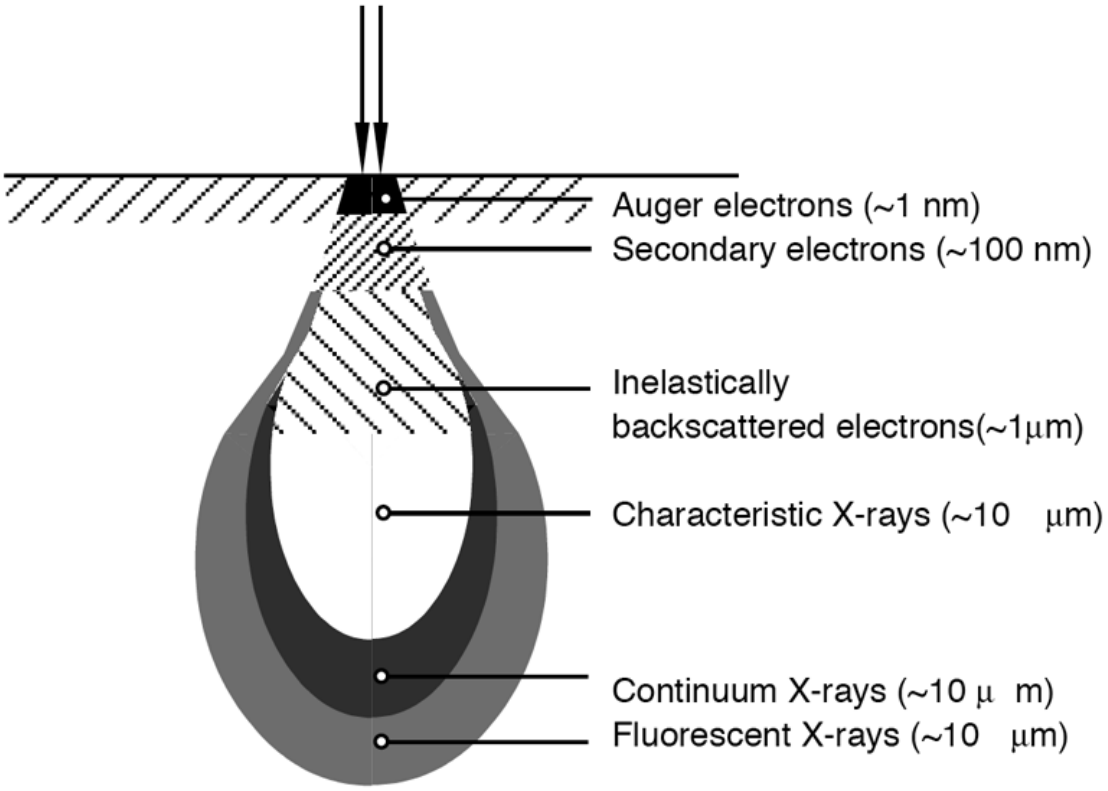

Figure 3-9. Diagram of regions within the interaction volume that generates various signals.[11]

The larger interaction volume for backscattered electrons (BSE) is sensitive to the mean atomic number of the atoms, which provide information on variation in sample composition. This is important for imaging metal oxide pigments, which would be much brighter than the organic binder. The large interaction volume of BSEs would also enable observation of pigments at the subsurface, and grant a more complete picture of

pigment distribution. This is demonstrated in the SEM images of Figure 3-10, which were taken from the same cross-section area on a pigmented specimen and with similar

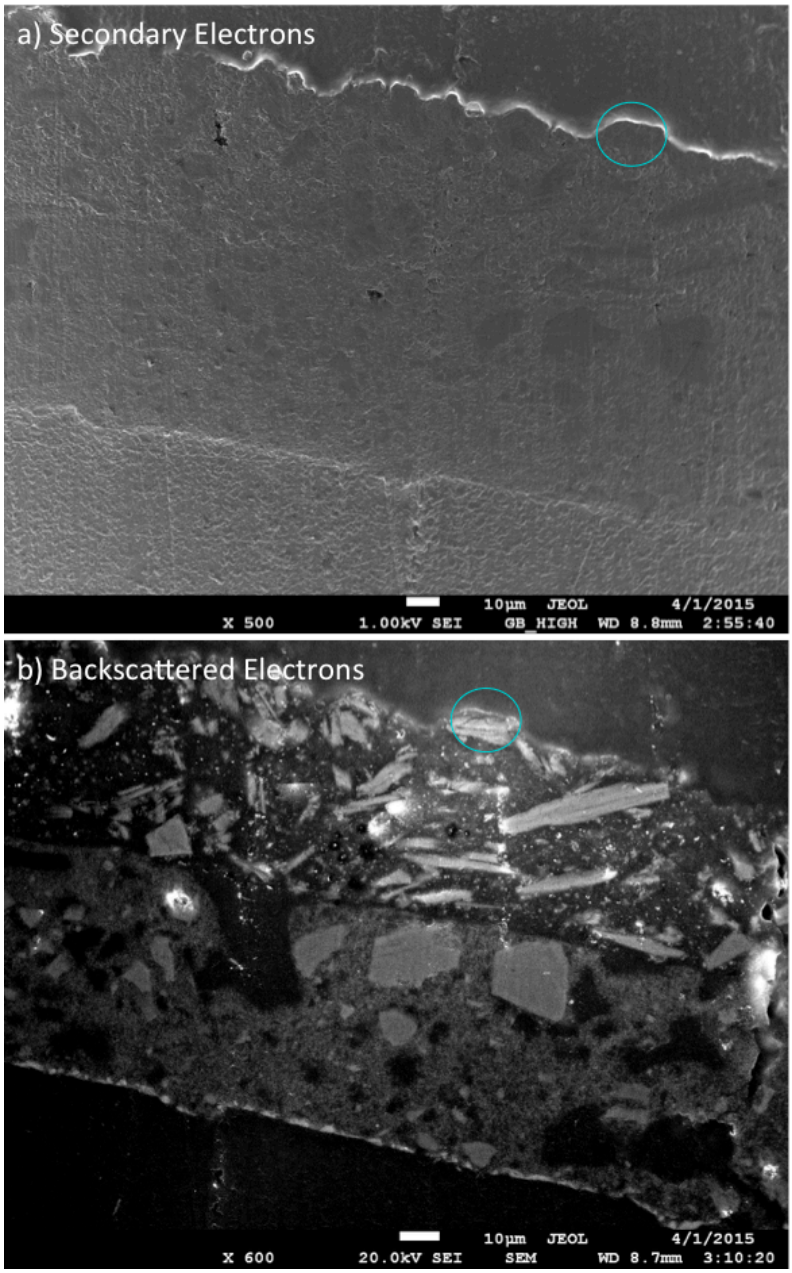

Figure 3-10. Comparison of cross-sectioned pigmented coating at similar magnifications under accelerating voltages of a) 1 kV, and b) 20 kV. The circle marks the same area in both micrographs to orient the reader.

magnifications. The lighter regions in 3-10b are pigments, which yield more backscattered electrons than the surrounding binder.

The ease of viewing pigments under an accelerating voltage large enough to induce backscattering is the reason why SEM complements TEM. Without pigments, the small scattering cross-sections of carbon, oxygen, and nitrogen yield poor contrast between the phases alone.

3.2.3 Focus depth

One of the exceptional features of SEM is its depth of focus, which is a function of the convergence angle ϕ of the electron beam and the magnification M (Figure 3-11). Noting that $\tan\phi \approx \phi$ at $\tan\phi << 1$, the depth of focus R is given as

$$R = \frac{2r}{\phi} = \frac{0.1 \text{ mm}}{\phi M} \qquad (3\text{-}12)$$

where $2r$ is the beam diameter that produces a corresponding spot on the display that is discernible to the human eye (~0.1 mm).

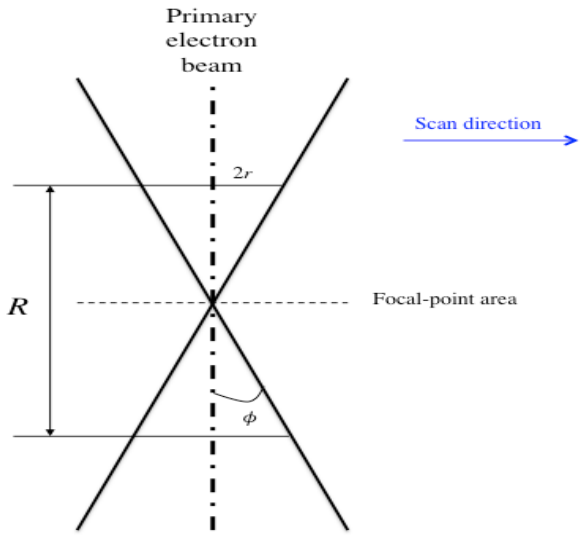

Figure 3-11. Schematic of depth of focus for SEM.[1]

A light microscope at 200X magnification has a focus depth at just a few microns; the SEM has a depth of focus in the mm region at the same magnification. This larger focus depth was important for imaging rough surfaces or cross-sections with sloped surfaces.

3.2.4 SEM equipment

The SEM used was a LEO1550 with a Robinson backscatter detector. It also was equipped with an EDX detector with iXRF electronics and software. As stated, the typical accelerating voltage was 20 kV, which was high enough to image metal oxide pigments via backscattered electrons; 1 keV was sometimes used for topographic analysis (Figure 3-10). However, as insulators, polymers are prone to charging effects, in which a buildup of charge on the sample is caused by a difference between the number of incoming electrons and the number of outgoing electrons as SEs and BSEs. Samples with conductor properties can be connected to the ground potential and thus eliminate accumulation of charge. Insulators can be rendered into conductors by being sputter-coated with a layer of gold before insertion into the SEM vacuum chamber. Coating samples were thus sputter-coated with an Edwards 150B gold sputterer for 30 seconds, which yielded a gold layer of ~5 nm thickness.

3.3 Energy dispersive x-ray spectroscopy (EDX)

Imaging of surface structures or compositional variations on a surface is sometimes inadequate for full characterization of the specimen. This rings especially true for pigmented coatings, where metal oxide particles are embedded in the polymer matrix. Their composition can be identified and quantified by X-ray microanalysis. The

characteristic x-rays are generated by inelastic collisions of incident beam electrons with the orbital electrons of specimen atoms (Figure 3-12). The beam also achieves sensitivity with the specimen bulk due to the greater sampling depth of the characteristic x-rays (Figure 3-12).

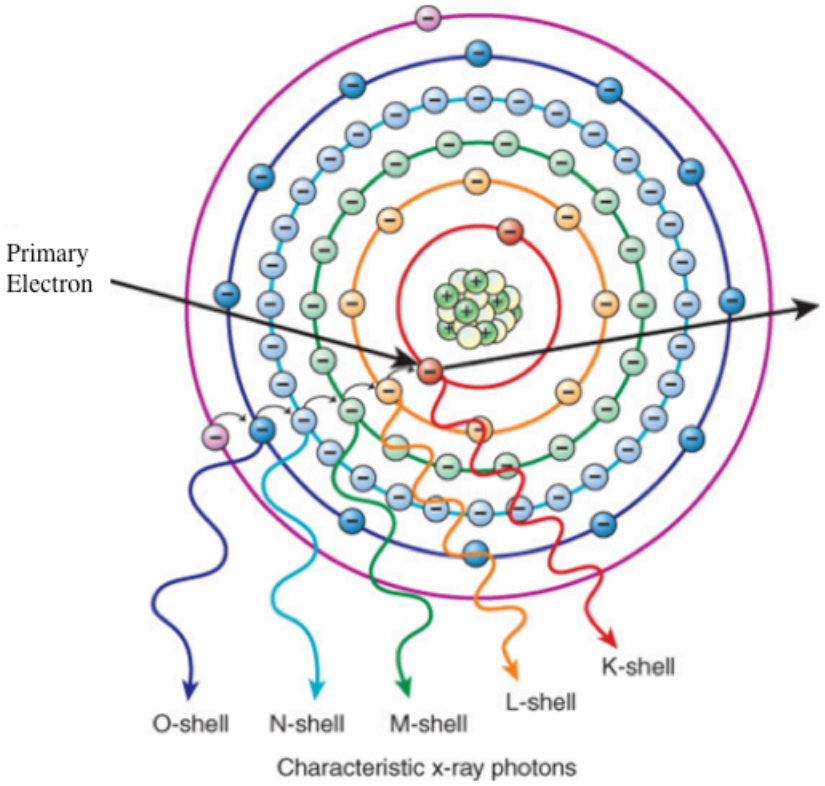

Figure 3-12. Illustration of characteristic x-ray generation by incident electron. All photons shown are α transitions.[12]

The inner orbital shells are designated by K, L, M …, which refer to quantum numbers 1, 2, 3 …, respectively. A primary electron knocks out a localized electron and excites the atom to a higher energy state for a limited time. The vacancy in the electron orbital then is filled and the atom relaxes, releasing the excess energy as a secondary effect via emission of an x-ray, or alternatively through the emission of an Auger electron (Figure 3-9). The energy of the emitted x-ray photon is equal to the difference in two excited energy states. Any transition from a higher energy level to lower K, L, or M

shells are dubbed K, L, and M radiations, respectively. The nomenclature also includes Greek letters α, β, and γ that refer to groups of lines with similar wavelengths, with α being the most intense, since it refers to a transition between adjacent quantum levels. The transitions are also indicated by numerical subscripts to distinguish the lines` within each subgroup. For example, a transition from the L2 subshell to the K shell results in a $K_{\alpha 2}$ x-ray photon. A $K_{\beta 1}$ photon is emitted by the transition from the M3 level to the K level. Such transitions are specific to the element and are easily measured. In addition to the characteristic x-rays, the spectrum also contains a continuum stemming from bremsstrahlung (braking radiation). Bremsstrahlung results from Coulomb interactions of primary electrons through varying electric fields.

3.4 References

1. Michler, G. H., *Electron Microscopy of Polymers*. Springer: Berlin, 2008; p 494.
2. Broglie, L. d., XXXV. A tentative theory of light quanta. *Philosophical Magazine Series 6* **1924,** *47* (278), 446-458.
3. Williams, D. B.; Carter, C. B., *Transmission Electron Microscopy: A Textbook for Materials Science*. Plenum Press: New York, New York, 1996; p 729.
4. Sawyer, L.; Grubb, D.; Meyers, G. F., *Polymer Microscopy*. 3rd ed.; Springer: New York, New York, 2008; p 540.
5. Hayat, M. A., *Principles and Techniques of Electron Microscopy: Biological Applications*. 4th ed.; Cambridge University Press: Cambridge, England, 2000; p 564.
6. Smith, R. W.; Bryg, V., Staining Polymers for Microscopical Examination. *Rubber Chemistry and Technology* **2006,** *79* (3), 520-540.
7. Trent, J. S.; Scheinbeim, J. I.; Couchman, P. R., Electron microscopy of PS/PMMA and rubber-modified polymer blends: Use of ruthenium tetroxide as a new staining agent. *Journal of Polymer Science: Polymer Letters Edition* **1981,** *19* (6), 315-319.
8. Osmium Tetroxide; SDS No. 201030 [Online]; Sigma-Aldrich, Saint Louis, MO. http://www.sigmaaldrich.com/catalog/product/sial/201030?lang=en&region=US (accessed June 30, 2016).
9. Frasca, J. M.; Parks, V. R., A routine technique for double-staining ultrathin sections using uranyl and lead salts. *The Journal of Cell Biology* **1965,** *25* (1), 157-161.
10. Wittke, J. H. Electron Microprobe Laboratory. http://nau.edu/cefns/labs/electron-microprobe/glg-510-class-notes/instrumentation/.

11. Microscopy. https://sites.ualberta.ca/~ccwj/teaching/microscopy/ (accessed August 1, 2016).
12. lubyntx Ch_6_ X-ray Production. https://quizlet.com/132808638/ch_6_-x-ray-production-flash-cards/ (accessed August 8, 2016).

Chapter Four

Initial Preparation of Cross-Sections and Their Analysis by Raman Spectroscopy

4.1. Introduction

This chapter represents the initial steps toward characterization of the coatings. The objective was to identify the phases within the first of two fully cured polymer blends analyzed in this study. The blend herein is referred to as Blend A. Chemical mapping was initially performed on the blend surface via ATR-FTIR, but failed to discern differences between the phases. Mapping with Raman spectroscopy also failed. These failures were the motivations for preparation of cross-sectioned samples.

4.2 Experimental methods

4.2.1 Optical microscopy

Digital optical microscopy was used to record observations of embedded cross-section samples, particularly of the size and distributions of domains. OM measurements were performed on a Meiji microscope equipped with a Nikon digital camera DXM1200 and Nikon ACT-1 software.

4.2.2 Fourier transform infrared spectroscopy (FTIR)

ATR-FTIR spectra were recorded on a Thermo Scientific Nicolet™ iS50 FTIR Spectrometer with a Smart Performer™ ATR attachment and constant pressure tower. An MCT detector collected 64 scans of the sample. Film samples were analyzed with a

diamond crystal. DRIFTS was performed on the same spectrometer with a Spectra Tech attachment.

4.2.3 Raman spectroscopy

Raman spectra and maps were acquired using a Thermo Scientific Nicolet Almega™ dispersive spectrometer coupled to an Olympus microscope with 10X and 50X objective lens. The instrument used a 785 nm laser with a 3.1 μm spot size. High-quality spectra were acquired by scanning a sample 30 times using a ten-second-collection time. For mapping acquisitions, samples were placed on double-sided tape to ensure complete stability. Each spectrum was acquired via 15 scans using five-second-collection time. Typical step-sizes were 5-7 μm.

4.2.4 Initial cross-section preparation

A cross-section must be smooth and flat for prepared analysis by spectroscopy. The first approach to obtaining clean cross-sections consisted of cryo-fracturing coating specimens after immersion in liquid nitrogen, but this technique failed to provide the necessary flat cross sections. The next approach was to embed the coating and substrate into an epoxy resin; the substrate was either steel or aluminum release foil. The resin was a 2:1 ratio of EpoThin™ epoxy resin with EpoThin™ epoxy hardener under vacuum. Up to five specimens can be embedded in this procedure. The epoxy pot is ground down by a an Allied High Tech Products MetPrep semi-automatic grinder/polisher with 120 grit Al_2O_3 sandpaper, then 400 grit, 800 grit, and 1200 grit. The user switches to polishing cloth and sprays 3 μm diamond solution every 30 seconds; then repeats with 0.25 μm

diamond suspension. Employing this technique yielded very smooth cross-section surfaces, as seen in Figure 3-2.

4.2.5 Final cross-section preparation

Cross-section samples of the blend and its single component counterparts were prepared by polishing with the MOPAS hand-held dry polisher (Jaap Enterprise, Amsterdam, Holland).[1-2] Fragments of each of the coatings were embedded within the polyester resin Bio-Plastic™ (Ward's Science, New York), which was allowed to cure for 72 hours prior to polishing. The commercially available polyester embedding resin consisted of 50% unsaturated polyester prepolymers, 40% styrene monomer, and 10% methyl methacrylate. The cured Bio-Plastic blocks were then cut to remove excess material in order to fit into the MOPAS hand-polisher jig. Dry polishing was performed using 6" × 6" Micro-Mesh™ silicon carbide abrasive cloths using different grades starting at 1800 mesh and ending at 12,000 mesh to produce a one micron finish. Dry polishing was performed for each grade until a homogeneous polish was observed using optical microscopy.

4.3 Results

Sample morphology was examined by both optical and electron microscopy. The two techniques were selected due to their ease of use and their complementary nature in terms of observing polymer domains. SEM can observe domains in the clears, but they are faint, even with increased contrast via software. Once a sample cross-section is prepared, it has become a routine procedure to first find an area with interesting

morphology, and then find the same area with the SEM for corroboration. Microscopic analysis of the initial set of clear films is displayed in Figure 4-1. Phase separation is clearly exhibited in the blend. However, spectroscopic characterization at the surface did not lead to definite identification of the phases at the surface.

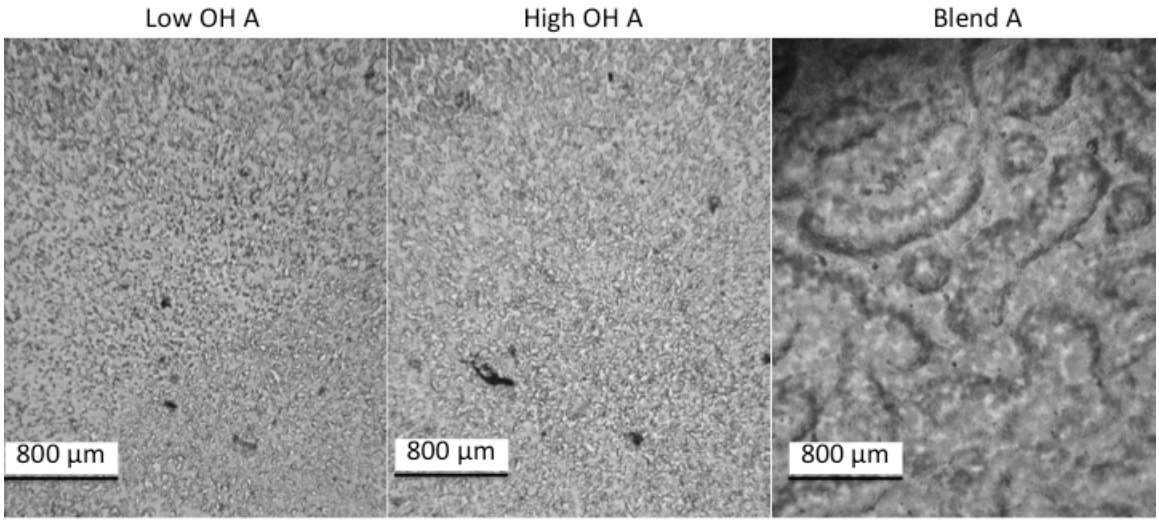

Figure 4-1. Optical micrographs of surfaces of a) low hydroxyl content film; b) high hydroxyl content film; c) Blend A.

With the cross-sections prepared, chemical inhomogeneities can be discerned by chemical mapping, including contaminants. The cross-sections reveal that the domains are encapsulated by the polymer matrix, which may explain the difficulty in acquiring spectra with different peak structure with respect to polymer phase. However, it became clear that wet polishing produces its own set of artifacts that can cast doubt on the authenticity of data.

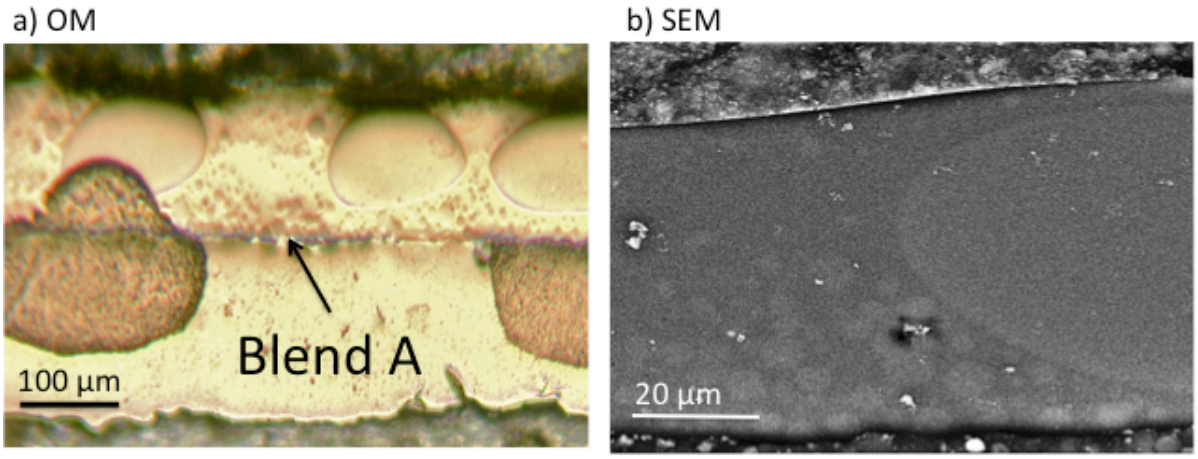

Figure 4-2. Cross-section of Blend A that were prepared by wet-polishing; a) digital optical micrograph; b) scanning electron micrograph.

As seen in Figure 4-2a), optical micrographs revealed diamond particles littering the cross-section surface, and SEM/EDX scans revealed Al_2O_3 droplet-sized stains as well. The result led to Raman spectra laden with fluorescence, or with potential artifacts from the polishing materials. The height differences between the epoxy, polyurethane sample, and Al substrate may be due to uneven swelling from the wet polishing; in any case, these height differences ruined the intimate contact needed by the ATR objective. This led to a search for a polishing method that minimizes contamination while keeping the embedding resin and polyurethane coating in the same plane.

This contamination refocused efforts toward dry-polishing. Samples were thus embedded within polyester Bio-Plastic™ resin, cut into 0.5" × 0.5" × 0.25" fragments, and underwent dry polishing to a 1 μm finish. The resultant surface (Figure 4-3) is not as smooth as that obtained from wet polishing, but it leaves little to no contamination from the polishing and is thus suitable for spectroscopic analysis. The white spots might be artifacts of the cross-section surface being roughened by the combination of small

domains and scratches from the polishing cloths. Traces of SiC may also be possible, but SiC has not been detected by spectroscopy.

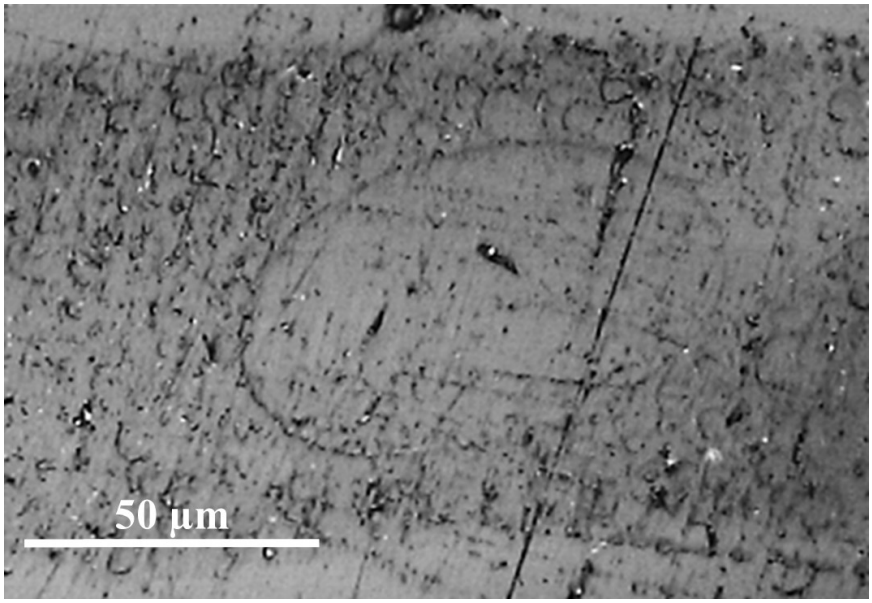

Figure 4-3. Micrograph of polished cross-section of Blend A.

Raman spectra from the polymer matrix and the encapsulated domain are presented in Figure 4-3. Emphasis is placed on the double-bond region (2000 cm^{-1} – 1600 cm^{-1}) because there are clear differences between the phases. The spectrum for the polymer matrix has two strong peaks at 1630 cm^{-1} and 1605 cm^{-1}. In the domain, the peak at 1630 cm^{-1} is nearly absent, while the 1605 cm^{-1} is highly diminished. The stark contrast in intensity for the peak at 1630 cm^{-1} with respect to phase was the motivation for its selection as a spectroscopic marker for chemical mapping.

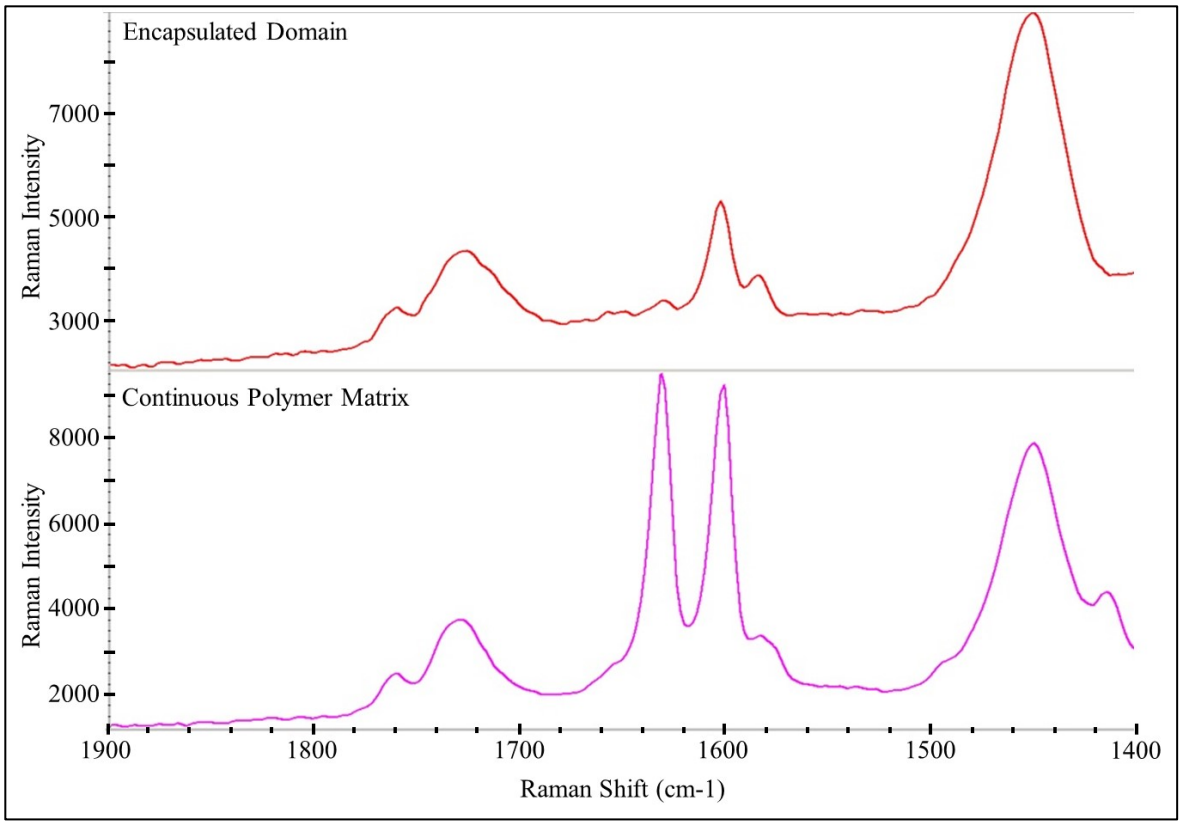

Figure 4-4. Raman spectra of the encapsulated domain (top) and the continuous polymeric matrix (bottom) of cross-sectioned Blend A film.

The chemical map of the cross-section surface generated from the marker peak is displayed in Figure 4-5. It corresponds very well to the micrograph in Figure 4-3. Blue corresponds to the lowest intensity of the marker peak; red corresponds to the highest.

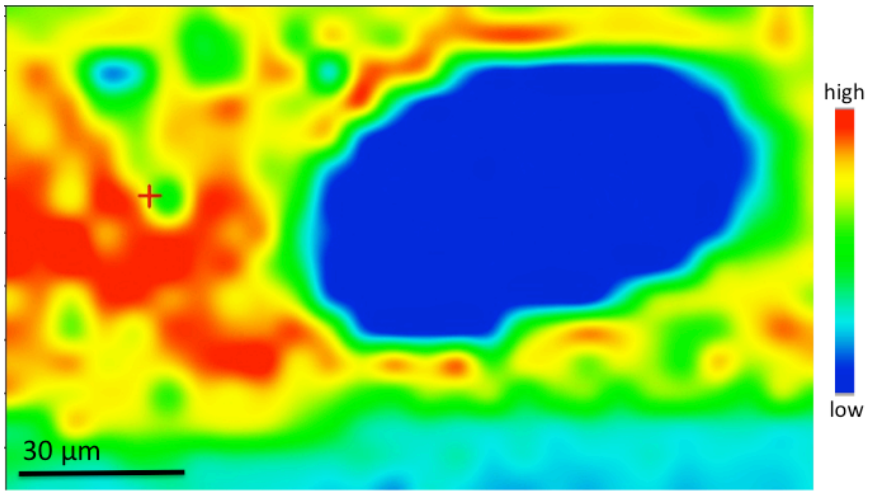

Figure 4-5. False-color map of the Raman marker peak at 1630 cm^{-1}. Red corresponds to high intensity, and blue corresponds to low intensity.

Raman spectroscopy was then applied toward cross-sectioned samples of single component polyurethane films. Spectra acquired from each of the two coatings are presented in Figure 4-6. They clearly illustrate that the domain consists of the high hydroxyl content resin due to the near-absence of the marker peak at 1630 cm^{-1}, whereas its prominence in the low hydroxyl content resin is consistent with the polymer matrix. This is rendered clearer when spectra from both phases of the blend and the single component films are thus stacked together in Figure 4-7. The process of how the phases in this blend and in another blend are identified will be discussed in more detail in Chapter 5.

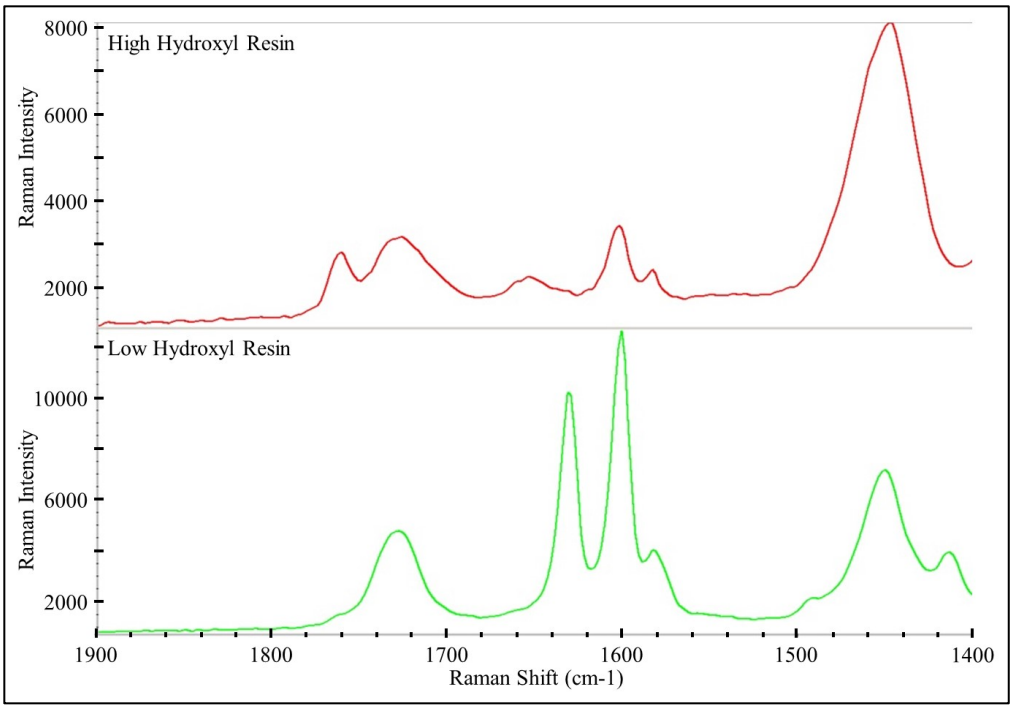

Figure 4-6. Raman spectra of single component films; (top) high hydroxyl resin; (bottom) low hydroxyl resin.

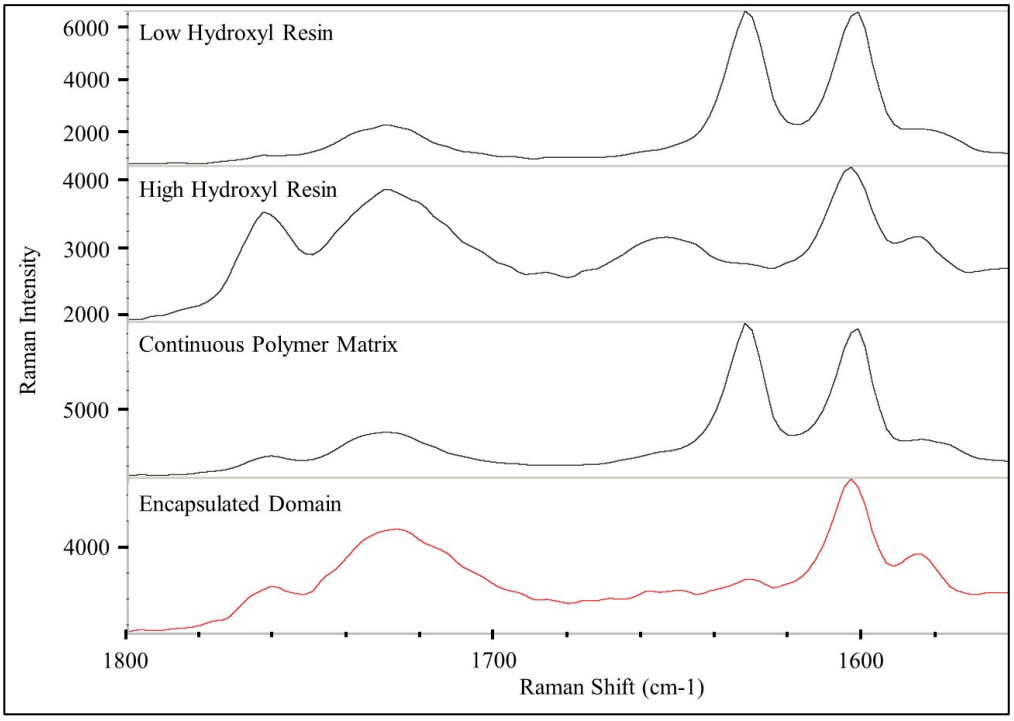

Figure 4-7. Stacked Raman spectra from both single component films and the phases of the blend.

4.4 Conclusion

Conclusive identification of the domains present in Blend A was performed using Raman spectroscopy on dry-polished cross-section samples. Spectroscopic differences between polymer phases were observed in the frequency region from 1580 cm^{-1} to 1650 cm^{-1}. The difference manifested in a marker peak at 1630 cm^{-1}. The aromatic peak at 1600 cm^{-1} also became more intense, identifying itself as clearly linked to the marker peak. This peak is absent in the high hydroxyl content resin as well as being or almost completely absent in domains. This serves as conclusive evidence that the domains and the high hydroxyl content resin are the same polymer.

4.5 References

1. Loon, A. v. Color Changes and Chemical Reactivity in 17th-Century Oil Paintings. PhD Dissertation, University of Amsterdam, Archetype Publications, 2008.
2. Prati, S.; Sciutto, G.; Catelli, E.; Ashashina, A.; Mazzeo, R., Development of innovative embedding procedures for the analyses of paint cross sections in ATR FTIR microscopy. *Analytical and bioanalytical chemistry* **2013,** *405* (2-3), 895-905.

Chapter Five

Selective Staining for Enhanced Micro-Raman Spectroscopy

5.1 Introduction

Current and future advancements in volatile organic compound (VOC) reduction have been approached through the adaptation of powder coatings for exterior applications due to the absence of solvent in their application.[1] Powder coatings are formulated in several gloss ranges, including low gloss, but the powder coating market has yet to see durable powder formulations that exhibit matte gloss due to difficulty in controlling the chemistry and morphology necessary for durable and easily reproducible powder films.[2-4]

Gloss reduction in liquid coatings is generally performed through the addition of commercial flattening agents for the generation of micro-texture at the coating surface upon solvent evaporation and subsequent film shrinkage.[2] The surface micro-texture reduces the amount of incident light reflected in a singular direction and thus leads to a matte finish.[2] One caveat concerning powder coatings is that low loadings of pigments, fillers and other additives are necessary to ensure that the melt viscosity remains low in order to evenly wet over the substrate and to ensure adequate pigment dispersion.

In order to circumvent the increase in PVC and the subsequent increases in yield values and viscosity, polymer blends have been utilized in powder coatings for gloss reduction. Polymer blends are used to generate multiple indices of refraction from the binder due to polymeric phase separation and domain formation without the addition of extra flattening agents. The presence of multiple indices of refraction within the binder

allows multiple scattering of light, thereby reducing the film transparency and by extension the gloss.[5] The roughened surface arises from differences in curing rates for each component resin.[2] For example, incompatible polyester resins with large differences in hydroxyl content have been blended and upon their subsequent curing, the resins phase separated to form a stable heterophase structure that persisted after full cure.[2] Blends of high and low carboxyl functionalized polyester resins have also produced low gloss powder coatings using the same principle of induced phase separation and domain formation.[3-4] In addition to gloss reduction, there are other reasons for industrial interests in coatings with immiscible resin blends, as they can provide a method for producing very finely dispersed microstructures that can significantly enhance the mechanical properties and durability of the film.[6-8]

Information about multicomponent samples such as polymer blends can be discerned from vibrational spectroscopies. FTIR and Raman spectroscopy can be used to identify the different components if the spot sizes are adequate. With the advent of FTIR mapping in the 1980s, it has become possible to analyze the spatial distribution of the components within a sample. FTIR mapping is typically performed via point-by-point mapping using a microscope fitted with a computer-controlled motorized stage.[9] Even with automation, point-by-point mapping is highly time-consuming, and the diffraction limits keep aperture sizes within 25-50 μm, which is comparable to most domain diameters in this study. This makes lateral resolution an important consideration for chemical mapping, which is governed by the Rayleigh criterion:[10]

$$r = 0.61\frac{\lambda}{\mathrm{NA}}, \qquad (5\text{-}1)$$

where r is the distance between two measurement points, λ is the wavelength of the radiation, and NA is the numerical aperture defined as:

$$\mathrm{NA} = n\sin\theta, \qquad (5\text{-}2)$$

where n is the refractive index of the immersion medium between the objective and the sample (2.4 for ZnSe and diamond ATR crystals), and θ is the half-angle of the maximum cone of light that can enter or exit the condenser or objective. If the distance is $2r$, then objects at both points are completely resolved, whereas they are barely resolvable at r.

The limits of the ATR objective make Raman microspectroscopy attractive because the practical diffraction limit is on the order of the excitation wavelength. The spot size is thus reduced 10-fold and makes it possible to adequately delineate domain morphology. As the spot size of the 785 nm laser used in this study is 3.1 μm, domains as small as 10 μm could be accurately mapped if the step size of the point-by-point scan is equal to the laser spot size.

The spectra from polymer components inside a blend possess several non-overlapping peaks that allow diverse methods for chemical mapping. Chemical mapping is typical for samples with highly heterogeneous components. For example, FTIR mapping was used to characterize the morphology of a polyvinyl chloride/poly(methyl methacrylate) blend, with PMMA being the dispersed phase.[11] Another approach utilized energy dispersive x-rays (EDX) with scanning electron microscopy (SEM) to identify the two layers in self-stratified coating systems by detecting halogen moieties in one of the layers.[12]

Articles that feature chemical mapping of blended thermosets have yet to be found. The closest example is an FTIR image of an epoxy thermoset cured on a temperature gradient, which effectively generated a multilayered coating.[13] All epoxy layers differed only by their cure temperatures, but did not possess polymeric domains. It seems less likely the literature would feature instances of chemical mapping of blended powder coatings. In this study, we describe a procedure for producing reproducible chemical maps of blended thermosets at a level sufficient for identifying and detailing domains.

The constituent resins of the blends in this study are both acrylic polyurethanes that differ only by their hydroxyl content prior to reaction with the polyisocyanate curative. The curative compatibilizes the acrylic resins when they are extruded together prior to application on a metallic work piece. Thus, the composition of the dispersed phase would exhibit only subtle differences that would not be detected in typical mapping operations. This is the motivation for producing cross-section samples, where domains could be more easily investigated. Droplet domains constitute the dispersed phase, while the continuous phase constitutes the polymer matrix.

Cross-sectioning methods were adapted from the conservation science community, where the samples tend to be precious historical artifacts with complex chemistries.[14] Adaptation of conservation science procedures toward modern paints led to a controlled study of domain identification using selective staining with styrene monomer. Raman spectroscopic mapping of a cross-section sample embedded within polyester identified the domains within the thermoset films generated from the blended

system.[15] Understanding the composition (high OH vs low OH) of the domains is important for optimizing the coating performance.

5.2 Experiment

5.2.1 Coating preparation

The examined blends in the study were prepared in a manner similar to that presented by Mahn[16] except no pigments were added. The blending was performed through combination of high and low hydroxyl (OH) group functionalized polymeric resins. These resins have vastly different hydroxyl group functionalities that exhibit considerably different polar and hydrogen bonding interactions when blended, which gives rise to their immiscibility. All materials were utilized as acquired unless otherwise noted. The acrylic resins with high and low hydroxyl group functionality (20-400 OH) and Resiflow were purchased from Estron Chemical (Calvert City, KY). Benzoin was purchased from GCA Chemical Corporation. The blocked isocyanate was an ε-caprolactam blocked IPDI polyisocyanate curative and was purchased from Evonik Industries (Parsippany, NJ). Film formulations were prepared by weight as shown in Table 5-1 below.

Table 5-1. Coating formulations by percentage based upon raw material weights

Raw Material	Clear Blend	High OH Resin Film	Low OH Resin Film
High OH Resin	**26.0**	**37.1**	**–**
Low OH Resin	**26.0**	**–**	**73.6**
Blocked Isocyanate	**46.0**	**60.9**	**24.4**
Flow Agent	**1.2**	**1.2**	**1.2**
Benzoin	**0.8**	**0.8**	**0.8**

Raw materials were manually dry-blended, then melt mixed using a twin screw extruder at about 120 ˚C. The extruded material was squeezed through chilled rollers and the cooled material was ground using a rotor mill. The ground powder particle size was further classified by using a 106 μm (140 mesh) sieve. Powder formulations from above were electrostatically applied to tin plated steel substrates to a dry film thickness of 2.0 – 2.5 mils using a standard gravity fed powder coating cup gun. Coatings were then cross-linked in an oven at 204 °C for 12 minutes to generate the thermoset films. The elevated temperatures are required for viscosity reduction for flow inducement to ensure even wetting of the substrate, and to liberate the ε-caprolactam blocking group in order to generate the free isocyanate necessary for cross-linking. Coatings were cooled to room temperature prior to subsequent analysis.

5.2.2 Optical microscopy

Digital optical microscopy was used to record observations of embedded cross-section samples, particularly of the size and distributions of domains. OM measurements were performed with two microscopes. The first was an Olympus BX51 microscope that was equipped with an Olympus UC30 digital camera and used Olympus Stream Essentials 1.9.2 software. The second was a Meiji microscope equipped with a Nikon digital camera DXM1200 and used Nikon ACT-1 software. It was used in conjunction with Raman imaging.

5.2.3 Differential scanning calorimetry (DSC)

DSC was performed for each of the coatings using a TA Instruments (New Castle, DE) Q20 DSC equipped with a TA Instruments Refrigeration Cooling System (RCS). Coatings were cycled from 30 °C to 85 °C at 10 °C/min to remove thermal memory followed by two cycles from -30 °C to 220 °C at 10 °C/min to determine the glass transition temperature for each of the formulations.

5.2.4 Raman spectroscopy

Raman spectra and maps were acquired using a Thermo Scientific Nicolet Almega™ dispersive spectrometer coupled to an Olympus microscope with 10X and 50X objective lens. The instrument used a 785 nm laser with a 3.1 μm spot size. High-quality spectra were acquired by scanning a sample 30 times using a ten-second-collection time. For mapping acquisitions, samples were placed on double-sided tape to ensure complete stability. Each spectrum was acquired via 15 scans using five-second-collection time. Typical step-sizes were 5-7 μm.

5.2.5 Cross-section sample preparation

Cross-section samples of the blends and their single component counterparts were prepared by polishing with the MOPAS hand-held dry polisher (Jaap Enterprise, Amsterdam, Holland).[14, 17] Free film specimens of each of the coatings were embedded within the polyester resin Bio-Plastic™ (Ward's Science, New York), which was allowed to cure for 72 hours prior to polishing (Figure 5-1a). The commercially available polyester embedding resin consists of 50% unsaturated polyester prepolymers, 40% styrene monomer, and 10% methyl methacrylate. The cured Bio-Plastic blocks were then

cut to remove excess material in order to fit into the MOPAS hand-polisher jig. Dry polishing was performed using 6" × 6" Micro-Mesh™ silicon carbide abrasive cloths using different grades starting at 1800 and ending at 12000 to produce a 1 μm finish. Dry polishing was performed for each grade until a homogeneous polish was observed using optical microscopy.

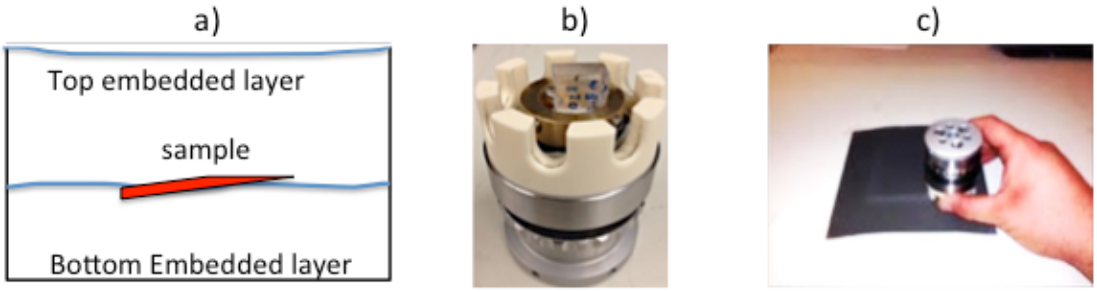

Figure 5-1. (a) Illustration of sample specimen embedded between two layers of the polyester embedding resin; (b) MOPAS hand polisher with polyester resin block containing embedded film specimen inserted; (c) MOPAS hand-held polisher and Micro-Mesh abrasive cloth.

5.2.6 Styrene vapor staining

Coating sample fragments were placed on an aluminum mesh, which was suspended in a 100 mL beaker above 10-20 mL of monomeric styrene. The beaker was capped with parafilm in order to create a styrene-saturated headspace for vapor staining experiments. Vapor staining was performed on samples from one hour, 24 hours and 72 hours to observe styrene vapor infiltration at room temperature. The 24- and 72-hour stained low OH and blended samples experienced severe morphological changes from extensive wetting and possible dissolution, whereas one-hour stained samples did not show any discernable change according to optical microscopy.

5.3 Results/Discussion

5.3.1 DSC analysis and optical microscopy of the blend surface

Thermoset films created from individual acrylic resin and blends of two acrylic resins with high and low hydroxyl functionality were analyzed to understand polymeric phase separation. Two independent blends (Blend A and Blend B) each composed of a high and low hydroxyl functionalized resin displayed distinct polymeric domain morphologies. Films of the individual constituent resins displayed no polymeric phase separation via the absence of distinctive domain morphologies. Differential scanning calorimetry (DSC) analysis of Blend A and films of the individual constituent resins are shown in Figure 5-2.

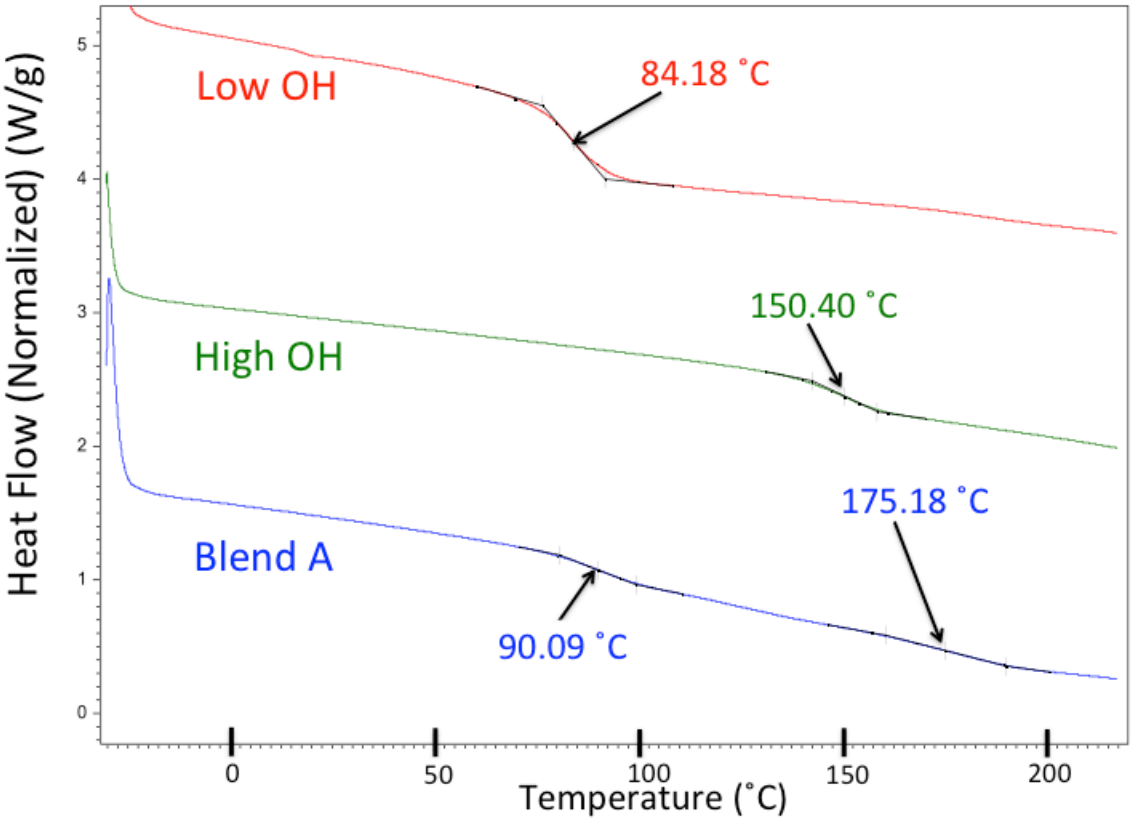

Figure 5-2. DSC thermogram of Blend A (bottom curve) and the single component high OH (middle curve) and low OH (top curve) resin films.

The DSC measurements for Blend A yielded T_g values of 90.09 ˚C and 175.18 ˚C, thus signifying two polymeric phases. The low hydroxyl functionalized constituent film

displayed a singular T_g at 84.18 ˚C while the high hydroxyl functionalized constituent film also displayed a singular T_g at 150.10 ˚C; both indicate singular polymeric phases. The DSC thermograms for Blend B and films based upon the individual high hydroxyl and low hydroxyl functionalized resins are shown in Figure 5-3. The thermoset film of Blend B also displayed two T_g values, and was thereby indicative of two polymeric phases at 105.42 ˚C and 177.67 ˚C. The single component resins indicated the presence of polymeric phases with the T_g of that low hydroxyl functionalized resin film at 82.13 ˚C and the T_g of the high hydroxyl functionalized film at 137.79 ˚C. The increased T_g's in the blends were largely a result of higher NCO:OH indexing, which may indicate increased quantities of urea linkages relative to urethane linkages.[18]

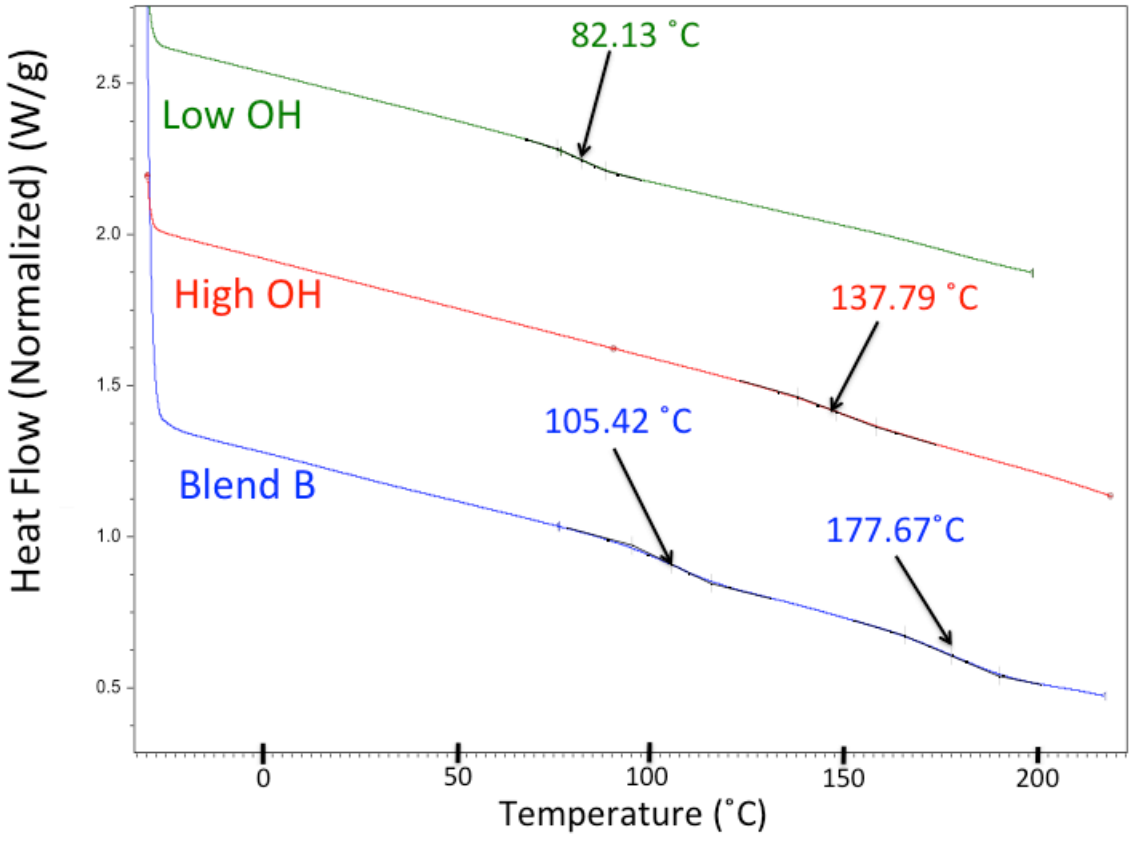

Figure 5-3. Differential Scanning Calorimetry thermogram of Blend B (bottom curve) and its components as individual films. The high OH film is the middle curve; the low OH film is the top curve.

Under optical microscopy, Blend A exhibited droplet domains with lengths or diameters between 20 and 500 μm.. The domains in Blend B ranged from 20 μm to 250 μm. Figure 5-4 features an optical micrograph of the Blend B surface that shows the domains appearing as hills on the film surface, and is illustrate the surface roughened by the immiscibility of the high hydroxyl and low hydroxyl content resins.

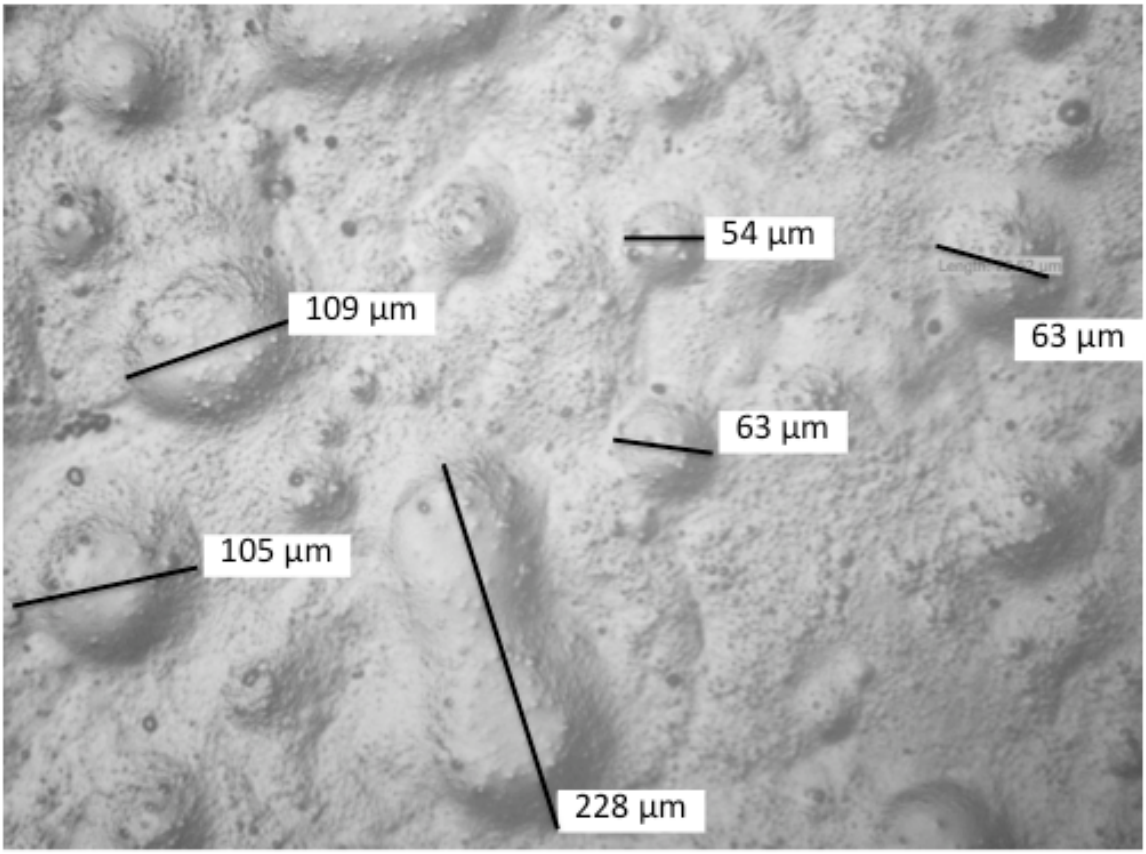

Figure 5-4. Optical micrograph of Blend B surface with measurements of some domain diameters and lengths.

5.3.2 Raman spectroscopy of coating surfaces and embedded cross-sections

Prior to embedding and cross sectioning, Raman spectra from the surfaces of both blends and the four individual resin films were collected. Raman spectra from the phases of Blend A and the individual constituent resin films are presented in Figure 5-5. The free C=O peak at 1760 cm^{-1} varies significantly between single component films, but

shows little variation between phases in the blend. The other peaks shown in Figure 5-5 also show little variation. The peak at 1655 cm^{-1} was found to be a C=O from remaining deblocked caprolactam[19], and was too small to be useful for chemical mapping. It was presumed that the domain morphologies should exhibit different concentrations in urethane linkages and thus prove useful for chemical mapping from the surface analysis via peak heights or peak area. However, the Raman mapping analysis did not detect significant differences between the two phases for either blended film based upon the surface analysis of the carbonyls alone. Further mapping analysis utilizing other peaks (e.g., aromatic, C–C backbone, etc.) also failed to yield results differentiating the distinct phases from the surface analysis.

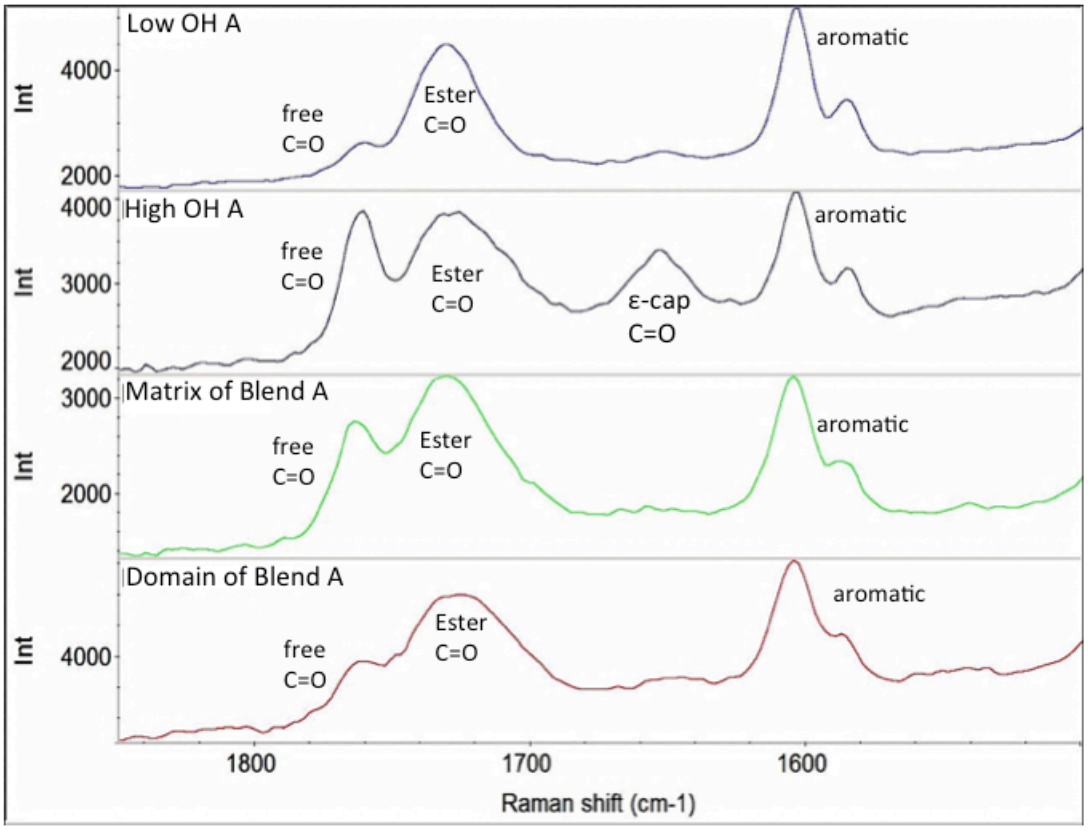

Figure 5-5. Stacked Raman spectra of single component films and phases of Blend A.

Polished cross sectioned samples of Blend A and of the individual constituent resin films embedded within polyester resin were analyzed via Raman micro-spectroscopy. Micro-Raman analysis of the cross-section samples of Blend A and the individual constituent films yielded a stark contrast to previous observations made for the free films. Raman spectra acquired from the continuous polymer matrix of Blend A and the low hydroxyl constituent resin film possessed an extra peak at 1630 cm^{-1}, while the high OH film and domains either possessed no such peak, or it was highly diminished (Figure 5-6).

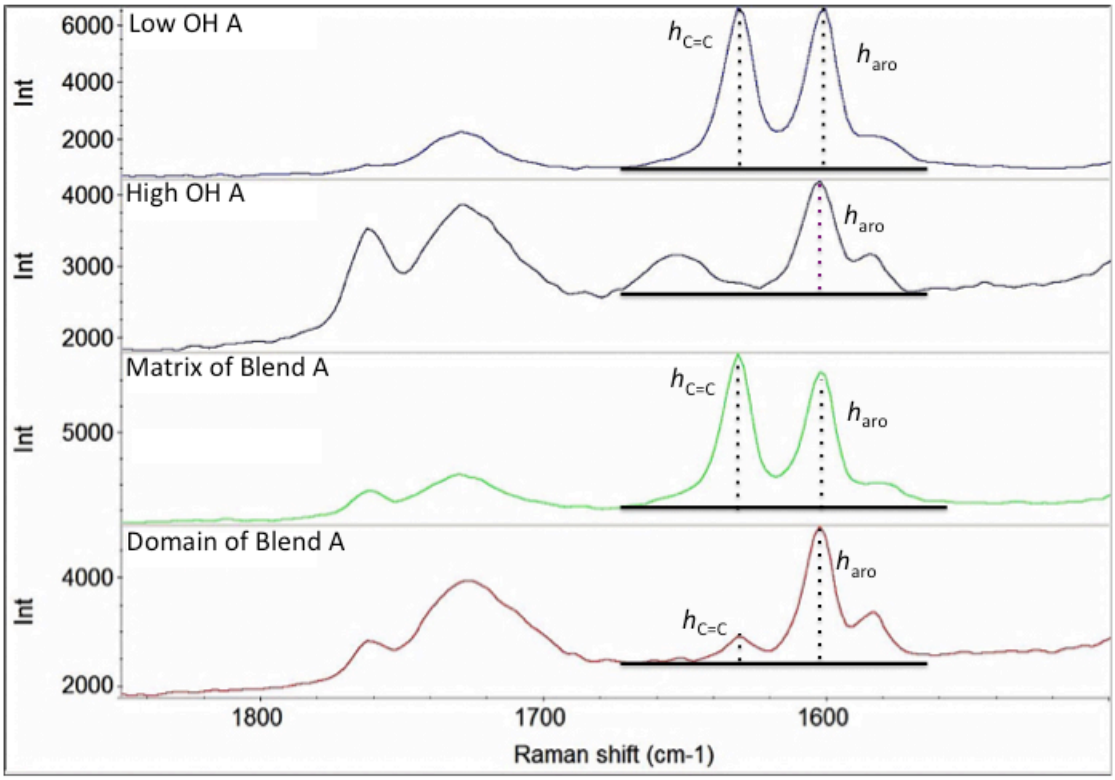

Figure 5-6. Stacked Raman spectra from polyester-embedded cross-sections of Blend A with marker peak heights indicated on a baseline; top: low OH Raman spectrum; middle top: high OH Raman spectrum; middle bottom: Raman spectrum of polymer matrix; bottom: Raman spectrum of domain.

5.3.3 Domain identification by Raman mapping

This extra peak at 1630 cm^{-1} peak stemmed from a conjugated alkene that belonged to styrene monomer.[20] It is used as a crosslinker for the polyester embedding resin.[21] Styrene is a relatively nonpolar molecule and consequently displays high intensities in Raman compared to FTIR because styrene is a very strong Raman scatterer.[22] This selective infiltration led to the utilization of the conjugated alkene peak as a spectroscopic marker peak. Figure 5-6 also shows the neighboring aromatic peak becoming much greater in intensity when there is an alkene peak. Both peaks were thus selected for chemical mapping with a peak height ratio. The ratio is calculated by

$$R = h_{C=C}/h_{aro} \quad (5\text{-}3)$$

where R is the peak height ratio, $h_{C=C}$ is the peak height of the alkene moiety, and h_{aro} is the peak height of the aromatic moiety.

Chemical maps were generated for both the constituent resin films and Blend A (Figures 5-7 and 5-8) in order to characterize the cross-section samples with respect to monomeric styrene infiltration. The peak height analysis shown in Figure 5-6 was utilized to generate two types of chemical maps, which are displayed in Figure 5-7 for the individual constituent resin films. Figures 5-7a – 5-7c illustrate the analysis of the high hydroxyl functionalized constituent resin film with respect to styrene infiltration based upon the peak height of the alkene marker peak. This map does not use the ratio because the lack of monomeric styrene in the polyurethane layer normalized the ratio to the point where noise had an outsized influence on the map and reduced the contrast between the regions. Mapping with the alkene peak height alone was better for contrasting between the regions. The lack of such a marker peak in Figure 5-7c illustrates the absence of infiltration throughout the cross-linked film. Figures 5-7d – 5-7f show the Raman

mapping analysis of the low hydroxyl functionalized constituent resin film based upon *R*. The Raman map in Figure 5-7f clearly shows the large amount of monomeric styrene throughout the cross-linked film. Both chemical maps show the constancy of the alkene peak in the polyester regions (red in 5-7c, blue in 5-7f) in all spectral acquisitions, and thus provided a consistent signature for chemical mapping.

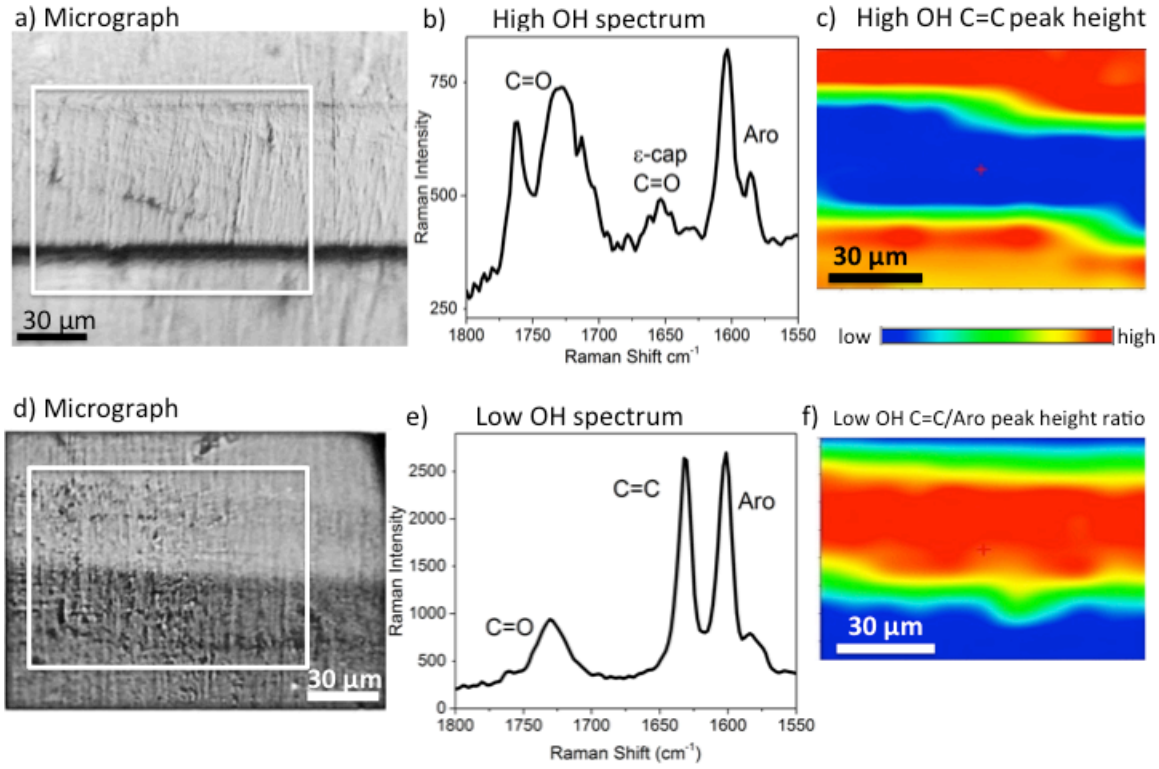

Figure 5-7. a) Optical micrograph of high OH cross-section; b) close-up on high OH aromatic and carbonyl peaks; c) alkene peak height map of high OH cross-section; d) optical micrograph of low OH cross-section; f) close-up on low OH aromatic, alkene and carbonyl peaks; e) alkene/aromatic peak height ratio map of low OH cross-section.

Raman mapping was performed to monitor the styrene infiltration within Blend A (Figure 5-8). Individual spectra comparison for a domain and the continuous polymer matrix of Blend A are shown in Figure 5-8b. Styrene infiltration is clearly present within the continuous polymer matrix and nearly absent within the domain. Two spectral maps were generated in order to fully observe styrene infiltration within the blended film

(Figures 5-8c and 5-8d). Mapping of the alkene peak height (Figure 5-8c) provided excellent contrast of styrene infiltration and subsequently domain identification. A styrene infiltration gradient within the blended film was also generated using *R* (Figure 5-8d). The gradient infiltration of monomeric styrene in the Raman map in Figure 5-8 also provides great contrast for domain identification within Blend A. Raman chemical maps in Figure 5-8 indicate that monomeric styrene exhibits the highest infiltration into the continuous polymer matrix, similar to that observed for the low hydroxyl constituent resin film. Comparative analysis of Raman maps from Figures 5-7 and 5-8 provide conclusive evidence that the domain within Blend A originates from the high hydroxyl constituent resin and that the continuous polymer matrix is consistent with the low hydroxyl constituent resin. Styrene infiltration and subsequent observation with Raman spectroscopy has become a tool for domain identification within the coating blend. The alkene peak was deemed useful as a marker peak for Raman mapping on other samples. alkene peak was deemed useful as a marker peak for Raman mapping on other samples.

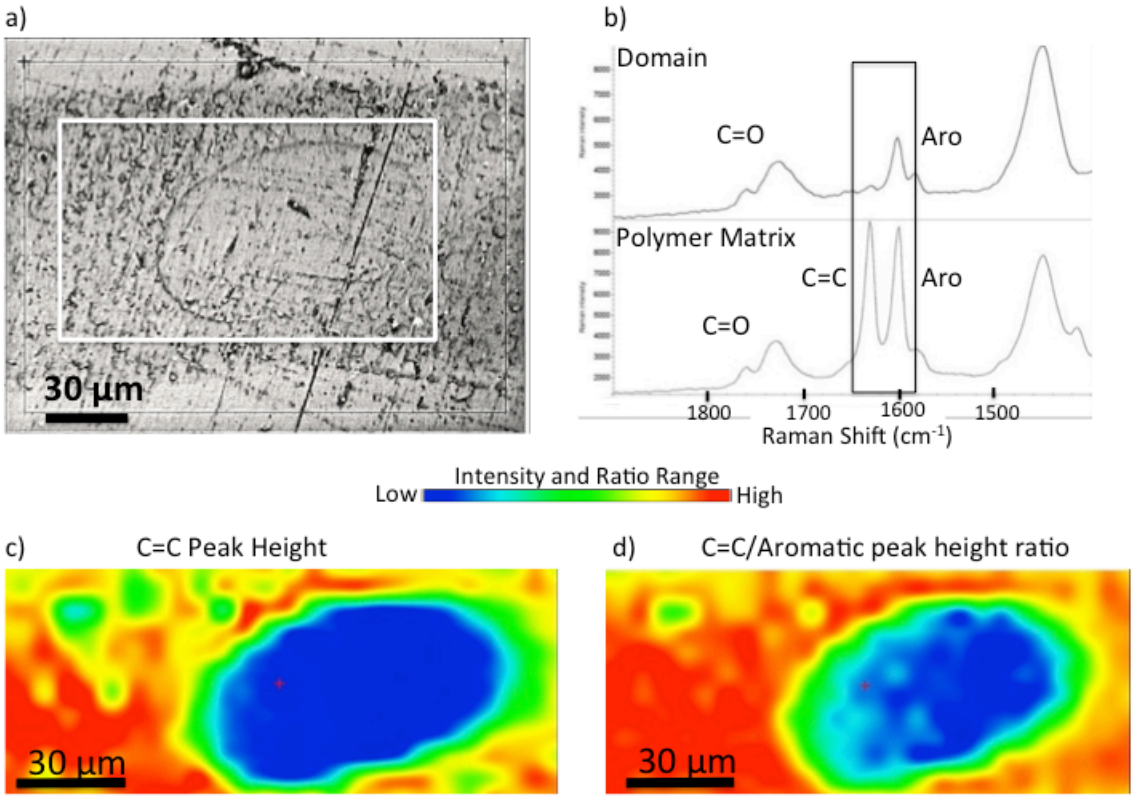

Figure 5-8. a) Optical micrograph of mapped region; b) selective infiltration in polymer Matrix; c) C=C peak height map; d) ratio of the C=C/aromatic peaks.

Raman analysis for infiltration of monomeric styrene was extended as a technique for domain identification in Blend B. Cross-section samples of Blend B and the individual constituent resin films were prepared using the same embedding and polishing process as Blend A. The individual constituent resin films exhibited similar infiltration patterns of styrene from the polyester resin, where the high hydroxyl functionalized resin film displayed resistance to contamination. The Raman mapping results for the cross-section sample of Blend B are presented in Figure 5-9. The optical micrograph (Figure 5-9a) shows two large domains in the cross-section, a spherical shaped domain in the center similar to the domains observed in the micrograph of Blend A (Figure 5-8a), and another large elongated domain in the lower left of 5-9a. As previously observed for Blend A, the monomeric styrene preferentially infiltrated the continuous polymer matrix, while the

domains were relatively impervious. The alkene marker peak height map (Figure 5-9b) provides the greatest contrast for domain identification with both domains displaying the lowest peak heights for the alkene peak. The peak height ratio map (Figure 5-9c) shows the degree of infiltration within the domains, as evidenced by the green annulus of intermediate infiltration surrounding the spherical globule; even the center of the domain has minor styrene infiltration. The flattened domain in the lower left portions of the micrograph and maps exhibits the least amount of styrene infiltration (dark blue). The green interphase region may be a partial product of interpolation performed by the mapping software because the step size is 5 μm. The degree of infiltration throughout the domains (Figure 5-9c) could indicate density of cross-linking within the film based upon gradients observed in the peak height map. This phenomenon has been considered as an explanation of solvent resistance by this class of polyurethanes.[23]

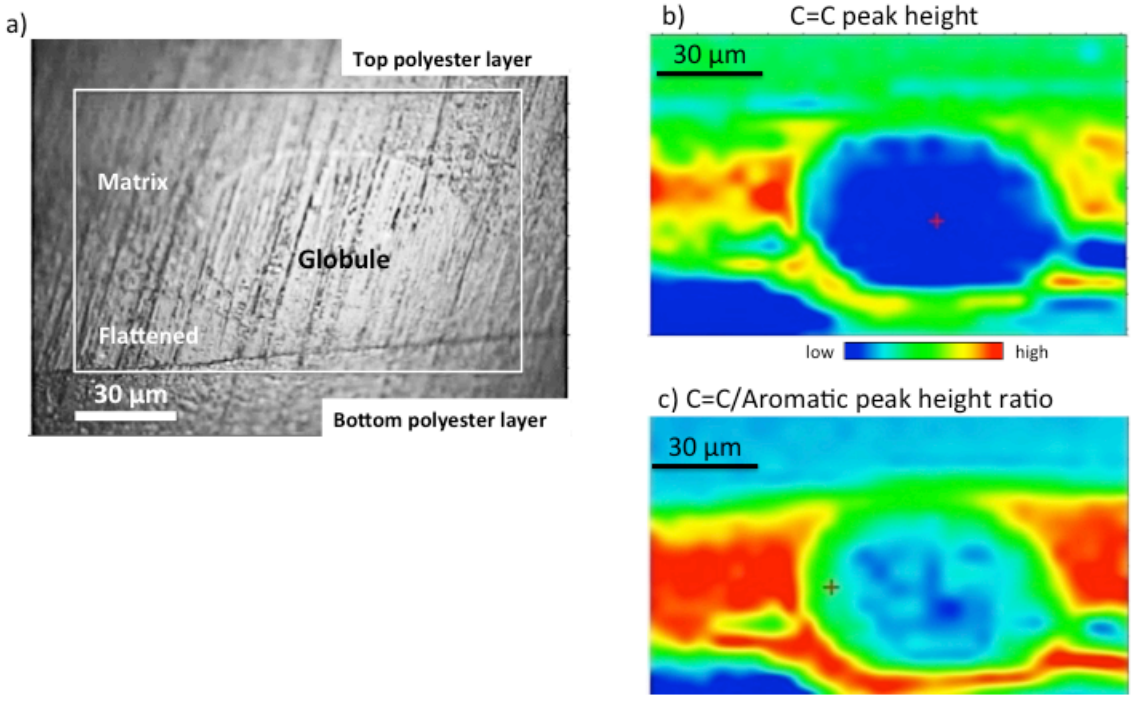

Figure 5-9. a) Optical micrograph of Blend B cross-section; b) Alkene peak height map; c) alkene/aromatic peak height ratio map.

Blend B was subsequently embedded within fast-cure epoxy to observe if cross-sections can be prepared without contamination from the embedding resin (Figure 5-10). If the coating remained chemically intact after embedment, then a peak intrinsic to the coating itself could be used to analyze it. The Raman spectra in Figure 5-10 clearly show the absence of the styrene marker peak. The ensuing domain identification was attempted with the free and ester C=O peaks. Mapping of the free carbonyl peak height revealed that the peak intensity was less inside this domain than in the continuous polymer matrix. In contrast, the ester C=O peak exhibited a homogeneous distribution throughout the blended polyurethane film. Additional Raman maps were generated from other peaks for this cross-section, but the large domain was observable only with the free C=O peak.

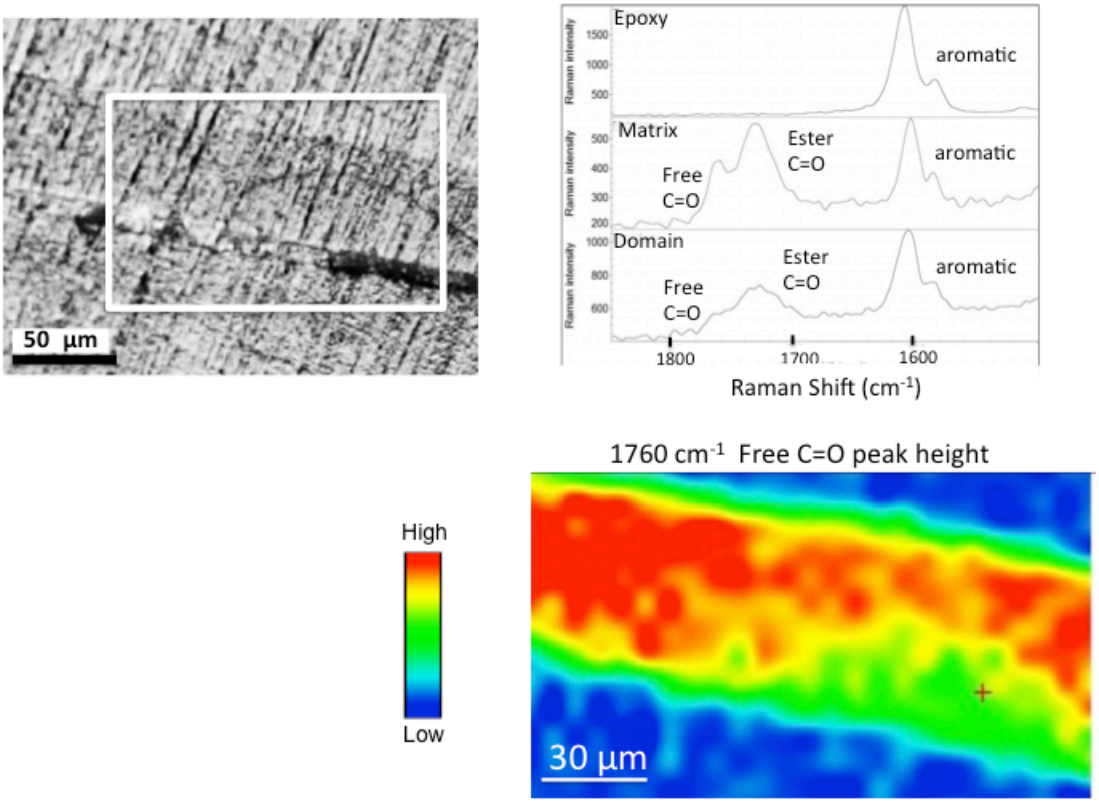

Figure 5-10. Raman analysis of Blend B cross-section embedded in fast-cure epoxy.

5.3.4 Controlled staining with styrene vapor

The results from the polyester-embedded cross-section samples motivated the consideration of styrene vapor staining as a viable approach toward domain identification by Raman mapping. Styrene monomer is highly volatile at room temperature, and thus could be easier to control the degree of infiltration. Coating samples of Blend B and the individual constituent resins were vapor stained with styrene monomer for 72 hours followed by analysis with Raman spectroscopy (Figure 5-11).

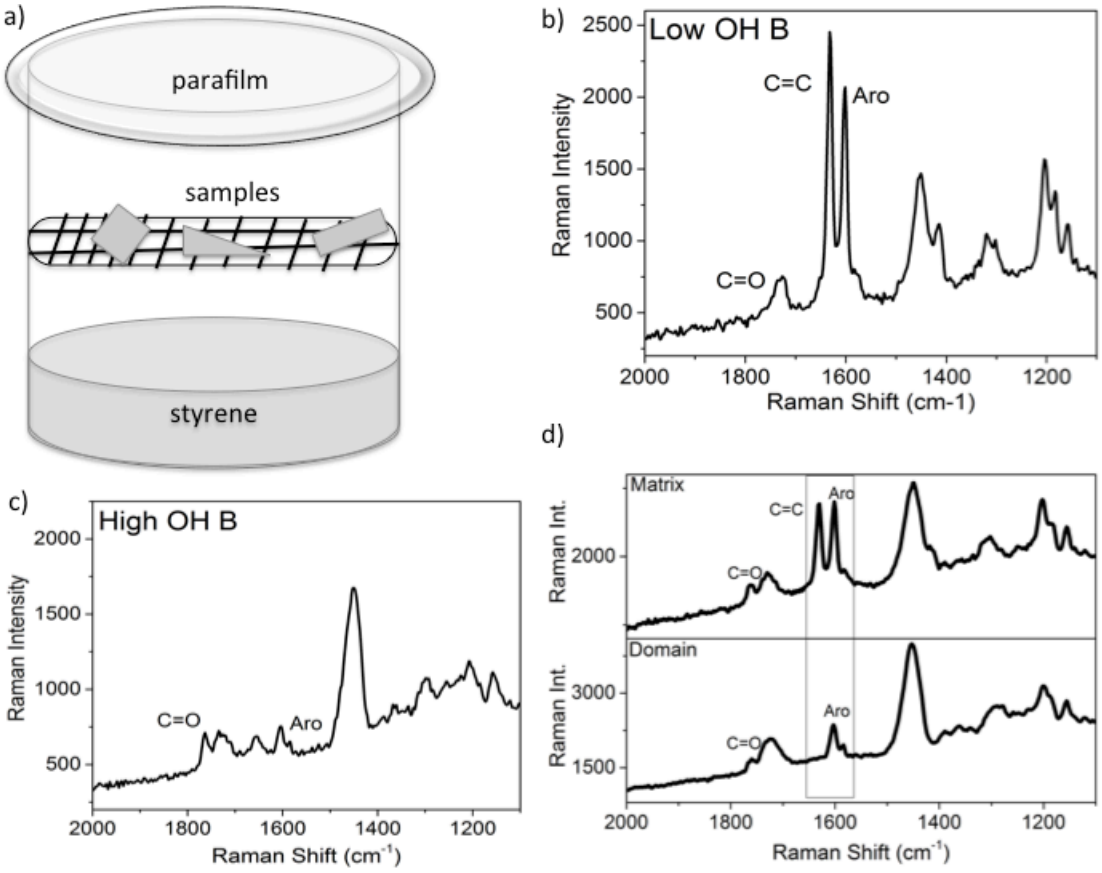

Figure 5-11. a) Apparatus for vapor staining; b) Low OH film after 72 hours in headspace; c) High OH film after 72 hours; d) Blend B after 72 hours.

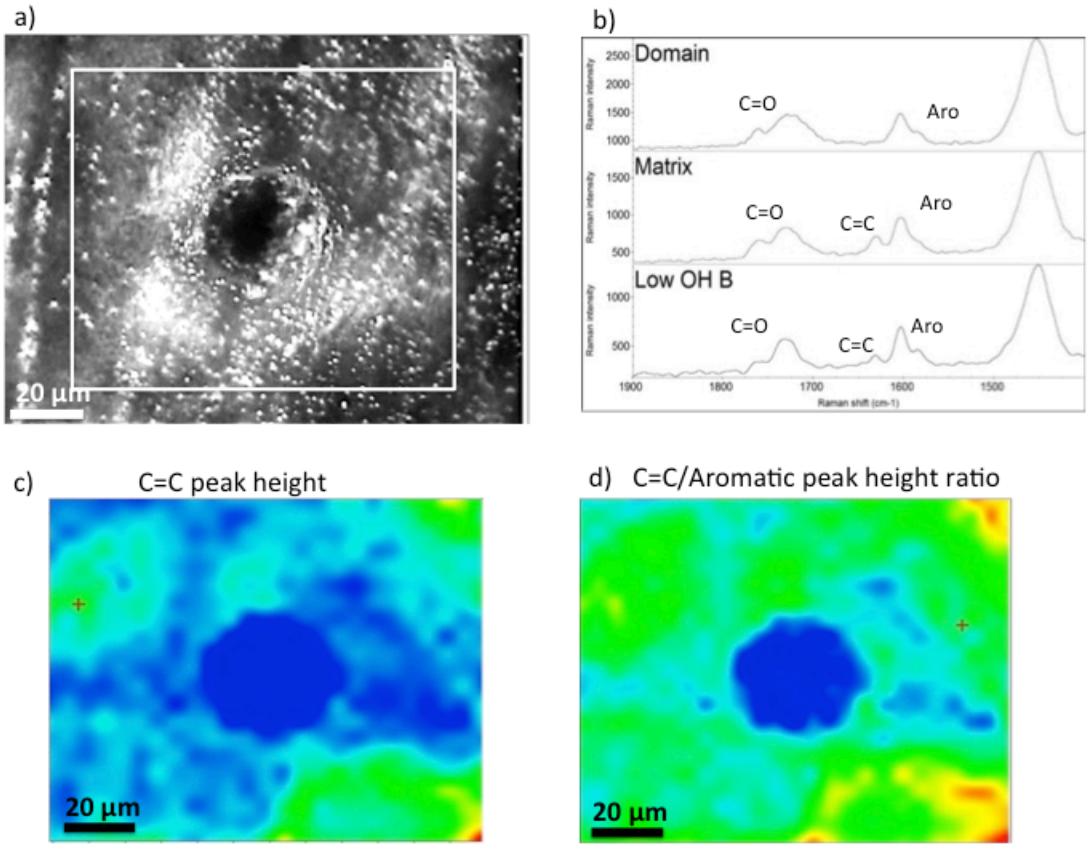

Figure 5-12. a) Dark field optical micrograph of Blend B surface; b) small styrene peaks in matrix and low OH spectra; c) alkene peak height map; d) alkene/aromatic peak height ratio map.

The results show that after 72 hours of exposure to a saturated styrene atmosphere, only the low hydroxyl constituent resin film and the continuous polymer matrix phase of Blend B were heavily contaminated (Figure 5-11b and 5-11d). The high OH domain in 5-11d was uncontaminated, but Raman analysis on other domains indicated minor infiltration with small alkene peaks. The vapor staining experiment was repeated for 24 hours with similar results to the 72-hour exposure shown in Figure 5-11. In order to determine the minimum time needed for detectable infiltration by the Raman spectrometer, vapor staining of Blend B was performed in 10-minute intervals until the alkene peak was detected. It took one hour of vapor staining to observe the alkene peak

in the low OH film and Blend B matrix (Figure 5-12b). Chemical mapping with $h_{C=C}$ and with R (Figure 5-12c and 5-12d, respectively) provided good contrast of the domain in the center of the dark-field micrograph in Figure 5-12a from one hour of staining. The results in Figures 5-11 and 5-12 demonstrate that styrene can be utilized as a controlled selective staining agent for polymeric films. The one-hour vapor staining procedure was repeated for Blend A. The infiltration gradients observed in Blend A were consistent with the optical microscopy observations and also with observations of its cross-section. The vapor staining procedure further confirms that the contaminant from the polyester-embedding process is monomeric styrene, and that the degree of infiltration can be controlled using this method.

Styrene vapor staining was also attempted on the epoxy embedded cross-section sample. The Blend B matrix did not possess alkene peaks with intensities similar to the spectra in Figure 5-11 until after four hours in styrene atmosphere. This may be due to the reduced surface area for styrene vapor to infiltrate.

Selective staining as a characterization method is normally applied for electron microscopy. Staining agents are typically high-density metal compounds such as osmium tetraoxide, and are used to visualize polymer phases and morphology.[24] Here, the staining agent is a low-density solvent and has been applied toward vibrational spectroscopy. It has been used in this study to visualize and compositionally identify polymer phases and morphology. Selective staining for spectroscopy may thus complement microscopy techniques for analyzing polymeric cross-sections such as for TEM. Future work may include application of heavy metal staining for microscopy on these cross-sectioned samples and correlate the resultant electron micrographs with the Raman chemical maps.

5.4 Conclusion

Characterization of polymeric domains within two resin blended thermoset films has been performed via a novel spectroscopic analysis protocol. The polymeric phase separation observed within these resin blended thermoset films is a targeted method for the generation of new matte gloss durable exterior powder coatings. DSC and optical microscopy confirmed the existence of two distinct polymeric phases in the blended films. However, concrete chemical differentiation of the observed domains was difficult using standard spectroscopic techniques without any sample manipulation.

Chemical differentiation of the polymeric phases was performed using a novel spectroscopic protocol involving the selective staining of the low hydroxyl constituent resin with monomeric styrene. Coating samples were embedded within a polyester resin, which contaminated the low hydroxyl functionalized phase of the thermoset blend. Monomeric styrene is used as a crosslinker for unsaturated polyester prepolymers. The monomeric styrene infiltrated the low OH resin within the blends and induced a signature peak in the Raman spectra at 1630 cm^{-1}, which stemmed from the conjugated alkene in styrene monomer. Raman chemical mapping of this peak for the cross-section samples revealed that it was consistently observed within the continuous polymer matrix and nearly absent within the encapsulated domains. Comparative analysis with the single component resins revealed that styrene infiltration was observed only within the low OH resin and thus enabled differentiation of the polymeric phases within the blends.

Additional insight on styrene infiltration was gained through staining of coating surfaces using styrene in the vapor phase at room temperature. Coating samples were selectively stained when placed within a saturated styrene atmosphere at various time

intervals. Selective vapor staining was performed on Blend B for 72-, 24-, and one-hour exposure times. The low hydroxyl constituent thermoset film and the continuous polymer matrix of the Blend B were still selectively stained, but the level of staining could be controlled using this method. The styrene marker peak was very intense within the low hydroxyl constituent resin and the continuous polymer matrix of Blend B for the 72- and 24-hour time intervals. The Raman mapping results for a sample vapor-stained for one hour was consistent with the results from the 72 and 24-hour staining intervals, albeit the styrene signals were vastly reduced due to limited time of immersion. The styrene vapor-staining procedure for one-hour exposure time was then performed on Blend A to further confirm the domain identification and validity of the test parameters. The components in Blend A exhibited the same infiltration response to the vapor as Blend B. The vapor staining method is thus consistent and reproducible.

Elimination of styrene infiltration in cross-section samples was also performed to confirm contamination and experiment with identification of domains utilizing peaks intrinsic to the blended coatings. Blend B was embedded in fast-cure epoxy and cross-sectioned with the same procedure as before. Raman spectroscopy mapping of the free carbonyl peak at 1760 cm^{-1} produced the only satisfactory result for mapping of intrinsic peaks within the blended film. However, the reliability of domain identification in the absence of the styrene marker peak was greatly reduced. The epoxy embedded specimen was styrene vapor-stained, and alkene peaks with intensities similar to the intensities from the one-hour-stained samples emerged after 4 hours in styrene vapor atmosphere.

The authors have not found literature that describes selective staining of immiscible polymer blends in combination with micro Raman spectroscopy. Therefore,

spectroscopic analysis enhanced by selective staining of immiscible polymer blends via styrene appears to be a novel protocol. This selective staining may also serve to complement common microscopy techniques for analyzing polymeric cross-sections such as TEM. The domain identity is now largely confirmed and understanding their formation and development is the subject of further investigation.

5.5 References

1. Misev, T. A., Powder Coatings. In *Surface Coatings*, 2nd ed.; Paul, S., Ed. John Wiley & Sons: Chichester, England, 1996; pp 788-849
2. Richart, D. S., The Surface Topography of Powder Coatings and its Relation to Gloss. *Powder Coating* **1999,** *2*, 25-35.
3. Jacquin, J. D.; McCurdy, M. R.; Dennis, D. J.; Evangelista, M.; Favrin, D.; Minesso, A., New Resin Technology for Semi-Matte and Dull-Matte Powder Coatings—Part 1. *Powder Coating* **2009**, *9*, 37-41.
4. Jacquin, J. D.; McCurdy, M. R.; Dennis, D. J.; Evangelista, M.; Favrin, D.; Minesso, A., New Resin Technology for Semi-Matte and Dull-Matte Powder Coatings—Part 2. *Powder Coating* **2009**, *10*, 24-37.
5. Hare, C. H., *Protective Coatings: Fundamentals of Chemistry and Composition*. Technology Publishing Company: Pittsburgh, Pennsylvania, 1994; p 514.
6. Xue, L.; Zhang, J.; Han, Y., Phase separation induced ordered patterns in thin polymer blend films. *Progress in Polymer Science* **2012,** *37*, 564–594.
7. Verkholantsev, V. V.; Flavian, M., Epoxy/Thermoplastic Heterophase and self-stratifying coatings. *Modern Paint and Coatings* **1995,** *85* (11), 100-106.
8. Verkholantsev, V. V., Self-stratifying coatings for industrial applications. *Pigment and Resin Technology* **2003,** *32* (5), 300-306.
9. Bhargava, R.; Wang, S.-Q.; Koenig, L. J., FTIR Microspectroscopy of Polymeric Systems. In *Liquid Chromatography / FTIR Microspectroscopy / Microwave Assisted Synthesis*, Springer Berlin Heidelberg: Berlin, Heidelberg, 2003; pp 137-191.
10. Sato, H.; Unger, M.; Fischer, D.; Ozaki, Y.; Siesler, H. W., Characterization of Polymer Blends by Infrared, Near-Infrared, and Raman Imaging. In *Characterization of Polymer Blends: Miscibility, Morphology, and Interfaces*, First ed.; Thomas, S.; Grohens, Y.; Jyotishkumar, P., Eds. Wiley-VCH Verlag GmbH &Co. KGaA: Boschstrasse 12, 69469 Weinheim, Germany, 2015; pp 705-730.
11. Bhargava, R.; Wall, B. G.; Koenig, J. L., Comparison of the FT-IR Mapping and Imaging Techniques Applied to Polymeric Systems. *Applied Spectroscopy* **2000,** *54* (4), 470-479.
12. Baghdachi, J.; Perez, H.; Talapatcharoenkit, P.; Wang, B., Design and development of self-stratifying systems as sustainable coatings. *Progress in Organic Coatings* **2015,** *78*, 464–473.

13. Eidelman, N.; Raghavan, D.; Forster, A. M.; Amis, E. J.; Karim, A., Combinatorial Approach to Characterizing Epoxy Curing. *Macromolecular Rapid Communications* **2004,** *25* (1), 259-263.
14. Loon, A. v. Color Changes and Chemical Reactivity in 17th-Century Oil Paintings. PhD Dissertation, University of Amsterdam, Archetype Publications, 2008.
15. Giles, S. L.; Heller, N. W. M.; Clayton, C. R.; Walker, M. E.; Wytiaz, M. J.; Wynne, J. H., Novel Methods of Producing Low Reflectance Coatings Utilizing Synergistic Effects of Polymer Phase Separation. *ACS Applied Materials And Interfaces* **2016**, In Press.
16. Mahn, E. J. Low reflectance chemical agent resistant coating compositions. 20150259541 A1, 2015.
17. Prati, S.; Sciutto, G.; Catelli, E.; Ashashina, A.; Mazzeo, R., Development of innovative embedding procedures for the analyses of paint cross sections in ATR FTIR microscopy. *Analytical and Bioanalytical Chemistry* **2013,** *405* (2-3), 895-905.
18. Levine, F.; Escarsega, J.; Scala, J. L., Effect of isocyanate to hydroxyl index on the properties of clear polyurethane films. *Progress in Organic Coatings* **2012,** *74*, 572-581.
19. Reardon, T. J.; Barker, R. H., Pyrolysis and combustion of nylon 6. I. Effect of selected brominated flame retardants. *Journal of Applied Polymer Science* **1974,** *18* (7), 1903-1917.
20. Socrates, G., *Infrared and Raman Characteristic Group Frequencies: Tables and Charts*. 3rd ed.; John Wiley and Sons: Chichester, England, 2004.
21. Koenig, J. L.; Shih, P. T. K., Structure of Unsaturated Polyester Resins Crosslinked with Styrene as Studied by Raman Spectroscopy. *Journal of Polymer Science Part A-2: Polymer Physics* **1972,** *10* (4), 721-740.
22. Smith, E.; Dent, G., *Modern Raman Spectroscopy: A Practical Approach*. John Wiley & Sons: Chichester, England, 2005; p 210.
23. Gite, V. V.; Mahulikar, P. P.; Hundiwale, D. G., Preparation and properties of polyurethane coatings based on acrylic polyols and trimer of isophorone diisocyanate. *Progress in Organic Coatings* **2010,** *68*, 307-312.
24. Smith, R. W.; Bryg, V., Staining Polymers for Microscopical Examination. *Rubber Chemistry and Technology* **2006,** *79* (3), 520-540.

Chapter Six

Monitoring of Crosslink Density by Vibrational Spectroscopy and TEM

6.1. Introduction

Protective polymeric coatings are traditionally formulated with solvent for even application on a work piece, however environmental concerns regarding volatile organic compounds (VOCs) have led to increased production of powder coatings, which do not use solvent. When in melt form, powder coatings behave as non-Newtonian fluids that require a minimum shear stress, known as the yield value to impart flow and substrate wetting. Moreover, adding pigments to the binder increases the yield value, which is caused by the stiff pigment-polymer bonds that worsen flow and substrate wetting.[1] Several approaches to improve physicochemical properties of powder coatings included immiscible powder blends, thus adding more complexity to the coating system.[2-3] Such complexity in the coating formulation may hinder analysis and understanding of the curing process, which can provide valuable insight into continued optimization of physicochemical properties.

Aliphatic polyurethane chemistries in coatings are ubiquitous in the coatings industry and are prized for their high durability and protective properties that are produced from the crosslinking of polyols with polyisocyanates.[4] The urethane linkage within polyurethanes possess a well known propensity for complex H-bond behavior among carbonyls (C=O),[5-6] and is a significant source of interesting physical and chemical properties. Yen and Hong have previously demonstrated from four model

compounds and two polyurethanes[7] the deconvolution of high-resolution vibrational spectra to yield additional C=O peaks from hydrogen bonding.

In Chapter 5, the polymer components within the blend were identified via Raman analysis of selective staining with monomeric styrene in the fully cured coating. The two acrylic polyol reactants used to generate the polyurethane blends are immiscible without the isocyanate crosslinker because of the vast difference in their hydroxyl content, thus distinguishing them as high in hydroxyl number (high OH) or low in hydroxyl nmber (low OH). The ε-caprolactam blocked isocyanate serves as a compatibilizer and is stable under normal storage conditions. The deblocking and liberation of ε-caprolactam induces a marked decrease in melt viscosity and improves flow because the ε-caprolactam acts as a solvent prior to evaporation.[8] This internal solvation makes polyurethane powder coatings possess the best flow properties among powder thermosets.[1]

The application of incompatible polymeric resins in coating systems was first investigated by Funke, whose model was mostly based on the interfacial energy between phases as the driving force for phase separation; this phenomenon is fundamentally rooted in the reduction of free energy of mixing during heating above the melting temperature.[9] Funke later demonstrated layer-stratification in epoxy-acrylic powder coatings. The mechanism for these materials was driven by polymer incompatibility and the affinity of the polar groups for the lower layer being oriented toward the substrate thereby generating a surface energy gradient.[10] The gradient is likely rooted in the different polarities and types of intermolecular forces, as suggested from Hansen solubility parameters,[11] and provides a possible mechanism for phase separation in both self-stratified coatings and coatings with domain droplet morphologies.[12-17]

The crosslinking of blocked polyisocyanates with polynucleophiles is heavily dependent on several factors, including[18]

- structures of the polyisocyanate compatibilizer (curative), ε-caprolactam blocking agent, and nucleophile (polyol),
- polarity and hydrogen bonding potential of the coreactants,
- rates of diffusion and evaporation of the blocking agent,

With prior identification completed, spectroscopic monitoring of the coatings at various stages of development could be implemented;[19] this includes the polymer components in their reactant states before the cure commences. The domains' greater resistance to styrene monomer is explored in greater detail for quenched samples in this chapter. Extensive Raman and Fourier transform infrared (FTIR) spectroscopic analysis was performed to monitor reactants and products within the film structure as a function of curing time. This thorough investigation by vibrational spectroscopy was then correlated to trends observed in transmission electron microscopy (TEM) images of cross-section samples. TEM samples were stained with solutions of heavy metal salts for enhanced contrast. The improved resolution and clarity of the electron micrographs yielded greater insight in the correlations with curve-fitted high-resolution vibrational spectra.

6.2 Experiment

6.2.1 Coating preparation

The examined blends in the study were prepared in a manner similar to that presented by Mahn[20] except no pigments were added. The blending was performed through combination of a high and low hydroxyl (OH) group functionalized polymeric resins.

Only Blend B is analyzed in this chapter and subsequent chapters as well. All materials were utilized as acquired unless otherwise noted. The acrylic resins with high and low hydroxyl group functionality (20-400 OH) and Resiflow were purchased from Estron Chemicals (Calvert City, KY). Benzoin was purchased from GCA Chemical Corporation. The blocked isocyanate was an ε-caprolactam blocked IPDI polyisocyanate compatibilizer and was purchased from Evonik Industries (Parsippany, NJ). Film formulations were prepared by weight as shown in Table 5-1.

Raw materials were manually dry-blended, then melt mixed using a twin screw extruder at 120 ˚C. The extruded material was squeezed through chilled rollers and the cooled material was ground using a rotor mill. The ground powder particle size was further classified by using a 106 μm (140 mesh) sieve. Powder formulations from above were electrostatically applied to tin plated steel substrates to a dry film thickness of 50-100 μm using a standard gravity fed powder coating cup gun. Coatings were then cross-linked in an oven at 204 °C for 12 minutes to generate the thermoset films. The elevated temperatures are required for viscosity reduction for flow inducement to ensure even wetting of the substrate, and to liberate the ε-caprolactam blocking agent to generate free isocyanate necessary for cross-linking. Fully cured coatings were cooled to room temperature prior to subsequent analysis. Other samples were quenched by liquid nitrogen at different cure times for eventual analysis of morphological development within the coatings. Samples were quenched at 1, 1.5, 2, 2.5, 3, 4, 6, and 9 minutes into the cure.

6.2.2. Vibrational spectroscopy

Fourier transform infrared spectroscopy (FTIR), isothermal thermogravimetric analysis (TGA), and dynamic mechanical analysis (DMA) are typical methods for monitoring the two-step reaction, where deblocking is followed by crosslinking. Raman spectroscopy has been utilized in this study because of the small spot size of the laser (enabling monitoring individual domains), and its sensitivity toward nonpolar moieties that may not appear in FTIR spectra. Laser Raman spectroscopy (LRS) and FTIR are considered complementary vibrational techniques due to their sensitivities to different functional groups.[21]

A) Fourier Transform Infrared Spectroscopy (FTIR)

ATR-FTIR spectra were recorded on a Thermo Scientific Nicolet™ iS50 FTIR Spectrometer with a Smart Performer™ ATR attachment and constant pressure tower. An MCT-A detector collected 64 scans of the sample. Film samples were analyzed with a diamond crystal. DRIFTS was performed on the same spectrometer with a Spectra Tech attachment. Deconvolution was conducted with OMNIC software. All bands were calculated with Voigt curves due to the observed optimal fits.

B) Laser Raman Spectroscopy (LRS)

Raman spectra and maps were acquired using a Thermo Scientific Nicolet Almega™ dispersive spectrometer coupled to an Olympus microscope with 10X and 50X objective lens. The instrument used a 785 nm laser with a 3.1 μm spot size. High-resolution spectra were acquired by scanning a sample 30 times using a ten-second-collection time with the 50X objective and higher grating density. Deconvolution was

conducted with OMNIC software. All bands were calculated with Voigt curves due to the observed optimal fits.

6.2.3 Transmission electron microscopy (TEM)

TEM was utilized to provide domain identification and distribution throughout the bulk of the films. Microtome cross-section samples were prepared for TEM analysis using a Leica EM UC7 Ultra-Microtome (Wetzlar, Germany) with a diamond sectioning blade at STP; typical thicknesses were 100-150 nm.

Initial TEM experiments were performed using a FEI Bio TwinG2 Transmission Electron Microscope. The TEM was equipped with an AMT XR-60 CCD digital camera system for image collection. Bright field imaging measurements were performed at an accelerating voltage of 80 keV.

The second microscope was a JEOL JEM-1400 LaB6. It was equipped with a Gatan CCD digital camera for image collection and a TEAM™ EDS Analysis System for TEM with an Octane Silicon Drift Detector for elemental analysis. Bright field imaging was also performed at 80 keV.

To enhance contrast between polymer phases in TEM micrographs, heavy metal salts of uranyl acetate and lead citrate were used to stain the films. Coatings were immersed in 0.02 g/mL uranyl acetate in methanol for 10 minutes, followed by 0.003 g/mL aqueous lead citrate for 3 minutes. The heavy metals are effective electron shields that serve to darken the phases upon their acceptance by the appropriate material.

6.2.4 Analysis of micrographs by ImageJ

Analysis of micrographs was perfomed with ImageJ software. It was used to count holes in low-magnification micrographs. Holes appeared as circular white areas in the micrographs. The holes were counted by hand over multiple micrographs, which were tallied in a corresponding spreadsheet for the micrograph of interest. The following data were used to generate densities of holes in cross-sections for Table 6-3.

Low OH: 273 holes/5005 μm^2 = 0.054 holes/μm^2.

High OH: 1081 holes/1614 μm^2 = 0.67 holes/μm^2.

Blend Matrix: 423 holes/3229 μm^2 = 0.13 holes/μm^2.

6.3 Results/Discussion

6.3.1 Spectral evolution

Initial spectroscopic analysis had revealed four C=O peaks for deconvolution. Understanding these peaks should provide a spectroscopic basis for the different physicochemical properties of the phases. The monitoring of the individual reactants (including the polyisocyante curative) and the resultant single component and blended polyurethanes should provide a thorough understanding of the development of the powdering binder with respect to cure-time.

A) Double bond region

In low resolution LRS spectra, three carbonyl peaks can be discerned from the reactants of the composite film. The Raman spectra in Figure 6-1 provide a comparison of the vibrational bands observed for the reactants to the bands observed from the resultant films at two stages in the cure. The urea peak at 1760 cm^{-1} and the ε-caprolactam peak at 1650 cm^{-1} in the thermoset film originate from the polyisocyanate

compatibilizer, and are incorporated into the final product; the intensity of the ε-caprolactam peak is reduced at full cure, which likely indicates the evaporation of the blocking agent. The ε-caprolactam peak also upshifted by 5 cm^{-1} after the start of curing, which may be a result of the ε-caprolactam being in a free state, when it is no longer bonded to the compatibilizer. The peak at 1730 cm^{-1} in the cured films is an ester C=O that clearly originates from the polyol.

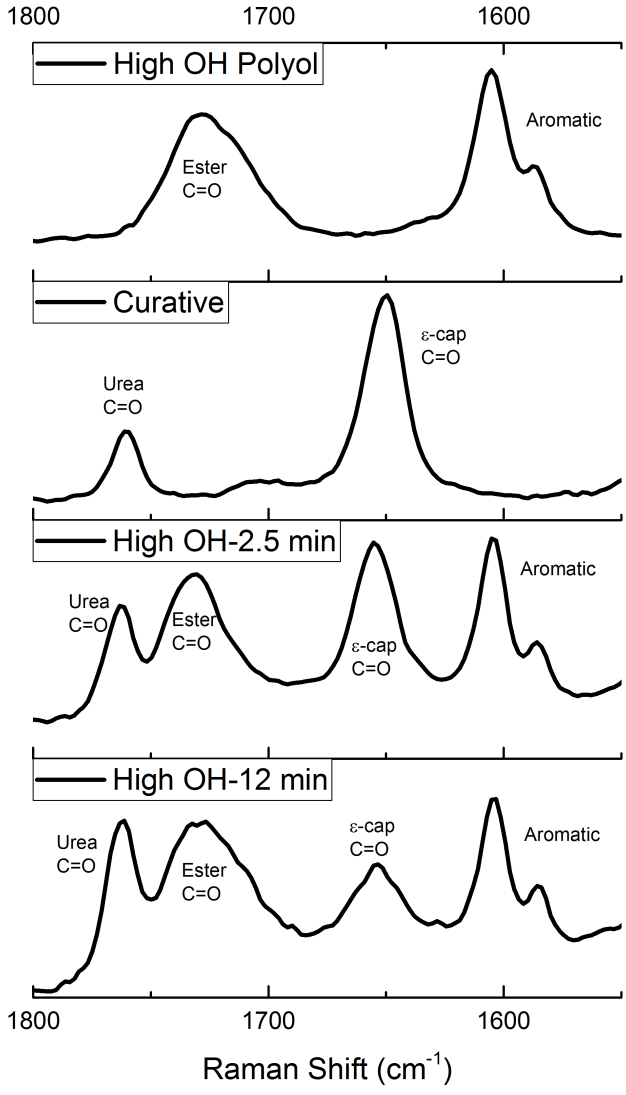

Figure 6-1. Raman spectra of the various carbonyl peaks found in reactants (upper two spectra) and PU product at two stages of cure.

A similar observation was made via comparative FTIR spectral analysis for the high OH polyurethane film and component polyol polyol and polyisocyanate in Figure 6-2. The OH and NH peaks in the high frequency region (Figures 6-2a-d) clearly coevolve with the carbonyl spectra in the double bond region (Figures 6-2e-h) during the cure, as is expected for polyurethanes. This observation is consistent for the low OH film and blend, and can be found in the supplemental information. The polyol represents the unreacted analogue to the polyurethane, and thus has only one C=O peak (Figure 6-2e), and one broad OH peak (Figure 6-2a). Prior to the cure, the compatibilizer has a large amide peak at 1700 cm^{-1} with shoulders at 1760 cm^{-1} and 1650 cm^{-1}, each of which has been labeled accordingly. Thus, under LRS, the urea peak dominates, while the amide peak appears as a small but broad bump at 1710 cm^{-1}-1700 cm^{-1}. During the cure, the amide peak shifts downward to 1690 cm^{-1} as it becomes urethane [7]. It is the largest peak in the 12-min cure high OH FTIR spectrum, with the ester C=O at 1725 cm^{-1} a close second.[23] For the blend and low OH, the ester C=O was observed to be the largest peak in all FTIR spectra for the blend and low OH. The considerable intensity of these two carbonyls may be the cause of the small shoulder at 3437 cm^{-1}, making it an overtone, and thus is labeled accordingly as 'overtone C=O' in Figures 6-2c and 6-2d.[7] The overtone is also at its largest for the high OH film.

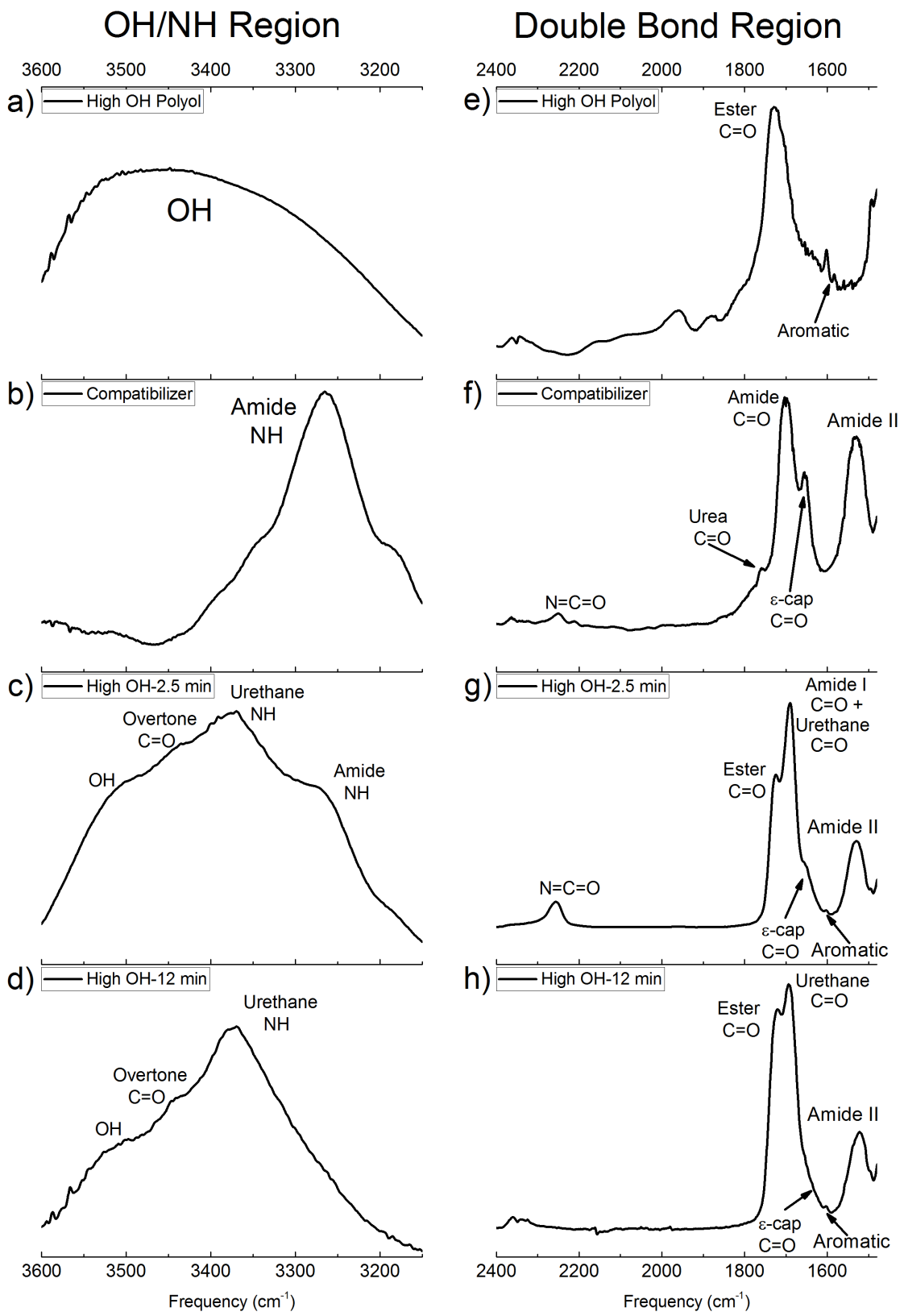

Figure 6-2. Stacked FTIR spectra of the reactants and reaction at two stages of the cure; a)-f): OH/NH region; e)-f): double bond region.

The urea C=O peak at 1760 cm^{-1} is largely absent in FTIR spectra, as are the aromatic peaks at 1600 cm^{-1} and 1584 cm^{-1}.[24] The high frequency of this carbonyl suggests it may stem from urea being part of a symmetric heterocylic compound.[24] Thus, this C=O is in a non-polar environment, and thereby illustrates the need for both vibrational spectroscopies in this study. The C=O peak at 1655 cm^{-1} also declines in the double bond region (Figures 6-2f-h); this behavior is observed in both LRS and FTIR and suggests that the ε-caprolactam blocking agent is the source of this C=O peak.[25] In the FTIR spectrum of the compatibilizer (Figure 6-2f), the C=O peak at 1700 cm^{-1} is labeled as an amide C=O, which is likely connected to the blocking agent. Once the ε-caprolactam blocked IPDI polyisocyanate compatibilizer is deblocked, this amide C=O becomes part of the N=C=O functionality.

B) Hydroxyl and amine region

Figure 6-2a shows that the polyol has a broad OH peak at 3520 cm^{-1}, which becomes diminished in the polyurethane spectrum at full cure. This suggests that there may be some OH groups that did not participate in urethane generation. It is possible that the polyol has secondary or tertiary OH groups that are unable to react with isocyanates due to steric hindrance. The NH peak at 3265 cm^{-1} stems from the compatibilizer in Figure 6-2b, which remains as a highly prominent band at 2.5 minutes of curing. The growth of the NH peak at 3370 cm^{-1} stems from generation of urethane crosslinks, while the blue-shift indicates weakening of hydrogen bonds. The high extinction coefficients upon the absorption frequencies of amine peaks renders them insensitive to conformational differences, and thus their deconvolution was not attempted in this study.[7]

6.3.2 Carbonyl deconvolution

The carbonyl moiety in polyurethanes can be highly complex due to numerous H-bond interactions and the different intramolecular environments that within the crosslinked polymer network.[7] Many chemical and mechanical properties stem from this moiety, and thus it is considerably emphasized in FTIR and LRS. The following Raman and FTIR spectra in this section starting at Figure 6-3 were conducted at high-resolution to identify potentially hidden peaks via spectral deconvolution. The high resolution Raman peaks show that the carbonyl peak at 1725 cm^{-1} has a small shoulder at its right side, which suggested there is more than one component within the observed band. The fitted Raman and FTIR spectra of the single component PUs are presented in Figure 6-3 with the calculated components fitting well with the experimental peaks in all cases. The intensity of the ε-caprolactam C=O band is nearly zero for the low OH PU (Figures 6-3a and 6-3b) while it retains significant intensity for the high OH PU (Figures 6-3c and 6-3d), thereby suggesting a nontrivial remnant of ε-caprolactam within the high OH PU film. The urethane band at 1690 cm^{-1} is much larger in both FTIR spectra and thus stemmed from the polyisocyanate. In the FTIR spectrum of the high OH PU film, the urethane C=O is the largest peak of the entire spectrum and thereby indicates greater urethane crosslink density; this was already corroborated in Chapter 5.

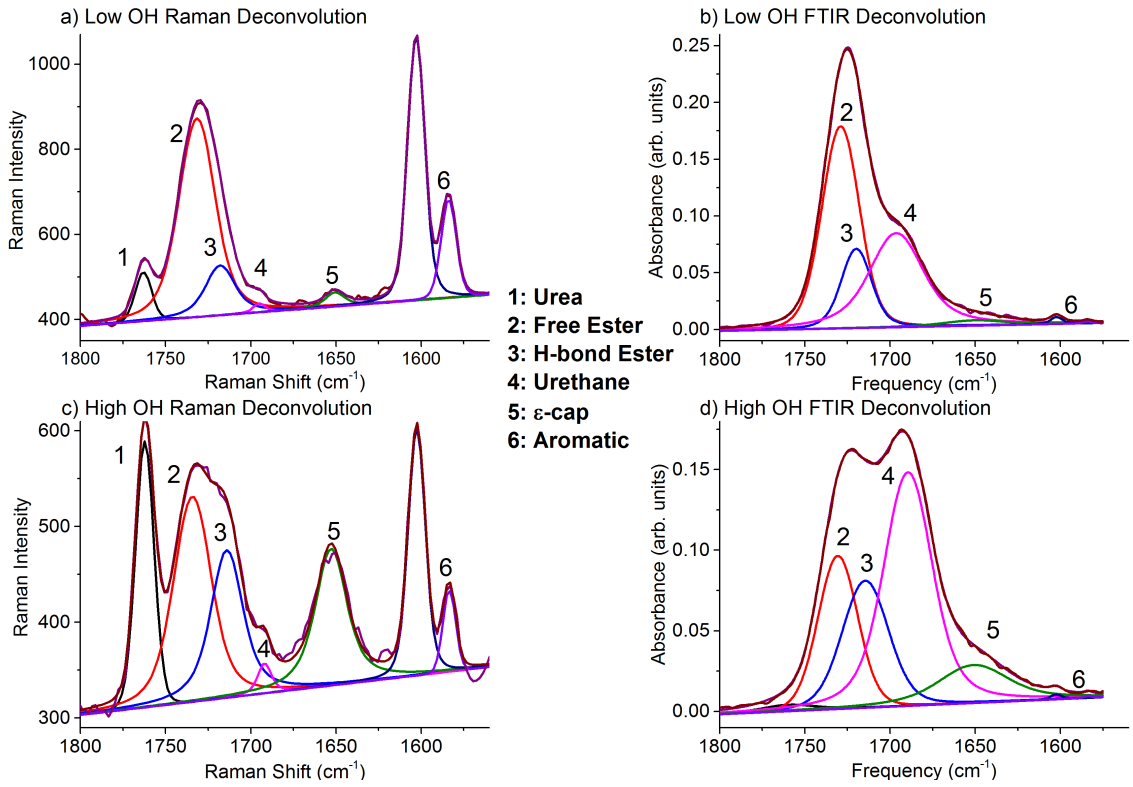

Figure 6-3. Fitted spectra of single component polyurethanes; a) Raman spectrum of low OH film; b) ATR-FTIR spectrum of low OH film; c) Raman spectrum of high OH film; d) ATR-FTIR spectrum of high OH film.

Deconvolution of the experimental C=O peaks in the reactants and single component (SC) films has yielded five C=O peaks in total. The previously hidden band is a H-bonded ester C=O, which was also found in deconvolution of the polyol spectra. This band was significantly larger for the high OH polyol and high OH polyurethane. As the two resins mainly differ by the hydroxyl content, it is assumed that the sources of H-bonding originate from the hydroxyl groups. The FWHM of this component showed little change before and after curing, indicating there may very well be a small number of hydroxyl groups remaining at full cure that participate in the hydrogen bonding. This finding may therefore rule out urethane-ester linkages, as previously discussed in section

6.3.1B about the NH and OH moieties. The characteristics of the five carbonyls are summarized in Table 6-1, with relevant references provided for each one.

Table 6-1. Assigned carbonyl peaks from LRS

Frequency (cm^{-1})	Relative Intensity (Raman)	Relative Intensity (IR)	Band Assignment	# Components	Reference
1760-1762	m	vw	ν(C=O) free urea	1	[23, 25]
1725-1730	m	vs	ν(C=O) ester (free & H-bond)	2	[26-27]
1690-1696	w	vs	ν(C=O) urethane	1	[7, 26-27]
1652-1655	vs	m	ν(C=O) ε-caprolactam	1	[24, 28]

vw = very weak; w = weak; m = medium; s = strong; vs = very strong

6.3.3 Correlating spectroscopy with morphology

Since FTIR is a macroscopic technique in this study, both polymeric phases of the blend were included in the corresponding spectra. However, when the blend was peeled off the substrate and measurements were made on the underside surface, the intensity of its urethane was quite close to the ester. This is illustrated in Figure 6-4, which features a transmission electron micrograph of the blend cross-section accompanied by FTIR spectra of the ester and urethane carbonyls. As also shown in Chapter 5, domains had accumulated at the tin substrate. This accumulation is what increased the urethane peak relative to the ester peak at the underside, and serves as evidence that the domains possess greater densities of urethane crosslinks in a manner akin to the high OH film.

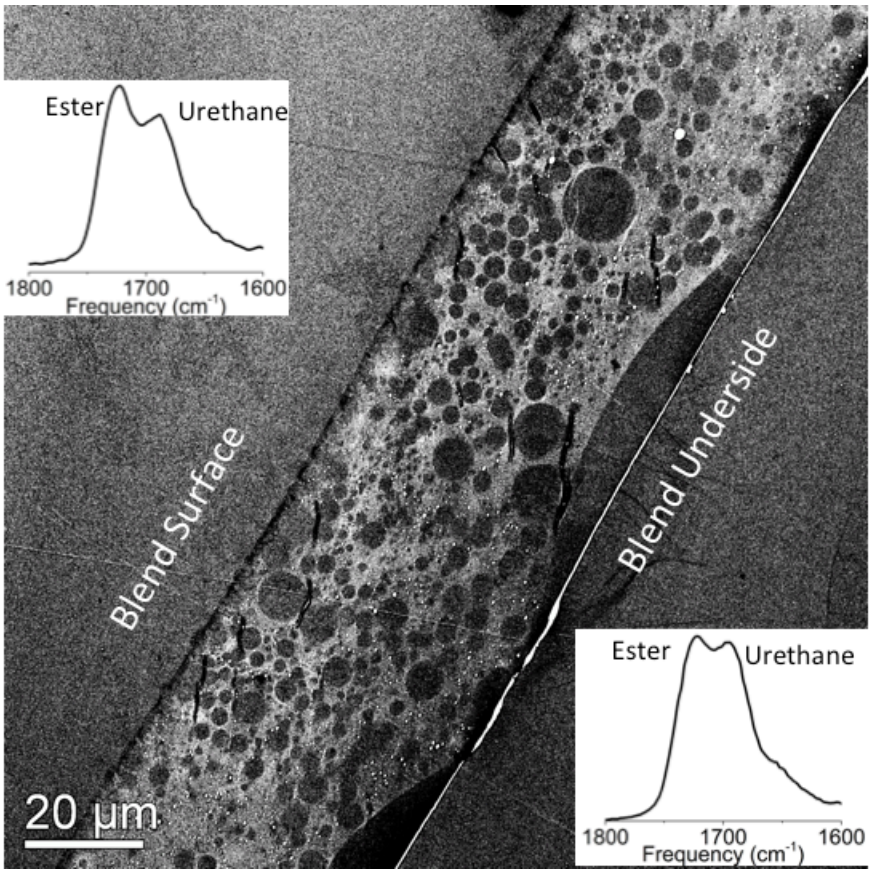

Figure 6-4. Transmission electron micrograph of the blend cross-section with FTIR measurements of ester and urethane C=O peaks. The left spectrum is measured from the surface; the right spectrum is measured from the underside.

Peak area ratios for the five C=O bands in each coating sample are listed in Table 6-2. The C=O peak areas are normalized with respect to the aromatic moiety peak at 1600 cm^{-1} because its intensity does not change during cure, and thus could be used as a standard for monitoring intensity changes of certain peaks. Stark differences could be discerned between the single component (SC) films, particularly for the urea, H-bonded ester, and ε-cap C=O bands. However, the peak area differences between the phases of the blend are significantly reduced in Table 6-2, which might be a sign of compatibilization, in which the polymer components mix with each other to a small degree. However, curve-fitting of the Raman spectra for the blend revealed the ester

C=O to be broader in the domain (not shown) and is thus consistent with the Raman spectra in Figure 6-4c. Note that among the three carbonyls associated with the compatibilizer (urea, urethane, and ε-cap), only the urethane peak area for the domains shows slight consistency with the high OH film in terms of differences in peak height; i.e, $A_{domain} > A_{matrix}$, $A_{highOH} > A_{lowOH}$. The other two curative carbonyls, which respond better to the Raman laser, do not exhibit this consistency. For example, the ε-cap peak area ratio is 6.14 for the low OH film and 57.50 for the high OH film; in the blend it is 15.20 for the polymer matrix and 7.31 for the domain.

Table 6-2. Raman peak area ratio of C=O (x/1600 cm^{-1} peak height × 100)

Frequency	Name of carbonyl	Low OH PU	High OH PU	Matrix	Domain
1650-1655	ε-cap	6.14	57.50	15.20	7.31
1690-1700	urethane	3.19	15.03	3.39	5.83
1710-1720	H-bond ester	23.5	64.6	24.5	43.2
1725-1735	free ester	58.6	74.0	81.4	52.2
1760-1762	urea	17.7	97.3	67.7	34.9

The inconsistencies in Table 6-2 may in part be explained by the different quantities of compatibilizer used to generate the films. For the SC films, less compatibilizer was used to generate the low OH film because the low OH polyol had fewer hydroxyl groups to react with isocyanates. Thus, in referring back to Table 5-1 for raw material weights of compatibilizer, $W_{High\ OH}/W_{Low\ OH} = 2.50$. However, the ratios of peak area ratios for each C=O from the curative are significantly greater. For urea: $A_{High\ OH}/A_{Low`\ OH} = 5.6$; for urethane: $A_{High\ OH}/A_{Low\ OH} = 4.8$; for ε-cap: $A_{High\ OH}/A_{Low\ OH} = 9.4$. According to a recent textbook by Smith and Dent, the relative intensities within a Raman spectrum are proportional to the concentration of the given species, the laser

power, and the Raman scattering cross-section; determining the scattering cross-section is very difficult, which necessitates calculations of peak ratios as used in this study.[30] Raman laser power was set to 100% in all spectral acquisitions. Thus, the discrepancies between the material weights and peak intensities may in part be explained by the scattering cross-section. For the ε-cap C=O peak, the outgassing of ε-caprolactam may have lowered its intensity even further.

The greater amount of curative that was used for the high OH film implies there was more ε-caprolactam to be liberated as a volatile solvent within the film. The higher concentration of volatiles within the film could leave markers within the film bulk such as holes within thin cross-sections prepared for TEM. The magnification for Figure 6-4 is too low to observe such holes, but they are readily observable at higher magnification in Figure 6-5. These holes may be trapped gas bubbles of ε-caprolactam, as it is a known emitted volatile from films generated from blocked isocyanates.[19] The TEM image of the low OH film (6-5a) has far fewer holes than the high OH film (6-5b), which could be related to the observation of a smaller ε-cap C=O peak in Figure 6-3 and Table 6-2. Note that the small dark particles in each image of Figure 6-5 are likely to be silica nanoparticles according to measurements by energy dispersive x-ray spectroscopy; they probably originate from the flow aid.

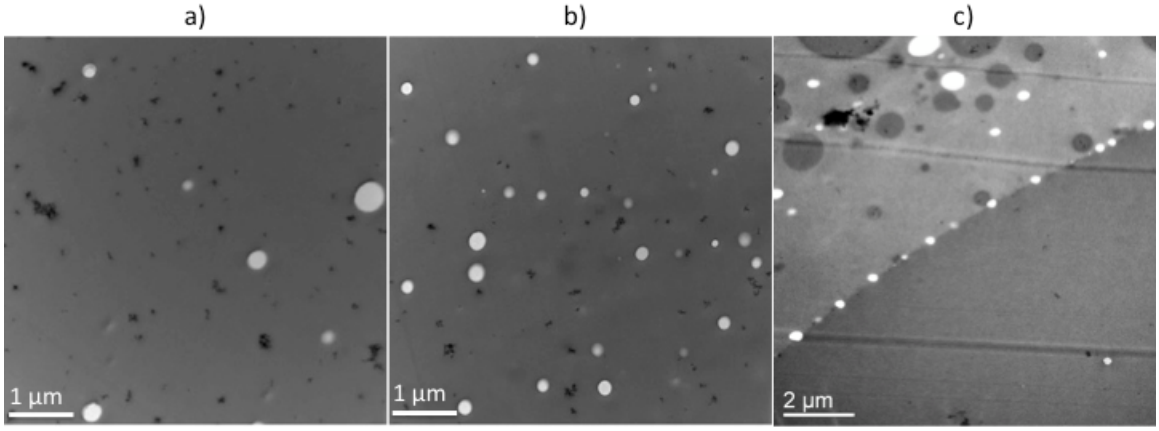

Figure 6-5. TEM images of cross-sectioned clear films at full cure; a) low OH film; b) high OH film; c) blend.

The number of holes found in the blend is also comparable to the number observed for the high OH film. The greater number of holes present the blend could again be attributed to the large quantity of curative in the formulation, as seen in Table 1. However, in the blend all of the holes are found in the continuous polymer matrix. The micrograph in Figure 6-5c shows a row of small holes residing at the boundary of a very large domain. Other micrographs of the blend consistently show holes to be located only in the matrix. The ε-caprolactam C=O peak area of the domain is about half that of the matrix. With analysis from ImageJ, and normalization with respect to the appropriate values from the low OH film, Table 6-3 shows good agreement between the ε-caprolactam C=O peak area and the number of holes, with exception of the data acquired for the domains. The breakdown of the correlation between ε-caprolactam C=O peak area and hole density for the domains could thus indicate their resistance to infiltration of ε-caprolactam, as was observed with styrene monomer in Chapter 5. According to Gite et al, the degree of resistance to solvent absorption is based on the crosslink density,[23]

where steric effects from the urethane crosslinks prevent small molecules from occupying otherwise free volumes.

Table 6-3. Relationship between ε-cap C=O peak area and hole density normalized to low OH film for appropriate column

Sample	ε-cap C=O ($A_x/A_{\text{Low OH}}$)	Hole Density ($\rho_x / \rho_{\text{Low OH}}$)
Low OH	1	1
High OH	9.4	12.3
Blend (matrix)	2.5	2.4
Blend (domain)	1.2	0

It is also evident from Table 6-2 the urea peak area ratios from the phases in the blend are not consistent with the urea peaks from the SC films. The ratio for the domain is nearly half that of the matrix. This discrepancy is not evident for the urethane peaks in Table 6-2 and in the FTIR spectra in Figure 6-4. The smaller urea and ε-cap C=O peak area ratios for the domains and the holes being sequestered into the matrix (Figure 6-5c) could thereby indicate a mechanism of exclusion by the domains. There is no diffusion gradient in the SC films like that of the blend. Hence, compatibilizer and deblocked ε-caprolactam molecules are trapped *in situ* within the high OH film, but are driven into the matrix from the domains within the blend.

6.3.4. Caprolactam variations with respect to cure time and cure temperature

The ε-caprolactam concentration for the single component films and both phases of the blend are plotted as peak height ratios Figure 6-6. Peak heights from raw Raman spectra were used instead of peak areas for convenience and to exclude noise from very small ε-caprolactam peaks in later-cure samples. ε-caprolactam peak heights were divided by the aromatic peak at 1600 cm^{-1} for normalization.

In Figure 6-6, the curve for the high OH SC film maintains the highest magnitude throughout the cure, and does not change significantly from 9 minutes to 12 minutes. This flat-lining may suggest that the film had crosslinked to the point of trapping the remaining ε-caprolactam before it could fully evaporate. At 6 minutes, the low OH curve also flatlines at a very small but nonzero value. For the blend, the peak height measured by LRS was consistently lower within the domains than in the polymer matrix, which again does not correspond to the results from the single component counterparts.

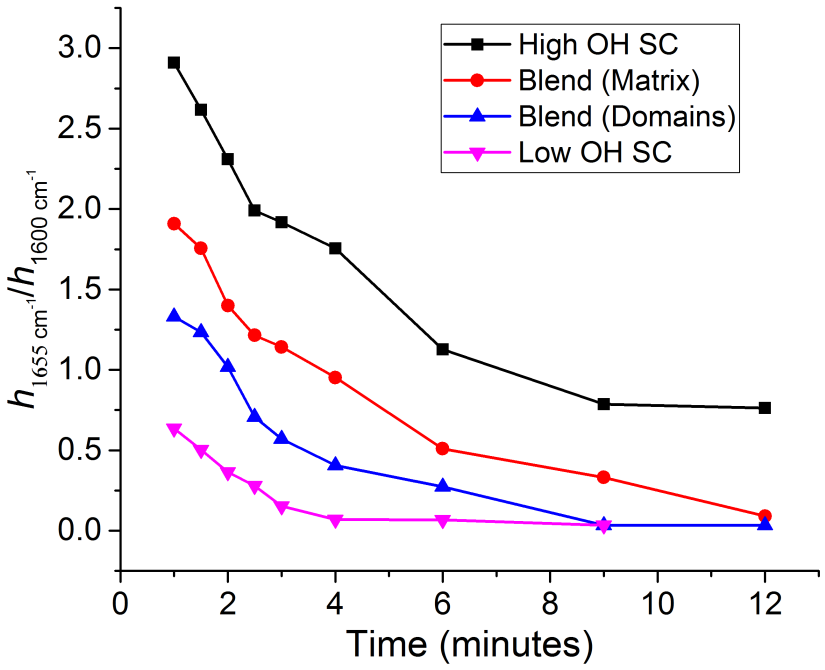

Figure 6-6. Raman peak intensity evolution for the ε-caprolactam vibration at 1655 cm^{-1} as a function of increasing cure time at 204 °C. Intensities are normalized with respect to the aromatic moiety at 1600 cm^{-1}.

Even at full cure, the ratio in the matrix is about thrice the ratio in the domains (0.091 and .033, respectively). Given the volatility and small size of the ε-caprolactam molecules, this finding lends further credence to the existence of a diffusion gradient between the phases within the blend. The gradient drives initial diffusion out of the domains before

resistance rises to significant levels. This drive does not exist in the high OH SC film, hence its high ε-caprolactam content at full cure.

6.3.5. Resistance to styrene solvent as an experimental model for resistance to caprolactam

In Chapters 4 and 5, the domains were identified by their response to the exposure of styrene monomer. Styrene exposure occurred as a function of cross-section sample preparation within a polyester embedding resin, which uses styrene as a crosslinker as the resin cures.[31] The polymer matrix was heavily contaminated with styrene monomer, while the domains showed little to no contamination. After embedding the SC films, only the low OH film was contaminated, while the high OH film remained unaffected. Since the domains and the high OH SC film were not contaminated, this led to the conclusion that the domains consisted of the high OH polyurethane.

This protocol of selectively staining the blended film with styrene could thus be applied toward quenched systems as a means of roughly monitoring changes in crosslink density when the coatings are cured at 204 ˚C. The concentration of styrene was measured by calculating the ratio of the conjugated alkene LRS peak at 1630 cm^{-1} over the aromatic peak at 1600 cm^{-1}. Chemical maps revealed concentration gradients within a given domain, while no such gradients were found in the polymer matrix. This suggests that domains vary considerably in their crosslink density. This necessitates plotting of peak heights with error bars. Figure 6-7 plots the concentration of styrene in the center of domains ≥ 100 μm in diameter (black curve). The center of a domain is typical where styrene concentrations are at its lowest. The error bars are the standard deviations of the peak heights from a set of 10 peak heights for each sample.

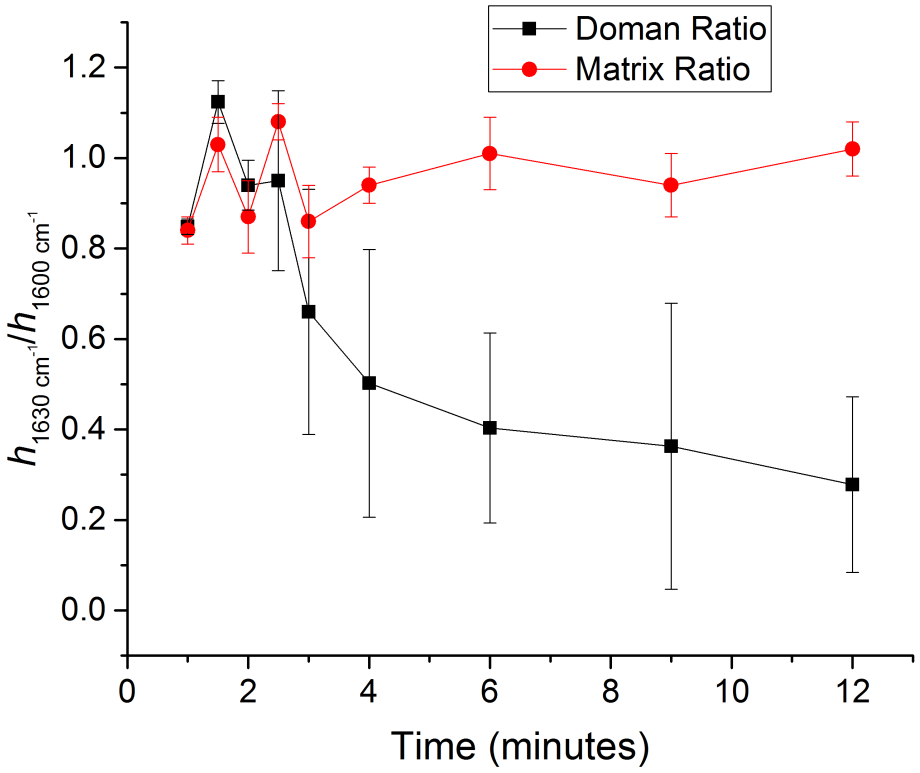

Figure 6-7. Raman peak height ratios in both phases of the blend for conjugated alkene vs aromatic styrene as a function of cure time.

The curves follow almost identical paths until they diverge at 2.5 minutes, when the error bars for the domain curve drastically increase, indicating that there was considerable variation in styrene infiltration among the domains; in some instances, there still was no difference in concentration between domain and matrix. Long error bars are a feature of the domain curve up to full cure, but the averages do indicate a downward trend suggestive of exponential decay, which thus indicates decreasing styrene absorption via increasing crosslink density.[23] In contrast, the curve for the matrix is roughly constant for the whole cure. Note that the Raman spectra used to generate Figure 6-7 were acquired about one week after the cross-sections were prepared. Subsequent analysis several months later showed significant decreases of peak intensities for samples cured at 2.5 minutes and before. No such decreases were observed for samples cured at 3 minutes

and later. It was at 3 minutes that differential scanning calorimetry had revealed the emergence of the second T_g, which may be a threshold where the crosslink density is high enough to trap volatile styrene monomer indefinitely. Domains have also been observed to grow in diameter as the cure progresses, which may lessen the concentration of styrene in the center. This growth will be discussed in greater detail in Chapter 7.

The film behaves as a dynamic system at an elevated temperature, and hence the deblocked caprolactam evaporates during the cure. The difference in peak intensities between the phases for the caprolactam C=O could be explained in terms of reduced free volume for the molecule to occupy, but small molecules and macromoleucles alike have elevated segmental mobility and diffusivity at high temperatures. In contrast, during the embedding process, styrene is introduced into a relatively static system under STP. Such stasis means the number of urethane crosslinks has been finalized for that sample. Its response to a solvent is thus a function of the crosslink density, and could be observed at the microscopic level.

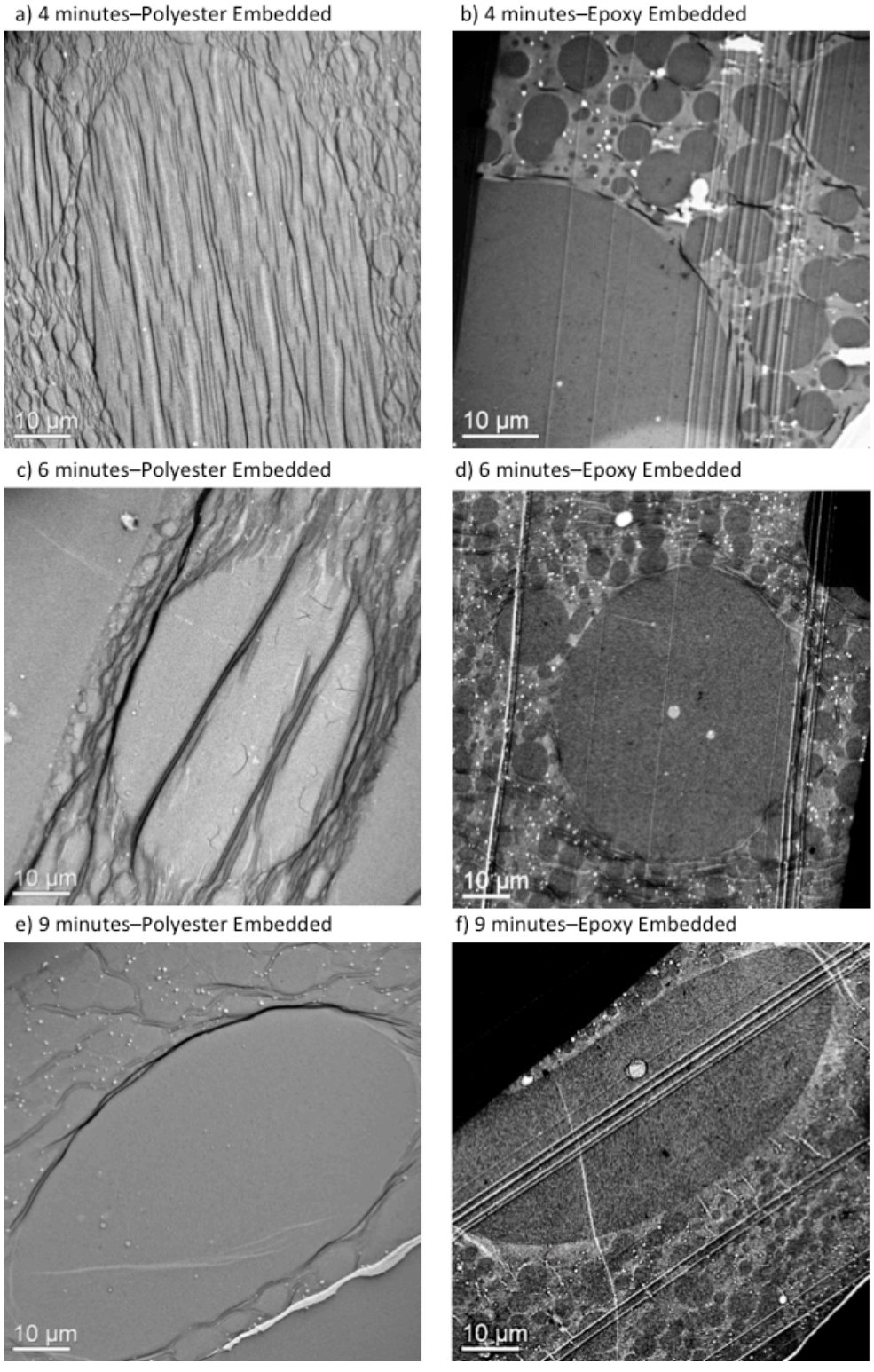

Figure 6-8. Comparison of cross-sections between different embedding resins as a function of cure time; a)-b) 4 minutes; c)-d) 6 minutes; e)-f) 9 minutes.

To illustrate the trend depicted in Figure 6-7, a series of TEM images of cross-sections are presented in Figure 6-8. In the left column are blended resin film samples embedded in polyester, while in the right are those same samples embedded in fast-cure epoxy. Embedment in epoxy leaves no contaminants in the coatings, hence no introduction of a plasticizer like styrene. Knife lines from the sectioning process are readily observed on the surfaces of the epoxy-embedded cross-sections, which are indicative of a stiff specimen;[32] no such lines are observed in the polyester-embedded cross-sections due to the plasticization. All samples were stained with heavy metals for contrast via TEM analysis, but it is clear that the styrene interferes with the contrast between the phases. The matrix and domains in the samples embedded in polyester appear to be wrinkled due to the incorporation of the plasticizer. The formation of wrinkles becomes reduced with respect to increasing cure time, but it still significantly affects the 9-minute samples, especially for the matrix. The overall trend is the decreasing damage to the morphology by the styrene as the cure progresses. Note that the micrograph in Figure 6-4 is of a fully cured sample embedded in polyester. When fully cured, the polymer film is able to resist plasticization by the styrene such that heavy metal staining adds contrast between the phases. This is the one sample that provided adequate contrast between the phases for selective staining with styrene for enhanced Raman spectroscopy, and with heavy metals for TEM. In quenched samples, as demonstrated in Figure 6-8, different embedding resins produce different morphologies. These results also demonstrate that choice of embedding resin for a sample must be carefully considered before cross sectioning via microtome.

6.4 Conclusion

This study has been a vibrational spectroscopic reaction monitoring of acrylic polyurethane coatings without pigments. The complementary nature of FTIR and LRS has been helpful for understanding the chemistry of the polymers at different stages of the crosslinking reaction from their intrinsic characteristics.

High resolution LRS and macroscopic FTIR spectra were acquired for the acrylic polyols, polyisocyanate curative, and the polyurethanes. Four C=O peaks were initially found. Three of the peaks originated from the curative: the ε-caprolactam C=O peak at 1655 cm^{-1}, free carbonyl peak at 1760 cm^{-1} (sensitive to Raman), and the urethane peak at 1692 cm^{-1} (sensitive to FTIR). Spectral curve fitting revealed the ester carbonyl peak to be comprised of two overlapping bands: a tall free band at 1730 cm^{-1} and a shorter H-bonded band at 1715 cm^{-1}. The ensuing curve fitting of the high-resolution Raman and FTIR spectra of the polyurethanes showed similar results for this peak, bringing the total number of observed carbonyls to five. The 1715 cm^{-1} component turned out to be broader and more intense in the high OH polyol, high OH polyurethane, and in the domains of the polyurethane blend. The likely source of hydrogen bonding for the ester C=O in the polyols is a small number of unreacted hydroxyl groups.

The urethane C=O was also larger in the high OH polyurethane, and is direct evidence of its higher crosslink density. In the blend, the intensity of this peak depended on where it was measured. At the surface, the intensity was somewhere between the high and low OH polyurethanes. At the substrate-film interface, the intensity was closer to the high OH polyurethane due to the accumulation of large domains adhering to the substrate.

TEM analysis showed large numbers of holes in the film cross-sections. These holes are suggestive of trapped volatile fluids of deblocked ε-caprolactam, which is a known emission during the cure, and acts as a solvent within the curing film. The number of holes appears to be correlated with the ε-cap peak intensity, as both values are highest for the high OH film. In the blend, the holes are located almost exclusively in the matrix, and have been observed at the boundary of a large domain. This indicates that domains resist infiltration by caprolactam molecules. With caprolactam behaving as a solvent, the domains appear to resist its infiltration in a manner similar to what has been previously observed with styrene monomer. The higher crosslink density in the domains restricts the volume allowed for small molecules to interact with the polymer chain.

Changes in solvent resistance were observed in quenched samples embedded in polyester, which introduced styrene as an external solvent into a static coating system. Styrene proceeded to exhibit decreasing degrees of penetration into the domains for longer cure times according to LRS. TEM analysis revealed plasticization of both phases that decreased in severity for longer cure times. In comparison with samples embedded in epoxy, it was evident that the interaction with styrene eliminated the enhanced contrast from heavy metal staining. Even without the enhanced contrast, it was evident at 6 minutes that the domains began to exhibit less plasticization than the matrix. At full cure, there was no plasticization from the styrene, and the sample responded well to selective staining with heavy metals. The phenomena observed at spectroscopic and microscopic levels could thus be explained by decreasing absorption of solvent via increasing crosslink density.

We thus have two instances of solvent resistance by the domains according to TEM:

- Almost all bubbles of caprolactam are located in the matrix, with a few observed to be emerging out of a domain boundary.
- Decreasing plasticization by introduced styrene in polyester-embedded samples as the cure time increases.

We also have two instances of solvent resistance by the domains according to LRS:

- The caprolactam C=O is consistently lower in the high OH domains throughout the cure, which does not match the results for the single component films.
- The enlarging concentration gradient for styrene between the phases as a function of cure time.

The behavior observed by spectroscopy and microscopy is thus explained as a result of the decreasing solvent absorption due to increasing crosslink density.

6.5 References

1. Misev, T. A., Powder Coatings. In *Surface Coatings*, 2nd ed.; Paul, S., Ed. John Wiley & Sons: Chichester, England, 1996; pp 788-849
2. Wicks, D. A.; Jr., Z. W. W., Blocked isocyanates III. Part B: Uses and applications of blocked isocyanates. *Progress in Organic Coatings* **2001,** *41*, 1-83.
3. Lee, S. S.; Koo, J. H.; Lee, S. S.; Chai, S. G.; Lim, J. C., Gloss reduction in low temperature curable hybrid powder coatings. *Progress in Organic Coatings* **2003,** *46* (4), 266-272.
4. Hare, C. H., *Protective Coatings: Fundamentals of Chemistry and Composition*. Technology Publishing Company: Pittsburgh, Pennsylvania, 1994; p 514.
5. Xue, L.; Zhang, J.; Han, Y., Phase separation induced ordered patterns in thin polymer blend films. *Progress in Polymer Science* **2012,** *37*, 564–594.
6. Lee, H. S.; Wang, Y. K.; Hsu, S. L., Spectroscopic analysis of phase separation behavior of model polyurethanes. *Macromolecules* **1987,** *20* (9), 2089-2095.

7. Yen, F.-S.; Hong, J.-L., Hydrogen-Bond Interactions between Ester and Urethane Linkages in Small Model Compounds and Polyurethanes. *Macromolecules* **1997,** *30* (25), 7927-7938.
8. Jr., Z. W. W.; Jones, F. N.; Pappas, S. P.; Wicks, D. A., *Organic Coatings: Science and Technology*. 3rd ed.; Wiley-Interscience: Hoboken, New Jersey, 2007; p 746.
9. Funke, W., New Aspects of Paint Films with Inhomogeneous Structures. *Progress in Organic Coatings* **1974,** *2* (4), 289-313.
10. Funke, W.; Murase, H., Uber die Bildung Mehrphasiger Filme Aus Pulverförmigen polymer-mischungen. In *15th FATIPEC Congress*, 1980; Vol. 2, pp 387-409.
11. Hansen, C. M., *Hansen Solubility Parameters: A User's Handbook*. 2nd ed.; CRC Press: Baca Raton, Florida, 2007.
12. Verkholantsev, V. V.; Flavian, M., Epoxy/Thermoplastic Heterophase and self-stratifying coatings. *Modern Paint and Coatings* **1995,** *85* (11), 100-106.
13. Verkholantsev, V. V., Heterophase and self-stratifying polymer coatings. *Progress in Organic Coatings* **1995,** *26*, 31-52.
14. Verkholantsev, V. V., Self-stratifying coatings for industrial applications. *Pigment and Resin Technology* **2003,** *32* (5), 300-306.
15. Langer, E.; Kuczyńska, H.; Kaminska-Tarnawska, E.; Łukaszczyk, J., Self-stratifying coatings containing barrier and active anticorrosive pigments. *Progress in Organic Coatings* **2011,** *71*, 162-166.
16. Abbasian, A.; Ghaffarian, S. R.; Mohammadi, N., Investigation of factors affecting stratification phenomenon in epoxy-acrylic coatings. *Iranian Polymer Journal* **2004**, 61-68.
17. Kuczyńska, H.; Langer, E.; Kamińska-Tarnawska, E.; Kulikov, D. A.; Indeikin, E. A., Study of self-stratifying compositions. *Journal of Coatings Technology and Research* **2009,** *6* (3), 345-352.
18. Baghdachi, J.; Perez, H.; Talapatcharoenkit, P.; Wang, B., Design and development of self-stratifying systems as sustainable coatings. *Progress in Organic Coatings* **2015,** *78*, 464–473.
19. Wicks, D. A.; Jr., Z. W. W., Blocked Isocyanates III: Part A. Mechanisms and chemistry. *Progress in Organic Coatings* **1999,** *36*, 148-172.
20. Fridrihsone-Girone, A.; Stirna, U.; Misāne, M.; Lazdiņa, B.; Deme, L., Spray-applied 100% volatile organic compounds free two component polyurethane coatings based on rapeseed oil polyols. *Progress in Organic Coatings* **2016,** *94*, 90-97.
21. Mahn, E. J. Low reflectance chemical agent resistant coating compositions. 20150259541 A1, January 23, 2015, 2015.
22. Chalmers, J. M.; Griffiths, P. R., *Handbook of Vibrational Spectroscopy*. Wiley: 2002; p 4000.
23. Gite, V. V.; Mahulikar, P. P.; Hundiwale, D. G., Preparation and properties of polyurethane coatings based on acrylic polyols and trimer of isophorone diisocyanate. *Progress in Organic Coatings* **2010,** *68*, 307-312.
24. Socrates, G., *Infrared and Raman Characteristic Group Frequencies: Tables and Charts*. 3rd ed.; John Wiley and Sons: Chichester, England, 2004.

25. Reardon, T. J.; Barker, R. H., Pyrolysis and combustion of nylon 6. I. Effect of selected brominated flame retardants. *Journal of Applied Polymer Science* **1974,** *18* (7), 1903-1917.
26. Young, C. N. Surface and Interfacial Study of Chemical Degradation in Polymer Composites and Coatings. Doctoral Dissertation, State University of New York at Stony Brook, Ann Arbor, 2013.
27. Keene, L. T.; Halada, G. P.; Clayton, C. R., Failure of navy coating systems 1: chemical depth profiling of artificially and naturally weathered high-solids aliphatic poly(ester-urethane) military coating systems. *Progress in Organic Coatings* **2005,** *52* (3), 173-186.
28. Keene, L. T.; Vasquez, M. J.; Clayton, C. R.; Halada, G. P., Failure of navy coating systems 2: failure pathways of artificially weathered navy coating systems applied to chromate conversion coated AA2024-T3 substrates. *Progress in Organic Coatings* **2005,** *52* (3), 187-195.
29. Draye, A. C.; Persenaire, O.; Brožek, J.; Roda, J.; Košek, T.; Dubois, P., Thermogravimetric analysis of poly(ε-caprolactam) and poly[(ε-caprolactam)-co-(ε-caprolactone)] polymers. *Polymer* **2001,** *42* (20), 8325-8332.
30. Smith, E.; Dent, G., *Modern Raman Spectroscopy: A Practical Approach*. John Wiley & Sons: Chichester, England, 2005; p 210.
31. Koenig, J. L.; Shih, P. T. K., Structure of Unsaturated Polyester Resins Crosslinked with Styrene as Studied by Raman Spectroscopy. *Journal of Polymer Science Part A-2: Polymer Physics* **1972,** *10* (4), 721-740.
32. Scheirs, J., *Compositional and Failure Analysis of Polymers: A Practical Approach*. John Wiley & Sons: Chichester, England, 2000; p 766.

Chapter Seven

How Droplet Domains Evolve

7.1 Introduction.

Powder coatings are an increasingly popular technology due to the absence of solvent in their application. That leaves the binder as the majority component in coating formulation (often ~75%). The binder in powder coatings typically consists of one polymeric resin; the exception is the binder analyzed in this study, which consists of two resins rendered immiscible due to large differences from their Hansen Solubility Parameters (HSP).[1] Both resins are acrylic polyurethanes, which have a long history in the powder coatings industry and continue to grow in importance because of the sheer diversity in applications.[2] Polyurethane powder coatings are thermosets and are the products of an unblocked isocyanate curative reacting with an OH-functionalized polynucleophile. They are highly durable in outdoor settings, and are typically utilized in high-gloss applications. The 2-component binder would expand the application of polyurethane powder coatings to low-reflectance settings, where matte gloss is desired.[3]

Previously, we identified both resins in the analyzed 2-component binder by Raman imaging of samples selectively stained with styrene vapor. Raman peaks unique to styrene were used as spectroscopic markers for the components; this marker peak was largely absent in the dispersed phase due to its crosslink density being greater than for the continuous phase, which is correlated with solvent resistance.[4] With the components identified, we proceeded with FTIR and Raman analysis of the reactants, single component resins, and blended resins in the double bond region (2000 cm^{-1} – 1600 cm^{-1}).

The ensuing deconvoluted spectra revealed a total of five carbonyl peaks, whose characteristics are specific to the resin of interest.

The application of incompatible polymeric resins in coating systems was first investigated by Funke, whose model was mostly based on interfacial energy between phases as the driving force for phase separation; this phenomenon is fundamentally rooted in the reduction of free energy of mixing during heating above the melting temperature.[5] Further work by Verkholantsev focused on changing surface tensions induced by solvent evaporation as a driving force for self-stratifying coatings (e.g., Marangoni effect).[6] Funke and Murase later demonstrated layer-stratification in epoxy-acrylic powder coatings; the phase separation for these materials was induced by polymer incompatibility and the affinity of the polar groups for the lower layer being oriented toward the substrate thereby generating a surface energy gradient.[7] Generally, self-stratified coatings receive greater attention in the literature than on so-called heterophase coatings which exhibit the dispersed droplet morphology.[6, 8-13] This morphology is commonly seen in polymer blends, and has been observed for the studied coatings under optical microscopy for the surface and cross-sections (see Chapter 5).

Blending polymers combines the properties of their components, and creates new properties unique only to that blend. The phase structure is a common influence on these unique properties, and is an outcome of the complex relationships of inner and outer parameters. Inner parameters include chemical structure and rheological properties of the pure components or blend composition; outer parameters include applied flow field and temperature. Adding a compatibilizer to the blend becomes another inner parameter that

serves to increase the adhesion between the components and thereby improve the mechanical properties.[14]

It has been established in Chapter 4 that the blend morphology contains a dispersed phase of the high hydroxyl content polyurethane. The phase separation gives rise to polydisperse domains that roughen the surface for diffuse and multiple scattering of light. This is the final study on the binder without added pigments. It investigates the underlying causes of the changing surface roughness (and by extension, optical properties) by correlating roughness measurements with spectroscopic intensities, rheology measurements taken near the cure temperature (T_c = 204 ˚C), and transmission electron microscopy (TEM) of cross-sections. As seen in Chapters Four-Six, most domains are encapsulated by the matrix, which leaves the cross-section as the optimal means of observing them. Domains with diameters ≥ 50 μm were easily observed under optical microscopy, but TEM enables facile observation of domains down into the submicron range.

Other studies of polymer blends include examining the surface morphology by scanning electron microscopy (SEM) with respect to their weight fractions,[15] or by location within the extruder . TEM was chosen because it is known to work very well with blends stained with heavy metals.[16] Samples were measured at full cure (12 minutes) and when quenched at different stages of the cure (1, 1.5, 2, 2.5, 3, 4, 6, 9, minutes). The early cure has smaller intervals because powder coatings are known to experience rapid changes in their surface morphology in the early stages of the cure due to sintering of powder particles.[17]

7.2 Experiment

7.2.1 Laser scanning confocal microscopy (LSCM)

LSCM was used to obtain information on surface characteristics of the coatings. LSCM measurements were performed on an Olympus LEXT OLS4000 using the LEXT software package. Images were gathered using a laser source at 405 nm with 50x optics providing 1076x magnification of the coating surfaces. The LEXT software package allowed the stitching of four magnified images together to provide measurements over 483 μm x 485 μm surfaces. Images were taken every 0.06 μm along the z-axis and were compiled to create a 3D image of the coating surfaces. Surface roughness parameters, depth profiling and macro size domain measurements were performed using the LEXT software package.

7.2.2 Fourier transform infrared spectroscopy (FTIR)

ATR-FTIR spectra were recorded on a Thermo Scientific Nicolet™ iS50 FTIR Spectrometer with a Smart Performer™ ATR attachment and constant pressure tower. An MCT detector collected 64 scans of the sample. Data acquisition and analysis were performed using the Thermo Scientific OMNIC 9.2.86TM software package. Samples were analyzed using a diamond ATR crystal.

7.2.3 Raman spectroscopy

Raman spectra and maps were acquired using a Thermo Scientific Nicolet Almega™ dispersive spectrometer coupled to an Olympus microscope with 10X and 50X

objective lenses. The instrument uses a 785 nm laser with a 3.1 μm spot size, and OMNIC 7.3TM software package.

7.2.4 Gloss measurements

Gloss measurements were obtained for each film using a BYK Gardner micro-TRI-gloss-S meter. Powder coatings were applied to black & white T12G Metopac™ (Metal) panels purchase from the Leneta Company. The powder coatings were applied to a dry film thickness of 50 – 100 μm using standard powder coating spray equipment and cured in a convection oven for 12 minutes at 204 ˚C.

7.2.5 Differential scanning calorimetry (DSC)

DSC was used to determine the glass transition temperature (T_g) of the polymer resins, powder formulations and cured films. The T_g is the temperature at which a polymer transitions from a glassy state to a rubber state. DSC was performed using a TA Instruments Q20 DSC instrument equipped with the DSC Refrigerated Cooling System (RCS) and a purge gas of nitrogen set to 50 mL/min. Samples of approximately 1-2 mg were placed into TA Instrument Tzero™ Aluminum pans, and an empty Tzero™ aluminum pan was used as reference. Powder and free film samples were analyzed using a cyclic method including an initial run from 30 °C to 85 °C at 10 °C/min followed by two consecutive cycles from -30 °C to 220 °C at 10 °C/min. DSC experiments were used to monitor the changes of the glass transition temperature as a function of formulation and oven curing. The T_g for the samples was determined from data in the second ramp

cycle. Based on these data, glass transition temperatures were found using the TA Universal Analysis program.

7.2.6 Optical microscopy

OM measurements were performed with two microscopes. The first was an Olympus BX51 microscope that was equipped with an Olympus UC30 digital camera and used Olympus Stream Essentials 1.9.2 software. It was used to analyze coating surfaces.

A Meiji microscope equipped with a Nikon digital camera DXM1200 and Nikon ACT-1 software was used to analyze coating cross-sections.

7.2.7 Rheology

Constant temperature measurements were performed with an Anton Paar MCR 301 with disposable 25 mm plates possessing a test gap of 1 mm. The resins were mixed in with specialty waxes and clays to give curing times under constant temperature and constant shear. The temperature was 200 ˚C. Experiments lasted for 30 minutes with measurements taken every six seconds. The measuring profile had the amplitude gamma set to 1%, and angular frequency set to 10 s^{-1}.

7.2.8 Transmission electron microscopy (TEM)

TEM was utilized to provide domain identification and distribution throughout the bulk of the films. Microtome cross-section samples were prepared for TEM analysis

using a Leica EM UC7 Ultra-Microtome (Wetzlar, Germany) with a diamond sectioning blade; typical thicknesses were 80-100 nm. Two microscopes were used.

Initial TEM experiments were performed using a FEI Bio TwinG2 Transmission Electron Microscope. The TEM was equipped with an AMT XR-60 CCD digital camera system for image collection. Bright field imaging measurements were performed at an accelerating voltage of 80 keV.

The second microscope was a JEOL JEM-1400 LaB6 TEM. This was equipped with a Gatan CCD digital camera for image collection and a TEAMTM EDS Analysis System for TEM with an Octane Silicon Drift Detector for elemental analysis of pigmented films. Bright field imaging was performed at 80 keV.

To enhance contrast between polymer phases in TEM micrographs, heavy metal salts of uranyl acetate and lead citrate were used to stain both clear films and pigmented coatings. Coatings were immersed in 0.02 g/mL uranyl acetate in methanol for 10 min, followed by immersion in 0.003 g/mL aqueous lead citrate for 3 min. The heavy metals are effective electron shields that serve to darken the phases upon their acceptance by the appropriate material.

7.2.9 Coating preparation

The examined blends in the study were prepared in a manner similar to that presented by Mahn[18] except no pigments were added. This was performed through blending of a high and low hydroxyl (OH) group functionalized polymeric resins. All materials were utilized as acquired unless otherwise noted. The acrylic resins with high and low hydroxyl group functionality (20-400 OH) and Resiflow flow agent were

purchased from Estron Chemicals (Calvert City, KY). Benzoin was used as an additive to prevent orange peel, and was purchased from GCA Chemical Corporation. The compatibilizer was a blocked isocyanate ε-caprolactam blocked IPDI polyisocyanate curative and was purchased from Evonik Industries (Parsippany, NJ). Film formulations were prepared by weight and are shown in Table 5-1.

Raw materials were manually dry-blended, then melt mixed using a twin screw extruder. The extruded material was squeezed through chilled rollers and the cooled material was ground using a rotor mill. The ground powder particle size was further classified by using a 106 μm (140 mesh) sieve. Powder formulations from above were electrostatically applied to tin plated steel substrates to a dry film thickness of 50-100 μm using a standard gravity fed powder coating cup gun. Coatings were then cross-linked in a convection oven at 204 °C for 12 minutes to generate the thermoset films. The elevated temperatures are required for viscosity reduction for flow inducement to ensure even wetting of the substrate, and to liberate the ε-caprolactam blocking group to generate free isocyanate necessary for cross-linking. Fully cured coatings were cooled to room temperature prior to subsequent analysis. Other samples were quenched by liquid nitrogen at different cure times for eventual analysis of morphological development within the coatings. Samples were quenched at 1, 1.5, 2, 2.5, 3, 4, 6, and 9 minutes into the cure.

7.3 Results

7.3.1 OM and LSCM of polymer blend surface

In Figure 7-1, quenched samples show stark changes in surface morphologies at magnifications of 50X. Relatively faint domains can be observed 1 minute into the cure, and they increase to greater prominence as the cure progresses. The LCM images clearly show the increasing roughness of the surface, while domains are observed from the beginning of the cure in the optical micrographs. Only four samples are shown for brevity, but they have large differences in their surface roughness. The roughness is graphed in Figure 7-2, which plots gloss indices measured at 60° and 85° incident angles. The OM images for 2.5 minutes and 9 minutes appear to show domain coarsening, but the low optical magnification of these images does not make this obvious. The roughness reaches its maximum at 9 minutes, which is also reflected in the corresponding laser confocal micrograph in Figure 7-1.

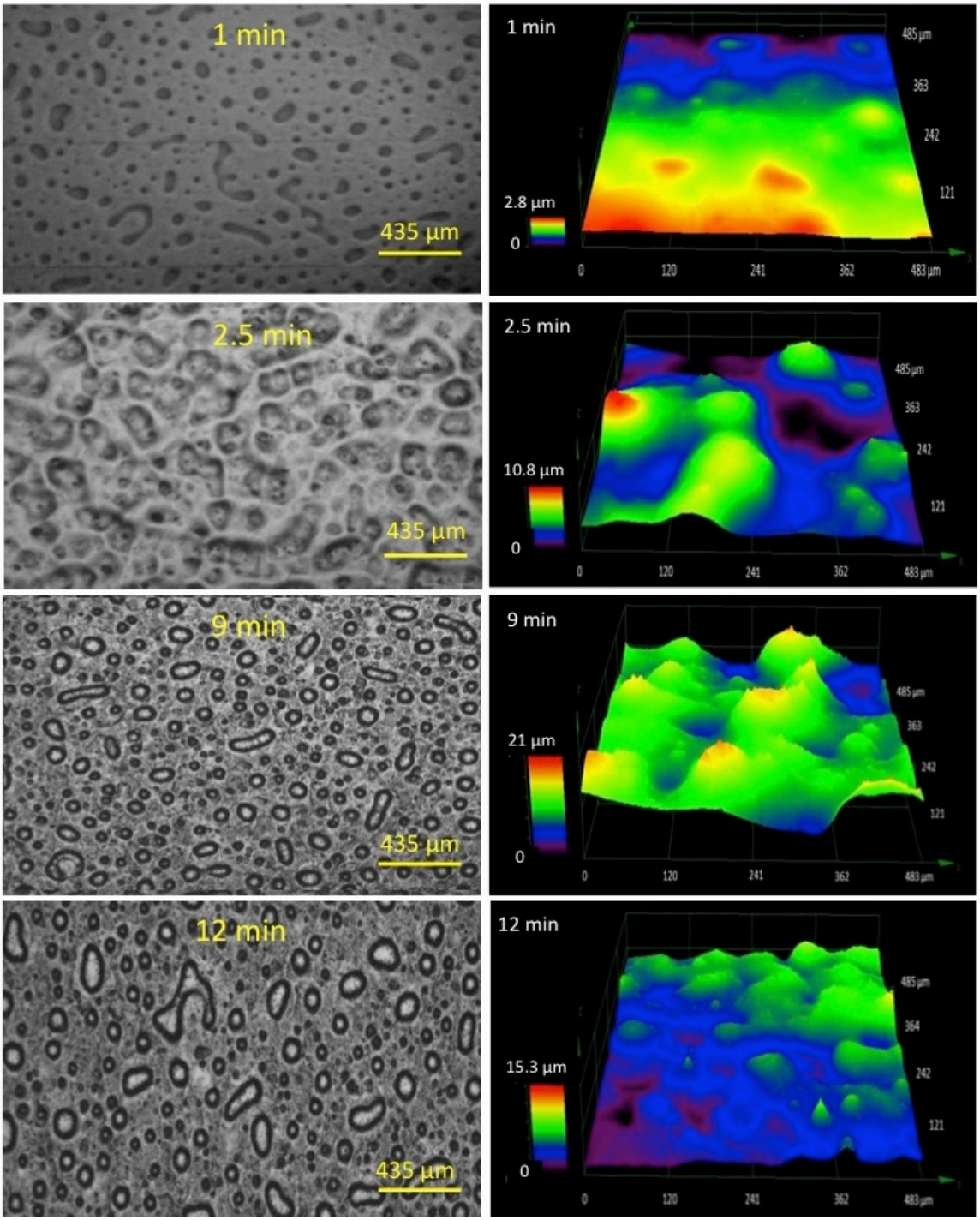

Figure 7-1. Optical micrographs (left) and laser confocal microscopy (right) of film surface showing development of domains and surface roughness.

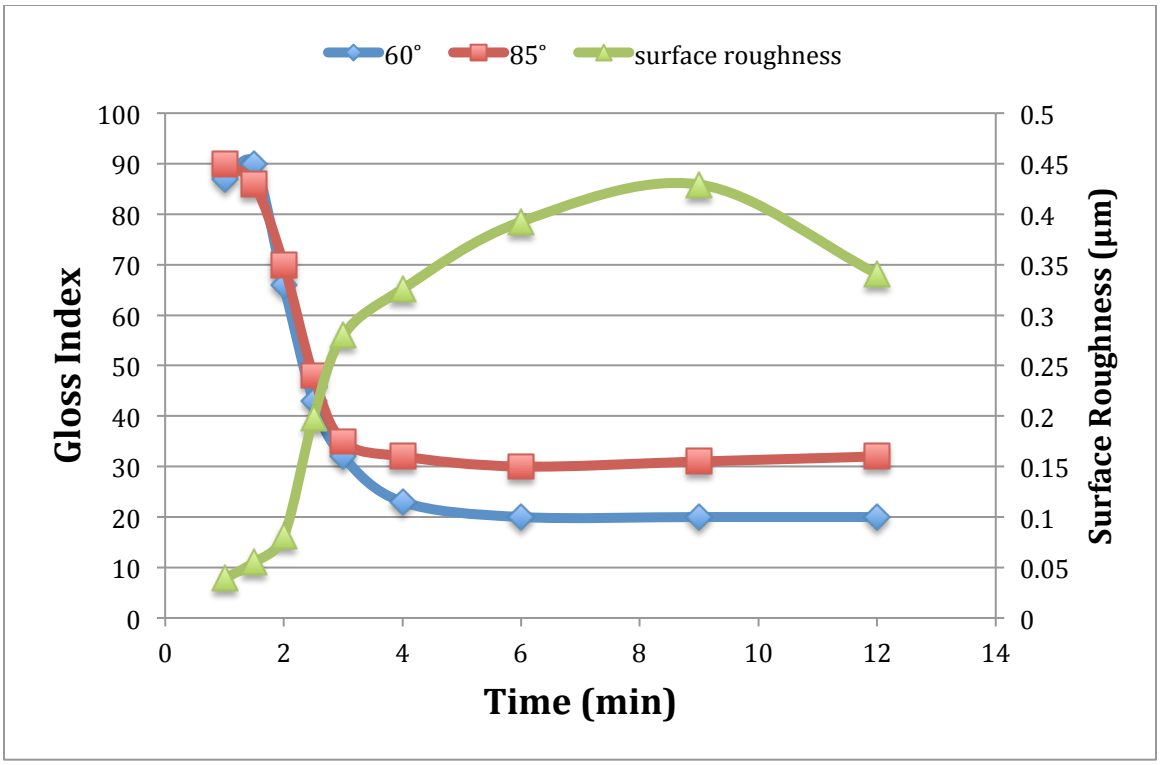

Figure 7-2. Inverse relationship observed for 60° and 85° gloss properties and mean surface roughness as a function of cure time.

7.3.2 DSC of quenched samples

The roughness has the greatest increase from 2 minutes to 3 minutes, which overlaps with the greatest declines in gloss. It is at 3 minutes where the 60° gloss plateaus and the roughness increases more slowly. This abrupt change in the development of roughness and gloss may mark a transition in the coating during the cure. This transition is corroborated by DSC measurements performed at NRL of the quenched films (Figure 7-3). There is also a marked decline in the roughness from 9 minutes (0.429 μm), where it has maximized, to 12 minutes (0.341 μm), where it has declined to a value comparable to 4 minutes (0.326 μm). This finding will be further elaborated in the discussion concerning transmission electron micrographs.

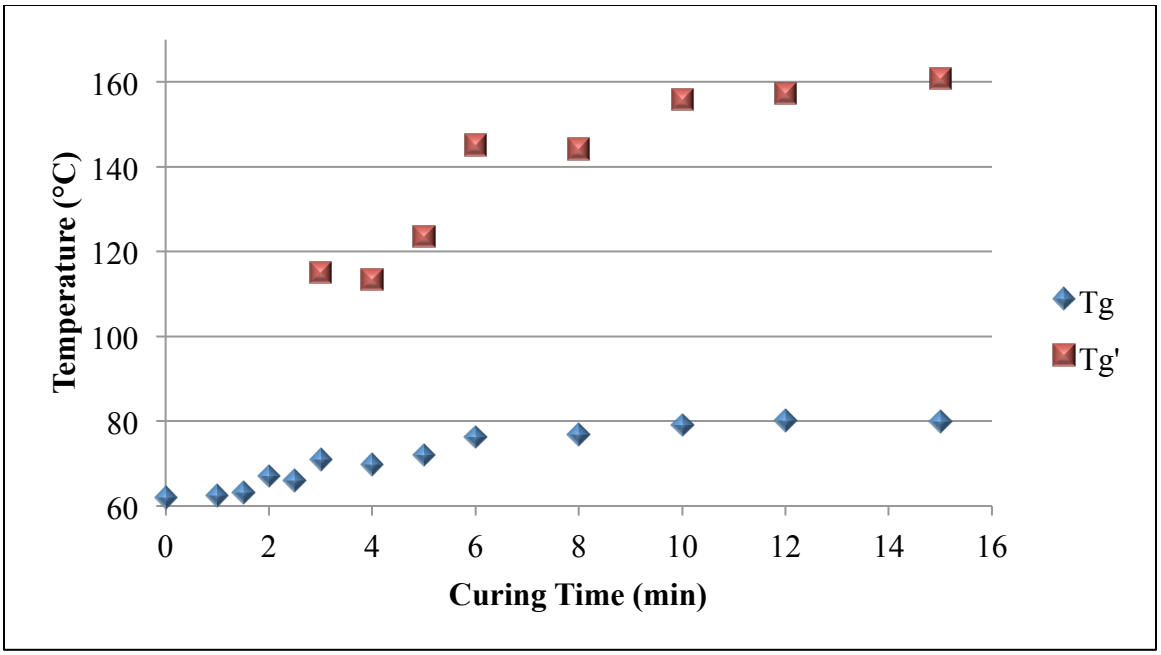

Figure 7-3. Glass transition temperature data from blend samples at different cure-time intervals at 204 ˚C.

DSC data show that the non-cured powder had a single T_g at approximately 62 ˚C. As time progressed, this T_g increased slightly to 71 ˚C at 3 minutes, where the secondary T_g emerges at 115.1 ˚C, thereby indicating phase separation. The T_g's at full cure are 80.0 ˚C, and 160.8 ˚C. DSC analysis of the single component clears revealed $T_g^{'}$ to stem from the high OH resin, which constitutes the dispersed phase (Chapter 5). Even though domains can be observed in the 1-minute cure via TEM, the two acrylic resins are still compatible enough to yield just one T_g that is similar to the low OH resin at 1 minute, but this may also be an outcome of the low crosslink density for both resin components at this stage.

7.3.3 Rheology of blended resins

Given the rapid changes in gloss and surface from 2 minutes to 3 minutes, there may be an underlying mechanism for such a finding. Rheology is an important parameter for powder coatings because even application on a substrate is necessary for coating performance.[17] This makes it important to measure film viscosity at the cure temperature, which helps determine the gel time. Gel time is defined as the time when the storage modulus (*G*') exceeds the loss modulus (*G*").[19-20] This threshold signifies the transition from a mostly viscous material to a mostly elastic material. The moduli are plotted in Figure 7-4, which shows gelation occurring at 342 seconds. Once this threshold is crossed, the thermoset should loose the ability to experience significant flow at 200 ˚C. Note that both curves do not exceed 100 Pa•s until at ~200 seconds. Prior to the gel point, the timespan with the largest difference between the moduli is between 2.5 and 3 minutes, which matches the timespan for the rapid roughness increase from Figure 7-2, thus indicating significant flow for the resin. This is important for understanding the morphologies depicted in upcoming transmission electron micrographs.

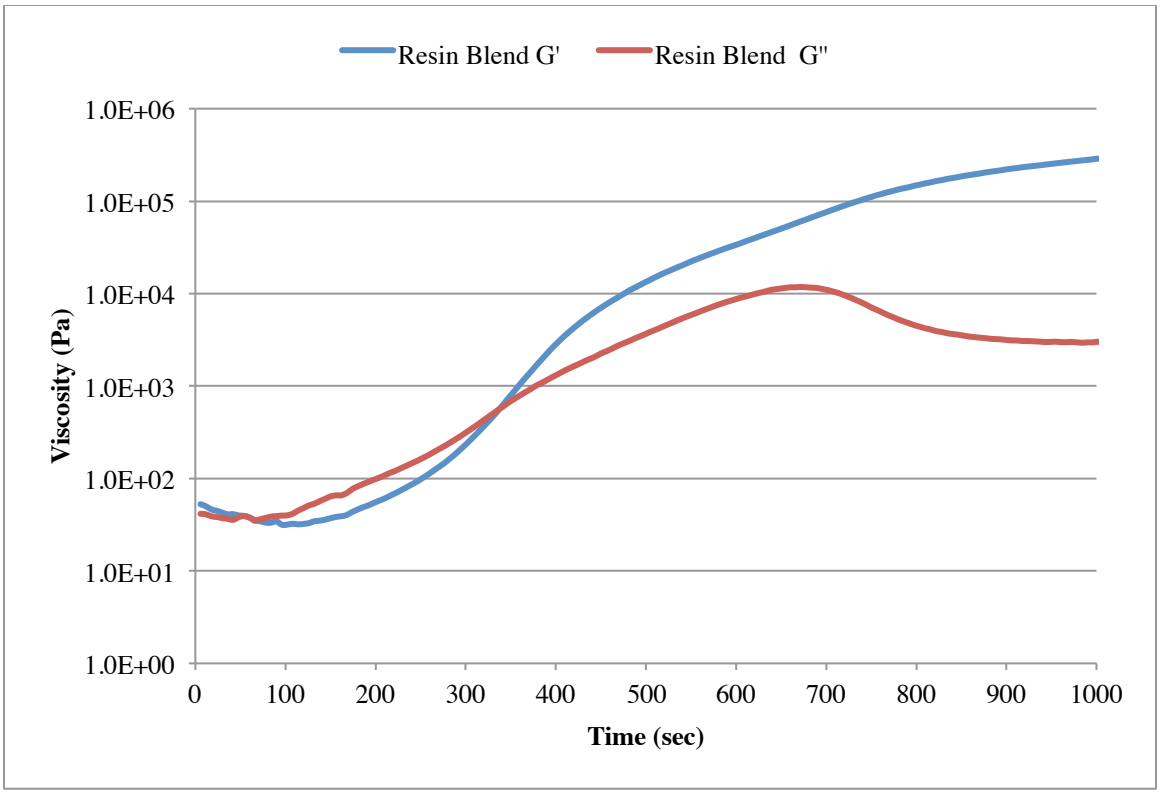

Figure 7-4. Resin blend measured at 200 ˚C cure with low shear oscillation.

7.3.4 Reaction monitoring by vibrational spectroscopy

Underlying the changes in morphology is the continuing chemical reaction between the polyisocyanate and the two acrylic resins. The peaks to monitor for the reaction are the isocyanate peak`[21] at 2255 cm^{-1} and the ε-caprolactam peak at 1655 cm^{-1}.[22] It was observed in Figures 6-1 and 6-2 that the intensities of these two peaks change significantly with respect to the cure, thus making them good candidates for reaction monitoring. The isocyanate peak was measured by ATR-FTIR. Dividing this peak by the aromatic peak at 700 cm^{-1} normalized the generated curves for blend and the single component films. In Figure 7-5, the fully cured blend has the highest NCO peak observed throughout the cure, except at 2.5 minutes. A small but significant isocyanate peak remains at full cure, which amounts to a remnant of deblocked but unreacted

compatibilizer, whereas the peak is largely gone for the single component films. That may be due to NCO overindexing, which is known to increase chemical resistance for polyurethane films.[23] For the blend, the largest change in NCO intensity is the decrease from 2 minutes to 2.5 minutes, which again correlates with the rapid increase in surface roughness 2-3 minutes.

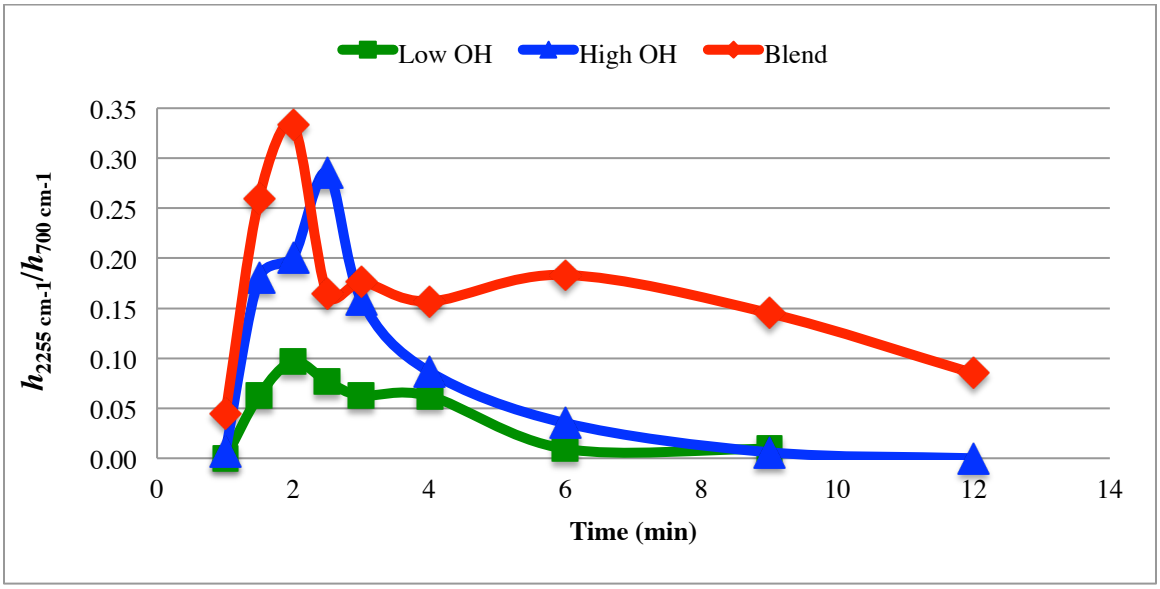

Figure 7-5. FTIR peak intensity evolution for the isocyanate vibration at 2255 cm^{-1} as a function of increasing cure time at 204 ˚C. Intensities are normalized with respect to the aromatic moiety at 700 cm^{-1}.

Thus, the data in Figure 7-5 may be linked with the data in Figure 7-2. Referring back to Chapter 6, Figure 6-6 shows that the rapid rise of the NCO blend peak 1-2 minutes into the cure indicates a rapid liberation of the blocking agent, which is followed by the rapid rise in surface roughness 2-3 minutes for Figure 7-2. The increasing roughness may be an outcome of the low viscosity induced by ε-caprolactam acting as a solvent, which is less concentrated in the domains due to their lower free volume vis-á-vis higher crosslink density.

7.3.5 Transmission electron micrographs

Through the high magnification possible by TEM analysis, we observed that the resins have not been completely compatibilized before curing occurs. Note that cross-sectioned powder particles did not exhibit selective staining. However, two discernible morphologies are found within the powders. One appears to be a porous continuous phase, where the voids (white holes in powder) may have resulted from trapped N_2 bubbles remaining from the acrylic polyol synthesis[4] and incomplete fusion. The other phase appears to consist of dispersed wormlike structures, (7-6a). At 1 minute, the worms appear to sinter into distinct domains, while the continuous phase surrounding them temporarily becomes more porous. The rest of the sample consists of a fibrous matrix with smooth domain droplets, some of which retain subtle signs of the wormlike structure. Among all of the domains observed under TEM for the 1-minute sample, about 54% of them were observed in a fibrous matrix, as seen in Figure 7-6c.

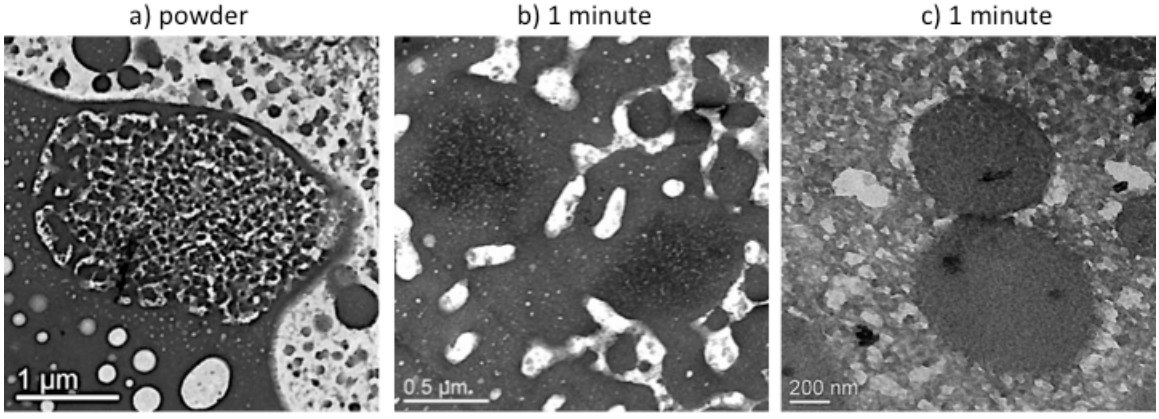

Figure 7-6. TEM analysis of domain nucleation in the cross-section; a) domain with wormlike morphology present in powder particle; b) wormlike structure coalescing into spherical domains; c) spherical domains connected to fibrils.

These coatings develop very complex cross-section morphologies during the cure, and thus warrant the grouping of the following electron micrographs into four datasets organized by degree of magnification, and before/after the emergence of T_g' in DSC

measurements (Figures 7-7, 7-8, 7-9, and 7-10, respectively). What counts as low or high magnification in this context is dependent on the quenched sample. For example, if the focus of a particular micrograph is on domains with diameters > 20 μm, then that qualifies it as low-magnification. High-magnification would then be on domains < 20 μm.

The first set presents the large domains before and during T_g' manifestation at 3 minutes. These early-cure samples were difficult to microtome due to their brittleness, which may be a result of shear stresses within the film bulk during sintering of the powder particles. This necessitated reliance on optical microscopy for viewing the cross-sectioned resin block of the 1 min sample that yielded the electron micrographs for Figure 7-7b and c. Even the 2-min sample largely disintegrated under the microtome, and thus no micrographs from this sample will be used here.

The large domains in all of the micrographs of Figure 7-8 appear to have a common orientation with respect to the tin substrate in the given sample. This orientation is indicated by the blue arrows in Figures 7-7a and 7-7c, where they are pointed down toward the substrate interface at an angle. Figure 7-7a is an optical micrograph of the 1-minute sample because it was too delicate to withstand the microtome blade; it nevertheless shows large domains possessing an orientation toward the film-substrate that is indicated by the blue arrow. Wrinkled domains can be seen in the 1.5-minutes sample; this will be elaborated upon in the discussion section. The 2.5- and 3-minute samples show oriented domain chains that suggest rapid coarsening that is influenced by hydrodynamics. As seen in the 1-minute sample, domains in the 2.5-minute sample appear to be commonly oriented toward the substrate at an angle. The large domains do

not exhibit this orientation, but the domain chains do. Similar orientations by domain chains have been observed in the 3-minute sample, but emphasis is now placed on the red

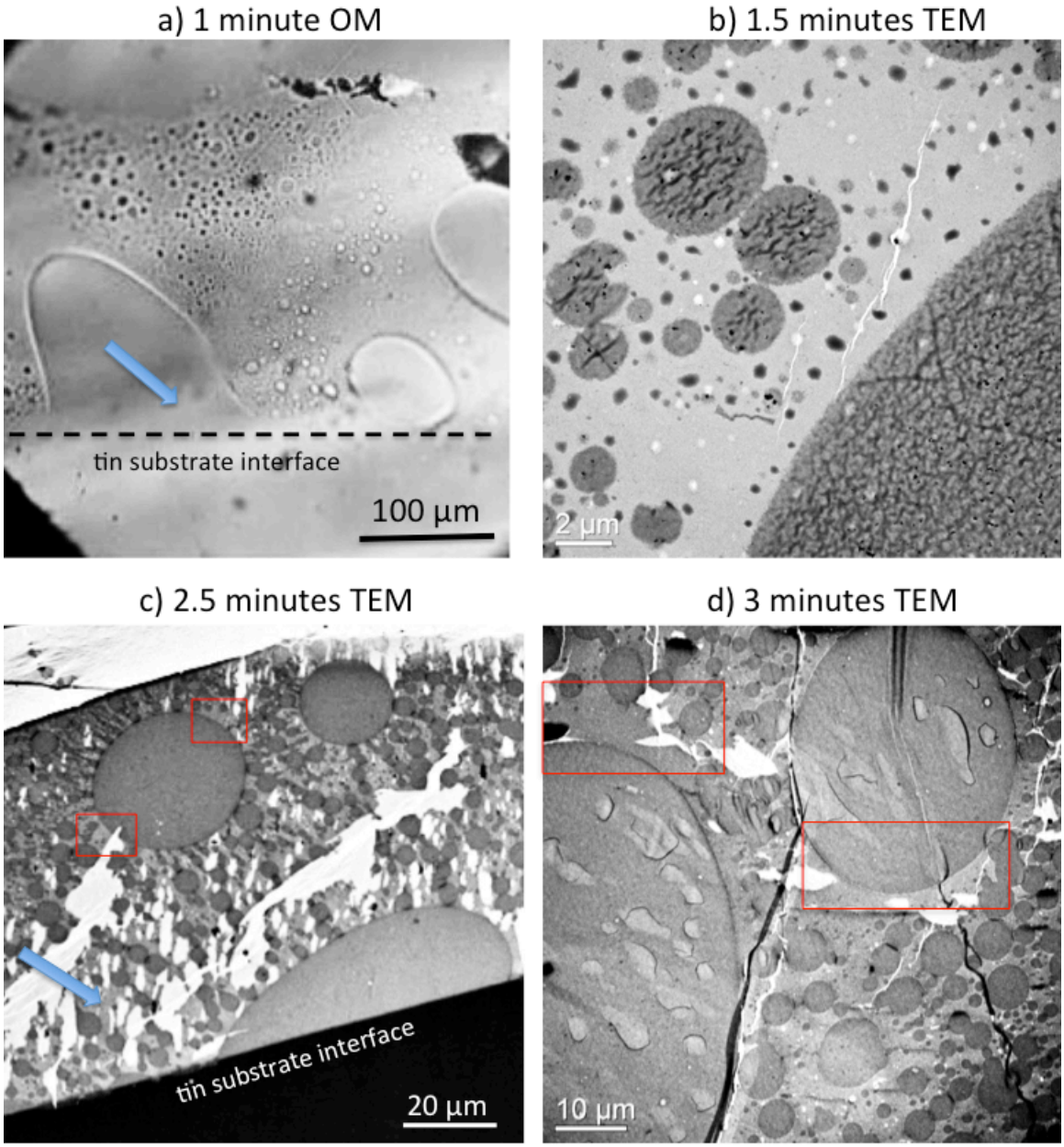

Figure 7-7. Low-magnification cross-sections up to 3 minutes. Blue arrows indicate orientation of large domains. Red boxes indicate a paucity of small domains connected to large domains.

boxes to indicate regions that do *not* have small domains being linked to the large ones; for most large domains, these paucities coincide with elliptical regions of highest

curvature, as seen in Figure 7-7d. This finding has been observed for almost all ellipsoid domains with major axes spanning 20 μm.

At cure times of 4 minutes or greater, sample tearing or cracking from the microtome became less pronounced as the cure progressed, which suggested increasing viscoelasticity for the films. Brittle films are more likely to disintegrate under the microtome, and thus the observed cracks and tears are artifacts of the stresses induced by the diamond blade. The large domains have smaller aspect ratios, but never become fully circular. At 6 minutes, the coarsening rate decreases, as evidenced by the smaller number of domains in contact with the large domain in Figure 7-8b. Its surface, while visibly roughened by the small domains beneath it, appears to be slightly bulging from the large domain 40 μm below. This bulging effect seems to continue for the 9 minute sample, as a few domains have been observed to be nearly as large as the coating thickness that comes into contact with the substrate, as seen in Figure 7-8c. This contact with the substrate may lead to the large domains eventually flattening onto the substrate, as seen in Figure 7-9d. Flattened domains are a feature of the films from the beginning of the cure (Figure 7-7a), but their number and size increase drastically in the interval from 9 minutes to 12 minutes of curing. Their presence may be an effect of lowered interfacial energy, as investigated by Funke and Murase.[7]

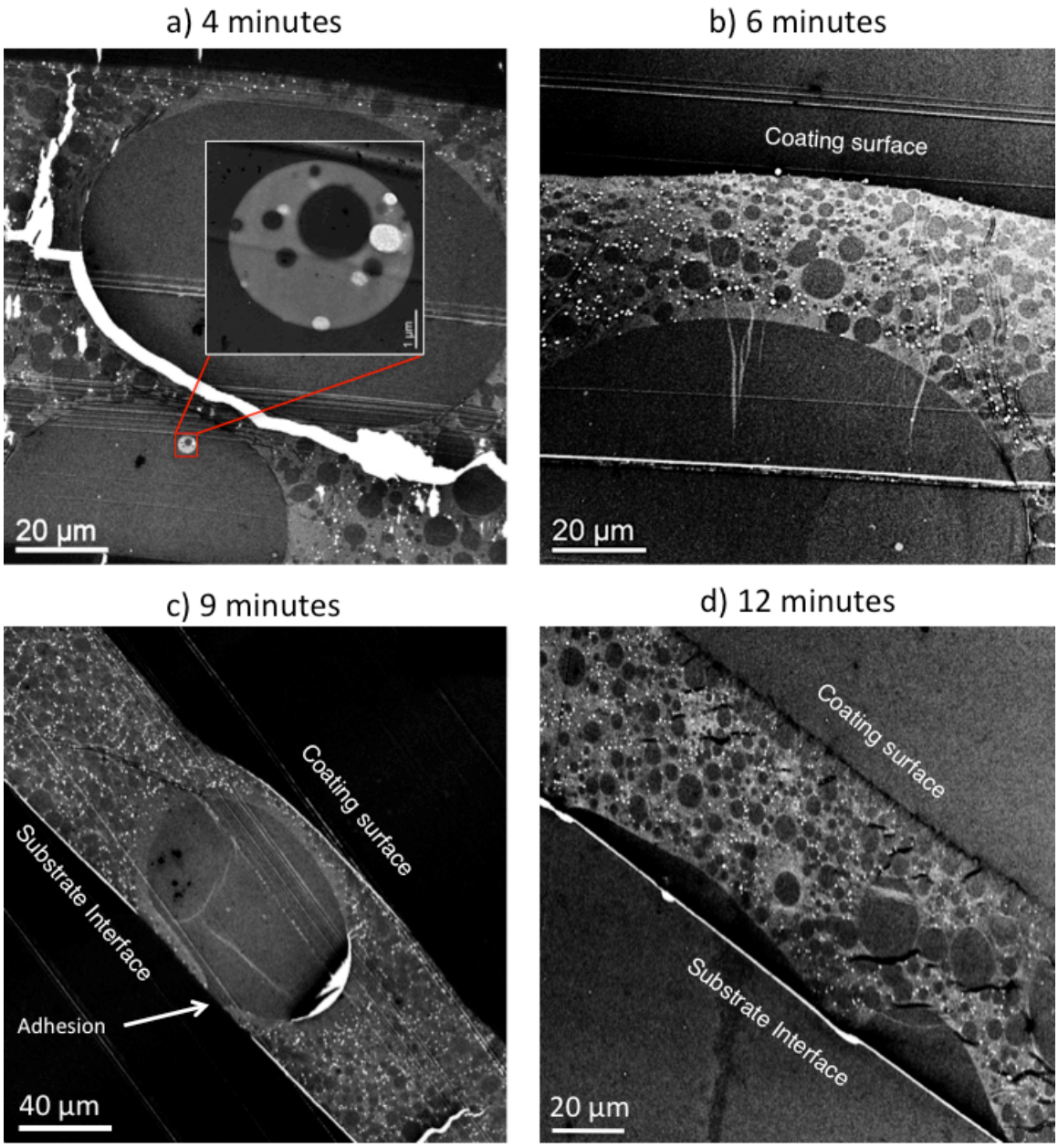

Figure 7-8. Low magnification electron micrographs of cross-sectioned films quenched 4-9 minutes and at full cure.

The samples shown in Figure 7-7 are presented in higher magnification for Figure 7-9, except for the 1-minute sample, which is shown in Figure 7-6 for high magnification. The domains in Figure 7-9a have visible interfaces, but they show similar degrees of staining with their proximal environments, which suggests that much of the high OH

material has yet to relax into domains. Figure 7-9b is a micrograph of domain chains merging into larger domains. At 3 minutes, there seems be a secondary phase transition, in which the droplet phase is accompanied by a cocontinuous phase within the matrix. This new cocontinuous structure appears to have both high OH and low OH polymers because the darker gray phase possesses a shade of grey very similar to that of the droplets. In the lower left of 9c, the darker phase appears to be actively diffusing into the adjacent droplet, as indicated by the white arrows This diffusion can also be seen in 9d; the darker component is close to depletion between the two nascent domains. This secondary phase transition coincides with the first measurement of $T_g^{'}$ (Figure 7-3) and will be discussed in subsequent paragraphs.

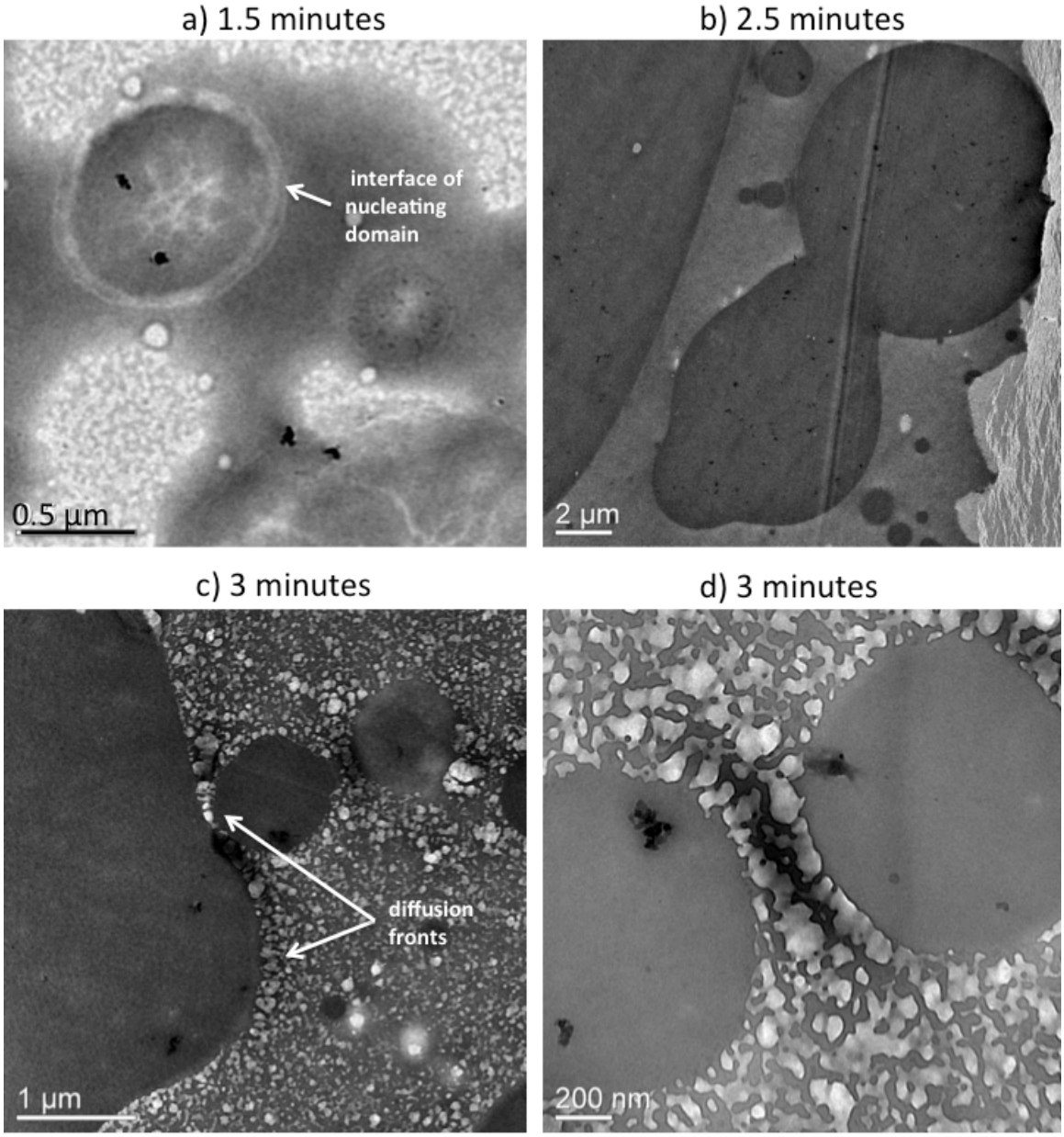

Figure 7-9. High magnification cross-sections of films quenched 1-3 minutes.

Micrographs of cross-sections quenched after 3 minutes suggest that the secondary phase transition is transient. Remnants of this transition might be found in Figure 7-10a from suggested hydrodynamic behavior. All micrographs in Figure 7-10 contain circular holes that suggest bubbles of trapped gasses. The lack of small domains around the large domain of 7-10c could be a depletion zone from the coarsening. A small

domain sandwiched between a flattened domain and large domain suggests that the increasing crosslink density also increased the energy barrier to coarsening to the point of nearly stopping it. In fact, the large domain is largely resting on top of the flattened domain.

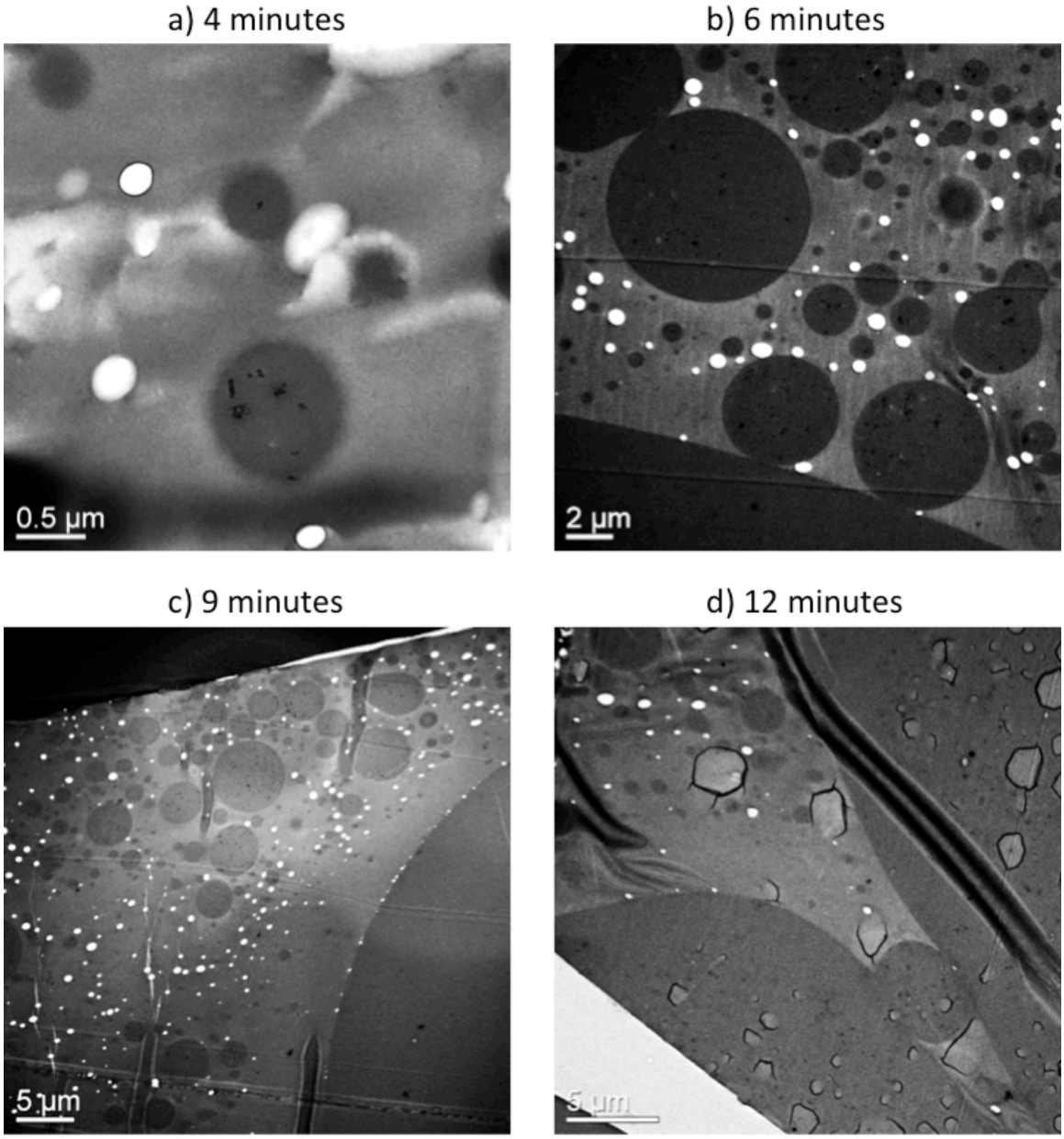

Figure 7-10. High magnification cross-sections of films quenched at 4-9 min and full cure.

Attempts at quantifying the distribution of domain areas are summed up in the histograms of Figure 7-11. The columns are organized around clusters of domain areas. Domains ≤ 2 μm^2 were excluded due to their sheer number, which would have dwarfed the numbers of large domains and thereby hide the trends. Typical numbers of counted domains were 300-500; later cure samples had greater numbers of larger domains, which reduced the total number that could be counted. Considering the high polydispersity of the domains, their nonstop growth throughout the cure, and their wetting behavior, no estimation of the volume could be obtained. What this stacked histogram represents is a rough trend of the observed nucleation and coalescence of the domains. Up to 9 min, there is an upward trend toward bigger domains in the 10-50 μm^2 and 50 μm^2 columns. There is a relatively large jump 2.5 min to 3 min in the percentage of domains being 10-50 μm^2, which suggests rapid coalescence. However, the 4 min columns do not conform to this behavior because of newly nucleated small domains, although domains > 50 μm^2 continue to gain in number. This is elaborated upon in the discussion section about the emergence of T_g'. Rapid coarsening resumes from 4 minutes to 6 minutes; domains 10-50 μm^2 experience another rapid rise in the composition of the total number counted. The coarsening rate slows down for 6-9 minutes; the 2-10 μm^2 and 10-50 um^2 columns show little change, but the 50+ um^2 column reached its highest percentage. The marked decline in the percentage of domains > 10 μm^2 at full cure is due to the flattened appearance from substrate wetting. This means the large domains take up less space in the coating cross-sectional area, leaving more domains ≤ 10 μm^2 to be counted.

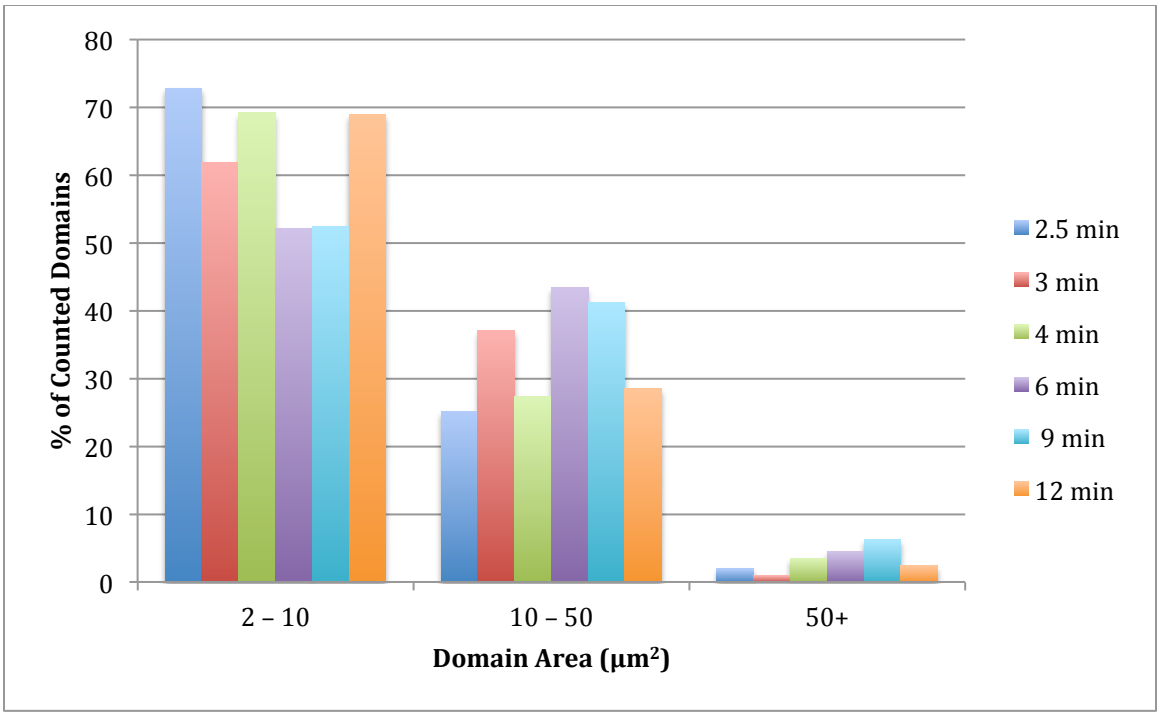

Figure 7-11. Histograms of domain areas for samples at different stages of the cure.

7.4 Discussion

7.4.1 Powder to 1.5 minutes: sintering of powder particles and nucleation of domains

The domains clearly undergo considerable changes from start to finish. In the powder, the lack of selective staining may be an effect of:

- very dark imaging from high sample density, as this is really extrudate material that had not yet experienced loss of mass from deblocking, and
- high compatibilization, even within the wormlike structures.

Uneven sample heating may have enabled observation of domains transitioning from encapsulated wormlike structures in the powder to smooth spherical domains. About 120 small domains ($d < 2\ \mu$m) have been observed in the transmission electron micrographs

of the 1-minute sample; about 46% of them were domains with wormlike structures inside of them, but appeared to be transitioning toward smooth structures, as seen in Figure 7-6. Moreover, these domains were probably not very crosslinked, as attested to by the absence of T_g' until 3 minutes. The wrinkled appearance of the large domains at 1.5 minutes (Figure 7-7b) is an indication of low crosslink density, as well as relaxation from stresses induced by the microtome or stick slip during cutting. The small amorphous drops surrounding the wrinkled domains in Figure 7-7b are shown in closer detail in Figure 7-10a, where we see nascent domains outlined by interfaces ~ 50 nm in length. Interfaces this long are characteristic of compatibilized polymer blends,[24] and have been observed in later cure times. It is suspected that wrinkling could be seen in microtomed large domains for the 1-min sample as well, but its fragility leaves this question unanswered. Another sign of compatibilization in the early cure is the fibrous network in the nascent matrix, which is key to good adhesion between the phases.[14] The fibrils are not observed in samples after 1 minute because the film may have completed the transition to a melt with immiscible droplets.

After deblocking, ε-caprolactam may exist as a liquid prior to evaporation, allowing it to act as a solvent. This solvation could be implied from the correlation of plotted data in Figures 7-2 to 7-5. For instance, the surface roughness in Figure 7-2 changes relatively little for 1 to 2 minutes. In the rheology data (Figure 7-4), the time at which *G*" surpasses *G*' (1 minute) coincides with the start of a rapid rise in the NCO peak height ratio in Figure 7-5 for the blend (red curve). Thus, rapid deblocking suggests the onset of significant resin flow, when boiling ε-caprolactam liquid can reduce the viscosity of the resin melt. The ε-caprolactam concentration was observed to decrease

throughout the cure, but there was enough of it in both phases to keep the viscosity low (Figure 6-6). This could be one of the causes of the rapid rise in surface roughness 2 minutes to 3 minutes in Figure 7-2. Thus, the film should not be considered as a quiescent (no flow) polymer system in the early cure.

7.4.2 2- to 3-minute interval: rapid coarsening

A necessary process in curing of powder coatings is the surface leveling via surface tension gradients (known as Marangoni flow),[25] which yields smooth finishes for typical powder coatings.[26] However, as a polymer blend, surface tension may manifest the opposite effect on the finish. Surface tension in powder coatings typically arise from inhomogeneous distribution of the powder particles, but the composite nature of this set of films could have an additive effect on the surface tension. On a macroscopic level, the tilted large domains in Figure 7-7a and the tilted orientation of domain chains toward the substrate in Figure 7-7c (indicated by blue arrow) suggest extensional flow from surface tension gradients. The low viscosity allows hydrodynamic forces to act on the domains and in some cases deform them into ellipsoids. Simultaneously, domains may ripen by inter-droplet diffusion via van der Waals forces and potentially from Brownian motion from thermal noise due to the high cure temperature.[27] According to Table 5-1, the high OH resin is 26% by weight of the total composition, which is considered a high content of the dispersed phase according to recent work by Fortelný et al.[28] This high concentration of domain droplets would make droplet-droplet collisions more likely and thus contribute to ripening. The diffusion mechanism is further elucidated in paragraphs discussing the later cure.

Both ripening mechanisms would couple to produce the rapid coarsening observed in the 2.5-minute and 3-minute samples. This rapid coarsening underlies the rapid surface roughening 2-3 minutes into the cure from Figure 7-2. The columns labeled "2-10 μm^2" and "10-50 μm^2" in Figure 7-11 embody this trend in rapid coarsening. At 2.5 minutes, 73% of the 404 counted domains have cross-section areas 2-10 μm^2, and 25% have areas 10-50 μm^2. At 3 minutes, 62% of the 310 counted domains are 2-10 μm^2, and 37% are 10-50 um^2. Very few domains > 50 μm^2 were found.

The capillary number *Ca* and the viscosity ratio $p = \eta_d/\eta_m$ can describe domain geometry in a flowing liquid matrix; η_d = domain viscosity, η_m = matrix viscosity. In this context, *Ca* is the ratio of the applied hydrodynamic stress on the droplet that deforms it and the interfacial tension, which attempts to preserve the spherical shape of the domain droplet for surface energy minimization according to Starý:[14]

$$Ca = \frac{\eta_m \dot{\gamma} d}{2\sigma}, \qquad (7\text{-}1)$$

where $\dot{\gamma}$ = shear rate, d = domain diameter, and σ = interfacial tension. If the hydrodynamic stress is large enough, *Ca* exceeds the critical capillary number Ca_{CR}, and the droplet elongates into an ellipsoid. Domains remain spherical for $Ca < Ca_{CR}$. The large domains in several micrographs are mostly elliptical, which could be a result of them being large enough to experience significant hydrodynamic stresses from extensional flow via surface tension gradients. The crosslink density in these domains must be low enough to allow such deformations to occur.

Puyvelde et al have proposed that the flow surrounding large domains can convey mobile compatibilizer molecules toward tips of the domains and exacerbate deformation. An inhomogeneously distributed compatibilizer produces a concentration gradient at the

interface and causes Marangoni stress (a stress from interfacial tension on the domain that opposes hydrodynamic stress) that tries to equalize compatibilizer concentration on the domain surface.[29] Evidence for this is seen in the drawn red boxes of Figures 7-7c and d. The surfaces of large domains are largely in contact with small domains except for the highlighted regions. Compatibilizers such as the polyisocyante curative act in various capacities to suppress coalescence in blends,[30] so regions with higher concentration of compatibilizer may suppress domain linkage. The large spherical domain in 7-8c could be at the beginning stages of deformation but it has regions largely free of domain linkages at opposite ends. 30 seconds later, the coupling of hydrodynamic flow and simple diffusion elongated these domains to ellipsoids (Figure 7-7d) while coarsening along elliptical minor axes.

7.4.3 Secondary glass transition and transient double phase separation

The images in Figures 7-9c and d suggest there is additional demixing occurring via spinodal decomposition upon initial detection of $T_g^{'}$ by DSC. A hint of such demixing via transient cocontinuity is also observed in 7-9a, but it is the 3-minute cross-section that displays this type of phase separation on a broader scale for the sample. This may be suggestive of lower critical solution (LCST) behavior,[14] in which the polymer solution had resided in the metastable region before $T_g^{'}$ emerges. The metastable region is where the nucleation and growth mechanism occurs, which leads to droplet domains. At the start of $T_g^{'}$, a critical concentration fluctuation facilitated a spinodal decomposition that did not disrupt the dispersed droplet morphology that was already present. Despite the higher T_g, the dark gray resin phase may possess a viscosity similar to the light grey

resin phase (especially as ε-caprolactam evaporates), and by extension, similar crosslink density after quenching. The crosslink density can be inferred from nanoindentation experiments (Figure 7-12) on the 2.5 and 3-minute samples, which show that both phases are similar in hardness in both samples.

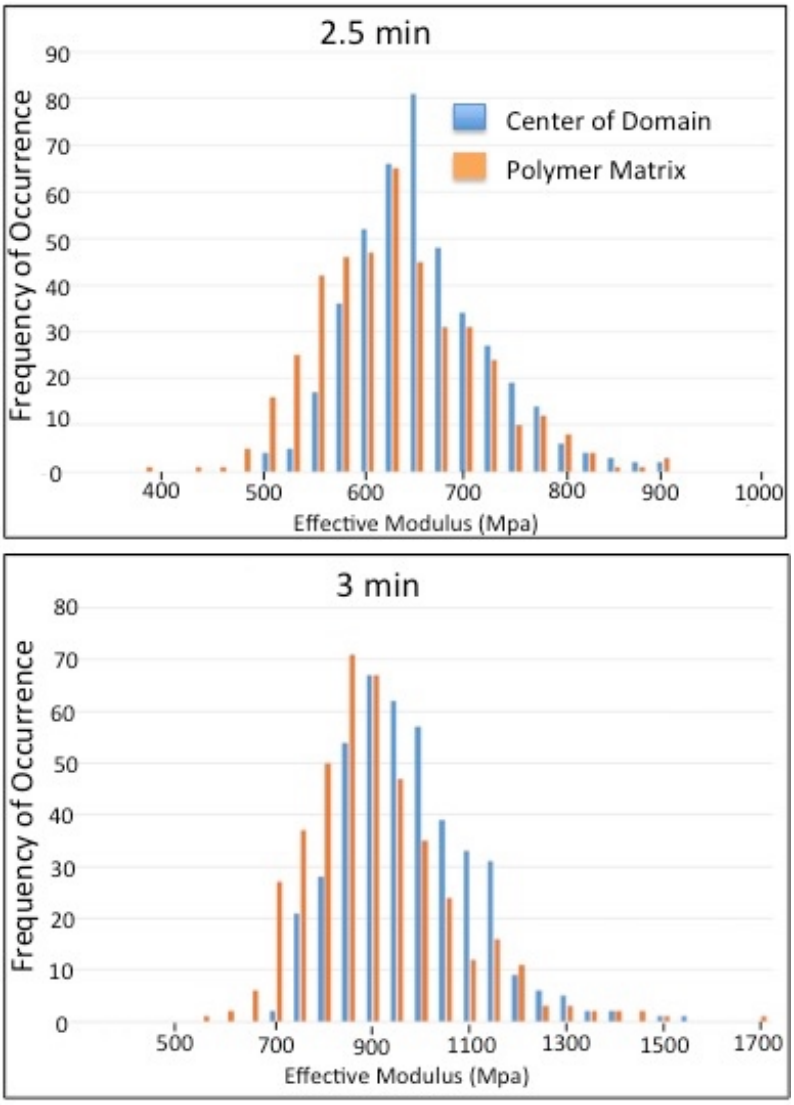

Figure 7-12. Nanoindentation hardness results for the 2.5 and 3-minute cross-sections. At 2.5 minutes, the average hardness for the matrix and domain is 625 MPa and 650 MPa, respectively. At 3 minutes, it is 850 MPa for the matrix and 900 MPa for the

domain. Thus, the difference in hardness is also increasing, and by extension, the crosslink density, which has been correlated with resistance to styrene infiltration in Chapters 5 and 6. Therefore, these hardness results in the early cure do suggest viscosity ratios to be close to unity at 204 ˚C.

Literature on spontaneous double phase separation in binary blends is scarce. Numerical simulations by Tanaka and Araki showed cases where droplet domains emerge within the cocontinuous structure and stabilize.[31] This would occur for systems with high fluidity. Conversely, this system with a dispersed morphology has cocontinuity emerging within the matrix that largely disappears in the 4-minute sample. In Figure 7-9d, the high OH component in the cocontinuous phase appears to diffuse into the domains; by 4 minutes, this component has been completely absorbed into extant or nascent domains. In Figure 7-10a, this disappearance is marked by possible visages of low OH material diffusing into apparent vacancies created by the nascent domains. Remnants of the cocontinuous phase could be found in large domains that contain low OH material (Figure 7-8a); a result of domain coarsening that was so rapid that some low OH regions were encapsulated before they could diffuse out. Such encapsulation has been observed at other cure times, but not at 3 minutes or before. In the 4-minute histograms of Figure 7-11, the 2-10 μm^2 column is 69%, which is 7% higher than for the corresponding 3-minute column; the 10-50 μm^2 column declined from 37% at 3 minutes to 27% at 4 minutes. The 50+ μm^2 column still rose from 1% at 3 min to 3.5 % at 4 minutes. These results indicate that several small domains had nucleated in this interval, but the very large domains continued to coarsen; domains with cross-section areas exceeding 1000 μm^2 were becoming more common at this stage of the cure, and have

been corroborated by observations of additional cross-sections under optical microscopy. The sudden rise in the number of small domains could be rooted in a phenomenon known as dynamical percolation-to-cluster transition.[32] This is attributed to Rayleigh instability of the percolating resin network, in which they disintegrate into spherical domains ≤ 2 μm due to interfacial perturbations,[33] several of which would diffuse into larger domains.

Another feature that arises after the transient double phase separation are the bubbles (white circular holes in Figure 7-10), which have been observed in cross-sections of single component films as well. The bubbles are almost exclusively found in the matrix of samples cured at 4 minutes or later. They are likely the result of caprolactam evaporating out of the film. The matrix was observed to maintain higher caprolactam signatures throughout the cure. Its crosslink density remains consistently lower than for the domains, which may underlie the consistent exclusion of the bubbles by the domains. Smaller free volumes in the domains mean there is less space for caprolactam molecules to occupy because increased crosslink density is correlated with decreased free volume. By extension, compatibilizer molecules should also be excluded by the domains, but experimental confirmation would require a small enough spot size to analyze the NCO peak in individual domains by FTIR.

7.4.4 Cure dynamics from 4 to 12 minutes

Following the transient phase separation, the coarsening rate has decreased, but not to insignificance. The large domains for the 4-minute sample still are ellipsoids, but with decreased aspect ratios because of:

- possible shape relaxation from Marangoni stresses as the increasing viscosity reduces hydrodynamic forces, and
- locations of domain growth fronts have been at the upper and lower interfaces (regions of lowest curvature), as observed by the linked domain chains from the 2.5- and 3-minute samples (Figure 7-7).

Domain chains still feature prominently at 4 minutes, but they are not similarly oriented as seen for 2.5-minute sample (Figure 7-7c). The perimeters of most large domains are still covered with small domains that eventually coalesce, but also retain the evidence for the uneven distribution of compatibilizer at opposing ends (regions of highest curvature).

From 6 minutes and later, domains appear to coarsen by diffusion alone. The gel point occurs at 5.5 minutes, and coalescence by diffusion becomes the dominant mechanism for the continued coarsening. The declining coarsening rate is suggested by the 2-10 μm^2 and 10-50 μm^2 columns in Figure 7-11 showing little change, while the 50+ μm^2 column grew from 4.5% to 6.2%. Domains tend to relax into spheres to minimize the surface free energy, but the largest domains seem to be locked in as ellipsoids. Small domains can be seen in contact with large domains without showing signs of ripening; such behavior suggests the increasing crosslink density has imposed a sizable energy barrier to coalescence (Figures 7-10b and 7-10d). The small domain resting in between two very large domains in Figure 7-10d is one of many domains 2-5 μm in diameter sandwiched between the two large ones and thereby indicating that domains are transitioning into nonadsorbing hard spheres at full cure.

The barrier to coalescence has yet to grow large enough to cap the size of the largest domains ($d \geq 50\ \mu m$), as they seem to expand to the point of pushing the film

surface upwards (Figures 7-9b and 7-9c). The surface roughness plot in Figure 7-2 reaches its maximum at 9 minutes, and that is when the bulging is most pronounced. Thus, the surface roughness is augmented by waviness that is caused by domains growing as large as the film thickness itself (Figure 7-7c). The paucity of small domains proximal to the largest domains seems to form a depletion zone that does not have bubbles except at the interface of the large domain itself (Figure 7-10c).

The decline in roughness from 9 minutes to 12 minutes could be caused by the very large domains wetting the tin substrate and thereby flatten. In Figure 7-8c, part of the large domain has already adhered to the substrate interface. The culprits behind the sudden adhesion to the substrate could be the high interfacial tension of the domains and the possible thinning of the film via mass loss due to outgassing ε-caprolactam, which is close to depletion at 9 and 12 minutes in both phases (Figure 6-6).

Flattened domains have been a part of the cross-section since the beginning (Figure 7-7a), but it is at full-cure that the majority of large domains have flattened from substrate adhesion. Table 7-1 summarizes the behavior of large domains over a 2 mm distance from a series of optical micrographs. Listed are the surface areas in μm^2 of the cross-sectioned domains with respect to cure-time. The last column is the ratio of domains adhered to substrate over globular domains suspended in the continuous phase. The first three cure times are not included for brevity. The row of ratios indicates that the domains were initially slow to adhere to the substrate, but by 6 minutes of cure, adhered domains had become the majority. This ratio remained nearly constant up to 9 minutes. By 12 minutes, large globular domains were a small minority.

Table 7-1. Surface areas of cross-sections of domains over a 2 mm distance plus the ratio of adhered domains to globules (A/G).

Time (min)	2.5	3	4	6	9	12
Surface area adhered (A) (μm^2)	6949	12934	14133	34262	30119	36352
Surface area globule (G) (μm^2)	50793	40934	34285	20709	18352	8059
A/G	0.14	0.32	0.41	1.65	1.64	4.51

The flattening occurred because the high surface energy of the tin substrate may be closer to the interfacial energy of the high OH phase than to the low OH phase.[7] This is corroborated by the observed total encapsulation of black nanoparticles that were confirmed via EDAX to be silicon-based flow aid. A high surface energy also makes it unlikely that the domains coarsen by Ostwald ripening, which is an observed phenomenon for immiscible polymer blends with low interfacial energy.[34] This will be a major focus in the next chapter when pigments are introduced into the polymer blend.

7.5 Conclusion

An immiscibly blended polyurethane powder coating consisting of two components that highly differ by their hydroxyl (OH) content was cured in a convection oven at 204 ˚C for 12 minutes. It has been analyzed by diverse techniques in powdered form and quenched at different stages of the cure in order to observe morphological changes throughout the cure. According to LCM, the surface roughness rose rapidly 2-3 minutes into the cure, peaked at 9 minutes, and then slowly declined to a roughness similar to the 4-minute sample. The roughness profile is a macroscopic manifestation of several underlying processes that occur in the coating bulk. For instance, DSC showed

the secondary T_g manifesting at 3 minutes, which coincides with the end of the rapid rise in roughness and is the T_g for the high OH dispersed phase. Rheology measurements performed at 200 ˚C showed that from 1 minute to 5.5 minutes, $G'' > G'$, indicating significant flow for the resins for this timespan. In the early cure, the reduced moduli suggest a lowered viscosity that may stem from the high cure temperature and liberated ε-caprolactam blocking agent. This molecular liberation was discerned by FTIR analysis of the isocyanate peak at 2255 cm^{-1}.

The concentration of volatile ε-caprolactam was analyzed by monitoring the carbonyl peak at 1655 cm^{-1} by Raman spectroscopy for both phases in the blend and single component resins. The concentration declined with respect to time. The high OH resin had the highest concentration, but this was not analogous for the domains. The domains may have less free volume for the ε-caprolactam molecules to occupy due to their crosslink density being greater than for the matrix. This exclusion by the domains may have added extra ε-caprolactam to the matrix, which further reduced its viscosity by acting as a solvent while it boiled out of the film. The low viscosity is one of the keys to the rapid rise in surface roughness for the early cure.

TEM of epoxy-embedded cross-sections stained with heavy metal salts was crucial to understanding the evolution of the coating morphology. This analysis allowed observation of domains in the blended powder, and thus indicated that the polyisocyanate curative did not fully compatibilize the two resins during extrusion. In the cure up to 3 minutes, domains with diameters ≥ 20 μm had deformed into ellipsoids that have tilted toward the substrate interface. Smaller domains typically formed chains that were similarly orientated toward the substrate and extended from the coating surface down

toward large domains or the substrate interface. This indicates a coupling between hydrodynamic forces and diffusion induced by chemical potential, which produced rapid coarsening. Domain coarsening is the underlying mechanism behind surface roughening. The low viscosity in the early cure merely accelerated the coarsening.

During the emergence of $T_g^{'}$ at 3 minutes, a transient secondary phase separation occurred in the matrix. The extant domains continued to coalesce, but the matrix consisted of a cocontinuous phase with nascent domains. This phase structure had almost disappeared at 4 minutes. Evidence of this transition may be found in a few domains that had circular regions sharing the same contrast as the matrix, which suggested that the high OH domains had encapsulated low OH material. The bubbles may also serve as evidence of this secondary transition, as they are found exclusively in the matrix, and may be linked to ε-caprolactam outgassing. Domains almost never had bubbles, which may suggest an exclusionary mechanism attributed to their higher crosslink density. Microtomed cross-sections of both single component coatings also contained bubbles, with a far greater number of them observed in the high OH coating.

In the later cure, most of the ε-caprolactam had outgassed, which raised the film viscosity and thus slowed down the rate of domain coarsening. Diffusion via van der Waals attractions with Brownian motion from thermal noise was the likely remaining mechanism behind the coarsening, since the surface energy of a domain tends to shrink as its diameter grows. At 9 minutes, the surface roughness and the largest domains reached their maxima. In the cross-section, these domains were nearly as large as the coating thickness, which appeared to induce a wavy pattern on the surface. Loss of mass from outgassing ε-caprolactam might also have contributed to the surface waviness. The

shrinking coating layer may have "pulled" the large domains down toward the substrate and thereby triggering the adhesion. At full cure, a majority of these large domains were flattened from substrate wetting, which suggests that surface energy plays an important role in the morphology of the dispersed phase. This has important implications for the behavior of domains when pigments are added.

7.6 References

1. Hansen, C. M., *Hansen Solubility Parameters: A User's Handbook*. 2nd ed.; CRC Press: Baca Raton, Florida, 2007.
2. Schmitt, F.; Wenning, A.; Weiss, J. V., Diimeric isocyanates in polyurethane powder coatings. *Progress in Organic Coatings* **1998,** *34*, 227-235.
3. Jacquin, J. D.; McCurdy, M. R.; Dennis, D. J.; Evangelista, M.; Favrin, D.; Minesso, A., New Resin Technology for Semi-Matte and Dull-Matte Powder Coatings—Part 1. *Powder Coating* **2009,** *9*, 37-41.
4. Gite, V. V.; Mahulikar, P. P.; Hundiwale, D. G., Preparation and properties of polyurethane coatings based on acrylic polyols and trimer of isophorone diisocyanate. *Progress in Organic Coatings* **2010,** *68*, 307-312.
5. Funke, W., New Aspects of Paint Films with Inhomogeneous Structures. *Progress in Organic Coatings* **1974,** *2* (4), 289-313.
6. Verkholantsev, V. V., Heterophase and self-stratifying polymer coatings. *Progress in Organic Coatings* **1995,** *26*, 31-52.
7. Funke, W.; Murase, H., Uber die Bildung Mehrphasiger Filme Aus Pulverförmigen polymer-mischungen. In *15th FATIPEC Congress*, 1980; Vol. 2, pp 387-409.
8. Verkholantsev, V. V.; Flavian, M., Epoxy/Thermoplastic Heterophase and self-stratifying coatings. *Modern Paint and Coatings* **1995,** *85* (11), 100-106.
9. Verkholantsev, V. V., Self-stratifying coatings for industrial applications. *Pigment and Resin Technology* **2003,** *32* (5), 300-306.
10. Abbasian, A.; Ghaffarian, S. R.; Mohammadi, N., Investigation of factors affecting stratification phenomenon in epoxy-acrylic coatings. *Iranian Polymer Journal* **2004**, 61-68.
11. Kuczyńska, H.; Langer, E.; Kamińska-Tarnawska, E.; Kulikov, D. A.; Indeikin, E. A., Study of self-stratifying compositions. *Journal of Coatings Technology and Research* **2009,** *6* (3), 345-352.
12. Langer, E.; Kuczyńska, H.; Kaminska-Tarnawska, E.; Łukaszczyk, J., Self-stratifying coatings containing barrier and active anticorrosive pigments. *Progress in Organic Coatings* **2011,** *71*, 162-166.

13. Baghdachi, J.; Perez, H.; Talapatcharoenkit, P.; Wang, B., Design and development of self-stratifying systems as sustainable coatings. *Progress in Organic Coatings* **2015,** *78*, 464–473.
14. Starý, Z., Thermodyanamics and Morphology and Compatibilization of Polymer Blends. In *Characterization of Polymer Blends: Miscibility, Morphology, and Interfaces*, 1 ed.; Thomas, S.; Grohens, Y.; Jyotishkumar, P., Eds. Wiley-VCH Verlag GmbH &Co. KGaA: Boschstrasse 12, 69469 Weinheim, Germany, 2015; pp 93-131.
15. Fortelný, I.; Ostafińska, A.; Michálková, D.; Jůza, J.; Mikešová, J.; Šlouf, M., Phase structure evolution during mixing and processing of poly(lactic acid)/polycaprolactone (PLA/PCL) blends. *Polym. Bull.* **2015,** *72* (11), 2931-2947.
16. Michler, G. H., *Electron Microscopy of Polymers*. Springer: Berlin, 2008; p 494.
17. Misev, T. A., Powder Coatings. In *Surface Coatings*, 2nd ed.; Paul, S., Ed. John Wiley & Sons: Chichester, England, 1996; pp 788-849
18. Mahn, E. J. Low reflectance chemical agent resistant coating compositions. 20150259541 A1, 2015.
19. Winter, H. H., Can the gel point of a cross-linking polymer be detected by the G' G" crossover? *Polymer engineering and science* **1987,** *27* (22), 1698-1702.
20. Grillet, A. M.; Gloe, L. M.; Wyatt, N. B., *Polymer gel rheology and adhesion*. INTECH Open Access Publisher: 2012.
21. Wicks, D. A.; Jr., Z. W. W., Blocked Isocyanates III: Part A. Mechanisms and chemistry. *Progress in Organic Coatings* **1999,** *36*, 148-172.
22. Reardon, T. J.; Barker, R. H., Pyrolysis and combustion of nylon 6. I. Effect of selected brominated flame retardants. *Journal of Applied Polymer Science* **1974,** *18* (7), 1903-1917.
23. Crawford, D.; Escarsega, J., Dynamic mechanical analysis of novel polyurethane coating for military applications. *Thermochimica Acta* **2000,** *357-358*, 161-168.
24. Yukioka, S.; Inoue, T., Ellipsometric analysis on the in situ reactive compatibilization of immiscible polymer blends. *Polymer* **1994,** *35* (6), 1182-1186.
25. Duivenvoorde, F. L. Pigment dispersing in powder coatings: synthesis and use of block copolymer dispersing agents. Doctoral Dissertation, Technische Universiteit Eindhoven, Eindhoven, 2000.
26. Barletta, M.; Lusvarghi, L.; Mantini, F. P.; Rubino, G., Epoxy-based thermosetting powder coatings: Surface appearance, scratch adhesion and wear resistance. *Surface and Coatings Technology* **2007,** *201* (16–17), 7479-7504.
27. Nauman, E. B.; He, D. Q., Nonlinear diffusion and phase separation. *Chemical Engineering Science* **2001,** *56* (6), 1999-2018.
28. Fortelný, I.; Jůza, J.; Dimzoski, B., Coalescence in quiescent polymer blends with a high content of the dispersed phase. *European Polymer Journal* **2012,** *48* (7), 1230-1240.
29. Puyvelde, P. V.; Velankar, S.; Moldenaers, P., Rheology and morphology of compatibilized polymer blends. *Current Opinion in Colloid & Interface Science* **2001,** *6*, 457-463.
30. Van Hemelrijck, E.; Van Puyvelde, P.; Velankar, S.; Macosko, C. W.; Moldenaers, P., Interfacial elasticity and coalescence suppression in compatibilized polymer blends. *Journal of Rheology* **2004,** *48* (1), 143-158.

31. Tanaka, H.; Araki, T., Spontaneous Double Phase Separation Induced by Rapid Hydrodynamic Coarsening in Two-Dimensional Fluid Mixtures. *Physical Review Letters* **1998,** *81* (2), 389-392.
32. Takenaka, M.; Izumitani, T.; Hashimoto, T., Spontaneous pinning of domain growth during spinodal decomposition of off‐critical polymer mixtures. II. Scaling analysis. *The Journal of Chemical Physics* **1993,** *98* (4), 3528-3539.
33. Hsu, D.-Y.; Chou, C.-M.; Chuang, C.-Y.; Hong, P.-D., Percolation of Phase-Separating Polymer Mixtures. *ACS Macro Letters* **2015,** *4* (12), 1341-1345.
34. Fortelný, I.; Zivný, A.; Juno, J., Coarsening of the Phase Structure in Immiscible Polymer Blends. Coalescence or Ostwald Ripening? *Journal of Polymer Science: Part B: Polymer Physics* **1999,** *37*, 181-187.

Chapter Eight

Forced Flocculation via Pigment Segregation

8.1 Introduction

Most powder coatings are formulated for high gloss, in which low loadings of pigments are widely dispersed within the coating.[1-2] Dispersed pigments are possible when the pigment-to-volume concentration is low. Excess pigment loading can have deleterious effects on resin rheology during curing.[3] High loadings also increase the economic cost of the product. However, powder coatings are attractive due to the absence of solvents in their application.[4]

Among the resins used for powder coatings, the thermosets use low molecular weight polymers, and thus have relatively low viscosities upon their application.[5] Adding pigments induces an increase of the viscosity due to the greater occupation of the coating volume. This relationship between pigment concentration and volume is complex, and has been the subject of several empirical models in the literature. Among the most widely used is the Krieger-Dougherty model, which assumes the solid particles to be non-interacting spheres:[6]

$$\eta_r = \left(1 - \frac{\phi}{\phi_{\max}}\right)^{-[\eta]\phi_{\max}}, \qquad (8\text{-}1)$$

with ϕ_{max} the volume fraction at maximum packing and $[\eta]$ the intrinsic viscosity.

Replacing the non-interacting spheres with interacting particles, i.e., pigments, further add complexity to the rheology. Pigment-polymer interactions form a polymeric

adsorption layer around the pigments, which results in an increased effective volume fraction ϕ_{eff}:

$$\phi_{eff} = \phi\left(1+\frac{\delta}{r}\right)^2, \qquad (8\text{-}2)$$

with δ the adsorbed layer thickness and r the pigment radius. The pigment-polymer interactions further increase the viscosity, relative to that induced by non-interacting particles at the same ϕ.[7] As non-Newtonian fluids in molten form, powder coatings require a minimum shear stress to be exceeded in order to flow. This is known as the yield value, and results from the necessary energy for destroying the physical network structure created by the interparticle pigment interaction. Increasing the pigment-to-volume-concentration (PVC) increases this interaction that culminates in a higher yield value and viscosity. This subsequently affects the flow and leveling properties of the coating.[5] It has been shown that polymers with moieties capable of interacting with pigments can form ionic bonds on the pigment surface and eventually form thin polymer layers around the pigments (i.e., δ). This can reduce the melt viscosity of the powder and improve flow.[8]

Gloss is also affected by flow. In powder coatings, it is related to the microscopic smoothness of the film. Smooth planar surfaces reflect incident light with little distortion and thus exhibit high gloss, while microscopically rough surfaces scatter light. Once the flow is controlled, gloss can be varied by the following methods:[2, 9-10]

- Incorporating inorganic extenders into the binder
- Combinations of incompatible ingredients, e.g., waxes

- Blending resins with different reactivities; e.g., fast and slow-reacting resins, one resin with dual curatives, two resins with one curative, dispersed reactive catalysts, two resins with two curatives
- Combination of the above

The motivation for dead matte finishes in powder coatings is the expansion of new commercial applications for low volatile organic compound (VOC) emissions within the coating industry.

Surface energy has been used to describe the interaction between pigments and binders. This interaction can be characterized by the acid-base properties of the pigments and binder. The pigments in this study tend to be basic, since they are transition metal oxides (except for calcium silicate), while the binder consisting of acrylic polyols tends to be acidic. The acid-base chemistry lends itself to charge stabilization, in which an electrically charged double layer surrounds the pigment particle. All pigments share the same outer layer and thus repel each other when they come into close proximity. This is one model for how pigment dispersions are stabilized.[11]

Another mechanism for preserving the pigment dispersion is steric stabilization, in which a polymeric dispersing agent is adsorbed onto a pigment surface and creates an effective steric barrier that prevents the other particles from getting too close. This is a typical treatment for alumina/zirconia-coated titanium dioxide,[12] which in raw form would be difficult to disperse in a powder formulation.

In this study, all formulations utilize calcium silicate as a matting agent and two acrylic resins reacting with an ε-caprolactam-blocked IPDI curative. They are thus differentiated by prime pigments to impart the following colors: black, tan, and green.

The acrylic resins are rendered incompatible by differences in polarity and hydrogen bonding characteristics from Hansen Solubility Parameters.[13] Reactivity differences between the resins produce a dispersed phase within the binder that differs in crosslink density from the continuous phase, which roughens the surface and reduces gloss. Such a heterophase structure within the coating can improve mechanical properties such as scratch/mar resistance and adhesion durability.[14-15] The polymeric components have been identified in Chapters 4 and 5. Their spectroscopy has been described in Chapter 6, and the bulk evolution of the domains without pigments has been described in Chapter 7. This chapter describes the evolution of the domains with calcium silicate, carbon black, and magnetite pigments. The object here is to understand the effect pigments have on the phase separation process in order to produce highly roughened surfaces for low-reflectance outdoor applications. Up to now, the dispersion of pigments has been analyzed in single phase binders. How would a dispersion of pigments be affected when a dispersion of evolving polymeric droplets is incorporated into the binder? We have answered this question to a great degree with electron microscopy of cross-sectioned samples. The samples studied here were black films at different stages of the cure, including the powder before its application on a tin-plated steel substrate.

8.2 Experiment

8.2.1 Coating preparation

The examined blends in the study were prepared in a manner similar to that presented by Mahn.[16] Preparation of a low gloss pigmented coating was performed through blending of low and high hydroxyl group functionalized polymeric resins. All

materials were utilized as acquired unless otherwise noted. The acrylic resins with high and low hydroxyl group functionality (20 – 400 OH), and Resiflow were obtained from Estron Chemicals (Calvert City, KY). Benzoin was purchased from GCA Chemical Corporation. Calcium silicate was purchased from Nyco Minerals (Willsboro, NY). The blocked isocyanate was a ε-caprolactam blocked IPDI polyisocyanate curative and was purchased from Evonik Industries (Parsippany, NJ). Three colors were formulated according to published specifications.[17] The black coating was formulated at various weight percentages with carbon black and black iron oxide. The tan coating was formulated with titanium dioxide, carbazole dioxaiine violet, and various iron oxides. The green coating was formulated with acid insoluble green pigments mostly composed of chromium oxide, and traces of cobalt and zinc; carbazole dioxaiine violet, iron oxides, light stable orange and yellow organic pigments; zinc/magnesium ferrite or other mixed metal oxides.

Raw materials were dry-blended by hand, then melt mixed using a twin screw extruder at 120 ˚C. The extruded material was forced through chilled rollers and the resulting cooled material was ground using a rotor mill. The ground powder particle size was further classified by using a 106 μm (140 mesh) sieve. Powder formulations from above were electrostatically applied to tin plated steel substrates to a dry coating thickness of 2.0 – 2.5 mils using a standard gravity fed powder coating cup gun. Coatings were then cross-linked in an oven at 204 °C for 12 minutes to afford the thermoset. The elevated temperature was required to reduce the viscosity of the polymeric resins to induce flow, ensuring even wetting of the substrate, and to initiate

removal of the ε-caprolactam blocking group from the isocyanate. The resultant coatings were slowly cooled to room temperature prior to subsequent analysis.

Calcium silicate, chrome oxide, and magnetite received no surface treatment prior to mixing. Titanium dioxide particles were encapsulated by alumina and zirconia to increase exterior durability, then surface-treated with an organic dispersant.

8.2.2. Laser scanning confocal microscopy (LSCM)

LSCM was used to obtain information on surface characteristics of the coatings. LSCM measurements were performed on an Olympus LEXT OLS4000 using the LEXT software package. Images were gathered using a laser source at 405 nm with 50x optics providing 1076x magnification of the coating surfaces. The LEXT software package allowed the stitching of four magnified images together to provide measurements over 483 μm x 485 μm surfaces. Images were taken every 0.06 μm along the z-axis and were compiled to create a 3D image of the coating surfaces. Surface roughness parameters, depth profiling and macro size domain measurements were performed using the LEXT software package.

8.2.3. Gloss measurements

Gloss measurements were obtained for each film using a BYK Gardner micro-TRI-gloss-S meter. Powder coatings were applied to black & white T12G Metopac™ (Metal) panels were purchased from the Leneta Company. The powder coatings were applied to a dry film thickness of 50.8- 63.5 μm using standard powder coating spray equipment and cured in a convection oven for 12 minutes at 204 ˚C.

8.2.4. Optical microscopy (OM)

Digital optical microscopy was used to record observations of embedded cross-section samples, particularly of the size and distributions of domains. OM measurements were performed on a Meiji microscope equipped with a Nikon digital camera DXM1200 and Nikon ACT-1 software.

8.2.5. Transmission electron microscopy (TEM)

TEM was utilized to provide domain identification and distribution throughout the bulk of the films. Prior to analysis, most samples were embedded in fast-cure epoxy (West Systems, Michigan). Fully cured samples were embedded in Bio-plastic polyester resin (Ward's Science, New York), but this did not alter the morphology. Microtome cross-section samples were prepared for TEM analysis using a Leica EM UC7 Ultra-Microtome (Wetzlar, Germany) with a diamond sectioning blade at STP. Typical thicknesses were 100-150 nm, which is considered thick for TEM samples, but the extra thickness was necessary to preserve sample integrity due to extensive pullout of calcium silicate particles. This problem got worse as the pigment-to-volume concentration increased.

Initial microscopy experiments were performed using a FEI Bio TwinG2 Transmission Electron Microscope. The TEM was equipped with an AMT XR-60 CCD digital camera system for image collection. Bright field imaging measurements were performed at an accelerating voltage of 80 keV.

The second microscope was a JEOL JEM-1400 LaB6. It was equipped with a Gatan CCD digital camera for image collection and a TEAMTM EDS Analysis System

for TEM with an Octane Silicon Drift Detector for elemental analysis of pigments within the films. Bright field imaging was performed at 80 keV.

To enhance contrast between polymer phases in TEM micrographs, heavy metal salts of uranyl acetate and lead citrate were used to stain both clear films and pigmented coatings. Coatings were immersed in 0.02 g/mL uranyl acetate in methanol for 10 min, followed by immersion in 0.003 g/mL aqueous lead citrate for 3 min. The heavy metals are effective electron shields that serve to darken the phases upon their acceptance by the appropriate material.

8.2.6 Scanning electron microscopy (SEM)

The SEM used was a LEO1550 with a Robinson backscatter detector. Its accelerating voltage was 20 kV. It also has an EDAX detector with iXRF electronics and software. Cross-section samples were sputter coated with an Edwards 150B gold sputterer for about 30 seconds, which corresponds to ~ 5 nm thickness.

8.2.7 X-ray photoelectron spectroscopy (XPS)

Survey scans were performed with a pass energy of 100 eV. High-resolution scans were performed with pass energy of 50 eV which had a spacing of 0.1 eV and a 100 ms dwell time. Both types of scans were repeated 50 times and co-added using the VGX900i software program. The two angles of incidence were 90˚ and 60˚. XPS spectra were processed with CASAXPS software. All high-resolution peaks were curve-fitted with a Shirley background, and with products of Gaussian and Lorentzian line-shapes.

8.3 Results/Discussions

8.3.1 Surface analysis

The surface roughness of fully cured black coatings is illustrated in the LCM images of Figure 8-1. S_q values for the low OH, high OH, and blended films are 0.13 μm 0.40 μm, and 2.61 μm, respectively. The roughness is an order of magnitude greater for the blended black film due to the incorporation of phase separation within the binder.

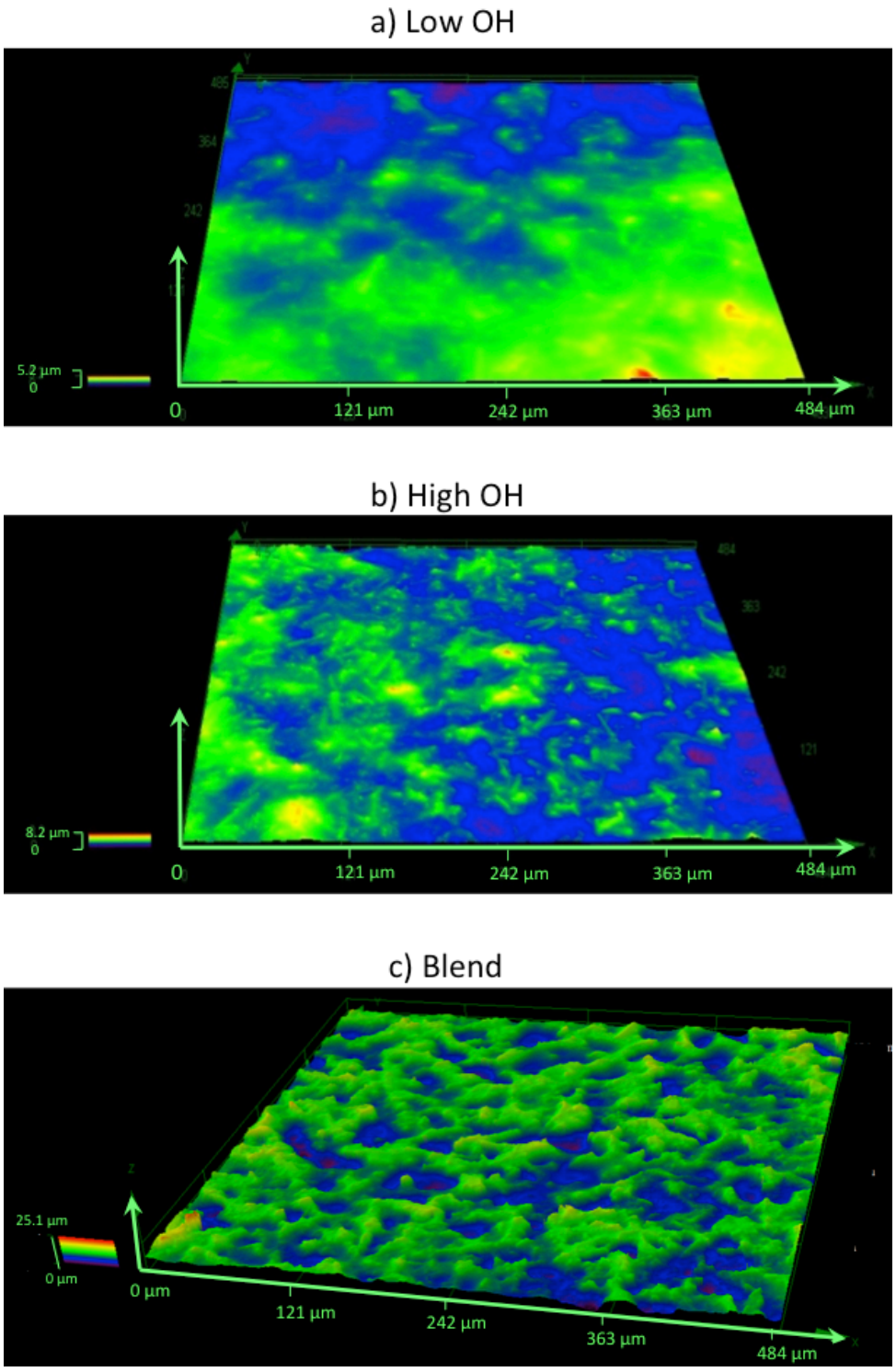

Figure 8-1. LCM images of black film surfaces; a) low OH; b) high OH; c) blend.

The gloss measured at two angles with respect to cure-time for the blended black films is plotted in Figure 8-2. Both gloss curves plateau at 2.5 minutes, which shows that

the pigments roughen the surface immediately, whereas without pigments, the gloss plateaus at 4 minutes for both angles (Chapter 7). In Chapter 5, it was observed via Raman spectroscopy that the domains began to become crosslinked enough 2.5 minutes into the cure to induce a concentration gradient of contaminant styrene from polyester embedding resin; the polymer matrix remained saturated with styrene, while the domains progressively reduced the infiltration of styrene. The beginning of resistance toward the infiltration of a contaminant solvent coincides with the plateauing of the gloss. The gloss is much more reduced and declines at a greater rate for the black films than for the clear films.

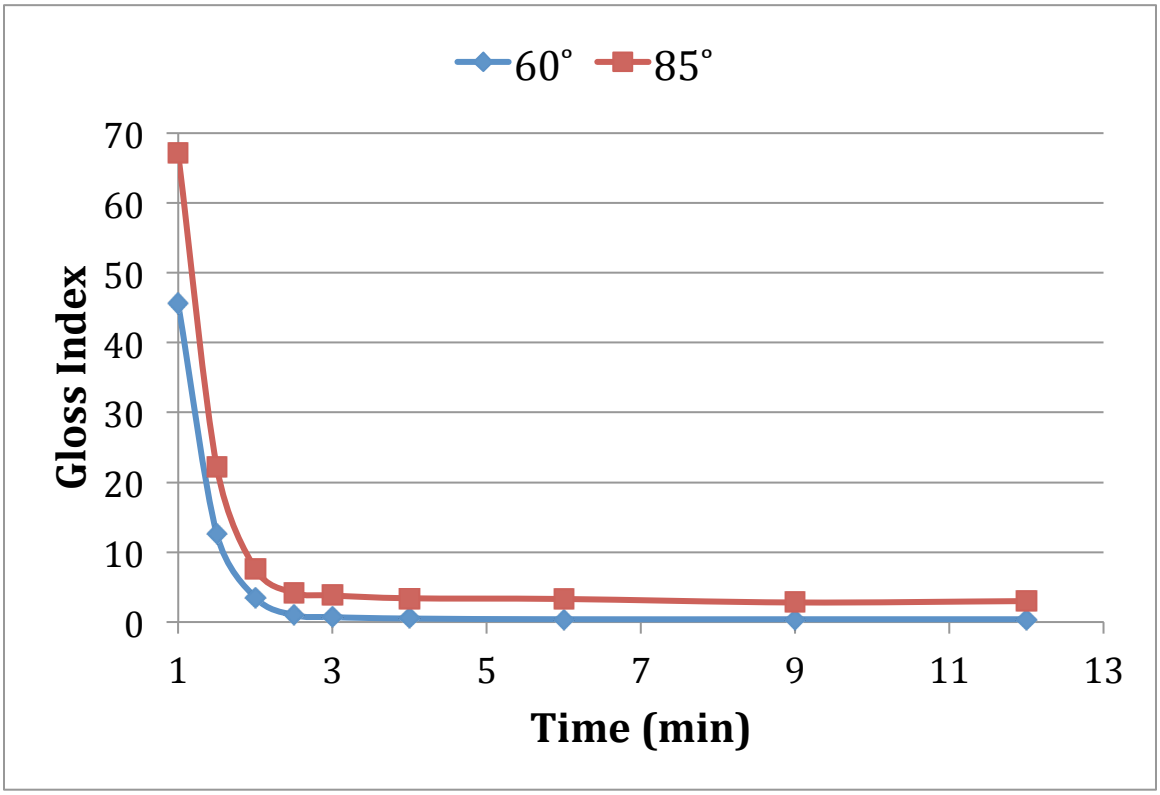

Figure 8-2. Gloss measurements of blended black coatings as a function of time.

Surface roughness measurments were also conducted on quenched film samples formulated with only the $CaSiO_3$ matting agent. While roughness measurements were

not conducted for quenched black films, the matting agent-only film serves as a good approximation for the black film due to their relatively similar roughnesses; i.e., S_q = 2.61 for the black film at full cure, and S_q = 1.99 μm for the matting agent-only film at full cure. As was evident for the clear films (Chapter 7), the roughness increases slowly in the early cure, followed by rapid roughening (1.5 minutes-4 minutes). However, the clear coating continued to roughen at a slower rate up to 9 minutes, followed by a decline in roughness from 9 minutes to 12 minutes. The roughness of the matting agent-only coating plateaued at 4 minutes. This plateauing may indicate that the viscosity of the resins increased to the point of effectively confining the pigments and domains in place; the film surface changes very little from that point onward.

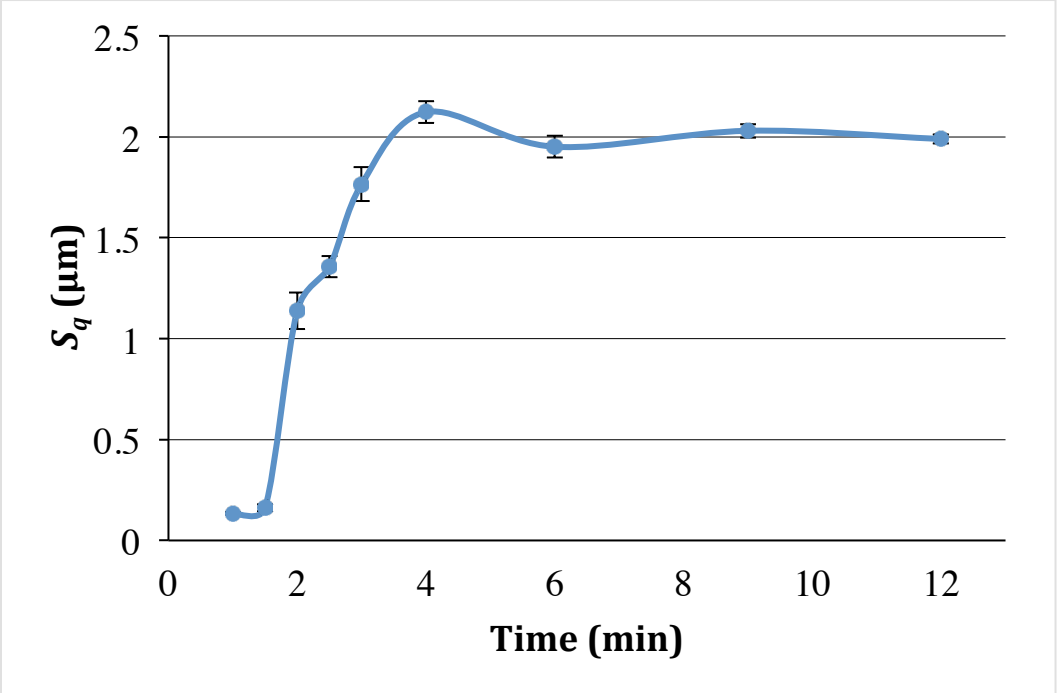

Figure 8-3. Evolution of surface roughness for clear coating formulated with only calcium silicate matting agent.

8.3.2 Correlating the surface with optical micrographs of cross-section

From the gloss and surface roughness measurments, it is apparent that the surface roughness is largely devleoped by the early cure, which also concides with the emergence of the second T_g (Chapter 7). This is supported by the optical micrographs of the cross-section at various times in Figure 8-4. These are the surfaces of the cross-sectioned resin blocks after microtome sectioning, which yields a very smooth finish. The coating surfaces are located at the upper epoxy-coating interfaces in Figures 8-4a-d. The coating surfaces in the 3-minute and 6-minute micrographs do not exhibit noticable change (8-4c and d) , which correlates with the plateauing curves in Figures 8-2 and 8-3. The morphology essentially achieves equilbrium four minutes into the cure.

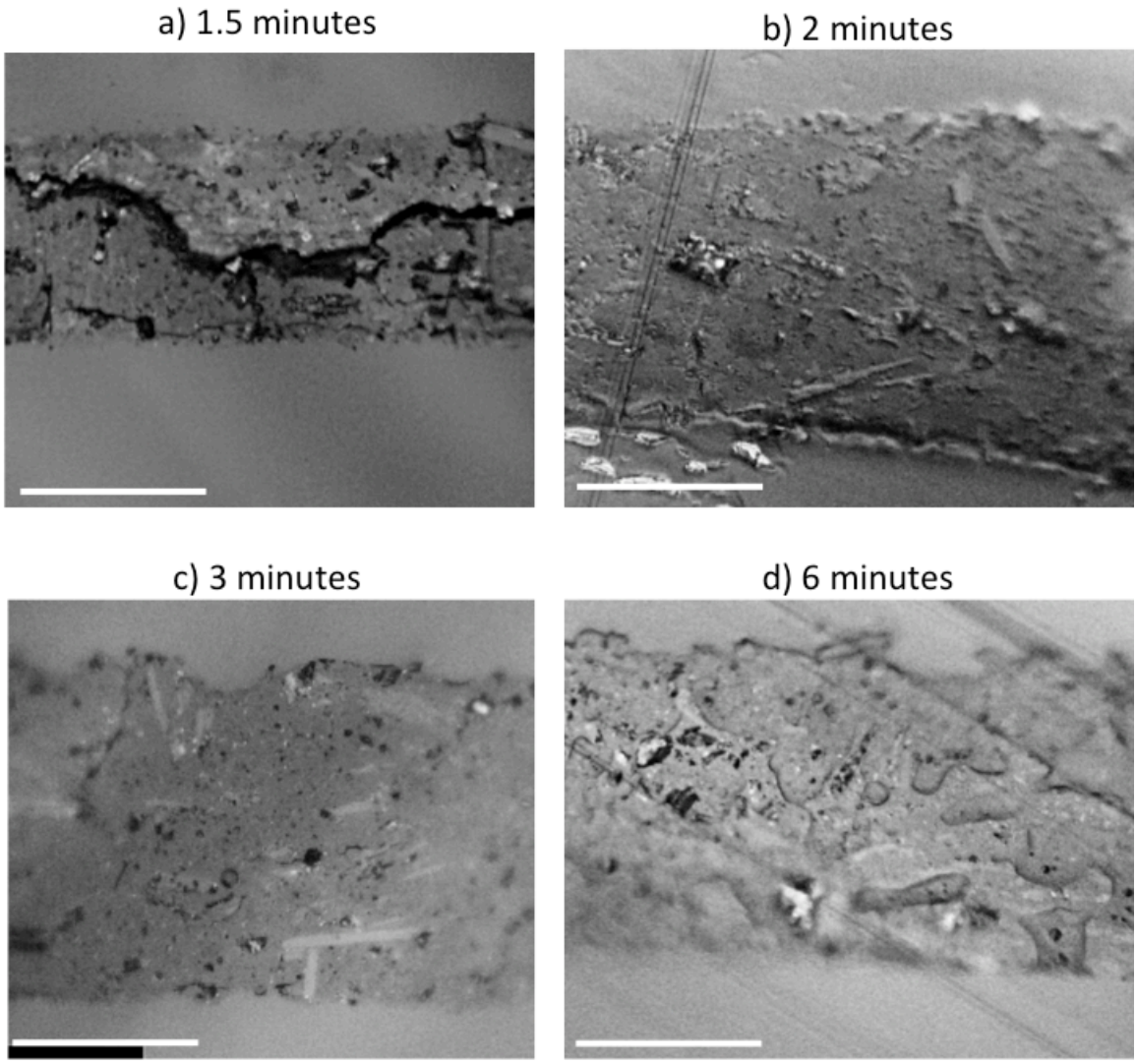

Figure 8-4. Optical micrographs of the cross-section for the black coating at different cure times. The white scale bar is 50 μm.

8.3.3 Electron microsocpy of cross-sectioned black films at various cure-times

The early cure clear films largely disintegrated under the microtome blade (Chapter 7), which did not bode well for the pigmented films. Low magnification images of the 1-minute samples was also unobtainable in the set of quenched black films due to brittleness. However, unlike the clears, a low magnification image of the 2-minute sample was obtained (Figure 8-5a). The image in 8-5a shows massive damage from the sectioning, but large and small domains are still observable. All images in Figure 8-5

show large white areas within the domains that are results of the blade pulling out pigments. These white areas suggest that the pigments were encapsulated within domains prior to pullout. This apparent containment of pigments will be a subject for further discussion.

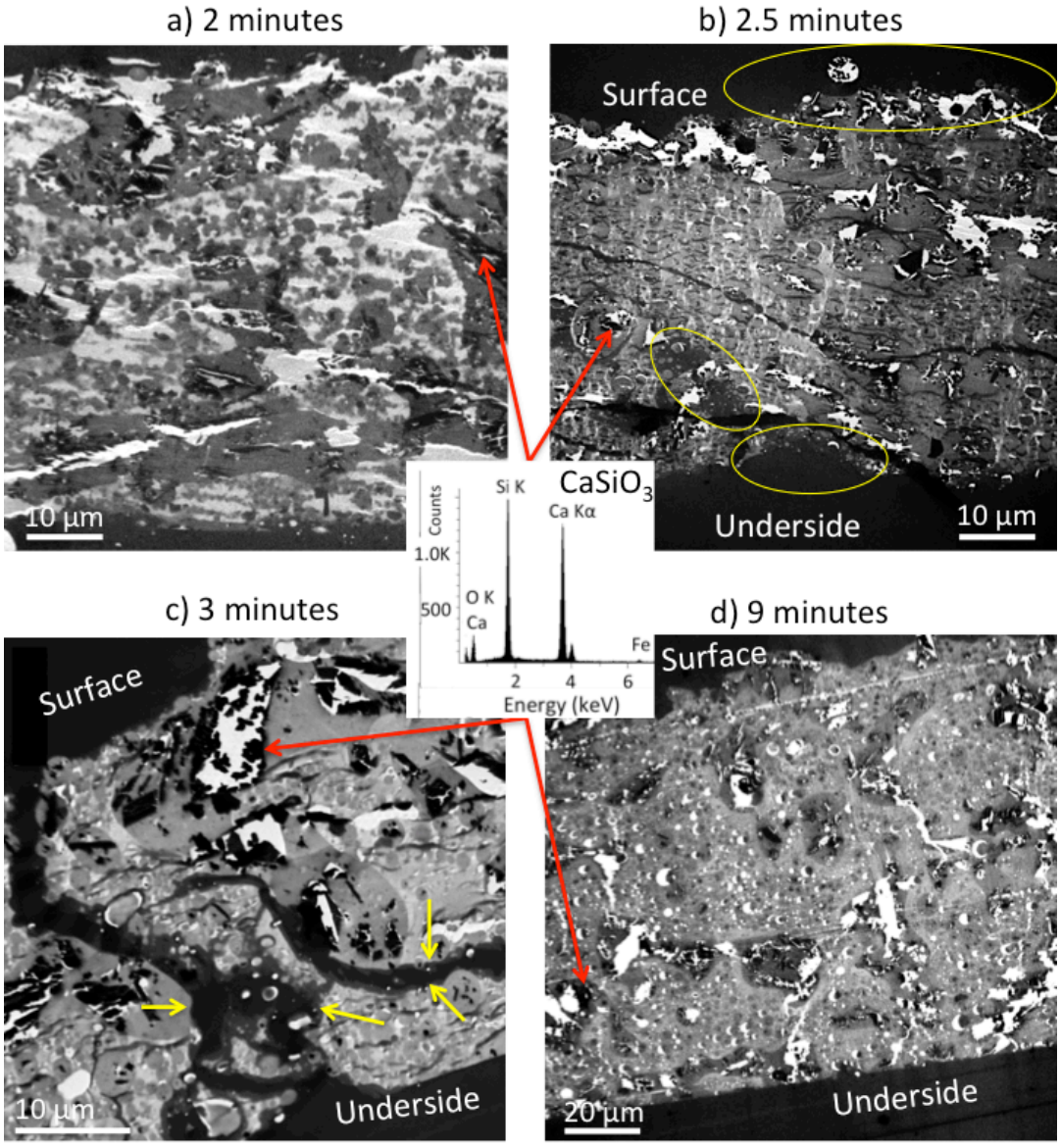

Figure 8-5. Low mag TEM of cross-sections of black films at various cure-times; a) 2 minutes; b) 2.5 minutes; c) 3 minutes; d) 9 minutes. Red lines connect the spectrum to matting agent particles.

Micrographs for the films cured at 2.5, 3, and 9 minutes (Figures 8-5b, c, & d) show obvious contrast between the phases, with domains consisting of dark grey regions, which is consistent with micrographs of the clears. Some calcium silicate particles are connected to the EDX spectrum by red arrows. The film integrity improves with cure time as the number of cracks in the cross-section lessens with each iteration. The iterations are also accompanied by increasingly drastic morphological differences between film topside and underside. The topside is easily discernible by the surface roughness, while the underside becomes more smooth due to interaction with the substrate. In micrographs of the early cures, the topside and undersides can be difficult to tell apart because of incomplete melting (indicated by yellow circles in 8-5b). In Figure 8-5c, the thin dark areas that permeate through the cross-section are examples of polymer that did not become a melt at the moment of quenching (indicated by yellow arrows). The clear film was converted into a melt by four minutes. However, the black film was accompanied by signs of incomplete melting all the up to 9 minutes of curing. This may be due to heat absorption by the pigments. Representative EDX spectra of two pigments used in the black films are shown in Figure 8-5. Carbon black is a second prime pigment for the black films, but cannot be distinguished from the polymer in EDX spectra.

In all TEM images in this study, including images of green and tan films, the large black needlelike particles are acicular silica. Cross-sections are 100-150 nm thick, while the silica particles are several microns long, which makes pullout due to microtome sectioning very likely. Pullout is observed in most of the large domains in Figure 8-5, and thus suggests most pigments have segregrated into the dispersed phase.

To investigate the point when pigments are absorbed into the domains, high magnification micrographs of the powder and early cure films are provided in Figure 8-6. The magnification is high enough to observe small magnetite particles (Fe_3O_4), and are thus identified by the EDX spectrum in the middle. The morophology of the black powder is largely similar to the clear powder analyzed in previous work, where the powder morphology has continuous regions with bubbles of possibly N_2 and dispersed wormlike regions. However, what is immediately apparent about the wormlike regions in the black powder is their consistent encapsulation of pigment particles. These wormlike regions have been established as domains (Chapter 7), and have already absorbed the acicular silica and prime pigments. The domain in Figure 8-6a is an ellipsoid with a high aspect ratio due to its encapsulation of the needle-like silica particle. Domains in the clear powder were approximately circular. At the onset of curing, the encapsulation continued under polymer sintering.

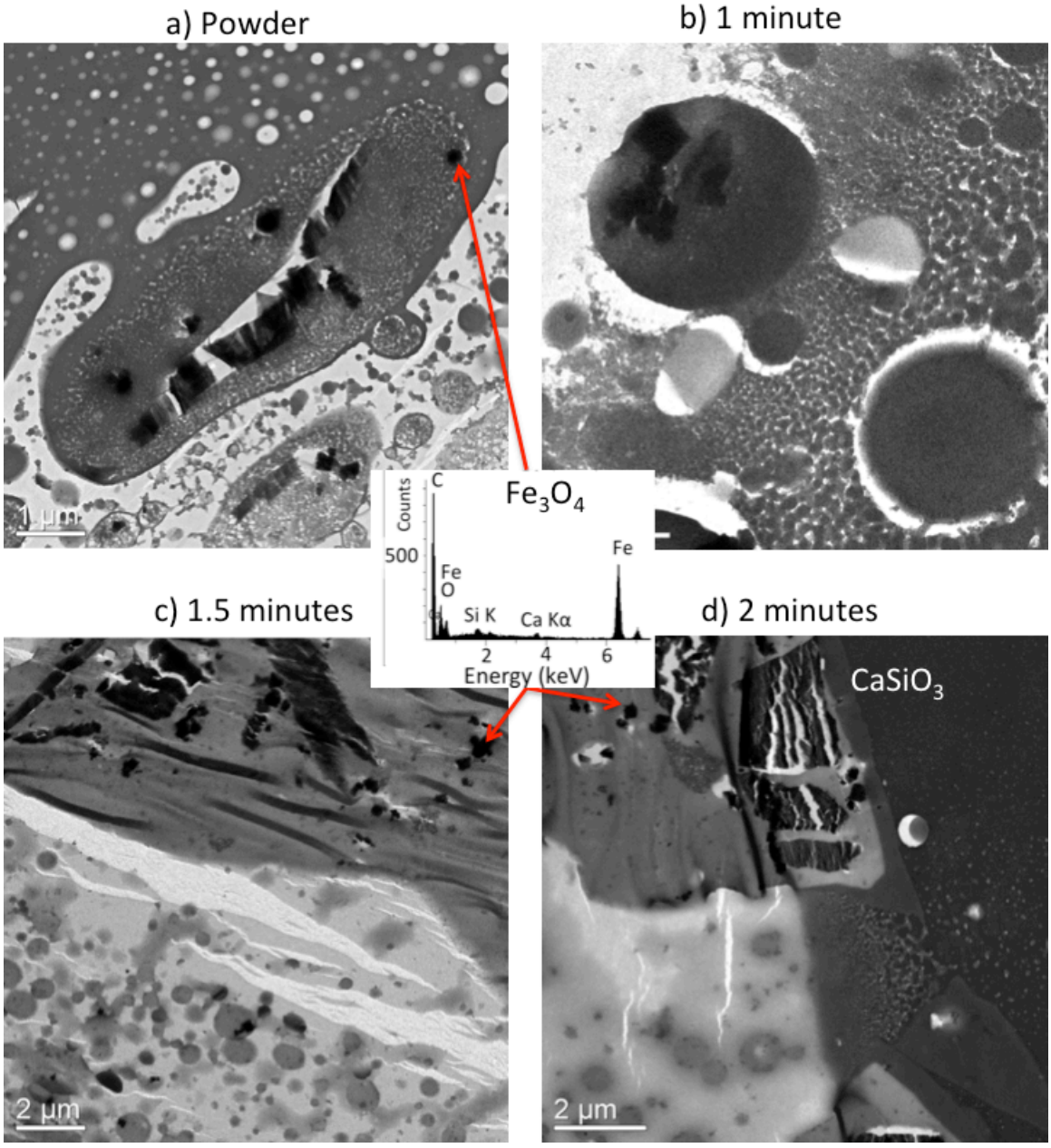

Figure 8-6. TEM of black powder before and during early cure.

In Chapter 7, domains in the 1.5-minute clear were extensively wrinkled from low crosslink density and potential relaxation from stresses induced by the microtome. Domains in the 1.5-minute black film have far fewer wrinkles than its clear counterpart. The wrinkles that do appear seem to be a result of the sectioned film folding upon itself

(Figures 8-6c and d). Amorphous and spherical domains alike also seem to merge at a rapid rate, which was also observed for the clears at this cure-time.

Figure 8-6d shows a large silicate particle surrounded by polymer melt in the center, which is characterized as light grey. The rest of the polymeric region ranges from dark grey to black, which indicates the polymer has not yet melted at this time. Calcium silicate is often used as a thermal insulator,[18] which may mean the silicate particles had interfered with the sintering process. The melt can be seen flowing out with domains interspersed within it. This uneven melting can also be observed in Figure 8-5c, where dark streaks span the entire cross-section. Domains can be seen nucleating out of these streaks. Such uneven melting has been observed in cross-sections up to the 9-minute sample.

Cross-sections at 2.5 and 3 minutes into the cure are shown in Figure 8-7. As was observed for the 3-minute clear, a percolating network that shares the same shade of grey now accompanies the domains, as exemplified in Figure 8-7a. For the clear, this emergence of percolation coincided with the onset of the second T_g. This network now permeates both the 2.5- and 3-minute black samples, whereas for the clear film it exists only at 3 minutes. The morphology of the percolating dark gray phase is very similar to its counterpart in the clear, as seen in Figure 8-7a. Its emergence coincides with the plateauing of the gloss at 2.5 minutes; for the clear the gloss plateaus thirty seconds later. Pigments thus add complexity to the curing dynamics, where the complexity manifests in the earlier onset of cocontinuity, while delaying some regions of the film from becoming a melt (see Figure 8-7c). However, the cocontinuous phase disappears by 4 minutes for the black and clear films, rendering it a transient secondary phase transformation.

Close inspection of the percolating resin network is displayed in Figure 8-7b. The white arrows point toward what are likely carbon black particles encapsulated within small segments of the percolating network that separated from the main network; this encapsulation at such a small scale is a testament to the degree of phase segregation for the pigments. At 3 minutes, the compressed appearance of the cocontinuous network in Figure 7-7c could be an omen of its transience. The white arrow points toward circular holes that is suggestive of a gas bubble. A hole in the center of 8-7b is also seen. It was explained in Chapters 5 and 6 that the gas is liberated ε-caprolactam. With pigments mixed in, the bubbles may push the percolating network toward the large pigments and thus compress it into thick lines of web-like material. The bubble in the center also is an indication of the outgassing caprolactam.

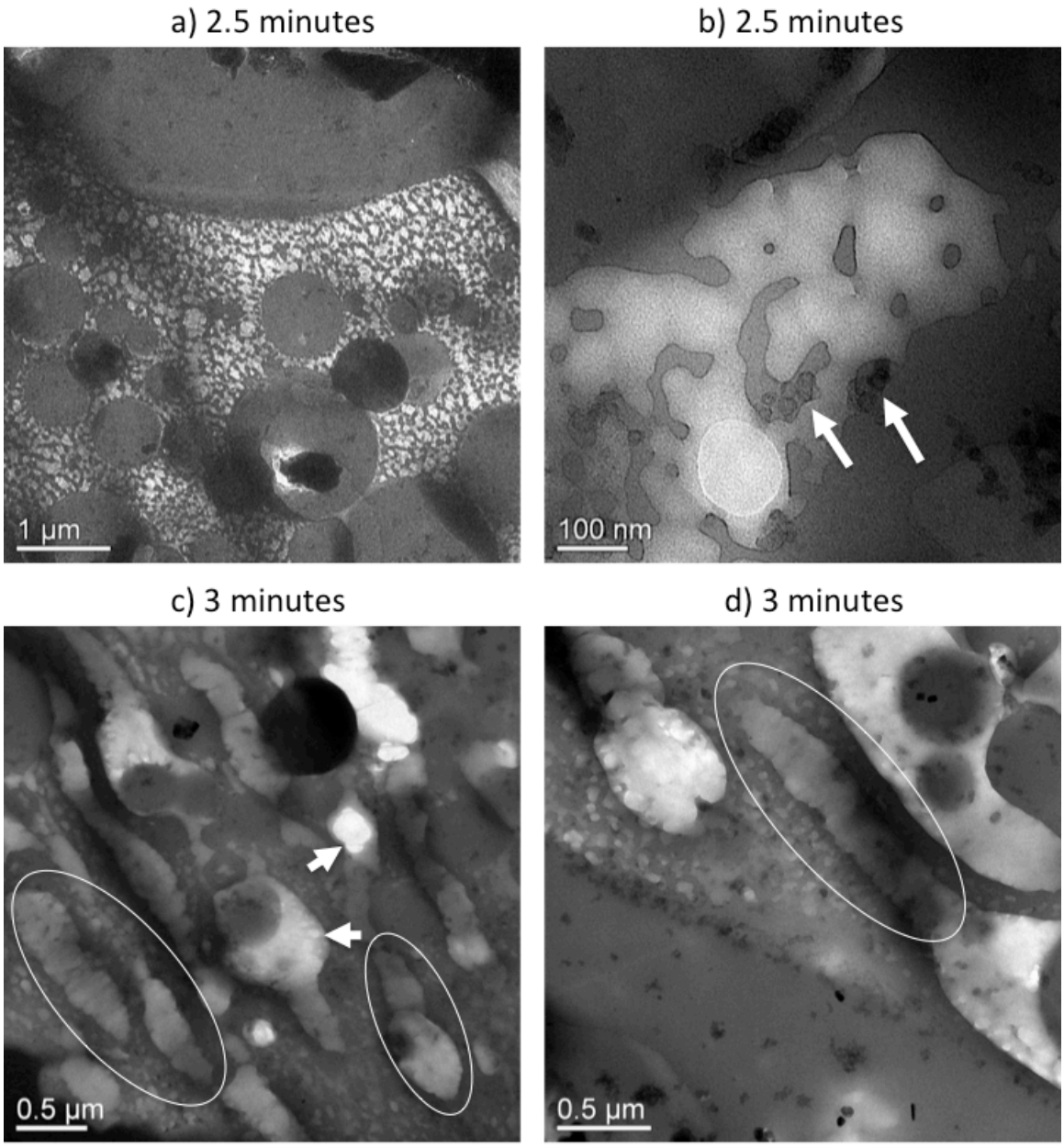

Figure 8-7. TEM images of the cross-sectioned black coating at 2.5- and 3-min cures.

Resin demixing may be another source of the compression, as indicated by the circled regions in Figures 8-7c and d that suggest the percolating network is splitting. The lighter shade of gray in the split suggests it is composed of low OH material. Another clue to its composition is that none of these light gray regions contain pigments. This splitting could be the start of the low OH resin becoming the continuous phase, as

the high OH material diffuses into the nascent and extant domains. The nearly white circles indicated by the white arrows in 8-7c appear to be bubbles of outgassing caprolactam. This is the manifestation of the percolation-to-cluster transition[19] that was discussed for the clear film, which displayed no such splitting. The addition of pigments may have effectively lengthened this transition such that it offered an opportunity for its observation by TEM.

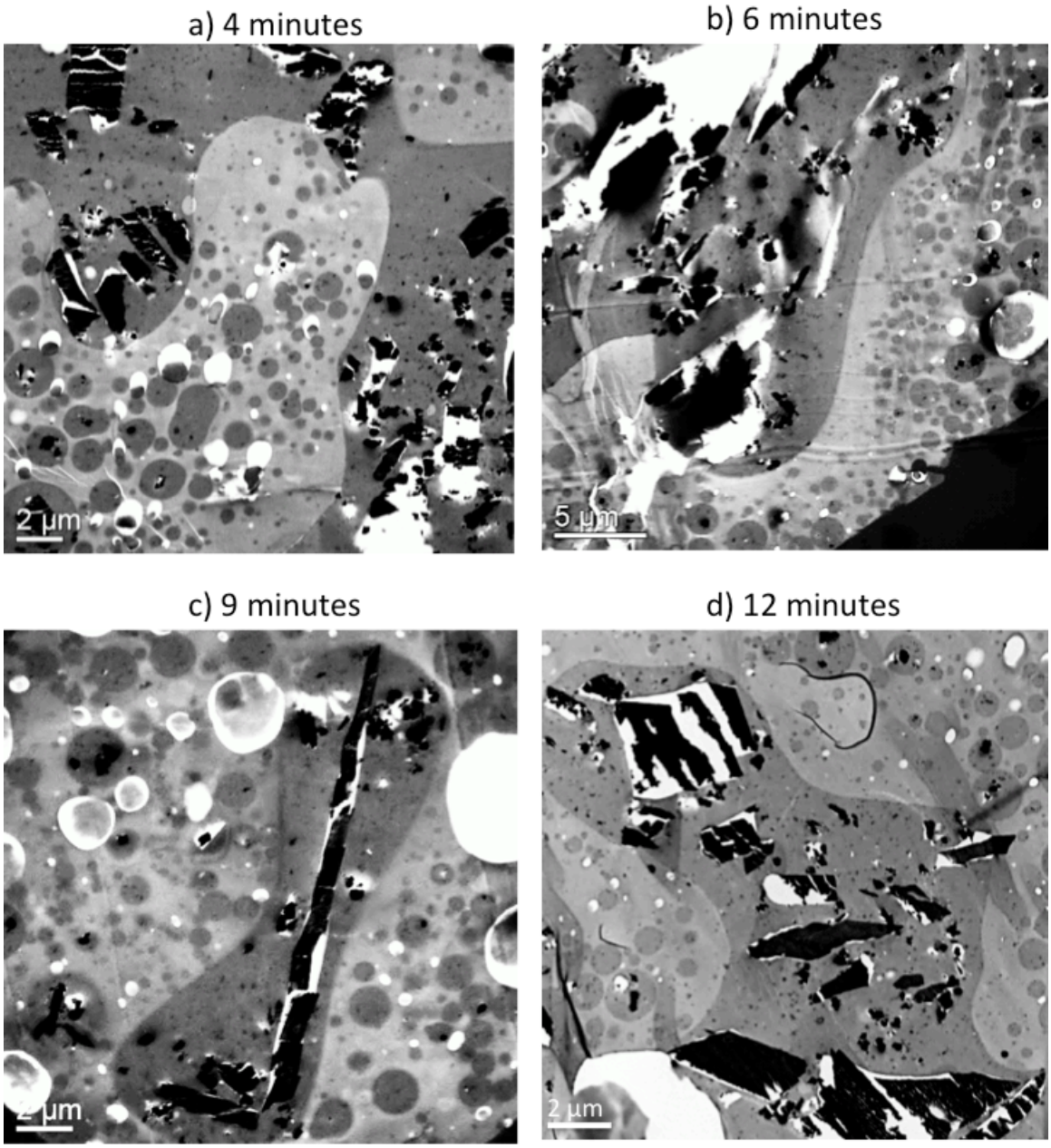

Figure 8-8. TEM images of cross-sectioned black coating at a) 4 minutes; b) 6 minutes; c) 9 minutes; d) 12 minutes.

Large amorphous domains in the coating bulk after 3 minutes are presented in Figure 8-8. Domains appear to change very little after the percolating phase disappears. Several small domains in the 4-minute sample (8-8a) show signs of coarsening, while the amorphous domain in the 6-minute (8-8b) sample does not have spherical domains in its

proximity, which suggests a depletion zone from the coarsening process; this has been observed for the clear samples at similar cure times (Chapter 7). As was observed in the clear film, the coalescence rate significantly slows down at 6 minutes, which is just past the gel point. Several domains in contact with each other appear to be compressed from repulsion rather than coalescence, which suggested a growing energy barrier toward coalescence due to continued crosslinking. This lack of apparent change for the domains conforms to the plateaued curves in Figures 8-2 and 8-3. In Chapter 7, the gel time for the clear film occurred at 5.5 minutes into the cure, but the domains continued to exhibit changes but at a slower rate. The uniformity of the domains in later-cure pigmented systems suggest that the gel point occurs at an earlier time, which is expected; adding pigments to the resins increases the viscosity, and by extension, may shorten the gel point.

8.3.4 Complementing TEM with SEM for cross-sections of fully cured black, tan, and green films

Figure 8-9 showcases the fully cured black coating surface via TEM and SEM. Both images feature the high surface roughness that characterize these coatings, but the TEM image shows that none of the pigments are exposed at the surface, as they are still encapsulated by the domains. The red line highlights the coating surface in 8-9b. This has important implications for optical engineering of surfaces, as this creates multiple indices for scattering within the film before light reaches a pigment particle. Numerous droplets of immiscible resin in the film may refract/reflect the light to the point where it returns to the surface. The addition of an extender pigment with high aspect ratio ($CaSiO_3$) scatters the light to even further where near opacity is achieved without prime pigments such as magnetite. It is when the pigments are forcibly flocculated by the

domains that the surface roughness increases by an order of magnitude relative to films prepared with single component resins.

The SEM image in 8-9b features the pigments in their natural state, as these were not subject to destructive forces from the microtome blade. The large needlelike particles are the $CaSiO_3$; the tiny particles are magnetite. The pigments in the SEM image are quite flocculated. Pigment segregation is not betrayed by the SEM images, but TEM with heavy metal staining consistently presents the segregation. The flocculation is not easily discerned from TEM images due to pullout, but it is quite apparent in the SEM image. These findings mark both electron microscopies as complementary techniques.

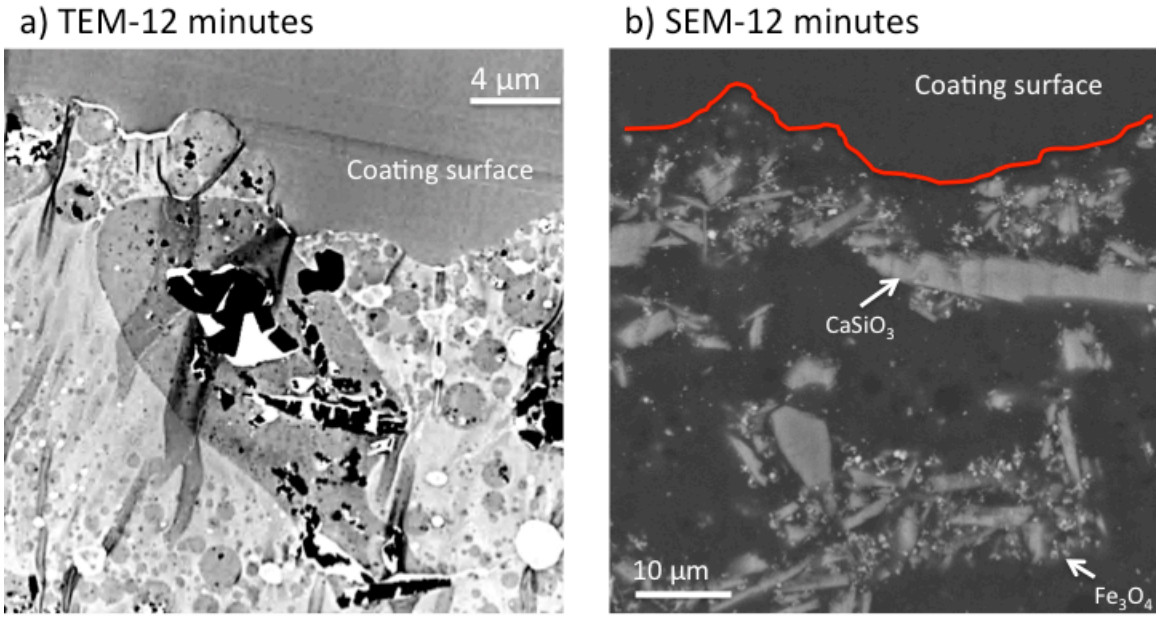

Figure 8-9. TEM and SEM images of cross-sectioned fully cured black coating.

Figure 8-10 shows micrographs of cross-sectioned tan coatings. The tan sample has the highest PVC among the three colors, and its pigments still segregate into the domains. The TiO_2 was pretreated with an organic surfactant for increased dispersion, but that did not prevent its subsequent flocculation. In fact, the pigment concentration in the domains became so high that the pigments effectively delineate the large domains in

the SEM image of Figure 8-10b. However, the high PVC for the tan exacerbated pigment pullout from microtome sectioning.

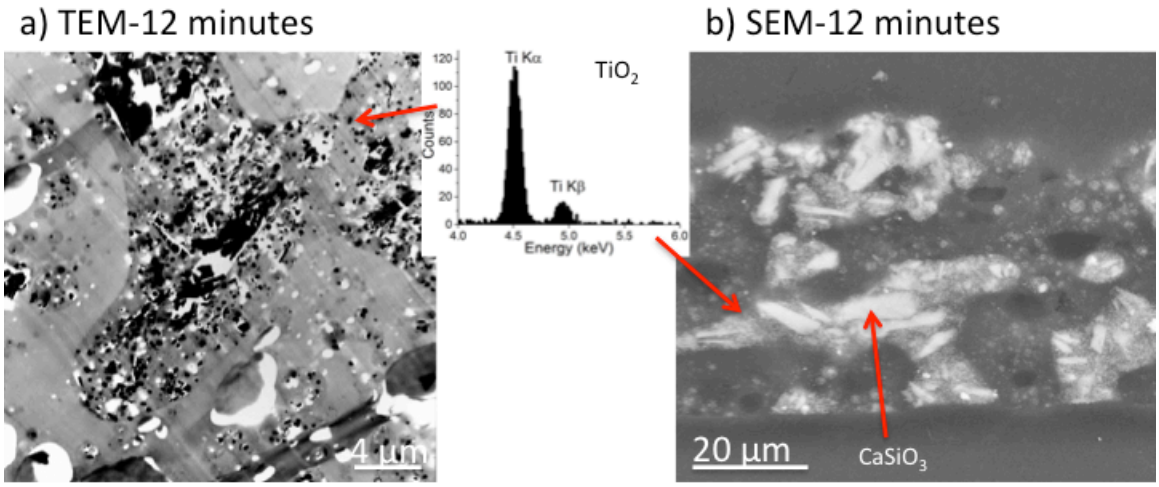

Figure 8-10. TEM and SEM images of fully cured tan coatings; red arrows connect the EDX spectrum to TiO_2 particles.

Pigment pullout was also a problem in preparing the cross-sections of the green sample, whose PVC lies between the black and tan films. Note that the Cu L peak in the EDX spectrum of Figure 8-11 stems from the copper grid in the TEM sample holder. The green film was applied as a topcoat onto an epoxy primer, which is evident in the bottom of Figure 8-11. This primer was found to alter the domain morphology at the primer-topcoat interface. Domain adhesion to the substrate has been observed in clear films starting at 1 minute, and in black films starting at 2 minutes, although adhered domains are suspected at 1 minute.

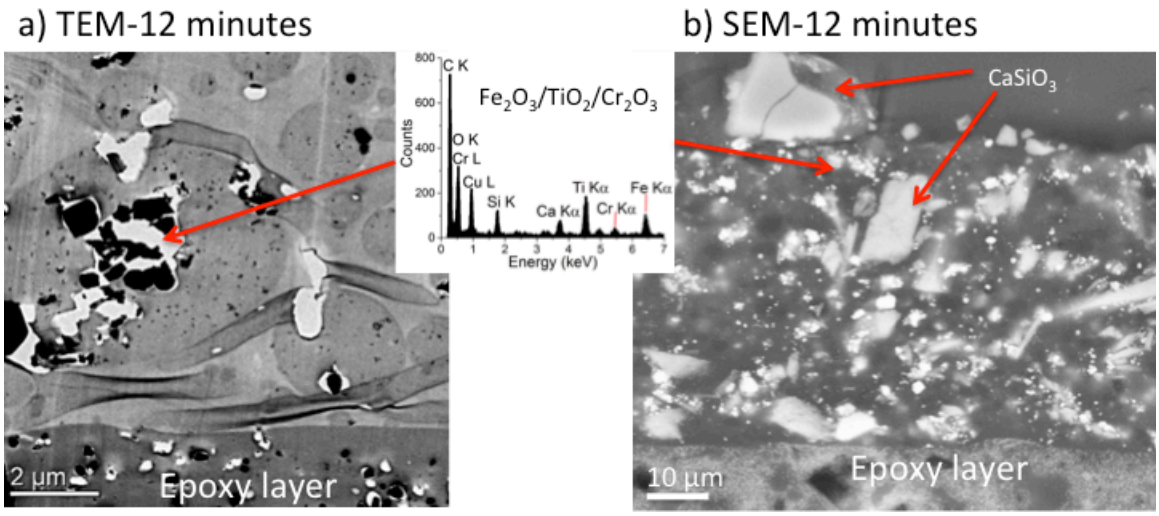

Figure 8-11. TEM and SEM images of cross-sectioned green coating on primer, plus EDAX spectrum of representative regions indicated by red arrows.

The primer also prevented domain adhesion for the black and tan films after their application. The contrast in domain behavior in proximity to the bare metal substrate is illustrated in Figure 8-12 for the black film. In 8-12a, an amorphous branched domain is observed adhering to the substrate interface in the center of the micrograph. However, in 8-12b, all of the proximal domains remain spherical. The lack of adhesion has also been observed in clear films that were applied on polytetrafluoroethylene (PTFE) coated aluminum substrates. PTFE has a surface energy of 21-22 mN/m, while epoxy is typically 42-46 mN/m.[15] The surface energy of metals are an order of magnitude higher than a resin surface.[20] The different behaviors exhibited by the domains with respect to their proximity to the substrate suggest that the interfacial energy of the high OH resin exceeds that of the low OH resin. Domains encapsulate the pigments because their interfacial energy differences are likely to be of smaller magnitude, while the interfacial energy of the low OH resin is likely more similar to PTFE and epoxy. According to a well cited paper by Funke and Murase, the segregation and domain adhesion to the

substrate is thermodynamically driven.[21] They analyzed a series of powder coatings blended with epoxy and acrylic resins that self-stratified into two layers. The base layer adhering to the substrate consistently was the resin with the larger of the two interfacial energies (epoxy). Considering that the segregation is observed in the powder before curing begins (Figure 8-6a), it may be unlikely that other factors such as reaction kinetics[22] caused the segregation.

8.3.5 Insight from XPS studies

The observed segregation may be thought of as a form of forced flocculation. Powder coatings are traditionally formulated for gloss ranges that require pigments to be well dispersed. Flocculated pigments can form clusters that increase the surface roughness and thereby lower the gloss, as observed in Figure 8-1c.[3] These clusters were likely formed during the extrusion; pigments were forced into the dispersed phase to form agglomerates, as attested by the TEM image of the powder in Figure 8-6a. Upon application, the sintering of the powder particles led to rapid coalescence of domains, which were already heavily loaded with pigments. These segregated agglomerates became segregated flocculates. This is possible due to the interfacial energy of the high OH resin being closer to the interfacial energies of the metal oxide pigments and tin substrate.

The film surfaces were analyzed by x-ray photoelectron spectroscopy, but the ensuing XPS spectra did not reveal metal peaks specific to the pigments. Since XPS sampling depth is limited to a few nanometers for polymers,[23] pigments would have to be right at the surface to be incorporated into the ensuing spectra. These results support the images in Figures 8-9a, in which pigments are generally > 10 nm below the surface.

As previously stated, the main difference between the two acrylic resins is their amount of hydroxyl moieties. The pigments have largely sequestered into the high OH resin before the cure even starts. It stands to reason that the greater number of hydroxyl groups in the high OH resin is the likely agency behind the segregation; i.e.; the high OH polyol is more acidic than its low OH counterpart, which makes more strongly bonding to basic metal oxide surfaces. The observation of pigment segregation in the powder (Figure 8-6a) means it must occur during the extrusion.

In the case of the black film, the magnetite and calcium silicate received no treatments prior to mixing. The long exposure to air meant the surfaces of these two pigments were likely covered with hydroxides of their own. Deconvolution of the O 1s XPS peak for both pigments did suggest the presence of a prominent OH band that increased when the incident angle for the x-ray beam was lowered to enhance surface sampling. The two mechanisms toward adhesion would be metal carboxylate bonds, or hydrogen bonding between the hydroxides of both polymer and pigment. The dominant mechanism cannot be determined, but it is likely that the cure temperature of 204 ˚C would increase the number of metal carboxylate bonds.

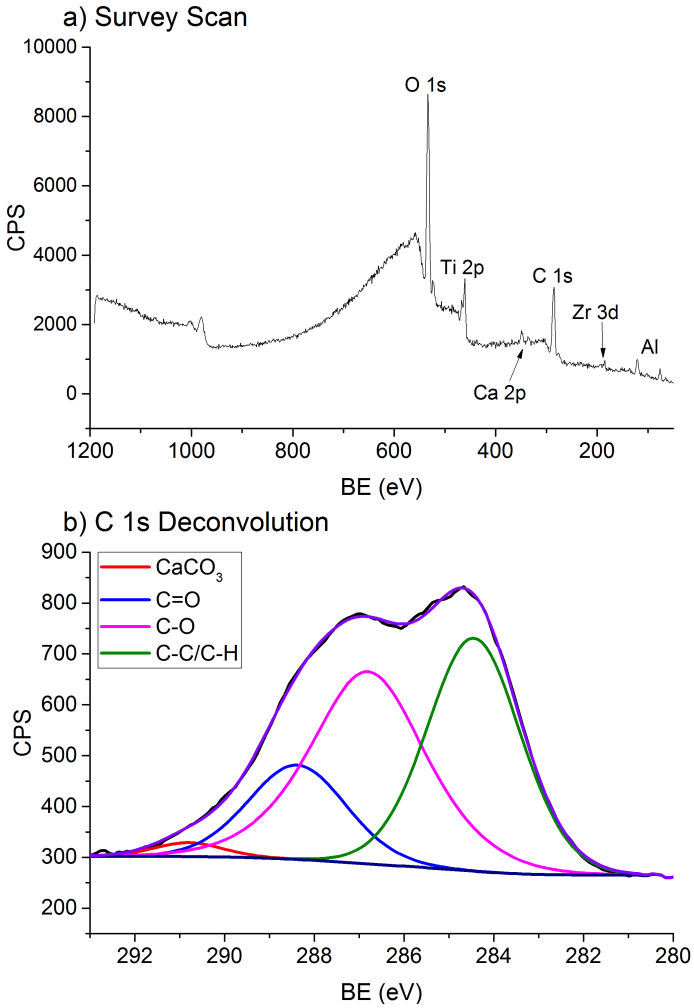

Figure 8-12. XPS spectra of TiO_2; a) wide scan; b) high-resolution C 1s.

In the case of TiO_2 for the tan film, despite its surface treatment with a resin for increased dispersion, Figure 8-10b shows heavy flocculation of the TiO_2 particles due to their sequestration into domains. Common organic coatings for TiO_2 include amines, amine salts, and polyols.[24] Figure 8-12a shows the wide scan XPS spectra. Prominent peaks include, Ti 2p at 450 eV, C 1s at 284.8 eV, O 1s at 531.5 eV.[25] The small Zr 3d peak at 185 eV[26] stems from the zirconia subshell that covers the TiO_2 particle. No N 1s peak is visible, which suggests the TiO_2 was not treated with an amine. Figure 8-12b shows a high resolution C 1s peak is largely a doublet due to dominance by the C–C/C–H

peak at 284.8 eV and the C–O peak at 286.7 eV. The important component is the C–O band, which is likely dominated by C–O–C and C–OH moieties. Next to the C–O band is a prominent C=O band at 288.5 eV. Both carbon-oxygen components indicate that the TiO_2 may have been treated with an acrylic polyol of its own. Thus, the organic coating around the TiO_2 particle appears to bond with the binder through the hydroxides as was observed with the untreated pigments in the black and green films, only now its greater compatibility with the high OH resin has greatly reduced the degree of dispersion.

8.4 Conclusion

Pigments have been incorporated into the immiscibly blended polyurethane binder to produce black, green, and tan coatings. The resins are rendered immiscible by their vastly different concentrations of hydroxyl groups prior to the curing reaction. The resin with the higher number of hydroxyl groups (high OH resin) constitutes the domains. The black coating has the lowest pigment-to-volume concentration (PVC) of the three colors, and thus has been selected to monitor how pigments affect the phase separation. When the binder consists of a single polyurethane component, the surface roughness for the resultant black film is an order of magnitude lower than for the blended black film; phase separation in the binder is thus a paramount requisite to produce a matte finish.

Gloss measurements of quenched black films at various cure times has shown that the gloss essentially plateaus 2.5 minutes into the cure. That is 1.5 minutes sooner than for the clear films. The gloss reduction is fast and more drastic for the black films. This is borne out in optical micrographs of the cross-sections, where there is little difference between samples cured for 3 minutes and 6 minutes.

Upon analysis by TEM, it was immediately evident that the large calcium silicate and the small magnetite particles exclusively resided in the dispersed phase, even within cross-sectioned powder particles. The early cure was also characterized by uneven heating, as evidenced by lighter gray regions proximal to $CaSiO_3$ particles.

At 2.5 minutes into the cure, a secondary phase transition emerged, in which the already present domains were accompanied by a percolating phase with a similar shade of gray. This phenomenon was previously observed for the clear film, but at 3 minutes. Both films had the percolating phase disappear by 4 minutes, making it transient. Signs of its transience have been suggested by apparent rifts in the percolating network, in which light grey material compresses the dark gray network into narrow streaks that eventually diffuse into extant domains and coalesce into nascent domains. The emergent light grey material may be the formation of the polymer matrix (low OH resin) as the two resins continue to demix. Observation of the rifts via TEM may be another aspect of the pigments interfering with the curing process. At 4 minutes and later, bulk morphology shows very little change up to full cure, which is another manifestation of the plateaued gloss and surface roughness.

Focus on the cross-sectioned surfaces of the different colored films shows that pigments are almost never exposed at the surface. This is also evidenced by the lack of metal peaks in photoelectron spectra. This means pigments always interact with light already refracted by one or more polymer interfaces, which is one cause of gloss reduction. The other, more important cause of gloss reduction is the forced flocculation of the pigments by the domains, even for pigments treated with a dispersant such as the TiO_2 for the tan films. Film shrinkage from mass loss via evaporating caprolactam may

also be a factor behind the high surface roughness, as the coating surface is then forced to conform to the shapes of the pigments at the surface even though they are in reality not exposed according to XPS.

The forced flocculation via encapsulation may be an outcome of the high OH resin having a far greater interfacial energy than the low OH resin. Hints of the segregation were previously observed in the clear film when its domains were observed wetting the tin plated substrate. The early onset of segregation and domains adhering to the tin substrate suggest thermodynamics to be the cause. The source of the higher interfacial energy in the domains may simply be their far greater number of hydroxyl groups. These hydroxides bond to other hydroxides already present on the pigments, surface-treated or untreated. Upon application on epoxy primers, domain adhesion was not observed, which may be due to the primer and low OH resin having interfacial energies of similar magnitude.

8.5 References

1. Duivenvoorde, F. L.; Nostrum, C. F. v.; Laven, J.; Linde, R. v. d., Improving Pigment Dispersing in Powder Coatings with Block Copolymer Dispersants. *Journal of Coatings Technology* **2000,** *72* (909), 145-152.
2. Richart, D. S., The Surface Topography of Powder Coatings and its Relation to Gloss. *Powder Coating* **1999,** *2*, 25-35.
3. Duivenvoorde, F. L.; Laven, J.; Linde, R. v. d., Diblock copolymer dispersants in polyester powder coatings. *Progress in Organic Coatings* **2002,** *45* (2-3), 127-137.
4. Misev, T. A.; van der Linde, R., Powder coatings technology: new developments at the turn of the century. *Progress in Organic Coatings* **1998,** *34* (1–4), 160-168.
5. Misev, T. A., Powder Coatings. In *Surface Coatings*, 2nd ed.; Paul, S., Ed. John Wiley & Sons: Chichester, England, 1996; pp 788-849
6. Krieger, I. M.; Dougherty, T. J., A Mechanism for Non‐Newtonian Flow in Suspensions of Rigid Spheres. *Transactions of The Society of Rheology* **1959,** *3* (1), 137-152.

7. Duivenvoorde, F. L. Pigment dispersing in powder coatings: synthesis and use of block copolymer dispersing agents. Doctoral Dissertation, Technische Universiteit Eindhoven, Eindhoven, 2000.
8. Ghiljadov, Z. K.; Erman, V. Y.; Tolstaya, S. N.; Uvarov, A. V., In *12th FATIPEC Congress*, 1974; p 617.
9. Wicks, D. A.; Jr., Z. W. W., Blocked Isocyanates III: Part A. Mechanisms and chemistry. *Progress in Organic Coatings* **1999,** *36*, 148-172.
10. Fletcher, T. E., A simple model to describe relationships between gloss behaviour, matting agent concentration and the rheology of matted paints and coatings. *Progress in Organic Coatings* **2002,** *44*, 25-36.
11. Tracton, A. A., *Coatings Materials and Surface Coatings*. CRC Press: Boca Raton, Florida, 2007; p 936.
12. Franklin, M.; Goldsbrough, K.; Parfitt, G.; Peacock, J., Influence of particle charge and resin adsorption on opacity of paint films pigmented with titanium dioxide. *Journal of Paint Technology* **1970,** *42* (551), 740.
13. Hansen, C. M., *Hansen Solubility Parameters: A User's Handbook*. 2nd ed.; CRC Press: Baca Raton, Florida, 2007.
14. Verkholantsev, V. V.; Flavian, M., Epoxy/Thermoplastic Heterophase and self-stratifying coatings. *Modern Paint and Coatings* **1995,** *85* (11), 100-106.
15. Verkholantsev, V. V., Self-stratifying coatings for industrial applications. *Pigment and Resin Technology* **2003,** *32* (5), 300-306.
16. Mahn, E. J. Low reflectance chemical agent resistant coating compositions. 20150259541 A1, January 23, 2015, 2015.
17. Formulations were prepared according to proprietary procedures, consistent with the requirements of U.S. Government specifications.
18. Kogel, J. E.; Society for Mining, M.; Exploration, *Industrial Minerals & Rocks: Commodities, Markets, and Uses*. Society for Mining, Metallurgy, and Exploration: 2006.
19. Hsu, D.-Y.; Chou, C.-M.; Chuang, C.-Y.; Hong, P.-D., Percolation of Phase-Separating Polymer Mixtures. *ACS Macro Letters* **2015,** *4* (12), 1341-1345.
20. Vitos, L.; Ruban, A. V.; Skriver, H. L.; Kollár, J., The surface energy of metals. *Surface Science* **1998,** *411* (1–2), 186-202.
21. Funke, W.; Murase, H., Uber die Bildung Mehrphasiger Filme Aus Pulverförmigen polymer-mischungen. In *15th FATIPEC Congress*, 1980; Vol. 2, pp 387-409.
22. Baghdachi, J.; Perez, H.; Talapatcharoenkit, P.; Wang, B., Design and development of self-stratifying systems as sustainable coatings. *Progress in Organic Coatings* **2015,** *78*, 464–473.
23. Briggs, D., *Surface Analysis of Polymers by XPS and Static SIMS*. Cambridge University Press: 1998; p 198.
24. Tyler, F. K., Tailoring TiO2 Treatment Chemistry To Achieve Desired Performance Properties. *Paint and Coatings Industry* February 2000, 2000, pp 32-34.
25. Watts, J. F.; Wolstenholme, J., *An Introduction to Surface Analysis by XPS and AES*. Wiley: 2003; p 212.
26. Brenier, R.; Mugnier, J.; Mirica, E., XPS study of amorphous zirconium oxide films prepared by sol–gel. *Applied Surface Science* **1999,** *143* (1–4), 85-91.

Chapter Nine

Investigation of Clear Coatings by XPS

9.1 Introduction

As coating performance is strongly tied to surface properties, x-ray photoelectron spectroscopy (XPS) is a natural analytical technique for coatings due to its surface and chemical sensitivity.[1] Interface chemistry may significantly differ from bulk chemistry, especially when bonding to the substrate is considered. Changes in peak height and position may provide important information on changes in surface chemistry. These changes manifest in the oxidation states and local chemical environment of the composing material. Therefore, the XPS spectra shown here compare chemistries from the coating-air and the coating-substrate interfaces. These changes are further investigated with angle-resolved XPS (ARXPS).

9.2 Instrumentation

A VG Scientific ESCA-3 x-ray spectrometer with an Al Kα source (1486.6 eV) was used to analyze clear coatings under ultra-high vacuum, where the operational pressure was 10^{-9} Torr. Survey scans were performed with a pass energy of 100 eV. High-resolution scans were performed with pass energy of 20 eV for the blends and 50 eV for the single component films, which had a spacing of 0.1 eV and a 100 ms dwell time. Both types of scans were repeated 50 times and co-added using the VGX900i software program. XPS spectra were processed with CASAXPS software.[2] Spectra were

calibrated with the polymer C–C bond at 285.0 eV, which conforms with calibration methods used by Beamson and Briggs for XPS spectra of polymers.[3] Two incident angles are used: the normal incident angle ($\theta = 90^\circ$) can penetrate a few nm beyond the surface, while $\theta = 60^\circ$ can lower the depth profile to better monitor chemical composition on the surface itself.[4]

9.3 Results/Discussion

9.3.1 Survey Scans of Airside and Substrate

As the tin substrate has been exposed to air prior to coating application, the substrate-air interface was likely dominated by tin oxide/hydroxide species. Metal oxide pigment interfaces would likely possess a preponderance of hydroxides, and thus the substrate would provide a good model for the interaction between polymer and pigment in the coating system.

The Sn peaks at 486 and 495 eV stem from partially exposed substrate.[5] No nitrogen peaks were observed, which suggests the nitrogen-based moieties segregated into the bulk.

The relative peaks areas and corresponding ratios of the C 1s and O 1s peaks for all sample interfaces are presented in Table 9-1. Starting with the sample air-sides (air-polymer interfaces), at $\theta = 90^\circ$ and 60°, the low OH and high OH films have low concentrations of oxygen species both at the surface and at the bulk. The blend has significantly higher concentration of oxygen species, and may be related to a surface energy phenomenon involving the resin components; i.e.; the segments of the low surface energy component (matrix) would have greater mobility than the high OH component

(domains), and thus is likely to be pushed up toward the surface. This corroborates the lack of surfaced domains with respect to the cross-section (Chapters 4-8).

Table 9-1. Atomic percentages at 90˚ and 60˚ incident angles of polymer interfaces.

Sample	θ (˚)	C %	O %	Ca %	Sn %	O/C
Low OH Air-side	90	83.49	15.34	1.17	0	0.18
	60	83.56	14.70	1.66	0.07	0.18
Low OH Substrate-side	90	69.77	29.36	0.87	0	0.42
	60	55.68	43.45	0.87	0	0.78
High OH Air-side	90	87.96	10.25	1.79	0	0.12
	60	82.74	15.57	1.68	0	0.19
High OH Substrate-side	90	71.97	25.77	1.14	0	0.36
	60	64.53	33.65	1.82	0	0.64
Blend Air-side	90	72.37	26.26	1.38	0	0.36
	60	56.76	41.86	1.24	0.14	0.46
Blend Substrate-side	90	80.13	18.32	1.2	0.35	0.22
	60	71.33	26.36	2.05	0.25	0.37
Substrate After Peeling	90	84.68	12.25	2.64	0.43	0.15
	60	74.90	22.50	2.43	0.18	0.30

The substrate-side of the samples generally has much higher oxygen content. O/C ratios for the sample substrate-sides at both angles are also in Table 9-1. Note that no tin substrate was present for these measurements, as the films were peeled off and turned upside down for sample mounting. The wide scan spectra for the SC films contained no Sn peaks. Peel failure occurred easily for the SC films, whereas it took more effort to peel off the blended film, which suggested that the blend experienced greater adhesion to the substrate than for the SC films. The substrate-side of the blend has the second highest Sn atomic percentage in Table 9-1, which has important implications for polymer adhesion, and will be discussed in a subsequent paragraph. A wide scan spectrum of the blend underside is shown in Figure 9-1, with Sn and Ca peaks indicated as well.

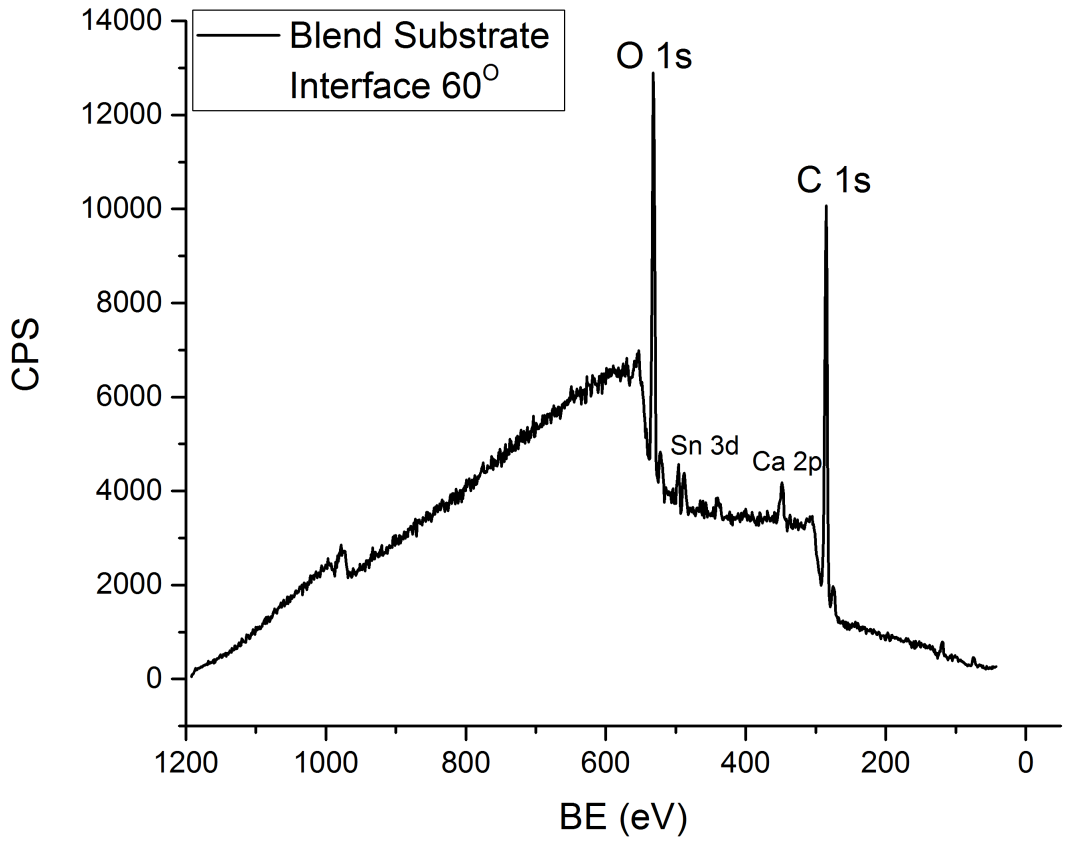

Figure 9-1. Survey scan of blend underside at 60° incident angle.

9-2.2 Airside

Curve fitting of the high-resolution C 1s spectra were resolved into five bands. These include aromatic carbon at 284.1-284.5 eV, C-C/C-H at 285.0 eV, C-O at 286.0-286.3 eV, C–N at 287.4-287.8 eV, and O-C=O at 289.0-289.5 eV. The detection of prominent aromatic peaks by FTIR and Raman spectroscopy necessitated the inclusion of the aromatic band into the fitting. According to Kassis *et al*., the binding energy of the aromatic band can be as low as 284.1 eV, which was observed for most samples in this study; the broadening and downshift in binding energy may be a consequence of complex inter- and intramolecular interactions by branched phenyl groups with polar groups.[6] The C-O peak may consist of ether, alcohol moieties, or carbon atoms secondary to ester

moieties.[7] The C=O peak consists of contributions from urethane[8-9] and ester moieties.[10] The C–N peak could be assigned to urea,[9, 11] but the lack of N 1s in the wide scan makes this a weak assignment. However, it is very large for the high OH airside, and could be partially correlated with the quantity of Isophorone diisocyanate (IPDI) curative (See Table 5-1). Moreover, Briggs Beamson also found the binding energy of the amide moiety within the heterocyclic ring of poly(N-vinylpyrrolidone) to be about 287.8 eV,[3] which serves as a good approximation for urea within a heterocyclic ring. The blend has the largest C–O at both angles, but it jumps drastically at 60°. This may be an outcome of surface energy gradients from phase separation pushing highly mobile C–O moieties toward the surface. The high OH film has the highest C–N band at 90°; at 60° the C–N band is highest for the low OH film. The C=O band is very small for all samples as expected since hard segments prefer the bulk due to their lower segmental mobility.[1, 11-12] Interestingly, the SC films appear to have slight surface enrichment of the C=O band. The low OH surface is also enriched with the C–N moiety, potentially suggesting that the crosslink density for the low OH is low enough to enable the necessary mobility for C=O and C–N moieties to diffuse toward the polymer surface.

Table 9-2. Contribution of different functionalities to envelope of deconvoluted C 1s XPS spectra at 60° and 90° incident angles and their ratios for air-side

Sample	θ (°)	C–O %	C–N %	C=O %	$\frac{\text{C–O(60°)}}{\text{C–O(90°)}}$	$\frac{\text{C–N(60°)}}{\text{C–N(90°)}}$	$\frac{\text{C=O(60°)}}{\text{C=O(90°)}}$
Low OH Air-side	60	25.9	16.9	5.1	0.90	1.64	1.2
	90	28.8	10.3	4.2	–	–	–
High OH Air-side	60	30.5	13.3	3.8	1.09	0.61	1.36
	90	28.1	21.8	2.8	–	–	–
Blend Air-side	60	49.7	5.6	4.0	1.4	0.5	0.59
	90	35.5	11.2	6.8	–	–	–

High-resolution spectra from the blend air-side are displayed in Figure 9-2. As discussed previously, the C 1s spectra show the C–C and C–O bands encompassing larger shares of the surface. This is also reflected in the O 1s spectra of A-2b and A-2c. According to Briggs and Beamson, $BE_{C=O}$ = 531.3-532.3 eV, which encompasses hydroxyl, urethane, urea, and ester; BE_{C-O} = 532.3-533.8 eV and consists of alcohol, ether, and single-bonded oxygen atoms in ester and urethane.[13] Hydroxyl groups likely originate from the aluminum foil and the tin substrate possessing thin hydroxide layers on their surfaces. The Al peaks are very small in the wide scan and thus indicate that Al–O/Al–OH bands contribute little to the O 1s peak. Very small Si peaks were detected in the survey scans, and are likely SiO_2 from the Resiflow flow agent. SiO_2 peaks range from 533.4-534.3 eV[5] and overlap with potential contamination from water, which also has a wide range (533.3-535.5 eV),[3] but the very small concentration of Si makes it unlikely to be a major contributor to the O 1s envelope, and thus not counted. The peak at 534 eV stems from possible water contamination within the polymer and on exposed substrate. From 90˚ to 60˚, the changes in C=O and C–O intensities in the C 1s spectrum reflect their counterparts in the O 1s spectrum. For example, at $\theta = 60^{\circ}$ the C–O has a larger share of the envelop for both the C 1s and O 1s. Also, note that the O–Sn peak at ~ 530 eV is slightly larger at 60˚, which is due to the greater exposure of the tin substrate to the x-ray beam.

As has been mentioned, all survey scans showed a small Ca 2p peak at 347 eV. The Ca 2s peak at 440 eV is also visible. The 2p peak is curve-fitted as shown in Figures 9-2e and 9-2f. What is apparent from the 90˚ scan is that the calcium peak is comprised of roughly equal parts $CaCO_3$ and CaO; the $CaCO_3$ peaks are located at 347.6 and 351.3

eV,[14] CaO peaks at 346.3 and 349.7 eV.[5] At 60°, $CaCO_3$ becomes the dominant calcium compound. This suggests that an outer carbonate layer covers the calcium-based particles in or on the film, which is what would be in contact with the polymer. Additionally, a portion of the C=O peak in the C 1s and O 1s spectra would have a $CaCO_3$ component that might widen the peak and shift the peak position to slightly higher binding energy, as the peak position of this component is 289.6 eV for C 1s, 531.3 eV for O 1s.[5] The $CaCO_3$ could have been a leftover pigment used in previous coating applications in the facility of origin, as it has been found in the polymer-substrate interfaces of all samples.

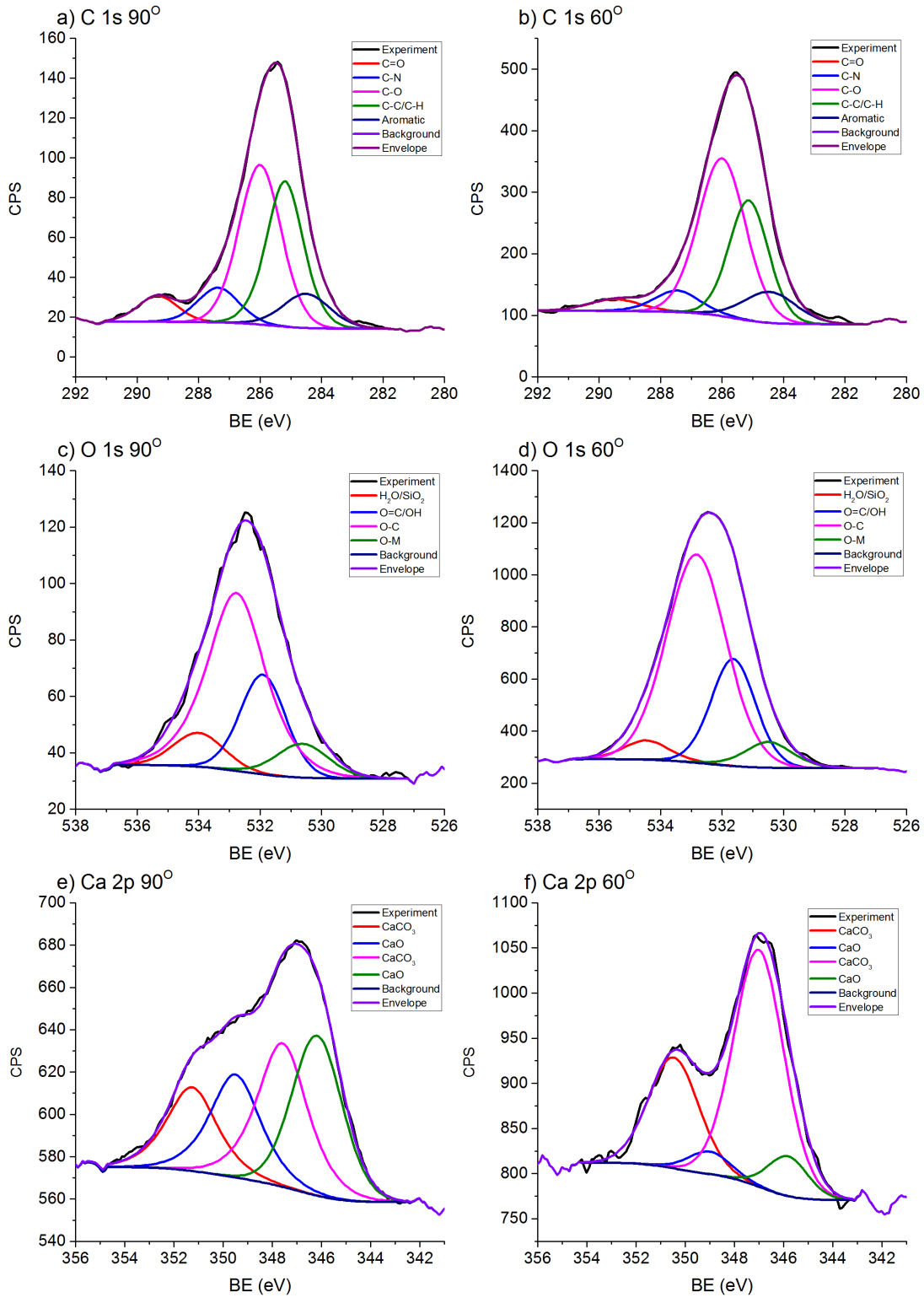

Figure 9-2. ARXPS spectra of the blend measured from the top surface; a) C 1s at 90˚; b) C 1s at 60˚; c) O 1s at 90˚, d) O 1s at 60˚, e) Ca 2p at 90˚, f) Ca 2p at 60˚.

9.3.2 Investigations of polymer adhesion

Intensities of bands within the C 1s spectrum of the substrate-sides and exposed substrate are displayed in Table 9-3. As previously mentioned, the polymer film was peeled off the substrate, and thus no tin substrate was sampled. As seen in Table 9-1, the O 1s peak is consistently larger than the C 1s peak for all substrate-sides. At 60˚, the O/C ratio increases, which suggests there are more oxygen atoms at the interface. The extra interfacial oxygen may originate from tin oxide or hydroxide deposits remaining on the polymer interface and consequently bonds with carbon or hydrogen bonds with highly mobile C–O components. This is implied in Table 9-3; an implication consistent with expectations regarding polymer-metal bonding, in which it is the oxygen that bonds the polymer with the metal.[15] The higher number of C–O bonds at the interface may be indicative of adhesion via M–O–C bonding or hydrogen bonding and is in line with the greater O/C ratio from Table 9-1.[16]

Also according to Table 9-3, the blend has slight enrichment of C=O content at the interface, but the SC resins have C=O groups preferring the bulk. The C–N moiety displays the most interesting behavior, as it does not change with respect to the incident angle for the low OH film, while diminishing for the high OH and blend films at 60˚.

Table 9-3. Contribution of different functionalities to envelope of fitted C 1s XPS spectra at 60˚ and 90˚ incident angles and their ratios for substrate-side and tin substrate

Sample	θ (˚)	C–O %	C–N %	C=O %	$\frac{\text{C–O}(60^\circ)}{\text{C–O}(90^\circ)}$	$\frac{\text{C–N}(60^\circ)}{\text{C–N}(90^\circ)}$	$\frac{\text{C=O}(60^\circ)}{\text{C=O}(90^\circ)}$
Low OH Substrate-side	60	50.6	10.1	4.6	1.49	1	0.44
	90	33.6	10.1	10.5	–	–	–
High OH Substrate-side	60	43.2	10.5	5.6	1.29	0.73	0.85
	90	32.9	14.4	6.6	–	–	–
Blend Substrate-side	60	50.6	5.9	4.3	1.8	0.33	1.16
	90	26.0	20.4	3.2	–	–	–
Substrate After Peeling	60	34.3	9.7	1.9	0.79	2.62	0.76
	90	43.6	3.7	2.5	–	–	–

High-res photoelectron spectra from the blend substrate-side are displayed in Figure 9-3. At 90˚, the C 1s substrate-side spectrum significantly differs from the airside 90˚ C 1s spectrum with respect to the C–N band (quantified in Table 9-3). At 60˚, the air-side and substrate-side C 1s spectra look nearly identical in that they are dominated by C–C/C–H and C–O bands. The enlarged C–N band at 90˚ suggests higher urea concentration, but there also could be isocyanate salts present at the interface. As urea contains a carbonyl bond, this higher urea band in the C 1s spectrum would likely enlarge the C=O peak in the corresponding O 1s spectrum. However, as indicated by Table 9-2, the presence of Sn peaks suggests there should be hydroxyl groups from the tin that affect the O 1s peak. Hydroxyl groups overlap with C=O, and thus gives rise to the C=O/OH band in Figures 9-2c-d and 9-3c-d. The substrate-side of the blend also has significant Ca contamination (Figure 9-1), and thus further increase the C=O/OH band. Significant contributions from O–C, H_2O, and O–M bands broaden the O 1s to the point where its FWHM is 3.54 eV, making it the widest O 1s peak in the sample set. The substrate was long exposed to air before application, allowing the formation of thick oxide/hydroxide layers on the tin substrate. This is why the O–Sn band positioned at 530.2 eV[17] is 35% of the envelope, which is formed from contributions by SnO, SnO_2 and mixtures of oxide species in between.

The Sn $3d_{5/2}$ peak is deconvoluted into two bands in Figures 9-3e and 9-3f. This is a best guess approach since the chemical states of tin oxides show considerable variation and overlap according to an extensive review of tin oxides by Batzill and Diebold.[18] The binding energy of SnO_2 ranges from 486.3 eV to 487.5 eV; SnO ranges from 485.6 eV to 486.9 eV. At 60˚, the SnO/SnOH peak is larger, which suggests that

the x-ray beam sampled the portion of the substrate cleaved at a point where more SnO was present. These tin deposits were sampled upside down, where the region that was closer to the bulk has now become closer to the surface.

The results above suggest that hydrogen bonding and possible covalent bonding through oxygen atoms between the metal and polymer are the likely mechanisms for adhesion. However, investigating adhesion with XPS alone is an extremely difficult endeavor. Chemini and Watts also analyzed the undersides of polymeric films, but also created thin layers (< 2 nm) of model compounds from dilute solutions (e.g., methylene diphenyl diisocyanate) to study the interfacial chemistry.[19] Their investigations suggested that isocyanates react with the hydroxylated steel to form a covalent bond between iron and urethane. The lack of an N 1s peak in the wide scan spectra renders this as an unlikely mechanism for adhesion for the coatings analyzed in this study. Several adhesion studies[4,20-21] utilized high-resolution time-of-flight secondary ion mass spectroscopy (ToF-SIMS) to complement XPS on the analysis of thin films of model compounds. Therefore, without the resources necessary to create nanometer-thick films of model compounds and access to ToF-SIMS, the investigation of adhesion by XPS remains incomplete.

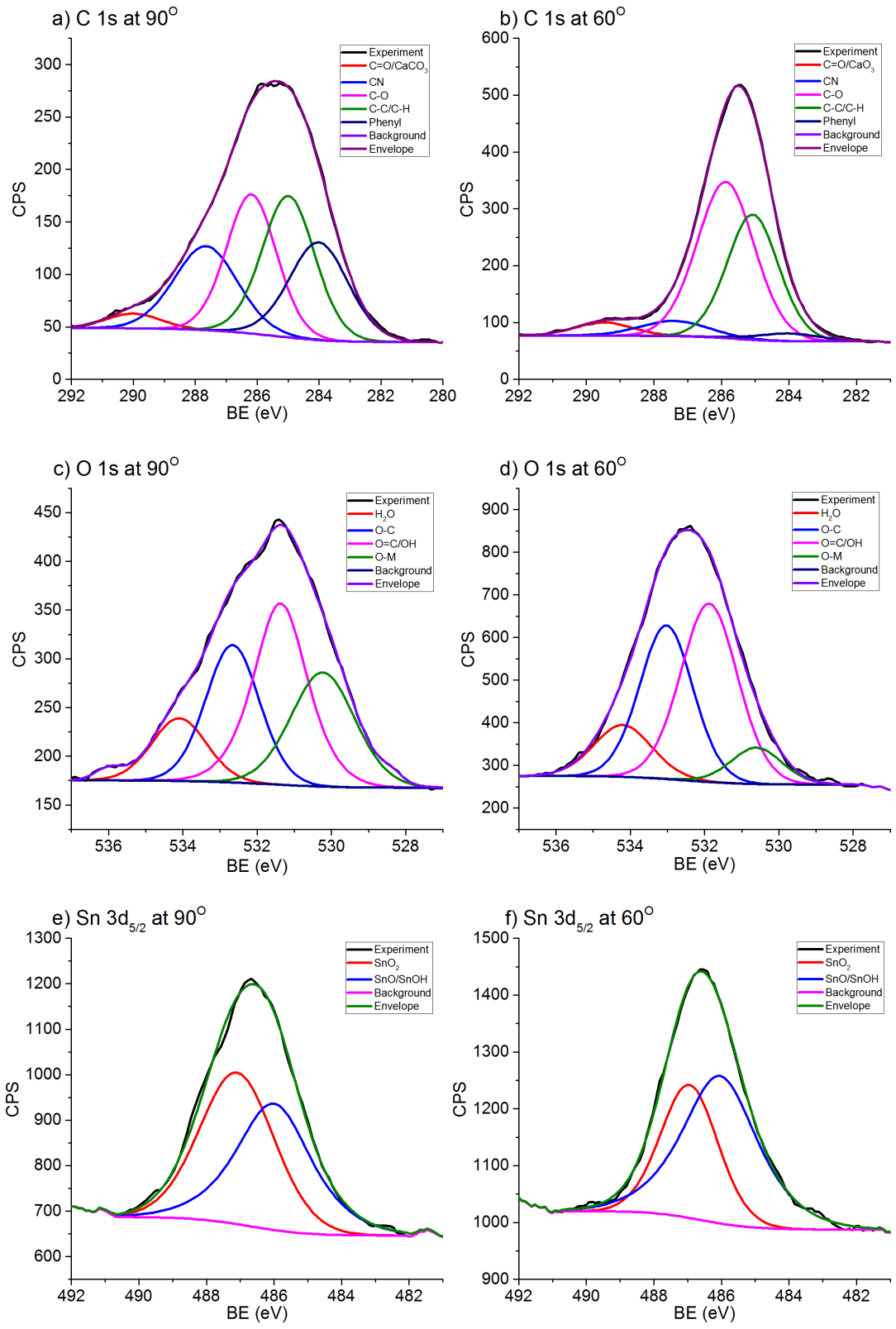

Figure 9-3. High-resolution XPS of blend substrate-side; a) C 1s at 90°; b) C 1s at 60°; c) O 1s at 90°; d) O 1s at 60°; e) Sn $3d_{5/2}$ at 90°; f) Sn $3d_{5/2}$ at 60°.

9.4 Conclusion

Comparison between survey scans of the airsides and substrate-sides revealed an accumulation of oxygen at the substrate-sides, especially when the incident angle was lowered to 60°. The source of the oxygen may stem from the tin oxide substrate, since metal substrates are known to have oxide overlayers. Traces of Sn were observed in the spectrum for the blend substrate-side, which indicated strong adhesion for the blend. All survey scans also showed contamination from Ca 2p and 2s peaks.

In the high-res C 1s spectra: Five bands were resolved, aromatic, C–C/C–H, C–O, C–N, and C=O. The C–N band is a weak assignment due to the lack of N 1s peaks in all survey scans, but better assignments were lacking. The C–N peak may be related to urethane/urea moieties. For the airside, the single component (SC) films showed significant surface enrichment of C–N and C=O; the blend showed very significant surface enrichment of C–O. The phase separation in the blend may have pushed mobile C–O moieties toward the surface. Four bands were observed in the high-resolution O 1s spectra: O–C, O=C, H_2O, and O–M. The metal is likely to be Ca or Sn. Angle variation produced little change among moieties.

On the substrate-side, where the mechanism of adhesion was investigated, ARXPS measurements revealed that the blend had a greater quantity of C–O moieties at 60°. 90° measurements revealed greater quantities of O–M and C–N moieties. This may be due to the location of the peel failure; i.e., failure occurred above the interface, and thus exposed a region that was less concentrated with SnO. These findings suggest that adhesion occurred through establishing carboxylate bonds. Hydroxide bonds may also have played a role, but this cannot be verified through XPS.

9.5 References

1. Mishra, A. K.; Chattopadhyay, D. K.; Sreedhar, B.; Raju, K. V. S. N., FT-IR and XPS studies of polyurethane-urea-imide coatings. *Progress in Organic Coatings* **2006,** *55* (3), 231-243.
2. Fairley, N. *CASAXPS*, 2.3.16; 2011.
3. Beamson, G.; Briggs, D., *High resolution XPS of Organic Polymers: the Scienta ESCA300 Database*. John Wiley: Chichester, England, 1992.
4. Watts, J. F.; Wolstenholme, J., *An Introduction to Surface Analysis by XPS and AES*. Wiley: Chichester, England, 2003; p 212.
5. Moulder, J. F.; Stickle, W. F.; Sobol, P. E.; Bomben, K. D., *Handbook of X-ray Photoelectron Spectroscopy: A Reference Book of Standard Spectra for Identification and Interpretation of XPS Data*. ULVAC-PHI Inc.: Chigasaki, Japan, 1995.
6. Kassis, C. M.; Steehler, J. K.; Betts, D. E.; Guan, Z.; Romack, T. J.; DeSimone, J. M.; Linton, R. W., XPS Studies of Fluorinated Acrylate Polymers and Block Copolymers with Polystyrene. *Macromolecules* **1996,** *29* (9), 3247-3254.
7. Perruchot, C.; Watts, J. F.; Lowe, C.; White, R. G.; Cumpson, P. J., Angle‐resolved XPS characterization of urea formaldehyde–epoxy systems. *Surface and Interface Analysis* **2002,** *33* (10‐11), 869-878.
8. Hearn, M. J.; Ratner, B. D.; Briggs, D., SIMS and XPS studies of polyurethane surfaces. 1. Preliminary studies. *Macromolecules* **1988,** *21* (10), 2950-2959.
9. Sanchis, M.; Calvo, O.; Fenollar, O.; Garcia, D.; Balart, R., Surface modification of a polyurethane film by low pressure glow discharge oxygen plasma treatment. *Journal of Applied Polymer Science* **2007,** *105* (3), 1077-1085.
10. Briggs, D.; Seah, M. P., *Practical Surface Analysis, Auger and X-ray Photoelectron Spectroscopy*. Wiley: 1990.
11. Chattopadhyay, D. K.; Sreedhar, B.; Raju, K. V. S. N., Effect of Chain Extender on Phase Mixing and Coating Properties of Polyurethane Ureas. *Industrial & Engineering Chemistry Research* **2005,** *44* (6), 1772-1779.
12. Chattopadhyay, D.; Sreedhar, B.; Raju, K., Influence of varying hard segments on the properties of chemically crosslinked moisture‐cured polyurethane‐urea. *Journal of Polymer Science Part B: Polymer Physics* **2006,** *44* (1), 102-118.
13. Briggs, D.; Beamson, G., XPS studies of the oxygen 1s and 2s levels in a wide range of functional polymers. *Analytical Chemistry* **1993,** *65* (11), 1517-1523.
14. Granados, M. L.; Poves, M. D. Z.; Alonso, D. M.; Mariscal, R.; Galisteo, F. C.; Moreno-Tost, R.; Santamaría, J.; Fierro, J. L. G., Biodiesel from sunflower oil by using activated calcium oxide. *Applied Catalysis B: Environmental* **2007,** *73* (3–4), 317-326.
15. Hare, C. H., *Protective Coatings: Fundamentals of Chemistry and Composition*. Technology Publishing Company: Pittsburgh, Pennsylvania, 1994; p 514.
16. Pokrajac, L. A., *Fundamental Studies of Polyurethane - Aluminum Adhesion [microform] : Phenyl Isocyanate Interaction with Prepared Aluminum Oxide Surfaces*. Thesis (M.Sc.)--University of Toronto: 1998.
17. Tselesh, A. S., Anodic behaviour of tin in citrate solutions: The IR and XPS study on the composition of the passive layer. *Thin Solid Films* **2008,** *516* (18), 6253-6260.
18. Batzill, M.; Diebold, U., The surface and materials science of tin oxide. *Progress in Surface Science* **2005,** *79* (2–4), 47-154.

19. Chehimi, M. M.; Watts, J. F., An XPS study of the steel-aromatic moisture-cured urethane interface. *Journal of Adhesion Science and Technology* **1992,** *6* (3), 377-393.
20. Shimizu, K.; Phanopoulos, C.; Loenders, R.; Abel, M. L.; Watts, J. F., The characterization of the interfacial interaction between polymeric methylene diphenyl diisocyanate and aluminum: a ToF‐SIMS and XPS study. *Surface and Interface Analysis* **2010,** *42* (8), 1432-1444.
21. Tardio, S.; Abel, M.-L.; Carr, R.; Watts, J., A Study of the Interfacial Interaction between Methylene Diphenyl Diisocyanate and Metals by XPS and ToF-SIMS. In *5th World Congress on Adhesion and Related Phenomena*, Nara, Japan, 2014.

Chapter Ten

Conclusions and Future work

10.1 Conclusions

Novel powder thermosets consisting of immiscible polyurethane resins have been extensively analyzed by spectroscopy and microscopy. These powder coatings were formulated for low-reflectance outdoor applications, where the surface is extensively roughened by a combination of matting agents and droplet domains within the binder. The composition of the domains was unknown at the start of this work.

The acrylic polyol resins were rendered immiscible via differences in the amount of hydroxyl content prior to crosslinking with an ε-caprolactam-blocked polyisocyanate compatibilizer. One resin had high numbers of hydroxides (high OH), the other resin had a low hydroxide number (low OH). The immiscibility produced a phase separation within the binder that resulted in a morphology of droplet domains. The domains served to roughen the coating surface for loss reflectance applications. Incorporation of matting agents and prime pigments further increased the surface roughness. The composition of the phases within the binder was unknown at the start of this work.

To identify the phases, a series of powder coatings were prepared without pigmentation, which enabled spectroscopic analysis of the binder by itself. These blends of clear films were accompanied by single component (SC) resin films, which served as controls in order to determine phase identification. The phases were successfully identified via micro-Raman analysis of coating cross-sections. Preparation of cross-

sections was accomplished by utilizing the MOPAS Polisher, which is designed to aid the analyst in dry-polishing for the generation of surfaces free of contamination from polishing media while retaining the necessary smoothness for good correlation between chemical heat maps and optical micrographs.

The identification of the domains was based on selective infiltration by styrene monomer, which originated from the polyester resin used to embed samples. This contaminant was eliminated when the films were embedded in epoxy, but styrene monomer became useful as a selective staining agent for Raman spectroscopy. As a non-polar entity, styrene was easily detected by the laser and thus produced a marker peak that featured prominently in the low OH SC resin and in the continuous polymer matrix of the blended coating. This peak was very small or absent in the high OH SC resin and in the domains. Styrene monomer was also introduced into the coatings as a vapor, and produced the same spectroscopic results with respect to the marker peak. This behavior served as strong evidence that the domains consisted of the high OH resin.

The identification was performed on films fully cured at 12 minutes at 204 °C. This prompted a monitoring the of the cure via FTIR and Raman spectroscopy of the reactants and films quenched at cure-times of 1, 1.5, 2, 2.5, 3, 4, 6, and 9 minutes. The double bond region (2000 cm^{-1} – 1600 cm^{-1}) was emphasized due to the presence of four carbonyl (C=O) peaks in the initial spectra of fully cured films. Analysis of the reactants and quenched films revealed three C=O peaks originating from the compatibilizer: urea, urethane, and ε-caprolactam blocking agent. Curve-fitting of high-resolution spectra revealed five carbonyl peaks in total, as the ester C=O was determined to consist of two components (free and H-bonded). Among the SC films, the high OH film had the greater

urea, urethane, and ε-caprolactam peaks. The urethane peak correlated with crosslink density. In the blend, this peak increased when measurements were performed at the film underside, which is consistent with the observed accumulation of domains at the substrate. However, the urea and ε-cap C=O peaks were smaller in the domains than in the polymer matrix, and thus was not consistent with the high OH film.

The discrepancy in peak intensity between the phases may be explained by higher crosslink density within the domains generating a diffusion gradient between the phases. One source of evidence for this is from transmission electron micrographs of epoxy-embedded cross-section samples stained with heavy metal salts for enhanced contrast. These micrographs revealed holes that resided almost exclusively in the matrix, which likely originated from trapped bubbles of free ε-caprolactam. Additionally, bubbles were observed at the outside of domain boundaries. When the phases were analyzed by Raman spectroscopy at the surface and epoxy-embedded cross-section, there was a consistent decline in the ε-cap peak for both phases throughout the cure while the intensity difference between them was maintained. The lower urea peak within the domains may have been due to a diffusion gradient between the phases that led to a higher concentration of compatibilizer within the matrix.

Selective staining with styrene was attempted with quenched samples. Raman analysis revealed that styrene monomer did not change concentration in the polymer matrix, but it did decrease in the domains as the cure time progressed. TEM analysis of the cross-sections revealed decreasing plasticization by styrene until it was no longer evident in fully cured films, which indicates a completion of the crosslinking reaction.

These samples also did not display enhanced contrast by the heavy metals until full cure was reached.

Data from vibrational spectroscopy and TEM was also complemented with data from DSC, LSC, and rheometry. The overall analysis of the combined data provided evidence for a mechanism of curing dynamics in terms of domain evolution. TEM revealed that domains were present in the powder, which meant the resins do not fully compatibilize into a single phase during extrusion. When the cure started, the surface roughness rapidly increased until at 3 minutes, when the second T_g was detected. Underlying the roughening was rapid coarsening of domains. Evidence suggests that this is the result of a coupling between hydrodynamic forces and coalescence by interdroplet diffusion. Coinciding with the second T_g was a secondary phase transition, in which the domains were accompanied by a cocontinuous network that disappeared at 4 minutes. The surface roughness increased at a slower rate in the 3-minute to 9-minute samples, then declines until full cure in the 12-minute sample. This slower rate is rooted in the viscosity increasing to the point of eliminating hydrodynamic forces, thus leaving coalescence as the remaining mechanism for domain coarsening. The maximum roughness is characterized by bulging from domains as large as the coating layer itself, which may have been thinned from mass loss due to outgassing of caprolactam. The bulges on the coating surface disappeared when the large domains flattened onto the substrate due to surface wetting. This wetting behavior is likely explained by interfacial energy gradients between the phases, with the domains possessing interfacial energies that are closer in magnitude to the tin substrate.

The evolution of the morphology was also investigated for pigmented films. It was immediately apparent that pigment particles of all shapes and sizes had segregated into the domains, even for the powder. This segregation was observed for black, green, and tan coatings. Pigments were best observed under SEM, and were largely flocculated due to the segregation by the phases, sometimes to the point where domains could be delineated. Hence, TEM and SEM complement each other as analytical techniques.

We propose that the ultra-low gloss results from the following:

- forced flocculation of pigment particles by the domains, and
- mass loss from evaporation of ε-caprolactam, which thinned the coating layer, thereby causing the coating surface to conform to the shapes of the pigments at the surface without ever allowing the pigments themselves to surface.

The pigment segregation is likely similar to the observed domain adhesion on the substrate, which is caused by the domains' higher interfacial energy likely rooted in the larger number of hydroxides in the high OH resin being able to hydrogen-bond with hydroxides on the surfaces of metal oxide pigment particles. When the substrate was pre-treated with an epoxy primer, domain adhesion did not occur, which may be due to the interfacial energies of the matrix phase and epoxy becoming more similar in magnitude.

10.2 Future work

In these experiments, the crosslink density was indirectly monitored by measuring the concentration of styrene monomer within the phases, but measurements of mechanical properties such as the Young's modulus and hardness would provide additional insight into the changing crosslink density with respect to cure-time.

Nanoindentation provided a direct measurement of local hardness for the 2.5-minute and 3-minute samples. Completing such measurements for all of the quenched samples and correlating the results with the absorption of styrene could strengthen the evidence for a relationship between solvent resistance and crosslink density.

Another area for future exploration is the interphase region between a domain and the matrix. With a length of ~ 50 nm, it was easily observed under TEM, but the necessary resolution for Raman spectroscopy was not accessible in this study. This region could be measurable with tip-enhanced Raman spectroscopy (TERS), which has resolutions into the nm range and could thereby probe how the resin chemistries change at the interphase. By extension, TERS may prove quite useful for investigating cross-sections of early cure-samples, when the large domains appear to be deformed by uneven distributions of compatibilizer at their interfaces. The data could verify theories described by Puyvelde et al. suggesting droplet deformation results from uneven distribution of compatibilizer around the domain boundry.[1]

Another viable technique for mapping could be near-edge x-ray fine structure absorption spectroscopy (NEXAFS). This technique has been used before by our group to investigate how paint strippers solvate polyurethane coatings.[2] It is highly sensitive to aromatic moieties, which are possessed by the polyurethanes and styrene monomer. Thus, it can be applied in investigating how styrene can selectively penetrate one phase. Styrene could be directly applied to coating surfaces, or as a vapor in a headspace. Changes to polymer chain configuration could be discerned, especially when considering differences in crosslink density. NEXAFS could also be used to investigate chemical

changes from prolonged weatherization, as durability is a critical property for outdoor coatings.

Given that metal oxide pigments were encapsulated by dispersed droplets, it stands to reason that other inorganic materials could be encapsulated by immiscible droplets within a binder. Polymeric encapsulation of inorganic particles has long been an area of interest in the biomedical industry,[3] but has seen little application in functional coatings.[4] The observed encapsulation in these coatings could be a technology worth exploring for coatings that utilize toxic materials such as zinc chromate. By better understanding of the interfacial energy gradients needed to enclose particles of various compositions, we may design such coating systems that meet the necessary demands while maintaining cost-effectiveness, durability and environmental benignancy.

10.3 Closing remarks

Unconventional methods of preparing cross-sections were needed to enable thorough analysis of complex coating systems by complementary spectroscopies (Raman, FTIR) and microscopies (TEM, SEM). By investigating the changing chemistry and coating morphology before, during, and after oven-curing, we have developed a comprehensive coating model that accounts for structure-property relationships between the surface and the bulk.

10.4 References

1. Puyvelde, P. V.; Velankar, S.; Moldenaers, P., Rheology and morphology of compatibilized polymer blends. *Current Opinion in Colloid & Interface Science* **2001,** *6*, 457-463.

2. Young, C. N. Surface and Interfacial Study of Chemical Degradation in Polymer Composites and Coatings. Doctoral Dissertation, State University of New York at Stony Brook, Ann Arbor, 2013.
3. Ladj, R.; Bitar, A.; Eissa, M. M.; Fessi, H.; Mugnier, Y.; Le Dantec, R.; Elaissari, A., Polymer encapsulation of inorganic nanoparticles for biomedical applications. *International Journal of Pharmaceutics* **2013,** *458* (1), 230-241.
4. Ghosh, S. K., Functional Coatings and Microencapsulation: A General Perspective. In *Functional Coatings*, Wiley-VCH Verlag GmbH & Co. KGaA: 2006; pp 1-28.